HIGH FREQUENCY NOISE MODELING AND MICROSCOPIC NOISE SIMULATION FOR SIGE HBT AND RF CMOS

Except where reference is made to the work of others, the work described in this dissertation is my own or was done in collaboration with my advisory committee. This dissertation does not include proprietary or classified information.

Yan Cui

Certificate of Approval:

Stuart M. Wentworth
Associate Professor
Electrical and Computer Engineering

Guofu Niu, Chair
Professor
Electrical and Computer Engineering

Foster Dai
Associate Professor
Electrical and Computer Engineering

Joe F. Pittman
Interim Dean
Graduate School

High Frequency Noise Modeling and Microscopic Noise Simulation for SiGe HBT and RF CMOS

Yan Cui

A Dissertation

Submitted to

the Graduate Faculty of

Auburn University

in Partial Fulfillment of the

Requirements for the

Degree of

Doctor of Philosophy

Auburn, Alabama
December 15, 2005

HIGH FREQUENCY NOISE MODELING AND MICROSCOPIC NOISE SIMULATION

FOR SIGE HBT AND RF CMOS

Yan Cui

Signature of Author

Date of Graduation

VITA

Yan Cui, daughter of Fengde Cui and Shuxian Song, spouse of Zhiming Feng, was born on 4 September, 1975, in JiaMuSi, Heilongjiang Province, P. R. China. She received her BS degree from Jilin University in 1995, majoring in Electronics Engineering. She received her MS degree from Jilin University in 1998, majoring in Electronics Engineering. In Spring 2002, she was accepted into the Electrical and Computer Engineering department of Auburn University, Auburn, Alabama, where she has pursued her Ph.D degree.

DISSERTATION ABSTRACT

HIGH FREQUENCY NOISE MODELING AND MICROSCOPIC NOISE SIMULATION FOR SIGE HBT AND RF CMOS

Yan Cui

Doctor of Philosophy, December 15, 2005
(M.S., Jilin University, 1998)
(B.S., Jilin University, 1995)

351 Typed Pages

Directed by Guofu Niu

RF bipolar and CMOS are both important in RFIC applications. Modeling of noise provides critical information in the design of RF circuits. Unfortunately, available compact models for both RF bipolar and CMOS, are typically not applicable for the GHz frequency range. In this dissertation, a new technique of simulating the spatial distribution of microscopic noise contribution to the input noise current, voltage, and their correlation is presented, and applied to both RF SiGe HBT transistor and RF MOSFET transistor.

For RF SiGe HBT transistor, bipolar transistor noise modeling and noise physics are examined using microscopic noise simulation. Transistor terminal current and voltage noises resulting from velocity fluctuations of electrons and holes in the base, emitter, collector, and substrate are simulated using the new technique proposed, and compared with modeling results. Major physics noise sources in bipolar transistor are qualitatively identified. The relevant importance as well as model-simulation discrepancy is analyzed for each physical noise source.

Moreover, the RF noise physics and SiGe profile optimization for low noise are explored using microscopic noise simulation. A higher Ge gradient in a noise critical region near the EB

junction, together with an unconventional Ge retrograding in the base to keep total Ge content below stability, when optimized, can lead to significant noise improvement without sacrificing peak cutoff frequency and without any significant high injection cutoff frequency rolloff degradation.

For RF MOSFET transistor, RF noise of 50 nm L_{eff} CMOS is simulated using hydrodynamic noise simulation. Intrinsic noise sources for the Y- and H- noise representations are examined and models of intrinsic noise sources are proposed. The relations between the Y- and H- noise representations for MOSFETs are examined, and the importance of correlation for both representations is quantified. The H- noise representation has the inherent advantage of a more negligible correlation, which makes circuit design and simulation easier.

The extrinsic gate resistance is important as well as the intrinsic drain noise current for noise modeling of scaled MOSFET. Accurately extract the gate resistance becomes an important issue. The frequency and bias dependence of the effective gate resistance are explained by considering the effect of gate-to-body capacitance, gate to source/drain overlap capacitances, fringing capacitances, and Non-Quasi-Static (NQS) effect. A new method of separating the physical gate resistance and the NQS channel resistance is proposed.

Finally, drain current excess noise factors in CMOS transistors are examined as a function of channel length and bias. The technology scaling are discussed for different processes. Using standard linear noisy two-port theory, a simple derivation of noise parameters is presented. The results are compared with the well known Fukui's empirical FET noise equations. Experimental data are used to evaluate the simple model equations. New figures-of-merit for minimum noise figure is proposed.

Acknowledgments

I would like to express my gratitude to my supervisor, Dr. Guofu Niu. Without him, this dissertation would not have been possible. I thank him for his patience and encouragement that carried me on through difficult times, and for his insights and suggestions that helped to shape my research skills. I appreciate his vast knowledge and skill in many areas, and his valuable feedback that greatly contributed to this thesis. I would like to thank the other members of my committee, Dr. Foster Dai, Dr. Stuart M. Wentworth, and Dr. John R. Williams for the assistance they provided.

Several people deserve special recognition for their contributions to this work. I would like to thank Yun Shi and Muthubalan Varadharajaperumal for their help with the DESSIS input deck, and Qingqing Liang, Ying Li and Xiaoyun Wei for their help with device measurement. I would like to thank Dr Susan Sweeney of IBM Microelectronics Communications R&D Center for her great help with noise measurement data. I would like to thank Dr. Stewart S. Taylor of Intel Corporation for helpful discussions. I would also like to thank Dr. J.D. Cressler of Georgia Institute of Technology for his contributions.

Finally, I am forever indebted to my parents for the support they provided me through my entire life and in particular, I must acknowledge my husband and best friend, Zhiming Feng, without whose love, and encouragement, I would not have finished this dissertation.

In conclusion, I recognize that this research would not have been possible without the financial assistance of the National Science Foundation under ECS-0119623 and ECS-0112923, the Semiconductor Research Corporation under SRC #2001-NJ-937, and Intel Corporation.

Style manual or journal used IEEE Transactions on Electron Devices (together with the style known as "aums"). Bibliography follows van Leunen's *A Handbook for Scholars*.

Computer software used The document preparation package TEX (specifically LATEX) together with the departmental style-file `aums.sty`. The plots were generated using VossPlot®, MATLAB®, TecPlot®and Microsoft Visio®.

TABLE OF CONTENTS

LIST OF FIGURES

List of Tables

Chapter 1

Introduction

Wireless communications have been thrived in the last decade, due to tremendously increasing demand for information need for connectivity. The rapid development of personal communication systems, such as cellular phones, cordless phones, GPS (global positioning system), and WLAN (wireless local area network), have aroused considerable interests in high frequency devices. The RFICs (radio frequency integrated-circuits) designs are among the most demanding design tasks. The recent bipolar and CMOS technologies provide relatively high cutoff frequencies (f_T). The RFICs have been the primary domain for modern bipolar and CMOS applications in GHz frequency range.

RF bipolar and CMOS are both important in RFIC applications. RF bipolar device is known for its low noise, low power consumption, high reliability and better thermal management, hence it can be used as the first stage LNA (low noise amplifier) of RF transceiver design. RF CMOS device is known for its high speed and high level of integration, therefore it is perfect for large-scale digital applications in RF transceiver design. Accurate models are critical in order to reduce design cycles and to achieve first-time success in implementation. Unfortunately, available compact models for both RF bipolar and CMOS, are typically not applicable for the GHz frequency range.

Modeling of noise provides critical information in the design of RF circuits. Lack of understanding of RF device noise presents a substantial barrier to the design of RF circuits. It is extremely inevitable procedure to understand the physical origin of broadband noise and incorporate in the noise modeling of RF devices.

1.1 RF Noise

Noise can be defined as “everything except desired signal”. Noise sources that can be reduced or eliminated using good shield system is called *Artificial* noise. For example, the noise sources that interfering with broadcasting signal for radio and TV. On the other hand, noise sources that is inherent in the system or devices itself and is irreducible is called *Fundamental* noise. For example, the snow pictures in analog TV sets. Fundamental noise is random yet can be statistically characterized. There are several types of fundamental noise sources: thermal noise, shot noise, flicker noise, and generation-recombination noise (G-R noise).

In RF bipolar and MOSFET transistors, thermal noise and shot noise are the main noise sources. Flicker noise is negligible in RF noise modeling, since its $1/f$ characteristic. G-R noise is much smaller than flicker noise, and can be generally neglected. Therefore we will not discuss flicker noise and G-R noise in this work. We will focus on thermal noise and shot noise in RF bipolar and MOSFET transistors.

1.1.1 Thermal Noise

A thermally-excited carrier in a conductor undergoes a random walk Brownian motion via collisions with the lattice of the conductor. As a result it produces fluctuations in the terminal characteristics. In 1927, Johnson discovered that the noise power spectrum of a conductor is independent of its material and the measurement frequency. He also found that noise power spectrum is determined only by the temperature T and electrical resistance R under thermal equilibrium:

$$< v_n^2 > = S_{v_n} \Delta f, \tag{1.1}$$

$$S_{v_n} = 4kTR, \tag{1.2}$$

$$< i_n^2 > = S_{i_n} \Delta f, \tag{1.3}$$

$$S_{i_n} = \frac{4kT}{R}, \tag{1.4}$$

where S_{v_n} and S_{i_n} are the power spectral density of v_n and i_n, respectively. k is the Boltzmann constant. Thermal noise is also called Johnson noise or Nyquist noise.

1.1.2 Shot Noise

Shot noise refers to the fluctuations associated with the *dc* current I_{DC} flow across a potential barrier. Shot noise is white noise, and is described as

$$< i_n^2 >= 2qI_{DC} \Delta f. \tag{1.5}$$

Two conditions are required for shot noise to occur: a flow of direct current and a potential barrier over which the carriers are extracted. In RF bipolar devices, base current shot noise and collector current shot noise are considered for the intrinsic device. In RF MOSFET transistors, shot noise dominates the noise characteristics only when the device is in the subthreshold region owing to the carrier transport in this region.

1.2 Noise Parameters

Signal-to-noise ratio describes the ratio of useful signal power and the unwanted noise power. When a combination of signal and noise go through a noisy two-port network, as shown in Fig. 1.1, both the signal and unwanted noise will be amplified at the same factor. In addition, the two-port network adds its own noise. Therefore, the signal-to-noise ratio becomes smaller after a noisy two-port network. Noise factor F is defined as the signal-to-noise ratio at the input divided by the signal-to-noise ratio at the output.

$$F = \frac{S_i/N_i}{S_o/N_o}, \tag{1.6}$$

it defines noise figure NF according to

$$NF = 10log_{10}(F). \tag{1.7}$$

It is a useful measure of the amount of noise added by the noisy two-port network. [10]

The noise figure of a two-port network is determined by the source admittance $Y_s = G_s + jB_s$, and the noise parameters of the circuit, including the minimum noise figure NF_{min}, the noise resistance R_n, and the optimum source admittance $Y_{opt} = G_{opt} + jB_{opt}$, through [11]

$$F = F_{min} + \frac{R_n}{G_s} \left| Y_s - Y_{opt} \right|^2, \tag{1.8}$$

$$NF_{min} = 10log_{10}(F_{min}). \tag{1.9}$$

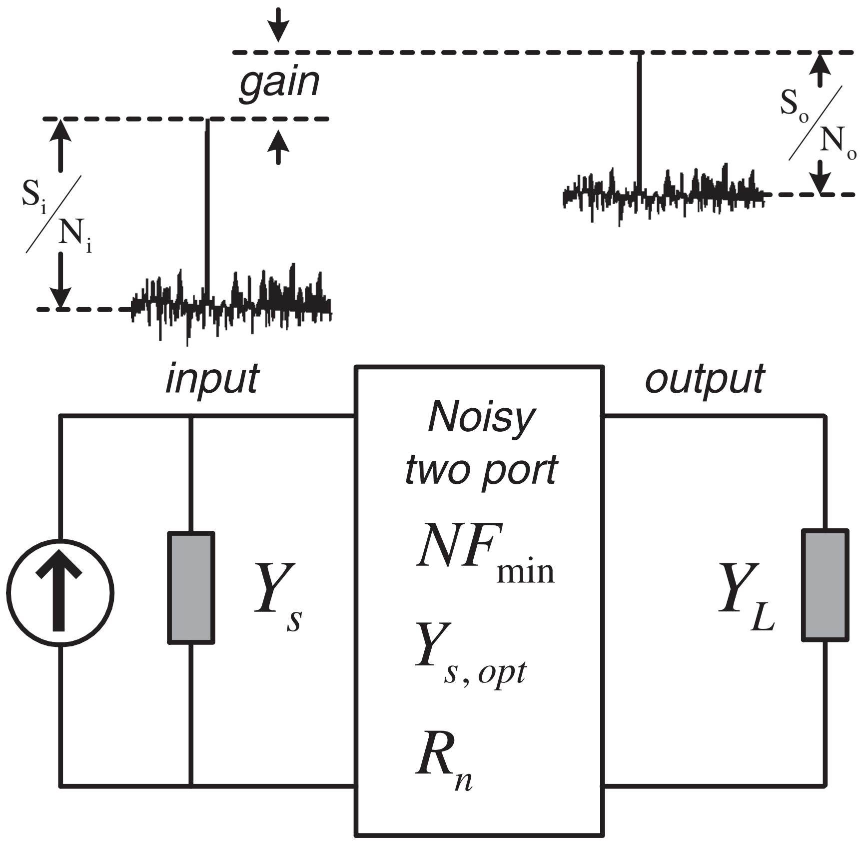

Figure 1.1: Illustration of definition of noise figure for a noisy two-port.

1.2.1 Minimum Noise Figure NF_{min}

The minimum noise figure NF_{min} is a very important parameter for noise. As self-explained in its name, NF_{min} determines the minimum noise figure for a noisy two-port network. NF reaches its minimum NF_{min} when $Y_s = Y_{opt}$. It indicates the attribute of the noisy two-port. The lowest possible NF_{min} is accordingly desired. For RF bipolar transistor and MOSFET transistor, NF_{min} is dependent on both bias and frequency.

1.2.2 Noise Resistance R_n

The noise resistance R_n determines the sensitivity of noise figure to deviations from Y_{opt}. A small R_n is desired to alleviate the deviations. For RF bipolar transistor and MOSFET transistor, R_n is frequency independent. R_n is only dependent on bias.

1.2.3 Optimum Source Admittance Y_{opt}

The optimum source admittance Y_{opt} determines the source admittance where NF reaches its minimum. The value of Y_{opt} indicates the "noise matching" source admittance for minimum noise figure, which normally differs from the "gain matching" source admittance for maximum power transfer. Y_{opt} has a real part of G_{opt} and an imaginary part of B_{opt}. For RF bipolar transistor and MOSFET transistor, G_{opt} and B_{opt} are dependent on both bias and frequency.

1.3 RF Bipolar Transistor Compact Noise Modeling

The noise of an RF bipolar device can be considered as a lumped base resistance with thermal noise voltage S_{v_b,v_b^*}, connected to an intrinsic transistor with an input noise current S_{i_b,i_b^*} and an output noise current S_{i_c,i_c^*}, as shown in Fig. 1.2. At low injection, the noise of the lumped base resistance can be modeled as $4kTr_b$ [1].

1.3.1 Lumped Base Resistance

It is possible to separate current crowding effects from all the effects that play a role in the intrinsic transistor [1]. This means the intrinsic transistor noise model is independent of base resistance and current crowding. All the current crowding effects are taken care of by a branch that contains the base resistance as shown in Fig. 1.3 [1]. The resulting noise current associated

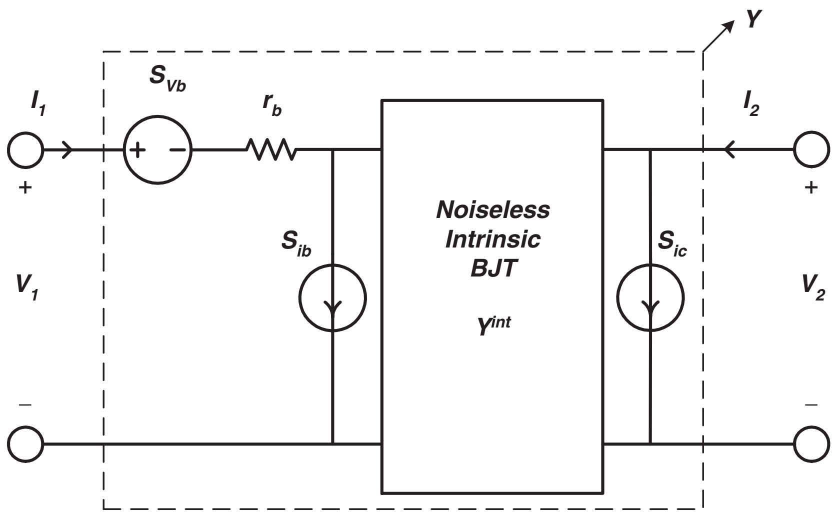

Figure 1.2: RF Bipolar transistor noise modeling.

with the lumped base resistance is no longer $4kTr_b$, instead [1] showed,

$$\Re(y_R) = 1/r_b.S_{i_R,i_R^*} = \frac{4kT}{r_b} + \frac{10}{3}qI_B. \tag{1.10}$$

At low injection, where I_B contribution can be neglected, $4kTr_b$ can still be used to describe the noise of the lumped base resistance. At high injection, the noise of the lumped base resistance is dominated by $\frac{10}{3}qI_B$ [1].

The intrinsic transistor noise modeling is separated from the lumped base resistance branch. Accurate noise modeling for the intrinsic transistor is needed. Different noise models have different expressions for the input noise current, the output noise current, and their correlation for the intrinsic transistor, as will be detailed below.

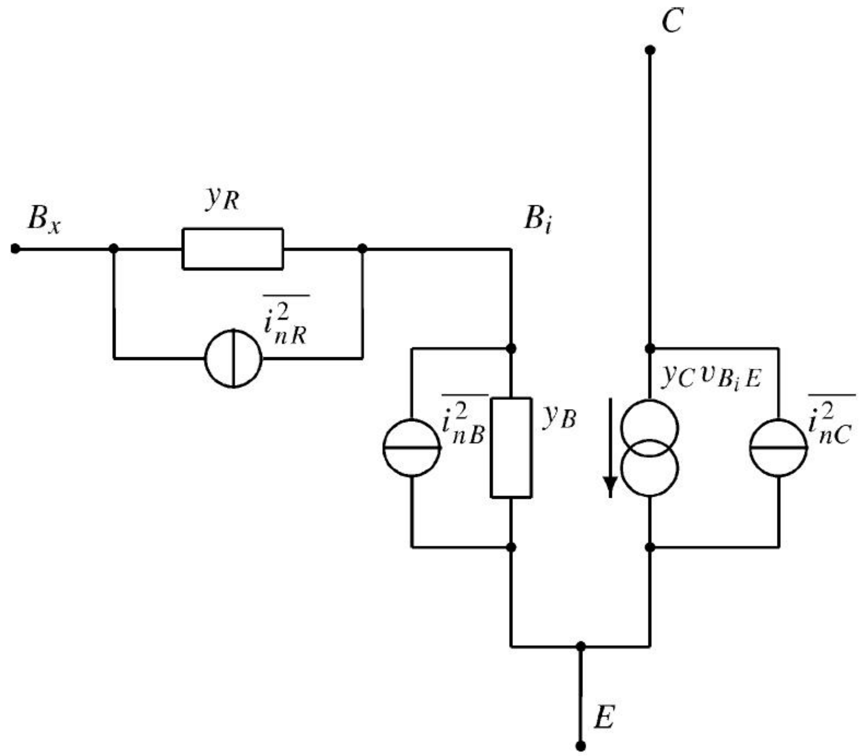

Figure 1.3: Equivalent circuit proposed for the intrinsic transistor together with the resistance of the pinched base [1].

1.3.2 SPICE Model

The SPICE model as shown in Fig. 1.4, is the essence of noise modeling in major CAD tools. The noise physics accounted for include: base resistance thermal noise S_{v_b,v_b^*}, and base current shot noise $2qI_B$, and collector current shot noise $2qI_C$ for the intrinsic transistor.

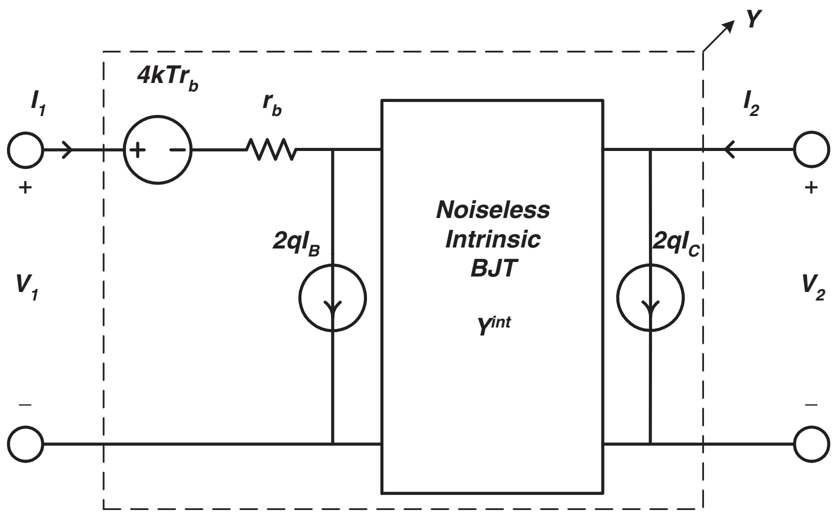

Figure 1.4: SPICE model for RF bipolar transistor.

In SPICE model, the noise of the intrinsic transistor is described by

$$S_{i_b,i_b^*} = 2qI_B, \tag{1.11}$$

$$S_{i_c,i_c^*} = 2qI_C, \tag{1.12}$$

$$S_{i_c,i_b^*} = 0. \tag{1.13}$$

Since the input noise current and the output noise current are both shot noise, they are only bias dependent, and do not depend on frequency. Moreover, the input and output noise currents are not correlated to each other in this model. This approach is used by SPICE Gummel-Poon, VBIC, Mextram, and Hicum models. The accuracy of such compact noise modeling, however, becomes worse at higher current densities required for high speed [3]. At high frequency or high current densities, the base and collector current noises are no longer shot like, and their correlation can becomes appreciable [12], as will detailed in chapter 4.

1.3.3 van Vliet Model

About 30 years ago, van Vliet proposed a general noise model in three-dimensional junction device of arbitrary geometry using transport noise theory for low injection [13]. The structure of the model is the same as the intrinsic transistor shown in Fig. 1.2. The van Vliet model is derived from rigorous microscopic noise theory of minority carrier transportation in the base region. Different from the SPICE model, the input noise current of van Vliet model is frequency dependent, which comes from the intrinsic Y parameter Y_{11}^{int}. Moreover, the input noise current and the output noise current are correlated to each other. The correlation term is related to the intrinsic Y parameters Y_{12}^{int} and Y_{21}^{int}, hence both bias and frequency dependent. In van Vliet model, the noise of the intrinsic transistor at low injection is described by

$$S_{i_b,i_b^*} = 4kT\Re(Y_{11}^{int}) - 2qI_B, \tag{1.14}$$

$$S_{i_c,i_c^*} = 2qI_C + 4kT\Re(Y_{22}^{int}), \tag{1.15}$$

$$S_{i_c,i_b^*} = 2kT(Y_{21}^{int} + Y_{12}^{int*}) - 2qI_C. \tag{1.16}$$

The noise of the intrinsic transistor is obtained from *dc* currents and *ac* Y-parameters, and no additional parameter is required.

For a simple small signal model of the intrinsic bipolar transistor as shown in Fig. 1.5,

$$Y_{11}^{int} = g_{be} + j\omega(C_{be} + C_{cb}), \tag{1.17}$$

$$Y_{12}^{int} = -j\omega C_{cb}, \tag{1.18}$$

$$Y_{21}^{int} = g_m e^{-j\omega\tau} - j\omega C_{cb}, \tag{1.19}$$

$$Y_{22}^{int} = j\omega C_{cb}, \tag{1.20}$$

where g_{be} is the input conductance, g_m is the transconductance, C_{be} is the EB capacitance, C_{cb} is the CB capacitance, and g_o is the output conductance. τ is the second-order time delay owing to the transcapacitance. Since

$$I_B \approx \frac{g_{be}}{kT/q}, \tag{1.21}$$

$$I_C \approx \frac{g_m}{kT/q}. \tag{1.22}$$

(1.16) can be further derived to

$$S_{i_c,i_b^*} = 2kT(g_m e^{-j\omega\tau}) - 2qI_C, \tag{1.23}$$

$$= 2qI_C\left(e^{-j\omega\tau} - 1\right). \tag{1.24}$$

Although the van Vliet model does not consider the CB space-charge-region (SCR) effect in its derivation, the correlation equation has included the carrier transport delay term as will discussed in the section 1.3.4.

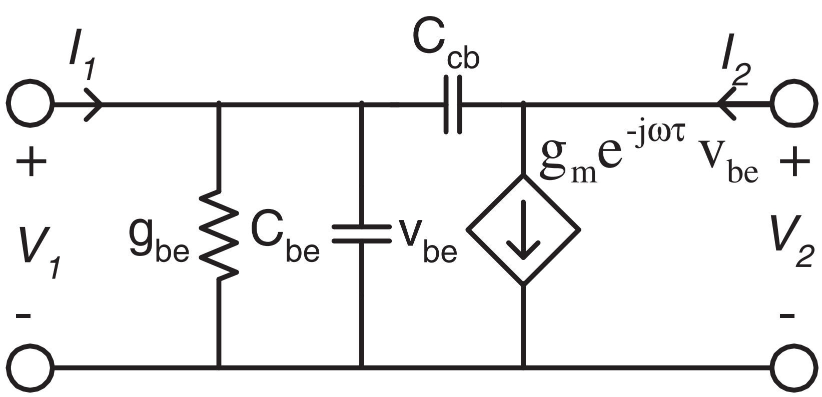

Figure 1.5: The small-signal equivalent circuit for intrinsic bipolar device.

At low frequency where $\tau \approx 0$, (1.14), (1.15) and (1.16) reduce to their low frequency expressions:

$$S_{i_b,i_b^*} = 2qI_B, \tag{1.25}$$

$$S_{i_c,i_c^*} = 2qI_C, \tag{1.26}$$

$$S_{i_c,i_b^*} = 0, \tag{1.27}$$

which are the same as the SPICE model expressions.

As will be discussed in details in chapter 4, the van Vliet model describes RF bipolar transistor noise well in low injection. For high current density, however, the van Vliet model for the low injection cannot accurately model the noise in the transistor. In [13], extra modification parameters are introduced for high current density based on low injection results. For example,

$$S_{i_b,i_b^*} = A(4kT\Re(Y_{11}^{int}) - 2qI_B), \tag{1.28}$$

where A is a modification factor. This provides us a way leading to a new noise model for bipolar transistor as discussed in chapter 4.

1.3.4 Time-delay and Phase-delay Model

Time-delay noise model is proposed by M. Rudolph in 1999 using common-emitter configuration, as shown in Fig. 1.6 [2]. The noise contributions of the input and output current sources i_c' and i_c'' related to the collector current I_C are caused by the same electrons. The electron noise sources injected from the emitter into the base, cross the CB junction, and then reach the collector. Therefore the correlation of these sources is given by a time delay $e^{-j\omega\tau}$, i.e.,

$$i_c'' = i_e' e^{-j\omega\tau}, \tag{1.29}$$

$$i_c' = i_e' - i_c'', \tag{1.30}$$

$$= i_c'' \left(e^{j\omega\tau} - 1\right). \tag{1.31}$$

Therefore $S_{i_c', i_c'^*}$, $S_{i_c'', i_c''^*}$, and their correlation are

$$S_{i_c'', i_c''^*} = 2qI_C, \tag{1.32}$$

$$S_{i_c', i_c'^*} = S_{i_c'', i_c''^*} \left| e^{j\omega\tau} - 1 \right|^2 = 2qI_C \left| e^{j\omega\tau} - 1 \right|^2, \tag{1.33}$$

$$S_{i_c', i_c''^*} = S_{i_c'', i_c''^*} \left(e^{j\omega\tau} - 1\right) = 2qI_C \left(e^{j\omega\tau} - 1\right). \tag{1.34}$$

The noise current source related to the base current I_b is assumed not to correlated with the others [2]. Therefore the input noise current S_{i_b, i_b^*}, the output noise current S_{i_c, i_c^*}, and their correlation S_{i_c, i_b^*} for time-delay model are

$$S_{i_b, i_b^*} = 2qI_B + 2qI_C \left| 1 - e^{j\omega\tau} \right|^2, \tag{1.35}$$

$$S_{i_c, i_c^*} = 2qI_C, \tag{1.36}$$

$$S_{i_c, i_b^*} = 2qI_C \left(e^{-j\omega\tau} - 1\right). \tag{1.37}$$

The phase-delay noise model is proposed by G.F. Niu in 2001 using common-base configuration [3]. The essence of the phase-delay noise model is shown in Fig. 1.7. The collector current shows shot noise only because the electron current being injected into the collector-base

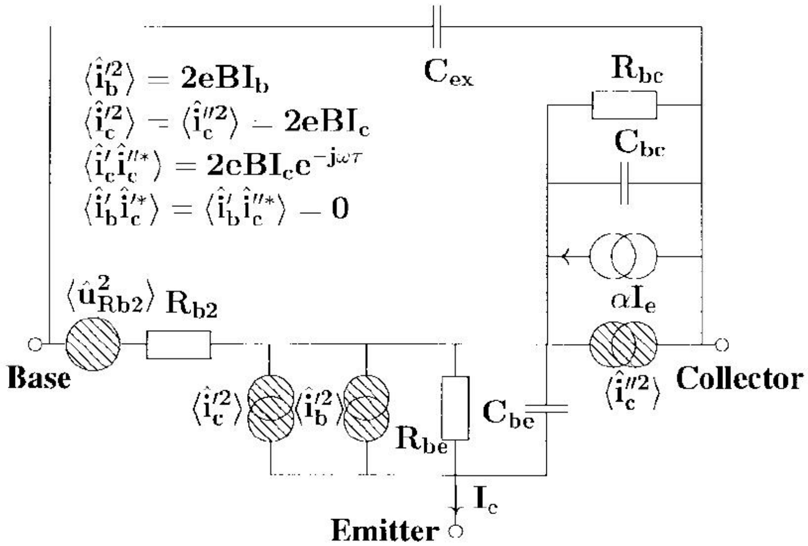

Figure 1.6: Time-delay noise model in [2].

junction from the emitter already has shot noise. The emitter current short noise consists of two parts, $S_{i_{ne},i^*_{ne}} = 2qI_C$, due to the electron injection into the base, and $S_{i_{pe},i^*_{pe}} = 2qI_B$, due to the hole injection into the emitter. The electron injection process and the hole injection process are independent of each other and hence not correlated. The transition of electrons across the collector-base junction, which is usually reverse biased, is a drift process, causing a delay version of the emitter electron injection induced shot noise,

$$i_{nc} = i_{ne}e^{-j\omega\tau_n}, \tag{1.38}$$

where τ_n is the transit time associated with the transport of emitter-injected electron shot noise current, which includes both the transit time in the base and the transit time in the CB junction.

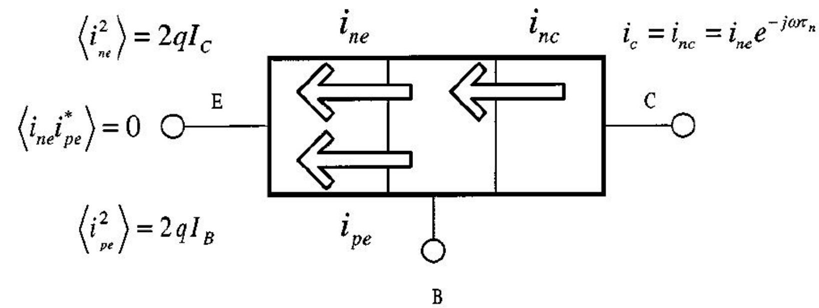

Figure 1.7: Phase-delay noise model in [3].

In common-base configuration model, the noise sources associated with the collector and emitter currents, i_c and i_e, are used,

$$S_{i_c,i_c^*} = S_{i_{nc},i_{nc}^*} = 2qI_C, \tag{1.39}$$

$$S_{i_e,i_e^*} = S_{i_{ne},i_{ne}^*} + S_{i_{pe},i_{pe}^*} = 2qI_C + 2qI_B, \tag{1.40}$$

$$S_{i_e,i_c^*} = 2qI_C e^{j\omega\tau_n}. \tag{1.41}$$

Common-base noise sources i_c and i_e can be easily converted to common-emitter noise sources i_b and i_c by equivalent circuit analysis

$$S_{i_b,i_b^*} = S_{i_e,i_e^*} + S_{i_c,i_c^*} - 2\Re(S_{i_c,i_e^*}), \tag{1.42}$$

$$S_{i_c,i_c^*} = S_{i_c,i_c^*}, \tag{1.43}$$

$$S_{i_c,i_b^*} = S_{i_c,i_e^*} - S_{i_c,i_c^*}. \tag{1.44}$$

Therefore (1.39) – (1.41) can be converted to the common-emitter version using (1.42) – (1.44)

$$S_{i_b,i_b^*} = 2qI_E + 2qI_C - 4qI_C \Re\left(e^{j\omega\tau_n}\right), \tag{1.45}$$

$$S_{i_c,i_c^*} = 2qI_C, \tag{1.46}$$

$$S_{i_c,i_b^*} = 2qI_C\left(e^{-j\omega\tau_n} - 1\right). \tag{1.47}$$

(1.45) can be further simplified to

$$S_{i_b,i_b^*} = 2qI_B + 4qI_C - 4qI_C \Re\left(e^{j\omega\tau_n}\right), \tag{1.48}$$

$$= 2qI_B + 2qI_C\left[2 - 2\Re\left(e^{j\omega\tau_n}\right)\right], \tag{1.49}$$

$$= 2qI_B + 2qI_C\left|1 - e^{j\omega\tau_n}\right|^2, \tag{1.50}$$

Note that if $\tau = \tau_n$, (1.50), (1.46), and (1.47) are the same as (1.35), (1.36), and (1.37). Although derived from different angle, the time-delay model and phase-delay model ultimately give the same noise model expressions. At low frequency, the time-delay model and phase-delay model can be further simplified to,

$$S_{i_b,i_b^*} = 2qI_B, \tag{1.51}$$

$$S_{i_c,i_c^*} = 2qI_C, \tag{1.52}$$

$$S_{i_c,i_b^*} = 0, \tag{1.53}$$

which are the same as the SPICE model expressions.

1.4 RF MOSFET Transistor Compact Noise Modeling

1.4.1 Gate and Drain Noise currents Modeling

The thermal noise of a MOSFET originates from the thermal noise sources in the channel as illustrated in Fig. 1.8, leading to drain thermal noise current S_{i_d,i_d^*} and induced gate thermal noise current S_{i_g,i_g^*} through capacitive coupling to the gate. Since both S_{i_d,i_d^*} and S_{i_g,i_g^*} are agitated by the thermal noise sources in the channel, they are correlated, and the correlation are imaginary due to the capacitive nature. This noise representation with gate noise current, drain noise current, and their correlation, as shown in Fig. 1.9, is called Y- noise representation as will further introduced in chapter 2.

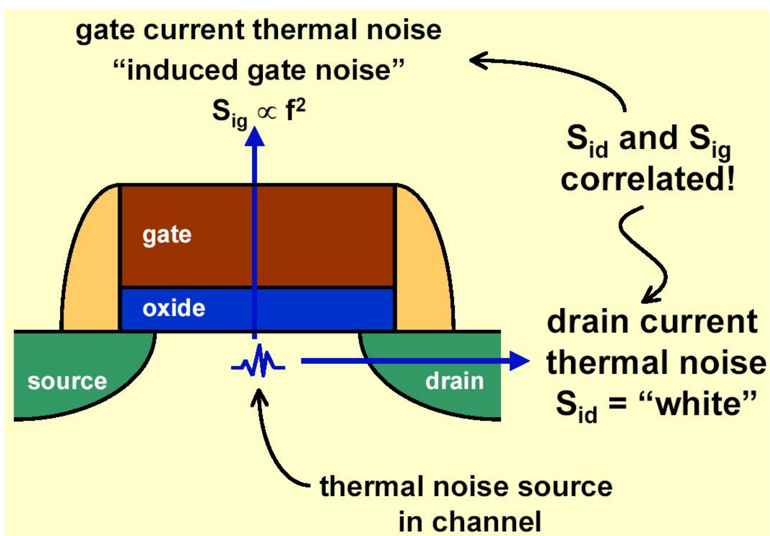

Figure 1.8: Thermal noise in MOSFETs [4].

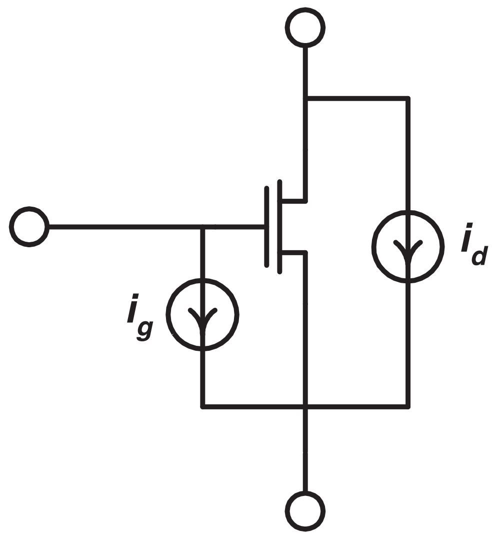

Figure 1.9: MOSFET noise model using gate noise current, drain noise currents, and their correlation.

1.4.1.1 van der Ziel Model

Based on the fact that the MOSFET is a modulated resistor, capacitively coupled to the gate, van der Ziel has proposed a thermal noise model for MOSFETs using impedance field method [14] [15]. This well-known van der Ziel model are widely used in MOSFET noise modeling. The drain noise current, induced gate noise current, and their correlation are modeled as [15],

$$S_{i_d,i_d^*} = \gamma_{g_{d0}} \cdot 4kTg_{d0}, \tag{1.54}$$

$$S_{i_g,i_g^*} = \beta 4kTg_g, \tag{1.55}$$

$$g_g = \eta \frac{\omega^2 C_{gs}^2}{g_{d0}}, \tag{1.56}$$

$$c = \frac{S_{i_g,i_d^*}}{\sqrt{S_{i_d,i_d^*} S_{i_g,i_g^*}}} = jx. \tag{1.57}$$

Here g_{d0} is the zero V_{ds} output conductance, g_g is the input conductance, and C_{gs} is the gate-to-source capacitance. $\gamma_{g_{d0}}$, β, η and x are model parameters. $\gamma_{g_{d0}} = \frac{2}{3}$, $\beta = \frac{4}{3}$, $\eta = \frac{1}{5}$ and $x = 0.395$ for long channel device in saturation region [15]. For short channel device, however, these model parameters deviate from their long channel value, and become bias dependent, as will discussed in chapter 6.

1.4.1.1 Klaassen-Prins Equation

Klaassen and Prins [16] have derived an equation to calculate the noise of a device using the local channel conductivities of the device. The so called Klaassen-Prins equation is extensively used to calculate the noise for long channel MOSFETs [17] [18] [6] [19]. The quasi-static *dc* differential equation for current I_d of a device is [16] [20],

$$I_d = g(V(x))\frac{dV(x)}{dx}, \tag{1.58}$$

where $g(V(x))$ is the local channel conductivity and $V(x)$ is the difference in electron quasi-Fermi potential in the inversion layer and the hole quasi-Fermi potential in the bulk at position x. For a very simple MOSFET,

$$g(V(x)) = \mu C_{ox} W(V_{gs} - V_{th} - V(x)), \tag{1.59}$$

$$= W\mu Q'_I(x), \tag{1.60}$$

where V_{gs} is the gate-source voltage, V_{th} is the threshold voltage, W is the width of the device, μ is the mobility, and C_{ox} is the oxide capacitance per unit area. $Q'_I(x)$ is the local inversion charge, whose integration over area gives the total inversion charge Q_I,

$$Q_I = \int_0^L W Q_I'(x)dx. \tag{1.61}$$

(1.59) shows that $g(V(x))$ is the highest near the source, and the lowest dear the drain.

The derivation of drain noise current can be best illustrated in Fig. 1.10. For the noise segment from x to $x + \Delta x$, a small voltage contribution $v_n(x)$ is added on top of $V(x)$. The noise voltage also leads to a change in the *dc* current through the device, with boundary condition $v_n(x)|_{x=0,L} = 0$ for input and output *ac* short ended condition [16] [20].

$$\begin{aligned}
I_d + \Delta i_d &= g[V(x) + v_n(x)]\frac{d}{dx}(V(x) + v_n(x)) + i_n(x), && (1.62)\\
&= \left[g(V(x)) + \frac{dg(V(x))}{dV(x)}v_n(x)\right]\left(\frac{dV(x)}{dx} + \frac{dv_n(x)}{dx}\right) + i_n(x), && (1.63)\\
&= g(V(x))\frac{dV(x)}{dx} + g(V(x))\frac{dv_n(x)}{dx} + \frac{dg(V(x))}{dx}v_n(x) + \frac{dg(V)}{dV}v_n(x)\frac{dv_n(x)}{dx} + i_n(x). && (1.64)
\end{aligned}$$

Here

$$g[V(x) + v_n(x)] = \left[g(V(x)) + \frac{dg(V(x))}{dV(x)}v_n(x)\right] \tag{1.65}$$

is used. Substituting (1.58) in (1.64), and

$$g(V(x))\frac{dv_n(x)}{dx} + \frac{dg(V(x))}{dx}v_n(x) = \frac{d}{dx}(g(V(x))v_n(x)), \tag{1.66}$$

Δi_d, the fluctuation in I_d, is

$$\Delta i_d = \frac{d}{dx}(g(V(x))v_n(x)) + i_n(x), \tag{1.67}$$

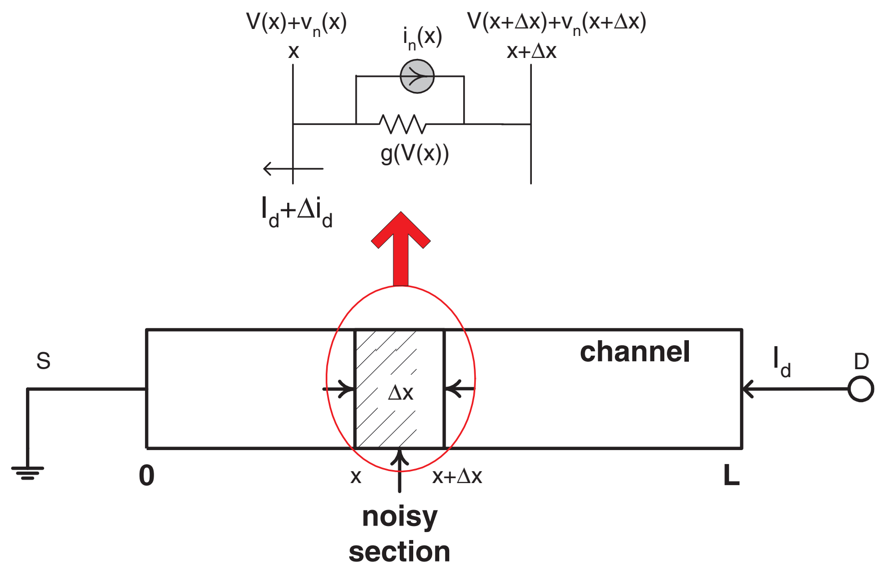

Figure 1.10: Illustration of drain noise current derivation.

Integrating both sides of (1.67), we have [16] [20],

$$\Delta i_d L = \int_0^L \frac{d}{dx}(v_n(x))g(V(x))dx + \int_0^L i_n(x) \cdot dx, \tag{1.68}$$

$$= \int_0^L i_n(x) \cdot dx, \tag{1.69}$$

since

$$\int_0^L \frac{d}{dx}(v_n(x))g(V(x))dx = v_n(x)g(V(x))|_0^L = g(V(L))v_n(L) - g(V(0))v_n(0) = 0, \quad (1.70)$$

Therefore the noise fluctuation in I_d is,

$$\Delta i_d = \frac{1}{L}\int_0^L i_n(x) \cdot dx. \quad (1.71)$$

Δi_d has a zero average $\overline{\Delta i_d} = 0$, and the noise spectral density is [16] [20],

$$S_{i_d,i_d^*} = \frac{\overline{\Delta i_d, \Delta i_d^*}}{\Delta f} = \frac{1}{L^2}\int_0^L \int_0^L \overline{i_n(x), i_n^*(x')} \cdot dxdx'. \quad (1.72)$$

For $i_n(x)$, we have [16] [17],

$$\overline{i_n(x), i_n^*(x')} = 4kTg(V(x))\Delta f \delta(x - x'), \quad (1.73)$$

where δ is the Dirac delta function. The drain thermal noise current is then found by substituting (1.73) into (1.72),

$$S_{i_d,i_d^*} = \frac{4kT}{L^2}\int_0^L g(V(x)) \cdot dx. \quad (1.74)$$

From (1.58), we have

$$dx = \frac{g(V(x))}{I_d}dV(x). \quad (1.75)$$

Substituting into (1.74), we have [16] [17] [18] [20] [21] [22] [23],

$$S_{i_d,i_d^*} = \frac{4kT}{L^2 I_d} \int_0^{V_d} g^2(V) \cdot dV. \tag{1.76}$$

(1.76) is known as Klaassen-Prins equations for thermal noise of a long channel MOSFET. (1.74) can be also expanded using (1.60),

$$S_{i_d,i_d^*} = \frac{4kT}{L^2} \int_0^L W \mu Q_I'(x) dx, \tag{1.77}$$

$$= \frac{4kT}{L^2} \mu Q_I. \tag{1.78}$$

(1.78) is used in models like BSIM.

For long channel device, the drain current I_d in saturation region is

$$I_d = \frac{\mu W C_{ox}}{L} \cdot \frac{1}{2} V_{gt}^2, \tag{1.79}$$

where $V_{gt} = V_{gs} - V_{th}$. Substituting (1.59) and (1.79) into (1.76),

$$S_{i_d,i_d^*} = \frac{4kT}{L^2 I_d} \int_0^{V_{gt}} \mu^2 W^2 C_{ox}^2 (V_{gt} - V)^2 \cdot dV, \tag{1.80}$$

$$= \frac{4kT}{L^2} \frac{2L}{\mu W C_{ox} V_{gt}^2} \cdot \mu^2 W^2 C_{ox}^2 \cdot \frac{1}{3} (V_{gt} - V)^3 \Big|_0^{V_{gt}}, \tag{1.81}$$

$$= 4kT \cdot \frac{2}{3} \cdot \frac{\mu W C_{ox}}{L} V_{gt}, \tag{1.82}$$

$$= 4kT \cdot \frac{2}{3} g_{d0}. \tag{1.83}$$

with

$$g_{d0} = \frac{\mu W C_{ox}}{L} V_{gt}. \tag{1.84}$$

(1.83) is the same as (1.54) in van der Ziel model for long channel device operating in saturation region.

1.4.1.3 Velocity Saturation in Short Channel Devices

In case of velocity saturation effects play a role, the general expression of noise source $i_n(x)$, (1.73), becomes [21] [24] [25] [20],

$$S_{i_n(x),i_n(x)^*} = 4kTg_0 \frac{D_n(E)}{D_n(0)}, \tag{1.85}$$

where $g_0(x) = q\mu_0 n(x) W L$ is the zero-field channel conductivity, $n(x)$ is the electron concentration at position x, $D_n(0) = kT\mu_0/q$ is the diffusion coefficient at zero electric field at the ambient temperature T. The velocity saturation make effects via the scalar noise diffusion coefficient $D_n(E)$,

$$D_n(E) = \frac{\mu_n(E)kT}{q}. \tag{1.86}$$

[20] and [6] argue that it is incorrect to take explicit carrier heating into account by using a temperature $T_e > T$ in (1.85) and (1.86) since $D_n(E)$ has already taken into account all nonequilibrium effects.

Moreover, consider the velocity saturation effects for short channel device, (1.60) becomes [20],

$$g(V(x)) = W\mu_0 Q_I'(x)\frac{1}{1+\frac{\mu_0}{v_{sat}}\frac{dV(x)}{dx}}, \tag{1.87}$$

$$= \frac{g_0(V(x))}{1+\frac{1}{E_{sat}}\frac{dV(x)}{dx}}, \tag{1.88}$$

where $E_{sat} = \frac{v_{sat}}{\mu_0}$ is the saturation electric field, and $g_0(V(x)) = W\mu_0 Q_I'(x)$. Therefore *dc* current for velocity saturation becomes,

$$I_d = \frac{g_0(V(x))}{1+\frac{1}{E_{sat}}\frac{dV(x)}{dx}}\frac{dV(x)}{dx}. \tag{1.89}$$

Integration on both sides gives,

$$I_d = \frac{1}{1+\frac{V_{ds}}{E_{sat}L}} \cdot \frac{1}{L}\int_0^{V_{ds}} g_0(V)dV, \tag{1.90}$$

$$= \frac{1}{1+\frac{V_{ds}}{E_{sat}L}} I_{d0}, \tag{1.91}$$

where I_{d0} is the I_d without velocity saturation effect. Similar derivation are performed, and the resulting drain noise current for velocity saturation is [20],

$$S_{i_d,i_d^*} = \frac{4kT}{I_d L^2}\frac{1}{\left(1+\frac{V_{ds}}{E_{sat}L}\right)^2}\int_0^{V_{ds}} g_0^2(V)dV, \tag{1.92}$$

[4] showed that this improved Klaassen-Prins equation has properly accounted for the velocity saturation effects.

In the case of channel length modulation, the conductivity $g(V(x))$ in the pinch-off region is low compared to that in the channel, which is shown in (1.59). From the improved Klaassen-Prins equation (1.92), the contribution of the pinch-off region can be neglected [26] [4]. However, the effective gate length L_{eff} should be used instead of L in (1.92) [26] [4].

1.4.1.4 BSIM4 Channel Thermal Noise Model

There are two channel thermal noise models in BSIM4, as shown in Fig. 1.11 [5]. One is charge-based model by selecting `tnoiMod=0`. The drain noise current is given by

$$S_{i_d,i_d^*} = \frac{4kT\mu_{eff}}{L_{eff}^2}|Q_{inv}| \cdot NTNOI, \tag{1.93}$$

which is essentially the same as (1.78). Here the parameter $NTNOI$ is introduced for more accurate fitting of short-channel devices.

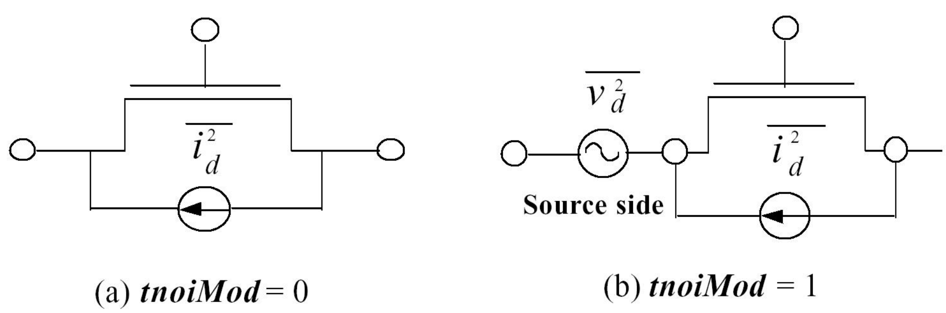

Figure 1.11: Schematic for BSIM4 channel thermal noise modeling [5].

The other is the holistic model by selecting `tnoiMod=1`. In this thermal noise model, all the short-channel effects and velocity saturation effect are automatically included. In addition, a source thermal noise voltage v_d is used to contribute to the induced gate noise with partial correlation to the channel thermal noise, as shown in Fig. 1.11 (b). The source noise voltage is given by

$$S_{v_d,v_d^*} = 4kT\theta_{tnoi}^2 \frac{V_{dseff}}{I_d}, \tag{1.94}$$

and

$$\theta_{tnoi} = RNOIB\left[1 + TNOIB \cdot L_{eff}\left(\frac{V_{gteff}}{E_{sat}L_{eff}}\right)^2\right], \tag{1.95}$$

where $RNOIB = 0.37$ is model parameter. The drain noise current is given by

$$S_{i_d,i_d^*} = 4kT\frac{V_{dseff}}{I_d}[G_{ds} + \beta_{tnoi}(G_m + G_{mbs})]^2, \tag{1.96}$$

and

$$\beta_{tnoi} = RNOIA\left[1 + TNOIA \cdot L_{eff}\left(\frac{V_{gteff}}{E_{sat}L_{eff}}\right)^2\right], \tag{1.97}$$

where $RNOIB = 0.577$ is model parameter.

However, BSIM4 noise model is not accurate. Fig. 1.12 shows comparison of S_{i_d,i_d^*} for the data and BSIM holistic model for the gate length of 0.18 μm device. Device width of 10 μm, and the number of fingers is 8. Data is obtained from Georgia Institute of Technology. Fig. 1.13 shows the noise parameters for the data and BSIM model. The results from BSIM model deviate from the data. A more accurate noise modeling is needed.

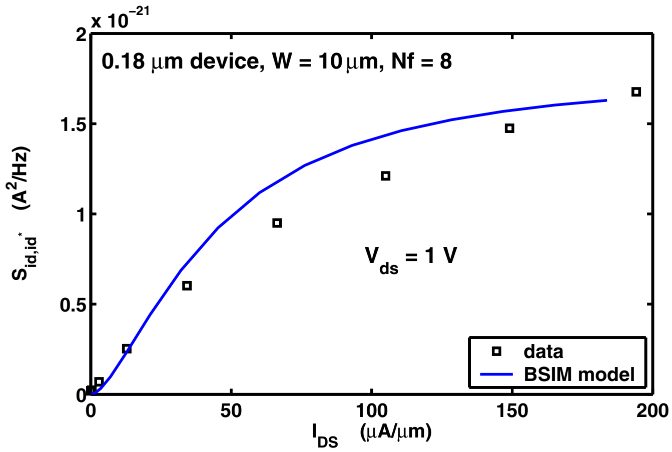

Figure 1.12: Comparison of S_{i_d,i_d^*} for the data and BSIM holistic model for 0.18 μm device. W = 10 μm, Nf = 8.

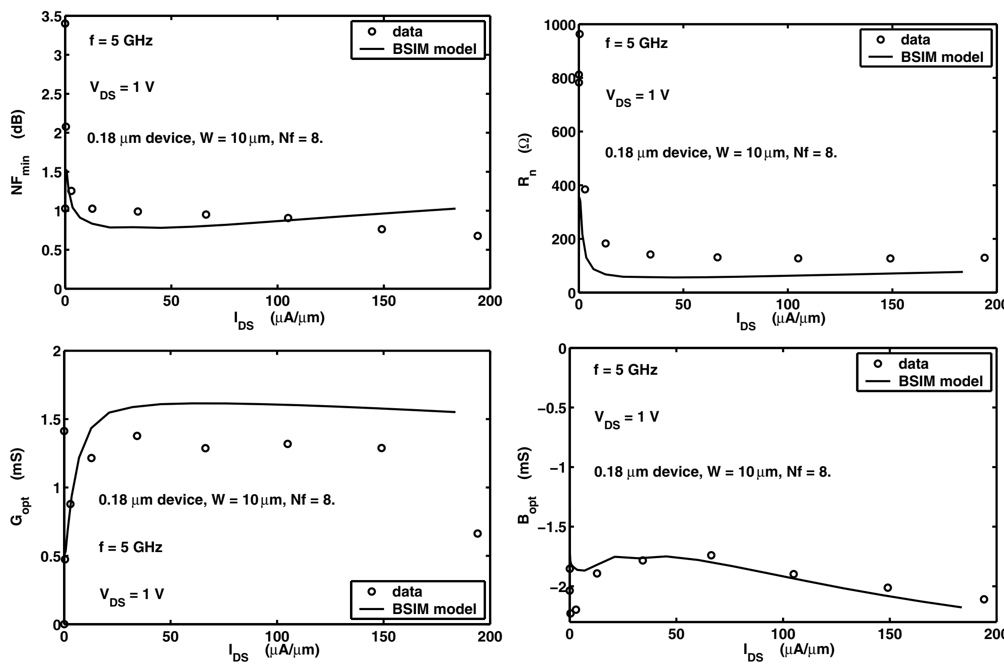

Figure 1.13: Comparison of noise parameters for the data and BSIM holistic model for 0.18 μm device. $W = 10$ μm, $Nf = 8$.

1.4.2 Gate Noise Voltage and Drain Noise Current Modeling

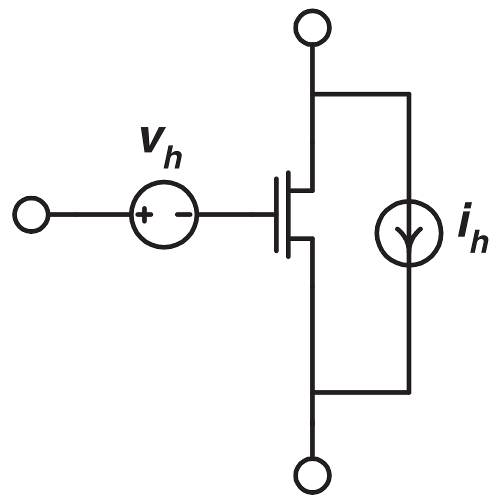

Figure 1.14: MOSFET noise model: Pospieszalski model

Different from gate and drain noise current representation, another widely accepted noise model in the GaAs community is the Pospieszalski model, which is based on the hybrid representation, as shown in Fig. 1.14 [27]. While the gate current noise in the van der Ziel model is frequency dependent and correlated to drain current noise, the Pospieszalski model uses an input voltage noise source S_{v_h,v_h^*}, which is frequency independent. An output noise current i_h is used in Pospieszalski model. S_{v_h,v_h^*} is proportional to the non-quasi-statistic channel resistance R_{gs}. S_{i_h,i_h^*} is proportional to the output conductance g_{ds}. Gate temperature T_g and drain temperature T_d are used in the model, function as coefficients as in van der Ziel model. Further, this model assumes that two noise sources have negligible correlation

$$S_{v_h,v_h^*} = 4kT_g R_{gs}, \tag{1.98}$$

$$S_{i_h,i_h^*} = 4kT_d g_{ds}, \tag{1.99}$$

$$S_{v_h,i_h^*} = 0. \tag{1.100}$$

Further investigations showed that this assumption is well satisfied in GaAs devices. However, no study has shown that it is valid for MOSFET devices. In this dissertation, Pospieszalski model is successfully applied to MOSFET devices in chapter 6.

1.4.3 Role of Gate Resistance

The gate resistance R_g is associated with a thermal noise voltage of $4kTR_g$. This gate thermal noise voltage is equivalent to an input noise current, an output noise current and a correlation, as shown in Fig. 1.15,

$$S_{i_g,i_g^*} = 4kTR_g|Y_{11}|^2 = 4kTR_g(\omega C_{gs})^2, \tag{1.101}$$

$$S_{i_d,i_d^*} = 4kTR_g|Y_{21}|^2 = 4kTR_g g_m^2, \tag{1.102}$$

$$S_{i_g,i_d^*} = j4kTR_g\omega g_m C_{gs}, \tag{1.103}$$

$$c = \frac{S_{i_g,i_d^*}}{\sqrt{S_{i_g,i_g^*} S_{i_d,i_d^*}}} = j1. \tag{1.104}$$

(1.101) shows that the gate resistance leads to a gate noise current that proportional to f^2, and behaves like the induced gate noise. This gate resistance related gate noise current overwhelms the induced gate noise for short channel devices. (1.102) shows that the gate resistance also leads to a drain noise current. The gate resistance related gate and drain noise currents are correlated as shown in (1.103). This indicates that reduction of the gate resistance R_g is really important for obtain low noise in MOSFET.

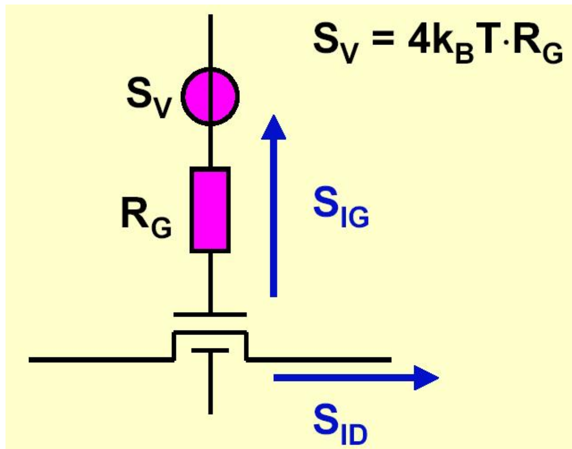

Figure 1.15: Role of gate resistance noise to gate noise current, drain noise current, and their correlation.

Although a metal silicide is added to the polysilicon gate to decrease its resistance, wide devices with short channels might still show a significant gate resistance. The gate resistance R_g consists of several parts: the resistance of the vias between metal1 and silicided polysilicon, the effective resistance of the silicide, and the contact resistance between silicide and polysilicon [28]. For a single polysilicon gate finger connected with both sides [6],

$$R_g = \frac{1}{12} R_{sh} \frac{W}{L} + \frac{1}{2} R_{sh} \frac{W_{ext}}{L} + \frac{1}{2} \frac{R_{via}}{N_{via}} + \frac{\rho_{con}}{WL}, \tag{1.105}$$

where R_{sh} is the silicide sheet resistance, R_{via} is the resistance of the metal1-to-polysilicon via, N_{via} is the number of such vias, ρ_{con} is the silicide-to-polysilicon specific contact resistance. W, L, and W_{ext} are depicted in Fig. 1.16. The factor 12 accounts for the distributed nature of the gate resistance and the use of contacts on both sides of the gate.

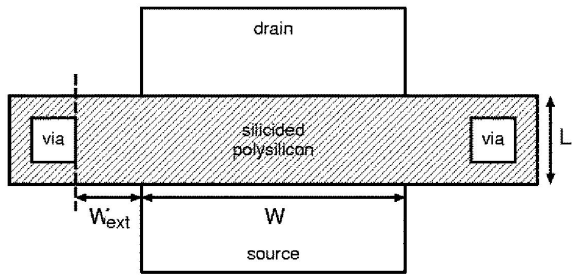

Figure 1.16: Schematic layout of a single gate finger, showing the meaning of W, W_{ext}, and L in (1.105) [6].

Narrow fingers, double-sided contacting, guard ring and abundant contacting lead to reduction in R_g. Using multiple devices in parallel to obtain larger devices is also a way to reduce R_g [4]. The width of finger, however, is optimized at 1 μm for 90 nm technology node transistor [29]. Further reduction in the width of finger does not further reduce R_g. It is generally accepted that the drain current noise and the gate resistance thermal noise are the dominant RF noise sources of interest in scaled CMOS [30]. Since R_g is important especially for short channel devices, accurate extraction of R_g plays a big role in compact noise modeling of modern CMOS, which will be detailed addressed in chapter 7.

Fukui first proposed a set of *empirical* NF_{min}, R_n and Y_{opt} equations for FETs based on his observation of experimental data on MESFETs [31] [32] [33], which involve an empirical Fukui's noise figure coefficient K_f, and other "constants," and transistor gate resistance R_g and transconductance g_m. The noise figure coefficient has since been frequently used as a figure-of-merit for comparing different technologies [34] [35] [36] [37] [38]. Recently, various equations of NF_{min}, R_n and Y_{opt} have been derived for CMOS with varying assumptions, by neglecting gate resistance noise and/or induced gate noise [39] [40] [41], and by assuming a bias independent ratio of $\gamma_{g_{d0}}$ to γ_{g_m}, which is problematic as detailed in chapter 8.

1.5 Dissertation Contributions

The following chapters provide detailed information about RF bipolar and CMOS noise in terms of device physics. To achieve these goals, this dissertation tackles various areas including microscopic noise simulation, Ge profile optimization in SiGe HBT device, noise characterization, and compact noise modeling.

Chapter 1 gives an introduction of definitions and classifications of RF device noise and noise parameters. Review of RF bipolar and CMOS noise models and the intrinsic noise sources in RF bipolar and CMOS devices is also given in chapter 1.

Chapter 2 introduces different noise representations for a linear noisy two-port network. The transformation matrices to other noise representations are given. Techniques of adding or de-embedding a passive component to a linear two-port network are discussed. Noise sources de-embedding for both MOSFET and SiGe HBT are given as examples which are repeatedly used later in this dissertation.

Chapter 3 presents a new technique of simulating the spatial distribution of microscopic noise contribution to the input noise current, voltage, and their correlation. The technique is first demonstrated on a 50 GHz SiGe HBT. The spatial distributions by base majority holes, base minority electrons, and emitter minority holes are analyzed, and compared to the compact noise model. This technique is also applied to a 120 GHz MOSFET transistor. The spatial distribution of drain noise current, gate noise current, and their correlation are analyzed.

Chapter 4 examines bipolar transistor noise modeling and noise physics using microscopic noise simulation. Transistor terminal current and voltage noises resulting from velocity fluctuations of electrons and holes in the base, emitter, collector, and substrate are simulated using a new technique proposed in chapter 3, and compared with modeling results. Major physics noise sources in bipolar transistor are qualitatively identified. The relevant importance as well as model-simulation discrepancy is analyzed for each physical noise source.

Chapter 5 explores the RF noise physics and SiGe profile optimization for low noise using microscopic noise simulation. A higher Ge gradient in a noise critical region near the EB junction reduces impedance field and hence minimum noise figure. A higher Ge gradient near the EB junction, together with an unconventional Ge retrograding in the base to keep total Ge content below stability, when optimized, can lead to significant noise improvement without sacrificing peak f_T and without any significant high injection f_T rolloff degradation.

In chapter 6, RF noise of 50 nm L_{eff} CMOS is simulated using hydrodynamic noise simulation. Intrinsic noise sources for the Y- and H- noise representations are examined and models of intrinsic noise sources are proposed. The relations between the Y- and H- noise representations for MOSFETs are examined, and the importance of correlation for both representations is quantified. The theoretical values of H- noise representation model parameters are derived for the first time for long channel devices. The H- noise representation correlation is shown theoretically to have a zero imaginary part. The H- noise representation has the inherent advantage of a more negligible correlation, which makes circuit design and simulation easier. Chapter 6 also experimentally extracts the H-representation noise sources using noise parameters measured on 0.25 μm RF CMOS devices. A simple yet effective model is proposed to model the H-representation noise sources as a function of bias. Excellent modeling results are achieved for all of the noise parameters up to 26 GHz, at all biases.

The gate resistance is important as well as the drain noise current for noise modeling of scaled MOSFET. Accurately extract the gate resistance becomes an important issue. Chapter 7 explains the frequency and bias dependence of the effective gate resistance by considering the effect of gate-to-body capacitance, gate to source/drain overlap capacitances, fringing capacitances, and Non-Quasi-Static (NQS) effect. A new method of separating the physical gate resistance and the NQS channel resistance is proposed. Separating the gate-to-source parasitic capacitances from the gate-to-source inversion capacitance is found to be necessary for accurate modeling of all of the Y-parameters.

Chapter 8 examines the differences between the g_{d0} and g_m referenced drain current excess noise factors in CMOS transistors as a function of channel length and bias. The technology scaling are discussed for 0.25 μm process, 0.18 μm process and 0.12 μm process. Using standard linear noisy two-port theory, a simple derivation of noise parameters is presented. The results are compared with the well known Fukui's empirical FET noise equations. Experimental data on a 0.18 μm CMOS process are measured and used to evaluate the simple model equations. New figures-of-merit for minimum noise figure is proposed. The amount of drain current noise produced to achieve one GHz f_T is shown to fundamentally determine the noise capability of the intrinsic transistor.

Finally Chapter 9 concludes the work in this dissertation.

CHAPTER 2

NOISE NETWORK ANALYSIS AND DE-EMBEDDING

This chapter introduces different noise representations for a linear noisy two-port network. The transformation matrices to other noise representations are given. Techniques of adding or de-embedding passive components to a linear two-port network are discussed. For example, the open-short de-embedding procedure is needed for measurement data to move the reference plane to the device terminals. Noise sources de-embedding for both MOSFET and SiGe HBT are given as examples which are repeatedly used later in this dissertation.

2.1 Noise Representations

A noisy two-port network can be described by a noiseless two-port network with input noise voltages or currents, and output noise voltages or currents. In general, there are four noise representations, including chain noise representation, Y- noise representation, Z- noise representation, and H- noise representation.

2.1.1 Chain Noise Representation (ABCD- Noise Representation)

Chain noise representation, or ABCD- noise representation, describes the noise of a two-port network with an input noise voltage v_a, an input noise current i_a, and their correlation, as shown in Fig. 2.1. The power spectral densities (PSD) of v_a, i_a, and their correlation are S_{v_a,v_a^*},

S_{i_a,i_a^*}, and S_{i_a,v_a^*}, respectively. The chain noise matrix is defined as

$$C_A = \begin{bmatrix} S_{v_a,v_a^*} & S_{v_a,i_a^*} \\ S_{i_a,v_a^*} & S_{i_a,i_a^*} \end{bmatrix} \tag{2.1}$$

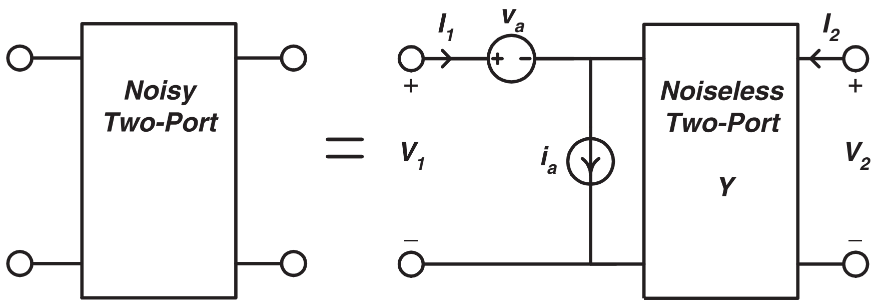

Figure 2.1: The chain noise representation of a linear noisy two-port network.

Chain noise representation is the most convenient because it is directly related to the noise parameters NF_{min}, R_n and $Y_{opt} = G_{opt} + jB_{opt}$ by [11]. The noise factor for a noisy linear two-port as shown in Fig. 2.2 is [42] [43]

$$F = \frac{S_i/N_i}{S_o/N_o},$$

$$= \frac{N_o}{G_p N_i}, \tag{2.2}$$

$$= \frac{N_i + N_i'}{N_i}, \tag{2.3}$$

$$= 1 + \frac{N_i'}{N_i}, \tag{2.4}$$

where $G_p = S_o/S_i$ is the power gain of the two-port, N_i is the input noise power delivered to the noisy two-port due to source noise current i_s, and N_i' is the noise power delivered to the noisy two-port due to v_a and i_a.

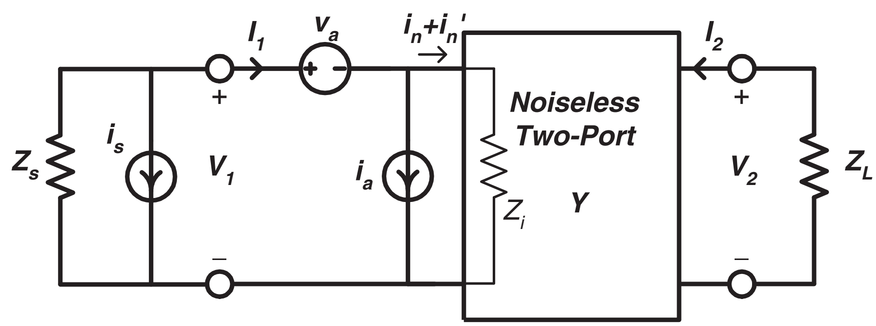

Figure 2.2: Noisy linear two-port network.

If Z_i denotes the input admittance of the two-port shown in Fig. 2.2, the noise current delivered by the source to the noise free two-port is

$$i_n = -i_s \frac{Z_s}{Z_i + Z_s}, \tag{2.5}$$

and

$$N_i =< i_n, i_n^* > \Re(Z_i), \tag{2.6}$$

$$=< i_s, i_s^* > \left| \frac{Z_s}{Z_i + Z_s} \right|^2 \Re(Z_i), \tag{2.7}$$

$$= 4kTG_s \frac{|Z_s|^2}{|Z_i + Z_s|^2} \Re(Z_i)\Delta f, \tag{2.8}$$

where Z_s is the source impedance, and $Y_s = 1/Z_s$ is the source admittance with a real part of G_s and an imaginary part of B_s. The noise current delivered to the noise free two-port by the correlated noise voltage and noise current of the noisy two-port is

$$i'_n = -v_a \frac{1}{Z_i + Z_s} - i_a \frac{Z_s}{Z_i + Z_s}, \tag{2.9}$$

and

$$N'_i =< i'_n, i'^*_n > \Re(Z_i), \tag{2.10}$$

$$= \left[< v_a, v_a^* > \frac{1}{|Z_i + Z_s|^2} + < i_a, i_a^* > \left| \frac{Z_s}{Z_i + Z_s} \right|^2 + 2\Re \left(< i_a, v_a^* > \frac{Z_s}{|Z_i + Z_s|^2} \right) \right] \Re(Z_i), \tag{2.11}$$

$$= \left[S_{v_a,v_a^*} + S_{i_a,i_a^*}|Z_s|^2 + 2\Re \left(S_{i_a,v_a^*} Z_s \right) \right] \frac{1}{|Z_i + Z_s|^2} \Re(Z_i) \Delta f. \tag{2.12}$$

Substituting (2.8) and (2.12) in (2.4),

$$F = 1 + \frac{S_{v_a,v_a^*} + S_{i_a,i_a^*}|Z_s|^2 + 2\Re \left(S_{i_a,v_a^*} Z_s \right)}{4kTG_s|Z_s|^2}, \tag{2.13}$$

$$= 1 + \frac{S_{v_a,v_a^*}|Y_s|^2 + S_{i_a,i_a^*} + 2\Re \left(S_{i_a,v_a^*} Y_s^* \right)}{4kTG_s}, \tag{2.14}$$

Let $S_{i_a,v_a^*} = G_u + jB_u$, we have

$$F = 1 + \frac{S_{v_a,v_a^*}|G_s + jB_s|^2 + S_{i_a,i_a^*} + 2\Re \left((G_u + jB_u)(G_s - jB_s) \right)}{4kTG_s}, \tag{2.15}$$

$$= 1 + \frac{S_{v_a,v_a^*}(G_s^2 + B_s^2) + S_{i_a,i_a^*} + 2(G_u G_s + B_u B_s)}{4kTG_s}. \tag{2.16}$$

To find out the optimum B_s to minimize noise factor F, $\frac{\delta F}{\delta B_s} = 0$,

$$\frac{2S_{v_a,v_a^*}B_s + 2B_u}{4kTG_s} = 0, \tag{2.17}$$

hence the optimum source susceptance B_{opt} is

$$B_{opt} = -\frac{B_u}{S_{v_a,v_a^*}}. \tag{2.18}$$

To find out the optimum G_s to minimize noise factor F, $\frac{\delta F}{\delta G_s} = 0$,

$$-S_{i_a,i_a^*} + G_s^2 S_{v_a,v_a^*} - B_s^2 S_{v_a,v_a^*} - 2B_u B_s = 0, \tag{2.19}$$

Substituting $B_s = B_{opt}$ in,

$$-S_{i_a,i_a^*} + G_s^2 S_{v_a,v_a^*} + \frac{B_u^2}{S_{v_a,v_a^*}} = 0, \tag{2.20}$$

hence the optimum source conductance G_{opt} is

$$G_{opt} = \sqrt{\frac{S_{i_a,i_a^*}}{S_{v_a,v_a^*}} - \frac{B_u^2}{S_{v_a,v_a^*}^2}}. \tag{2.21}$$

Substituting G_s and B_s using their optimum values G_{opt} and B_{opt} in (2.16), the minimum noise factor F_{min} is

$$F_{min} = 1 + \frac{\sqrt{S_{v_a,v_a^*}S_{i_a,i_a^*} - B_u^2} + G_u}{2kT}. \tag{2.22}$$

Note that $G_u = \Re(S_{i_a,v_a^*})$, and $B_u = \Im(S_{i_a,v_a^*})$, the noise parameters NF_{min}, R_n, G_{opt}, and B_{opt} finally are [43]

$$F_{min} = 1 + \frac{\sqrt{S_{v_a,v_a^*} S_{i_a,i_a^*} - [\Im(S_{i_a,v_a^*})]^2} + \Re(S_{i_a,v_a^*})}{2kT}, \tag{2.23}$$

$$= 1 + 2R_n \left(G_{opt} + \frac{\Re(S_{i_a,v_a^*})}{S_{v_a,v_a^*}} \right), \tag{2.24}$$

$$NF_{min} = 10 \log_{10}(F_{min}), \tag{2.25}$$

$$R_n = \frac{S_{v_a,v_a^*}}{4kT}, \tag{2.26}$$

$$G_{opt} = \sqrt{\frac{S_{i_a,i_a^*}}{S_{v_a,v_a^*}} - \left[\frac{\Im(S_{i_a,v_a^*})}{S_{v_a,v_a^*}} \right]^2}, \tag{2.27}$$

$$B_{opt} = -\frac{\Im(S_{i_a,v_a^*})}{S_{v_a,v_a^*}}, \tag{2.28}$$

where $\Re$ and $\Im$ stand for the real and the imaginary parts of a factor, respectively.

Solved from (2.24), (8.17), 8.18, and (8.19), the chain noise representation parameters S_{v_a,v_a^*}, S_{i_a,i_a^*}, and S_{i_a,v_a^*}, can be obtained using the noise parameters NF_{min}, R_n and Y_{opt} by [11],

$$S_{v_a,v_a^*} = 4kTR_n, \tag{2.29}$$

$$S_{i_a,i_a^*} = 4kTR_n \left| Y_{opt} \right|^2, \tag{2.30}$$

$$S_{i_a,v_a^*} = 2kT\left(F_{min} - 1\right) - 4kTR_nY_{opt}, \tag{2.31}$$

or in the format of noise matrix,

$$C_A = 4kT \begin{bmatrix} R_n & \frac{F_{min}-1}{2} - R_nY_{opt}^* \\ \frac{F_{min}-1}{2} - R_nY_{opt} & R_n|Y_{opt}|^2 \end{bmatrix}. \tag{2.32}$$

2.1.2 Y- Noise Representation

The Y- noise representation describes the noise of a two-port network with an input noise current i_1, an output noise current i_2, and their correlation, as shown in Fig. 2.3. The PSD's of i_1, i_2, and their correlation are S_{i_1,i_1^*}, S_{i_2,i_2^*}, and S_{i_2,i_1^*}, respectively. The Y- noise matrix is defined as

$$C_Y = \begin{bmatrix} S_{i_1,i_1^*} & S_{i_1,i_2^*} \\ S_{i_2,i_1^*} & S_{i_2,i_2^*} \end{bmatrix} \tag{2.33}$$

The output of microscopic noise simulation tool TAURUS are Y- noise representation parameters [44]. Y- noise representation is also commonly used in compact noise modeling of both RF bipolar and MOSFET transistors, as detailed later in section 1.3.2 and 1.4.1.

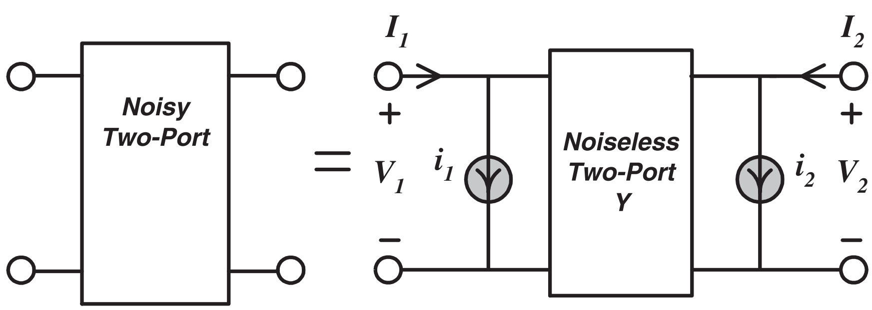

Figure 2.3: The Y- noise representation of a linear noisy two-port network.

Conversions between the chain noise representation parameters and the Y- noise representation parameters can be derived as follows. We denote Y as total admittance matrix. The *ac*

$I-V$ relations including noise for the representations shown in Fig. 2.1 and Fig. 2.3 are

$$\begin{pmatrix} I_1 - i_a \\ I_2 \end{pmatrix} = \begin{bmatrix} Y_{11} & Y_{12} \\ Y_{21} & Y_{22} \end{bmatrix} \cdot \begin{pmatrix} V_1 - v_a \\ V_2 \end{pmatrix}, \tag{2.34}$$

$$\begin{pmatrix} I_1 - i_1 \\ I_2 - i_2 \end{pmatrix} = \begin{bmatrix} Y_{11} & Y_{12} \\ Y_{21} & Y_{22} \end{bmatrix} \cdot \begin{pmatrix} V_1 \\ V_2 \end{pmatrix}. \tag{2.35}$$

Equating the noise terms of the two representations for both I_1 and I_2, we find the relations between (i_1, i_2) and (v_a, i_a),

$$i_1 = i_a - Y_{11} v_a, \tag{2.36}$$

$$i_2 = -Y_{21} v_a, \tag{2.37}$$

and

$$v_a = -\frac{1}{Y_{21}} i_2, \tag{2.38}$$

$$i_a = i_1 - \frac{Y_{11}}{Y_{21}} i_2, \tag{2.39}$$

where Y_{11} and Y_{21} are elements of Y matrix. Therefore, the Y- noise representation parameters S_{i_1,i_1^*}, S_{i_2,i_2^*}, and S_{i_2,i_1^*}, can be derived using the chain noise representation parameters S_{v_a,v_a^*},

S_{i_a,i_a^*}, and S_{i_a,v_a^*} as

$$S_{i_1,i_1^*} = S_{i_a,i_a^*} + |Y_{11}|^2 S_{v_a,v_a^*} - 2\Re(Y_{11}^* S_{i_a,v_a^*}), \tag{2.40}$$

$$S_{i_2,i_2^*} = |Y_{21}|^2 S_{v_a,v_a^*}, \tag{2.41}$$

$$S_{i_2,i_1^*} = Y_{21} Y_{11}^* S_{v_a,v_a^*} - Y_{21} S_{i_a,v_a^*}^*. \tag{2.42}$$

Alternatively, the chain noise representation parameters S_{v_a,v_a^*}, S_{i_a,i_a^*}, and S_{i_a,v_a^*}, can be derived using the Y- noise representation parameters S_{i_1,i_1^*}, S_{i_2,i_2^*}, and S_{i_2,i_1^*} as

$$S_{v_a,v_a^*} = \frac{1}{|Y_{21}|^2} S_{i_2,i_2^*}, \tag{2.43}$$

$$S_{i_a,i_a^*} = S_{i_1,i_1^*} + \left| \frac{Y_{11}}{Y_{21}} \right|^2 S_{i_2,i_2^*} - 2\Re\left(\frac{Y_{11}}{Y_{21}} S_{i_2,i_1^*} \right), \tag{2.44}$$

$$S_{i_a,v_a^*} = \frac{Y_{11}}{|Y_{21}|^2} S_{i_2,i_2^*} - \frac{1}{Y_{21}^*} S_{i_2,i_1^*}^*. \tag{2.45}$$

2.1.3 Z- Noise Representation

The Z- noise representation describes the noise of a two-port network with an input noise voltage v_1, an output noise voltage v_2, and their correlation, as shown in Fig. 2.4. The PSD's of v_1, v_2, and their correlation are S_{v_1,v_1^*}, S_{v_2,v_2^*}, and S_{v_1,v_2^*}, respectively. The Z- noise matrix is defined as

$$C_Z = \begin{bmatrix} S_{v_1,v_1^*} & S_{v_1,v_2^*} \\ S_{v_2,v_1^*} & S_{v_2,v_2^*} \end{bmatrix} \tag{2.46}$$

The output of microscopic noise simulation tool DESSIS are Z- noise representation parameters [45]. The simulation results in this work are done using DESSIS.

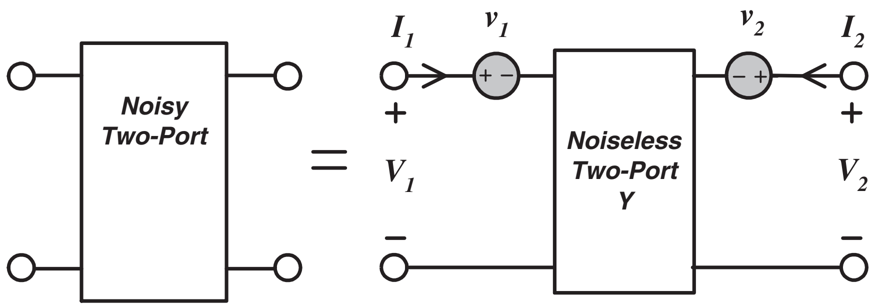

Figure 2.4: The Z- noise representation of a linear noisy two-port network.

Conversions between the chain noise representation parameters and the Z- noise representation parameters can be derived as follows. The *ac* $I - V$ relations including noise for the representations shown in Fig. 2.1 and Fig. 2.4 are

$$\begin{pmatrix} I_1 - i_a \\ I_2 \end{pmatrix} = \begin{bmatrix} Y_{11} & Y_{12} \\ Y_{21} & Y_{22} \end{bmatrix} \cdot \begin{pmatrix} V_1 - v_a \\ V_2 \end{pmatrix}, \tag{2.47}$$

$$\begin{pmatrix} I_1 \\ I_2 \end{pmatrix} = \begin{bmatrix} Y_{11} & Y_{12} \\ Y_{21} & Y_{22} \end{bmatrix} \cdot \begin{pmatrix} V_1 - v_1 \\ V_2 - v_2 \end{pmatrix}. \tag{2.48}$$

Equating the noise terms of the two representations for both I_1 and I_2, we find the relations between (v_1, v_2) and (v_a, i_a),

$$v_1 = v_a - \frac{Y_{22}}{Y_{11}Y_{22} - Y_{12}Y_{21}} i_a, \tag{2.49}$$

$$v_2 = \frac{Y_{21}}{Y_{11}Y_{22} - Y_{12}Y_{21}} i_a, \tag{2.50}$$

and

$$v_a = v_1 + \frac{Y_{22}}{Y_{21}} v_2, \tag{2.51}$$

$$i_a = \frac{Y_{11}Y_{22} - Y_{12}Y_{21}}{Y_{21}} v_2. \tag{2.52}$$

Therefore, the Z- noise representation parameters S_{v_1,v_1^*}, S_{v_2,v_2^*}, and S_{v_1,v_2^*}, can be derived using the chain noise representation parameters S_{v_a,v_a^*}, S_{i_a,i_a^*}, and S_{i_a,v_a^*} as

$$S_{v_1,v_1^*} = S_{v_a,v_a^*} + \left| \frac{Y_{22}}{Y_{11}Y_{22} - Y_{12}Y_{21}} \right|^2 S_{i_a,i_a^*} - 2\Re\left(\frac{Y_{22}}{Y_{11}Y_{22} - Y_{12}Y_{21}} S_{i_a,v_a^*} \right), \tag{2.53}$$

$$S_{v_2,v_2^*} = \left| \frac{Y_{21}}{Y_{11}Y_{22} - Y_{12}Y_{21}} \right|^2 S_{i_a,i_a^*}, \tag{2.54}$$

$$S_{v_1,v_2^*} = \frac{Y_{21}^*}{Y_{11}^*Y_{22}^* - Y_{12}^*Y_{21}^*} S_{i_a,v_a^*}^* - \frac{Y_{22}Y_{21}^*}{|Y_{11}Y_{22} - Y_{12}Y_{21}|^2} S_{i_a,i_a^*}. \tag{2.55}$$

Alternatively, the chain noise representation parameters S_{v_a,v_a^*}, S_{i_a,i_a^*}, and S_{i_a,v_a^*}, can be derived using the Z- noise representation parameters S_{v_1,v_1^*}, S_{v_2,v_2^*}, and S_{v_1,v_2^*} as

$$S_{v_a,v_a^*} = S_{v_1,v_1^*} + \left| \frac{Y_{22}}{Y_{21}} \right|^2 S_{v_2,v_2^*} + 2\Re\left(\frac{Y_{22}^*}{Y_{21}^*} S_{v_1,v_2^*} \right), \tag{2.56}$$

$$S_{i_a,i_a^*} = \left| \frac{Y_{11}Y_{22} - Y_{12}Y_{21}}{Y_{21}} \right|^2 S_{v_2,v_2^*}, \tag{2.57}$$

$$S_{i_a,v_a^*} = \frac{Y_{22}^*(Y_{11}Y_{22} - Y_{12}Y_{21})}{|Y_{21}|^2} S_{v_2,v_2^*} + \frac{Y_{11}Y_{22} - Y_{12}Y_{21}}{Y_{21}} S_{v_1,v_2^*}^*. \tag{2.58}$$

2.1.4 H- Noise Representation

The H- noise representation describes a noisy two-port network with an input noise voltage v_h, an output noise current i_h, and their correlation, as shown in Fig. 2.5. The PSD's of v_h, i_h, and their correlation are S_{v_h,v_h^*}, S_{i_h,i_h^*}, and S_{v_h,i_h^*}, respectively. The H- noise matrix is defined as

$$C_H = \begin{bmatrix} S_{v_h,v_h^*} & S_{v_h,i_h^*} \\ S_{i_h,v_h^*} & S_{i_h,i_h^*} \end{bmatrix} \tag{2.59}$$

H- noise representation is popular for compact noise modeling of GaAs MESFETs and HEMTs. As we will show in chapter 6, the H- noise representation is also advantageous for CMOS transistors. Therefore we are more concerned with the conversions between Y- noise representation parameters and H- noise representation parameters.

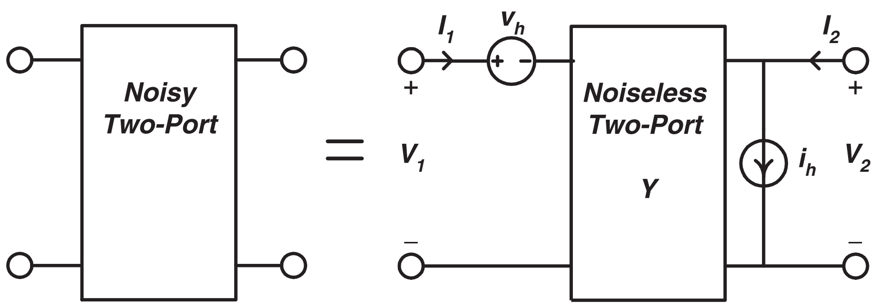

Figure 2.5: The H- noise representation of a linear noisy two-port network.

The $I - V$ relations including noise in Fig. 2.3 and Fig. 2.5 are given by:

$$\begin{pmatrix} I_1 - i_1 \\ I_2 - i_2 \end{pmatrix} = \begin{bmatrix} Y_{11} & Y_{12} \\ Y_{21} & Y_{22} \end{bmatrix} \cdot \begin{pmatrix} V_1 \\ V_2 \end{pmatrix}, \tag{2.60}$$

$$\begin{pmatrix} I_1 \\ I_2 - i_h \end{pmatrix} = \begin{bmatrix} Y_{11} & Y_{12} \\ Y_{21} & Y_{22} \end{bmatrix} \cdot \begin{pmatrix} V_1 - v_h \\ V_2 \end{pmatrix}. \tag{2.61}$$

Solving (2.60) and (2.61), i_1 and i_2 are related to v_h and i_h as

$$i_1 = -Y_{11} v_h \tag{2.62}$$

$$i_2 = i_h - Y_{21} v_h, \tag{2.63}$$

and

$$v_h = -\frac{1}{Y_{11}} i_1 \tag{2.64}$$

$$i_h = i_2 - \frac{Y_{21}}{Y_{11}} i_1. \tag{2.65}$$

Therefore, the Y- noise representation parameters S_{i_1,i_1^*}, S_{i_2,i_2^*}, and S_{i_1,i_2^*}, can be derived using the H- noise representation parameters S_{v_h,v_h^*}, S_{i_h,i_h^*}, and S_{i_h,v_h^*} as

$$S_{i_1,i_1^*} = |Y_{11}|^2 S_{v_h,v_h^*}, \tag{2.66}$$

$$S_{i_2,i_2^*} = S_{i_h,i_h^*} + |Y_{21}|^2 S_{v_h,v_h^*} - 2\Re(Y_{21} S_{v_h,i_h^*}), \tag{2.67}$$

$$S_{i_1,i_2^*} = Y_{11} Y_{21}^* S_{v_h,v_h^*} - Y_{11} S_{v_h,i_h^*}. \tag{2.68}$$

Alternatively, the H- noise representation parameters S_{v_h,v_h^*}, S_{i_h,i_h^*}, and S_{i_h,v_h^*}, can be derived using the Y- noise representation parameters S_{i_1,i_1^*}, S_{i_2,i_2^*}, and S_{i_1,i_2^*} as

$$S_{v_h,v_h^*} = \frac{1}{|Y_{11}|^2} S_{i_1,i_1^*}, \tag{2.69}$$

$$S_{i_h,i_h^*} = S_{i_2,i_2^*} + \left|\frac{Y_{21}}{Y_{11}}\right|^2 S_{i_1,i_1^*} - 2\Re(\frac{Y_{21}}{Y_{11}} S_{i_1,i_2^*}), \tag{2.70}$$

$$S_{v_h,i_h^*} = \frac{Y_{21}^*}{|Y_{11}|^2} - \frac{1}{Y_{11}} S_{i_1,i_2^*}. \tag{2.71}$$

2.2 Transformation to Other Noise Representations

The ABCD-, Y-, Z-, and H- noise representations can be transformed to another by the matrix operation:

$$C' = T \cdot C \cdot T^{\dagger}, \tag{2.72}$$

where C and C' are the original and resulting noise correlation matrices respectively, T is the transformation matrix given in Table 2.1, and $T^{\dagger}$ is the transpose conjugate of T. The ABCD, Y, Z and H two-port network parameters are used in Table 2.1. The conversion of ABCD, Y, Z and H parameters are given in Table 2.2.

	Original Representation			
	C_Y	C_Z	C_A	C_H
C'_Y	$\begin{bmatrix} 1 & 0 \\ 0 & 1 \end{bmatrix}$	$\begin{bmatrix} Y_{11} & Y_{12} \\ Y_{21} & Y_{22} \end{bmatrix}$	$\begin{bmatrix} -Y_{11} & 1 \\ -Y_{21} & 0 \end{bmatrix}$	$\begin{bmatrix} -Y_{11} & 0 \\ -Y_{21} & 1 \end{bmatrix}$
C'_Z	$\begin{bmatrix} Z_{11} & Z_{12} \\ Z_{21} & Z_{22} \end{bmatrix}$	$\begin{bmatrix} 1 & 0 \\ 0 & 1 \end{bmatrix}$	$\begin{bmatrix} 1 & -Z_{11} \\ 0 & -Z_{21} \end{bmatrix}$	$\begin{bmatrix} 1 & -Z_{12} \\ 0 & -Z_{22} \end{bmatrix}$
C'_A	$\begin{bmatrix} 0 & A_{12} \\ 1 & A_{22} \end{bmatrix}$	$\begin{bmatrix} 1 & -A_{11} \\ 0 & -A_{21} \end{bmatrix}$	$\begin{bmatrix} 1 & 0 \\ 0 & 1 \end{bmatrix}$	$\begin{bmatrix} 1 & A_{12} \\ 0 & A_{22} \end{bmatrix}$
C'_H	$\begin{bmatrix} -h_{11} & 0 \\ -h_{21} & 1 \end{bmatrix}$	$\begin{bmatrix} 1 & -h_{12} \\ 0 & -h_{22} \end{bmatrix}$	$\begin{bmatrix} 1 & -h_{11} \\ 0 & -h_{21} \end{bmatrix}$	$\begin{bmatrix} 1 & 0 \\ 0 & 1 \end{bmatrix}$

Table 2.1: Transformation matrices to calculate other noise representations

	Y	Z	A	H	S
Y	Y_{11} Y_{12} Y_{21} Y_{22}	$\frac{Z_{22}}{\Delta_Z}$ $\frac{-Z_{12}}{\Delta_Z}$ $\frac{-Z_{21}}{\Delta_Z}$ $\frac{Z_{11}}{\Delta_Z}$	$\frac{A_{22}}{A_{12}}$ $\frac{-\Delta_A}{A_{12}}$ $\frac{-1}{A_{12}}$ $\frac{A_{11}}{A_{12}}$	$\frac{1}{h_{11}}$ $\frac{-h_{12}}{h_{11}}$ $\frac{h_{21}}{h_{11}}$ $\frac{\Delta_H}{h_{11}}$	$Y_0\frac{1-S_{11}+S_{22}-\Delta_S}{1+S_{11}+S_{22}+\Delta_S}$ $Y_0\frac{-2S_{12}}{1+S_{11}+S_{22}+\Delta_S}$ $Y_0\frac{-2S_{21}}{1+S_{11}+S_{22}+\Delta_S}$ $Y_0\frac{1+S_{11}-S_{22}-\Delta_S}{1+S_{11}+S_{22}+\Delta_S}$
Z	$\frac{Y_{22}}{\Delta_Y}$ $\frac{-Y_{12}}{\Delta_Y}$ $\frac{-Y_{21}}{\Delta_Y}$ $\frac{Y_{11}}{\Delta_Y}$	Z_{11} Z_{12} Z_{21} Z_{22}	$\frac{A_{11}}{A_{21}}$ $\frac{\Delta_A}{A_{21}}$ $\frac{1}{A_{21}}$ $\frac{A_{22}}{A_{21}}$	$\frac{\Delta_H}{h_{22}}$ $\frac{h_{12}}{h_{22}}$ $\frac{-h_{21}}{h_{22}}$ $\frac{1}{h_{22}}$	$Z_0\frac{1+S_{11}-S_{22}-\Delta_S}{1-S_{11}-S_{22}+\Delta_S}$ $Z_0\frac{2S_{12}}{1-S_{11}-S_{22}+\Delta_S}$ $Z_0\frac{2S_{21}}{1-S_{11}-S_{22}+\Delta_S}$ $Z_0\frac{1-S_{11}+S_{22}-\Delta_S}{1-S_{11}-S_{22}+\Delta_S}$
A	$\frac{-Y_{22}}{Y_{21}}$ $\frac{-1}{Y_{21}}$ $\frac{-\Delta_Y}{Y_{21}}$ $\frac{-Y_{11}}{Y_{21}}$	$\frac{Z_{11}}{Z_{21}}$ $\frac{\Delta_Z}{Z_{21}}$ $\frac{1}{Z_{21}}$ $\frac{Y_{22}}{Z_{21}}$	A_{11} A_{12} A_{21} A_{22}	$\frac{-\Delta_H}{h_{21}}$ $\frac{-h_{11}}{h_{21}}$ $\frac{-h_{22}}{h_{21}}$ $\frac{-1}{h_{21}}$	$\frac{1+S_{11}-S_{22}-\Delta_S}{2S_{21}}$ $Z_0\frac{1+S_{11}+S_{22}+\Delta_S}{2S_{21}}$ $Y_0\frac{1-S_{11}-S_{22}+\Delta_S}{2S_{21}}$ $\frac{1-S_{11}+S_{22}-\Delta_S}{2S_{21}}$
H	$\frac{1}{Y_{11}}$ $\frac{-Y_{12}}{Y_{11}}$ $\frac{Y_{21}}{Y_{11}}$ $\frac{\Delta_Y}{Y_{11}}$	$\frac{\Delta_Z}{Z_{22}}$ $\frac{Z_{12}}{Z_{22}}$ $\frac{-Z_{21}}{Z_{22}}$ $\frac{1}{Z_{22}}$	$\frac{A_{12}}{A_{22}}$ $\frac{\Delta_A}{A_{22}}$ $\frac{-1}{A_{22}}$ $\frac{A_{21}}{A_{22}}$	h_{11} h_{12} h_{21} h_{22}	$Z_0\frac{1+S_{11}+S_{22}+\Delta_S}{1-S_{11}+S_{22}-\Delta_S}$ $\frac{2S_{12}}{1-S_{11}+S_{22}-\Delta_S}$ $\frac{2S_{21}}{1-S_{11}+S_{22}-\Delta_S}$ $Y_0\frac{1-S_{11}-S_{22}+\Delta_S}{1-S_{11}+S_{22}-\Delta_S}$
S	$\frac{Y_0(Y_0-Y_{11}+Y_{22})-\Delta_Y}{Y_0(Y_{11}+Y_{22}+Y_0)+\Delta_Y}$ $\frac{-2Y_{12}Y_0}{Y_0(Y_{11}+Y_{22}+Y_0)+\Delta_Y}$ $\frac{-2Y_{21}Y_0}{Y_0(Y_{11}+Y_{22}+Y_0)+\Delta_Y}$ $\frac{Y_0(Y_0+Y_{11}-Y_{22})-\Delta_Y}{Y_0(Y_{11}+Y_{22}+Y_0)+\Delta_Y}$	$\frac{Z_0(Z_{11}-Z_{22}-Z_0)+\Delta_Z}{Z_0(Z_{11}+Z_{22}+Z_0)+\Delta_Z}$ $\frac{2Z_{12}Z_0}{Z_0(Z_{11}+Z_{22}+Z_0)+\Delta_Z}$ $\frac{2Z_{21}Z_0}{Z_0(Z_{11}+Z_{22}+Z_0)+\Delta_Z}$ $\frac{Z_0(Z_{22}-Z_{11}-Z_0)+\Delta_Z}{Z_0(Z_{11}+Z_{22}+Z_0)+\Delta_Z}$	$\frac{A_{11}+A_{12}/Z_0-A_{21}/Z_0-A_{22}}{A_{11}+A_{12}/Z_0+A_{21}/Z_0+A_{22}}$ $\frac{2\Delta_A}{A_{11}+A_{12}/Z_0+A_{21}/Z_0+A_{22}}$ $\frac{2}{A_{11}+A_{12}/Z_0+A_{21}/Z_0+A_{22}}$ $\frac{-A_{11}+A_{12}/Z_0-A_{21}/Z_0+A_{22}}{A_{11}+A_{12}/Z_0+A_{21}/Z_0+A_{22}}$	$\frac{h_{11}-h_{22}-1+\Delta_H}{h_{11}+h_{22}+1+\Delta_H}$ $\frac{2h_{12}}{h_{11}+h_{22}+1+\Delta_H}$ $\frac{-2h_{21}}{h_{11}+h_{22}+1+\Delta_H}$ $\frac{h_{11}-h_{22}-1-\Delta_H}{h_{11}+h_{22}+1+\Delta_H}$	S_{11} S_{12} S_{21} S_{22}
$\Delta_Y = Y_{11}Y_{22} - Y_{12}Y_{21}$, $\Delta_Z = Z_{11}Z_{22} - Z_{12}Z_{21}$, $\Delta_H = h_{11}h_{22} - h_{12}h_{21}$, $\Delta_A = A_{11}A_{22} - A_{12}A_{21}$.					

Table 2.2: Conversions between two-port network parameters.

2.3 Adding Noisy Passive Components to a Noisy Two-Port Network

If the noise of the intrinsic two-port network is known, in order to calculate the noise of a complex network, one needs to start from the noise of the intrinsic two-port network, then procedurally add the noise of other noisy passive components to the intrinsic, which is called the "adding" procedure. Reversely speaking, if the noise of a complex network is known, one needs to remove the noise of each noisy passive component to calculate the noise of the intrinsic network, which is called the "de-embedding" procedure. Both the two-port network parameters and noise parameters are involved in either the adding procedure or the de-embedding procedure. Here only the adding procedure is discussed. The de-embedding procedure is just a reverse process. Basically, there are two kinds of cases to add noisy passive components to a noisy two-port network.

In transistor noise modeling, the raw data measured includes pad and interconnect. One common case is to add noisy passive components in parallel with a two-port network, as shown in Fig. 2.6. The added noisy passive components are denoted as Y_1, Y_2, and Y_3, with thermal noise current of $4kT\Re(Y_1)$, $4kT\Re(Y_2)$, and $4kT\Re(Y_3)$, respectively.

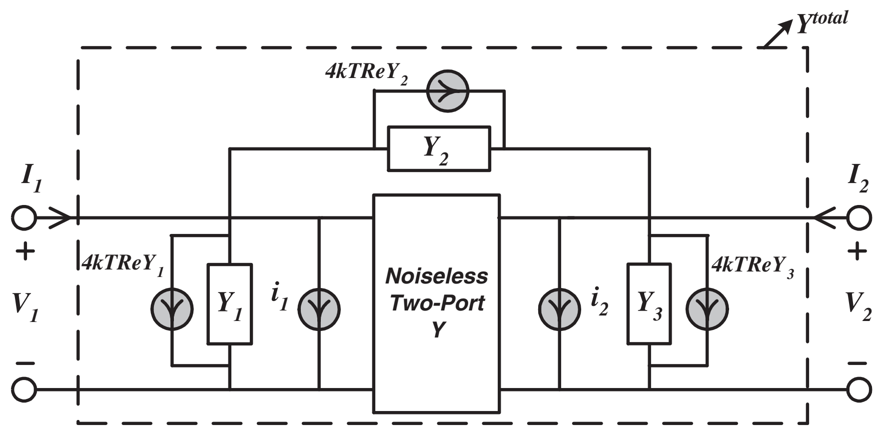

Figure 2.6: Adding noisy passive components parallel to a linear noisy two-port network.

The Y-parameter matrix of the noisy two-port network is denoted as Y. The Y-parameter matrix of after adding the passive components is

$$Y^{total} = Y + \begin{bmatrix} Y_1 + Y_2 & -Y_2 \\ -Y_2 & Y_3 + Y_2 \end{bmatrix} \tag{2.73}$$

Denote the input and output noise currents of the Y- noise representation after adding the passive components as i'_1 and i'_2. The $I - V$ relations including noise is Fig. 2.6 are given by:

$$\begin{pmatrix} I_1 - i_1 - Y_1 V_1 - i_{Y_1} - Y_2(V_2 - V_1) - i_{Y_2} \\ I_2 - i_2 - Y_3 V_2 - i_{Y_3} + Y_2(V_2 - V_1) + i_{Y_2} \end{pmatrix} = \begin{bmatrix} Y_{11} & Y_{12} \\ Y_{21} & Y_{22} \end{bmatrix} \cdot \begin{pmatrix} V_1 \\ V_2 \end{pmatrix}, \tag{2.74}$$

$$\begin{pmatrix} I_1 - i'_1 \\ I_2 - i'_2 \end{pmatrix} = \begin{bmatrix} Y_{11}^{total} & Y_{12}^{total} \\ Y_{21}^{total} & Y_{22}^{total} \end{bmatrix} \cdot \begin{pmatrix} V_1 \\ V_2 \end{pmatrix}, \tag{2.75}$$

$$\tag{2.76}$$

where

$$S_{i_{Y_1}, i^*_{Y_1}} = 4kT\Re(Y_1), \tag{2.77}$$

$$S_{i_{Y_2}, i^*_{Y_2}} = 4kT\Re(Y_2), \tag{2.78}$$

$$S_{i_{Y_3}, i^*_{Y_3}} = 4kT\Re(Y_3). \tag{2.79}$$

Equating the noise terms for both I_1 and I_2, we find the relations between (i_1, i_2) and (i'_1, i'_2),

$$i'_1 = i_1 + i_{Y_1} + i_{Y_2}, \tag{2.80}$$

$$i'_2 = i_2 + i_{Y_3} - i_{Y_2}, \tag{2.81}$$

and

$$S_{i'_1,i'^*_1} = S_{i_1,i^*_1} + 4kT\Re(Y_1) + 4kT\Re(Y_2), \tag{2.82}$$

$$S_{i'_2,i'^*_2} = S_{i_2,i^*_2} + 4kT\Re(Y_3) + 4kT\Re(Y_2), \tag{2.83}$$

$$S_{i'_1,i'^*_2} = S_{i_1,i^*_2} - 4kT\Re(Y_2), \tag{2.84}$$

or in the format of noise matrix

$$C_Y^{total} = C_Y + 4kT \cdot \Re \begin{bmatrix} Y_1 + Y_2 & -Y_2 \\ -Y_2 & Y_3 + Y_2 \end{bmatrix}, \tag{2.85}$$

where C_Y is the Y- noise matrix for the noisy two-port, and C_Y^{total} is the Y- noise matrix after adding the passive components to the noisy two-port.

The other common case is to add noisy passive components in series with the two-port network terminals, as shown in Fig. 2.7. The added noisy passive components are denoted as Z_1, Z_2, and Z_3, with thermal noise voltage of $4kT\Re(Z_1)$, $4kT\Re(Z_2)$, and $4kT\Re(Z_3)$, respectively.

The Z-parameter matrix of the noisy two-port network is denoted as Z. The Z-parameter matrix of after adding the passive components is

$$Z^{total} = Z + \begin{bmatrix} Z_1 + Z_2 & Z_2 \\ Z_2 & Z_3 + Z_2 \end{bmatrix} \tag{2.86}$$

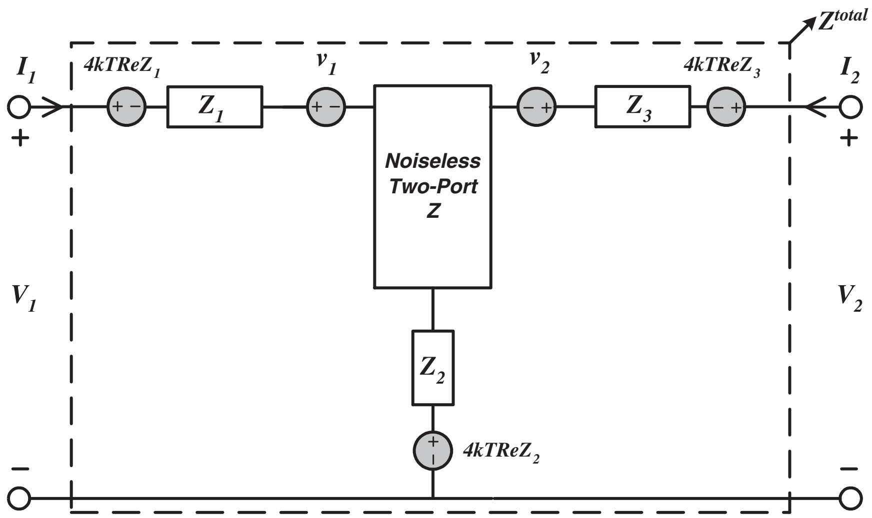

Figure 2.7: Adding noisy passive components in series with a linear noisy two-port network.

Denote the input and output noise currents of the Z- noise representation after adding the passive components as v_1' and v_2'. The $I - V$ relations including noise is Fig. 2.7 are given by:

$$\begin{pmatrix} V_1 - v_1 - Z_1 I_1 - v_{Z_1} - Z_2(I_1 + I_2) - v_{Z_2} \\ V_2 - v_2 - Z_3 I_2 - v_{Z_3} + Z_2(I_1 + I_2) + v_{Z_2} \end{pmatrix} = \begin{bmatrix} Z_{11} & Z_{12} \\ Z_{21} & Z_{22} \end{bmatrix} \cdot \begin{pmatrix} I_1 \\ I_2 \end{pmatrix}, \tag{2.87}$$

$$\begin{pmatrix} V_1 - v_1' \\ V_2 - v_2' \end{pmatrix} = \begin{bmatrix} Z_{11}^{total} & Z_{12}^{total} \\ Z_{21}^{total} & Z_{22}^{total} \end{bmatrix} \cdot \begin{pmatrix} I_1 \\ I_2 \end{pmatrix}, \tag{2.88}$$

(2.89)

where

$$S_{v_{Z_1}, v_{Z_1}^*} = 4kT\Re(Z_1), \tag{2.90}$$

$$S_{v_{Z_2}, v_{Z_2}^*} = 4kT\Re(Z_2), \tag{2.91}$$

$$S_{v_{Z_3}, v_{Z_3}^*} = 4kT\Re(Z_3). \tag{2.92}$$

Equating the noise terms for both V_1 and V_2, we find the relations between (v_1, v_2) and (v_1', v_2'),

$$v_1' = v_1 + v_{Z_1} + v_{Z_2}, \tag{2.93}$$

$$v_2' = v_2 + v_{Z_3} + v_{Z_2}, \tag{2.94}$$

and

$$S_{v_1', v_1'^*} = S_{v_1, v_1^*} + 4kT\Re(Z_1) + 4kT\Re(Z_2), \tag{2.95}$$

$$S_{v_2', v_2'^*} = S_{v_2, v_2^*} + 4kT\Re(Z_3) + 4kT\Re(Z_2), \tag{2.96}$$

$$S_{v_1', v_2'^*} = S_{v_1, v_2^*} + 4kT\Re(Z_2), \tag{2.97}$$

or in the format of noise matrix

$$C_Z^{total} = C_Z + 4kT \cdot \Re \begin{bmatrix} Z_1 + Z_2 & Z_2 \\ Z_2 & Z_3 + Z_2 \end{bmatrix}, \tag{2.98}$$

where C_Z is the Z- noise matrix for the noisy two-port, and C_Z^{total} is the Z- noise matrix after adding the passive components to the noisy two-port.

2.4 Open/Short De-embedding

The equivalent circuit diagram used for open-short de-embedding method is shown in Fig. 2.8, including both the parallel parasitics Y_{p1}, Y_{p2}, Y_{p3}, and the series parasitics Z_{L1}, Z_{L2} and Z_{L3} surrounding the transistor [7]. Denote the S-parameters of the measurement as S_{meas}, the S-parameters of the open de-embedding structure as S_{open}, and the S-parameters of the short de-embedding structure as S_{short}. Using the relations between Y- and S- parameters in Table 2.2, the Y-parameters of the measurement, the open and short de-embedding structure, Y_{meas}, Y_{open} and Y_{short} are obtained. Open and short de-embedding are performed for both Y-parameters and noise parameters to move the reference plane to the device terminals. The resulting Y-parameters and noise parameters are for the transistor. The MATLAB programming for Y-parameters and noise parameters open-short de-embedding is given in Appendix A.

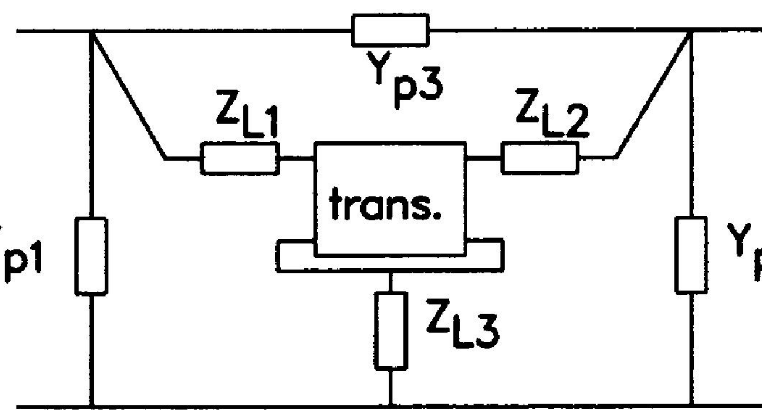

Figure 2.8: Equivalent circuit diagram used for open-short de-embedding method, including both the parallel parasitics Y_{p1}, Y_{p2}, Y_{p3}, and the series parasitics Z_{L1}, Z_{L2} and Z_{L3} surrounding the transistor [7].

2.4.1 Open De-embedding of Y-parameters and Noise Parameters

The Y-parameter for the open de-embedded transistor Y_{od} is [7]

$$Y_{od} = Y_{meas} - Y_{open}. \tag{2.99}$$

The short de-embedding structure also needs to be open de-embedded. The Y-parameter for the open de-embedded short de-embedding structure Y_{os} is [7]

$$Y_{os} = Y_{short} - Y_{open}. \tag{2.100}$$

Denote the noise parameters for measurement as NF_{min}, R_n and γ_{opt}, where

$$\gamma_{opt} = \frac{Y_0 - Y_{opt}}{Y_0 - Y_{opt}}. \tag{2.101}$$

Y_{opt} can be thus obtained by γ_{opt} as

$$Y_{opt} = Y_0 \frac{1 - \gamma_{opt}}{1 + \gamma_{opt}}. \tag{2.102}$$

The chain noise representation matrix of the measurement $C_{A,meas}$ can be thus obtained using (2.32). To perform open-short de-embedding, $C_{A,meas}$ needs to be transformed to the Y-noise representation matrix $C_{Y,meas}$ using (2.72),

$$C_{Y,meas} = T_{A-Y} \cdot C_{A,meas} \cdot T_{A-Y}^{\dagger}, \tag{2.103}$$

and T_{A-Y} is given by Table 2.1:

$$T_{A-Y} = \begin{bmatrix} -Y_{11}^{meas} & 1 \\ -Y_{21}^{meas} & 0 \end{bmatrix}, \tag{2.104}$$

where Y_{11}^{meas} and Y_{21}^{meas} are elements of Y_{meas} matrix. Therefore, the Y- noise representation matrix for open de-embedded transistor $C_{Y,od}$ is

$$C_{Y,od} = C_{Y,meas} - 4kT\Re[Y_{od}]. \tag{2.105}$$

2.4.2 Short De-embedding of Y-parameters and Noise Parameters

The Z-parameter for the short de-embedded transistor Z is [7]

$$Z = Z_{od} - Z_{os}, \tag{2.106}$$

where Z_{od} and Z_{os} are Z-parameter matrices of the open de-embedded transistor and the short de-embedding structure, respectively. Z_{od} and Z_{os} are obtained from Y_{od} and Y_{os} using Table 2.2.

For short de-embedding of the noise parameters, we need to start with the Z-noise representation matrix of the open de-embedded transistor $C_{Z,od}$,

$$C_{Z,od} = T_{Y-Z} \cdot C_{Y,od} \cdot T_{Y-Z}^{\dagger}, \tag{2.107}$$

and T_{Y-Z} is given by Table 2.1:

$$T_{Y-Z} = \begin{bmatrix} Z_{11}^{od} & Z_{12}^{od} \\ Z_{21}^{od} & Z_{22}^{od} \end{bmatrix}, \tag{2.108}$$

where Z_{11}^{od}, Z_{12}^{od}, Z_{21}^{od}, and Z_{22}^{od} are elements of Z_{od} matrix. The Z-noise representation matrix of the open-short de-embedded transistor C_Z is thus obtained,

$$C_Z = C_{Z,od} - 4kT\Re[Z_{os}]. \tag{2.109}$$

Fig. 2.9 – Fig. 2.16 show the bias and frequency dependence of the noise parameters NF_{min}, R_n, and Y_{opt} of raw measurement data, open de-embedding, and open-short de-embedding data. The results show that the short de-embedding is important for noise parameters de-embedding, and cannot be neglected.

2.4.3 Problems Encountered in MATLAB Programming for Open-Short De-embedding

The open-short de-embedding process is realized in MATLAB. The conversions of different noise representations can be accomplished using MATLAB matrices operation. However, unexpected imaginary part are obtained for some elements in the matrix which should be real numbers theoretically. Here, measurement data of 0.12 μm process measured in IBM is used as an example. $V_{gs} = 0.685$ V, $V_{ds} = 1.5$ V. At $f = 28$ GHz, CA for raw data is

$$CA = \begin{bmatrix} 0.39291636000000 & 0.01285241162005 - 0.02039784627097i \\ 0.01285241162005 + 0.02039784627097i & 0.00166866364322 \end{bmatrix}. \tag{2.110}$$

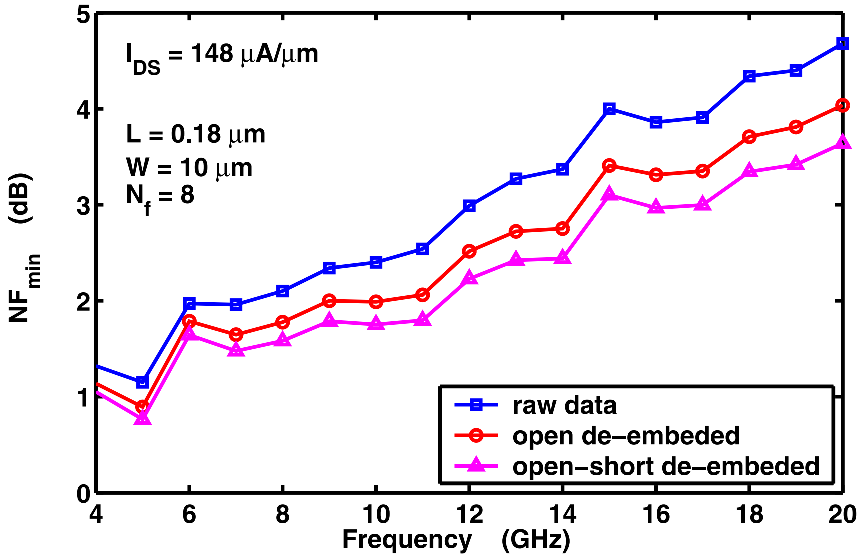

Figure 2.9: NF_{min} v.s. frequency. I_{DS} = 148 μA/μm. V_{DS} = 1 V.

The very first step is to transform chain noise representation matrix CA to Y- noise representation matrix CY using (2.103). The transform matrice T is

$$T = \begin{bmatrix} -0.02092695425297 - 0.06129572408422i & 1 \\ -0.06717448393087 + 0.14736069526087i & 0 \end{bmatrix}. \tag{2.111}$$

When realizing (2.103) in MATLAB, if the following code is used,

```
CA = [Sva, Siava'; Siava, Sia];
T = [-Y11, 1; -Y21, 0]; T_conjtrans = T';
CY = T * CA * T_conjtrans;
Si1 = CY(1,1); Si2 = CY(2,2); Si1i2 = CY(1,2);
```

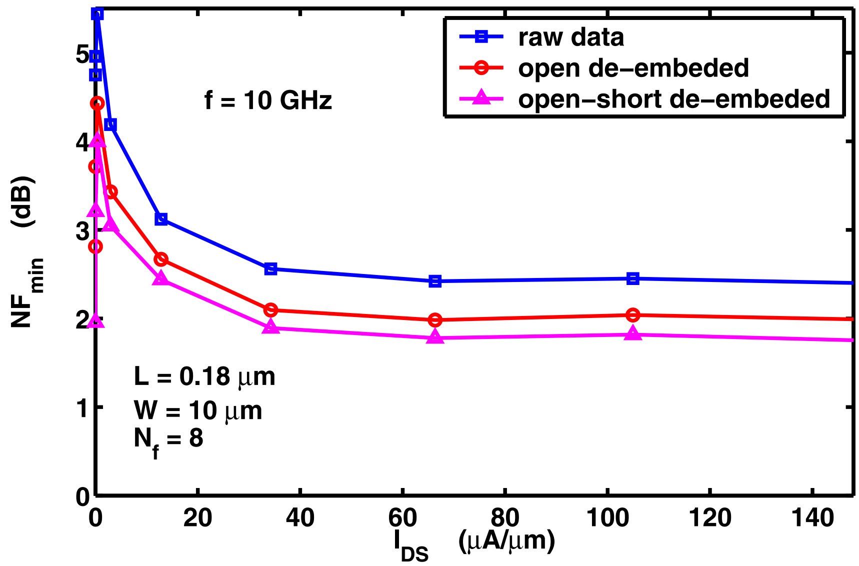

Figure 2.10: NF_{min} v.s. I_{DS} normalized by size of device. f = 10 GHz. V_{DS} = 1 V.

the resulting `Si1` is (0.00278463150577 - 0.00000000000000i), with neglegible imaginary part, which is theoretically wrong. The origin of the problem lies in the complex number operation in MATLAB. Let x be a complex number, and y be a real number. In MATLAB programming, `x*x'*y` gives a real number. However, `x*y*x'` gives a complex number with an imaginary part. Although the produced imaginary part is negligible for one step of calculation, the induced error cannot be neglected after multiple steps of similar operations. For example, the resulting the open-short de-embedded NF_{min} for the transistor using matrix operation is (1.45838190834363 + 0.01511935061286i), which has considerable imaginary part. Therefore MATLAB matrix operation cannot be directly used. Instead, detailed operations for each element of a matrix are applied:

```
CA = [Sva, Siava'; Siava, Sia];

T = [-Y11, 1; -Y21, 0]; T_conjtrans = T';
```

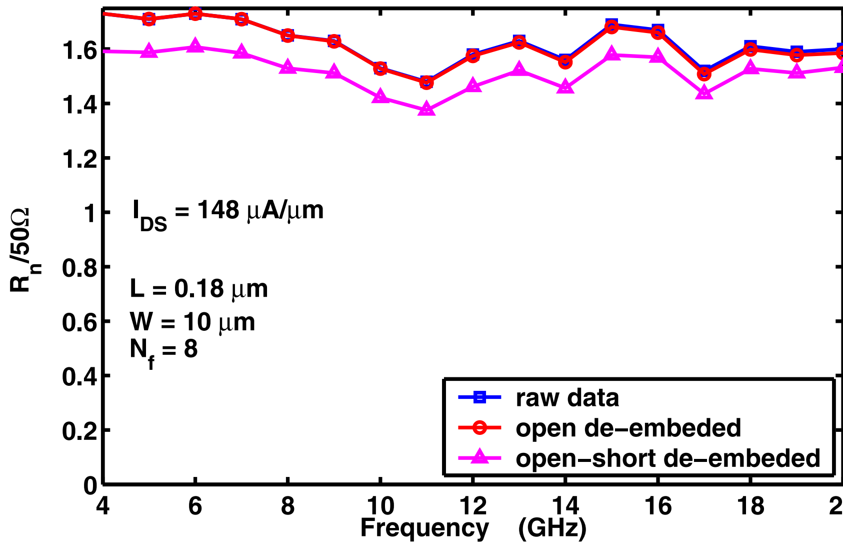

Figure 2.11: R_n v.s. frequency. $I_{DS} = 148\ \mu A/\mu m$. $V_{DS} = 1$ V.

```
CY(1,1) = (abs(T(1,1)))^2*CA(1,1) + (abs(T(1,2)))^2*CA(2,2)...

       + 2*real(T_conjtrans(1,1)*T(1,2)*CA(2,1));

CY(1,2) = T(1,1)*T_conjtrans(1,2)*CA(1,1)+T(1,2)*T_conjtrans(1,2)*CA(2,1)...

       +T(1,1)*T_conjtrans(2,2)*CA(1,2)+T(1,2)*T_conjtrans(2,2)*CA(2,2);

CY(2,1) = CY(1,2)';

CY(2,2) = (abs(T(2,1)))^2*CA(1,1) + (abs(T(2,2)))^2*CA(2,2)...

       + 2*real(T_conjtrans(2,2)*T(2,1)*CA(1,2));

Si1 = CY(1,1); Si2 = CY(2,2); Si1i2 = CY(1,2);
```

The resulting `Si1` is 0.00278463150577, which has no imaginary part. After multiple steps, the open-short de-embedded NF_{min} for the transistor is 1.45574769257762, which is slightly lower than the real part of the result using matrix operation.

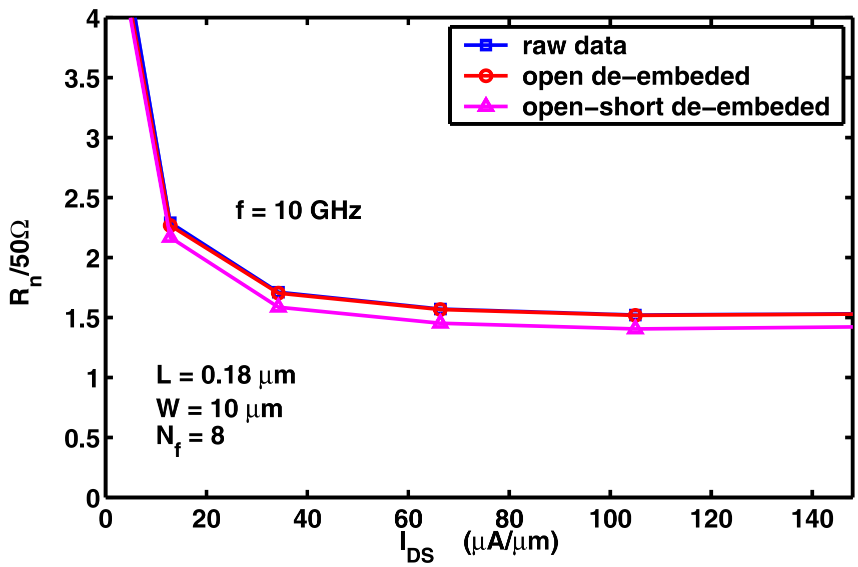

Figure 2.12: R_n v.s. I_{DS} normalized by size of device. f = 10 GHz. V_{DS} = 1 V.

2.5 Transistor Internal Noise De-embedding

MOSFET transistor i_g and i_d noise de-embedding procedure and SiGe HBT transistor i_b and i_c noise de-embedding procedure are discussed in this section. The techniques are repeatedly used in later chapters of this dissertation.

2.5.1 MOSFET Transistor i_g and i_d Noise De-embedding

The equivalent circuit of the transistor is shown in Fig. 2.17. Here R_g is the gate electrode resistance, and R_s and R_d are the source and drain series resistances. R_g, R_s and R_d all have the usual $4kTR$ thermal noise voltage. R_{gs} is the non-quasi-static (NQS) channel resistances. g_{ds} is the output conductance. g_m is transconductance. C_{gs} and C_{gd} are the gate to source and gate to drain capacitances. C_{db} is the drain to body junction capacitance, and R_{db} is the body

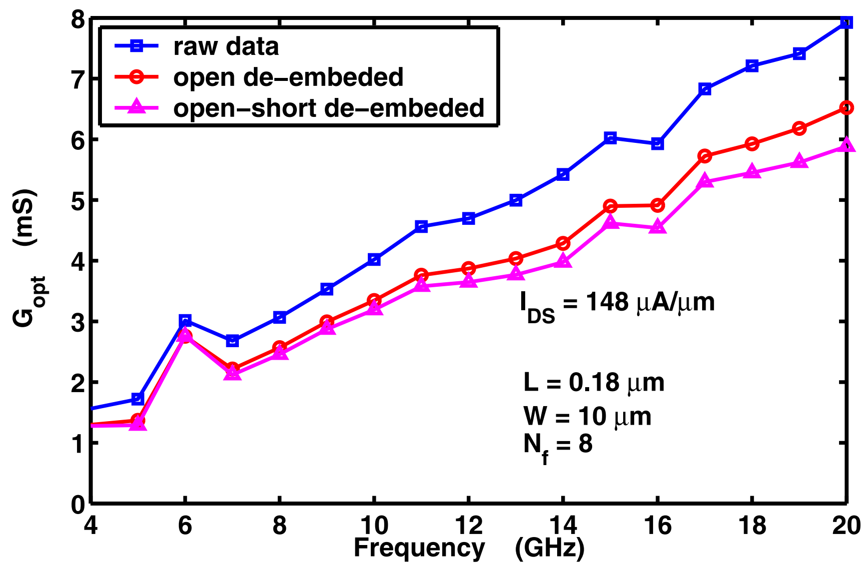

Figure 2.13: G_{opt} v.s. frequency. I_{DS} = 148 μA/μm. V_{DS} = 1 V.

resistance of the drain to body junction. R_{db} has the usual $4kTR$ thermal noise. The equivalent circuit parameters are extracted using the method described in [9]. Note that R_{gs}, and g_{ds} do not have the usual $4kTR$ thermal noise. Instead, i_g and i_d, the Y-noise representation parameters, are used to describe all of the noise from the intrinsic transistor.

Here we choose to define i_g and i_d as the Y-representation input and output noise current for the level II block shown in Fig. 2.17. The level II block consists of R_g, C_{gs}, the g_m controlled source and g_{ds}, and is the core part for noise modeling. The level I block is defined as the combination of the level II block with the branch of C_{gd}, and the branch of C_{db} and R_{db}. Next we need to extract the power spectral densities (PSD) of i_g, i_d, and their correlation, which we

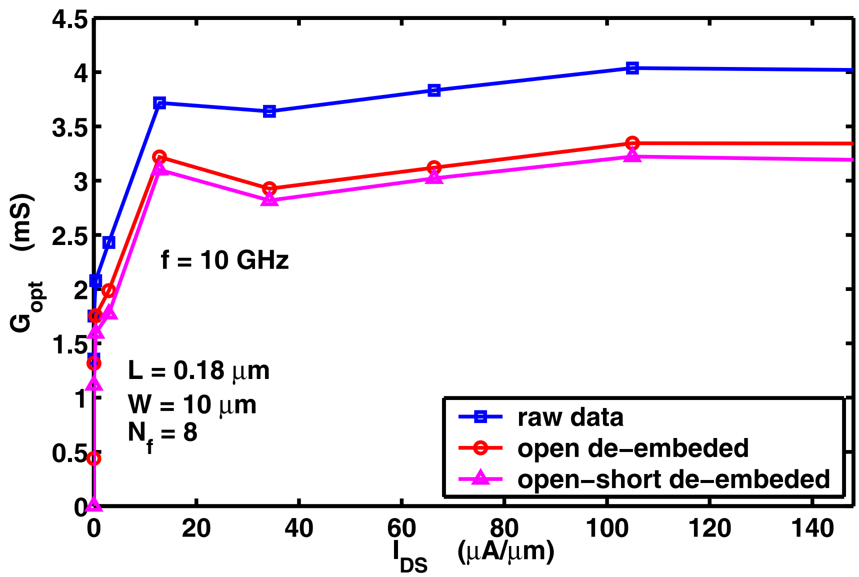

Figure 2.14: G_{opt} v.s. I_{DS} normalized by size of device. f = 10 GHz. V_{DS} = 1 V.

denote as $S^{II}_{i_g,i_g^*}$, $S^{II}_{i_d,i_d^*}$, and $S^{II}_{i_g,i_d^*}$. They can also be written using matrix notation as:

$$C_{Y_{II}} \triangleq \begin{bmatrix} S^{II}_{i_g,i_g^*} & S^{II}_{i_g,i_d^*} \\ S^{II}_{i_d,i_g^*} & S^{II}_{i_d,i_d^*} \end{bmatrix}, \tag{2.112}$$

where $C_{Y_{II}}$ is also referred to as the Y-representation noise matrix for the level II block.

Firstly, the thermal resistances outside of the level I block, R_g, R_s and R_d, need to be removed. Denote the Z-parameters of the level I block as Z_I, which is related to Z as

$$Z_I = Z - Z_1, \tag{2.113}$$

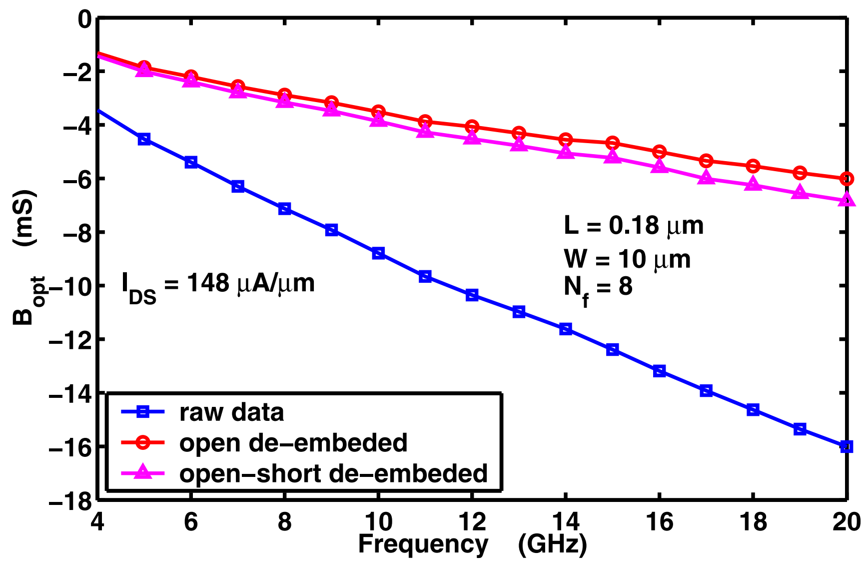

Figure 2.15: B_{opt} v.s. frequency. I_{DS} = 148 μA/μm. V_{DS} = 1 V.

where

$$Z_1 = \begin{bmatrix} R_s + R_g & R_s \\ R_s & R_s + R_d \end{bmatrix}. \tag{2.114}$$

Using the open-short de-embedded transistor Z- noise representation matrix C_Z, the Z- noise representation matrix of the level I block C_{Z_I} is

$$C_{Z_I} = C_Z - 4kT\Re[Z_1]. \tag{2.115}$$

The next step is to remove the branch of C_{gd}, and the branch of C_{db} and R_{db} to obtain the Y- noise representation matrix of the level II block $C_{Y_{II}}$. Y-parameters matrix of the level I block Y_I can be obtained from Z_I using Table 2.2. Therefore Y-parameters matrix of the level II block

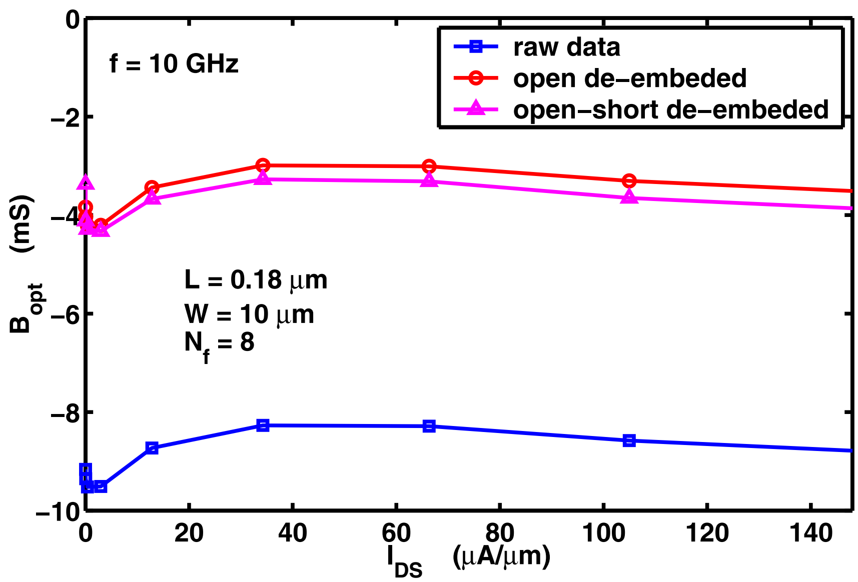

Figure 2.16: B_{opt} v.s. I_{DS} normalized by size of device. f = 10 GHz. $V_{DS} = 1$ V.

Y_{II} is,

$$Y_{II} = Y_I - Y_1, \tag{2.116}$$

$$Y_1 = \begin{bmatrix} j\omega C_{gd} & -j\omega C_{gd} \\ -j\omega C_{gd} & j\omega C_{gd} + \frac{j\omega C_{db}}{1+j\omega C_{db} R_{db}} \end{bmatrix}. \tag{2.117}$$

The Y-representation noise matrix for the level I block, C_{Y_I} can be obtained from C_{Z_I} as,

$$C_{Y_I} = T_{Z-Y} \cdot C_{Z_I} \cdot T_{Z-Y}\dagger, \tag{2.118}$$

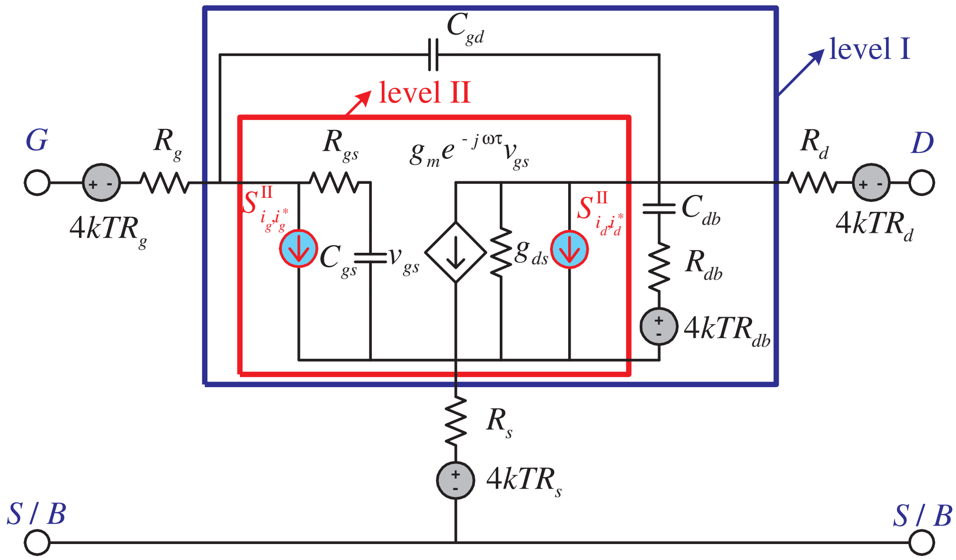

Figure 2.17: The small signal equivalent circuit model used with Y-representation noise sources.

and T_{Z-Y} is given by Table 2.1:

$$T_{Z-Y} = \begin{bmatrix} Y^I_{11} & Y^I_{12} \\ Y^I_{21} & Y^I_{22} \end{bmatrix}, \tag{2.119}$$

where Y^I_{11}, Y^I_{12}, Y^I_{21}, and Y^I_{22} are elements of Y_I matrix. Therefore the Y- noise representation matrix of the level II $C_{Y_{II}}$ is

$$C_{Y_{II}} = C_{Y_I} - 4kT\Re[Y_1]. \tag{2.120}$$

Thus, the i_g and i_d noise currents of MOSFET transistor are finally de-embedded from measurement data,

$$S^{II}_{i_g,i_g^*} = C_{Y_{II}}(1,1), \tag{2.121}$$

$$S^{II}_{i_d,i_d^*} = C_{Y_{II}}(2,2), \tag{2.122}$$

$$S^{II}_{i_g,i_d^*} = C_{Y_{II}}(1,2). \tag{2.123}$$

Fig. 2.18 – Fig. 2.20 shows the bias dependence of Y- noise current sources for the whole transistor and the intrinsic transistor for 0.24 μm gate length MOSFET transistor. $W = 4$ μm, number of finger Nf is 128. The gate resistance R_g is extracted using the advanced parameter extraction method in chapter 7. $R_g = 0.6$ Ω. Both the input and output Y- noise representation currents decreases after deembedding to the intrinsic device. The imaginary part of their correlation is also less for the intrinsic device.

2.5.2 SiGe HBT Transistor i_b and i_c Noise De-embedding

The process of SiGe HBT transistor i_b and i_c noise de-embedding is similar to the procedures in section 2.5.1. The thermal noise of a SiGe HBT transistor is simulated using 2-D DESSIS v9.0 simulation tool [45]. The output of DESSIS simulation tool is the Y- parameter and the Z- noise representation parameters S_{v_1,v_1^*}, S_{v_2,v_2^*} and S_{v_2,v_1^*} (S_{v_1,v_2^*} for DESSIS v7.0). Firstly we are interested in calculating the noise parameters NF_{min}, R_n and Y_{opt}, which inevitably involves the calculation of chain noise representation parameters S_{v_a,v_a^*}, S_{i_a,i_a^*}, and S_{i_a,v_a^*} from Z-noise representation parameters.

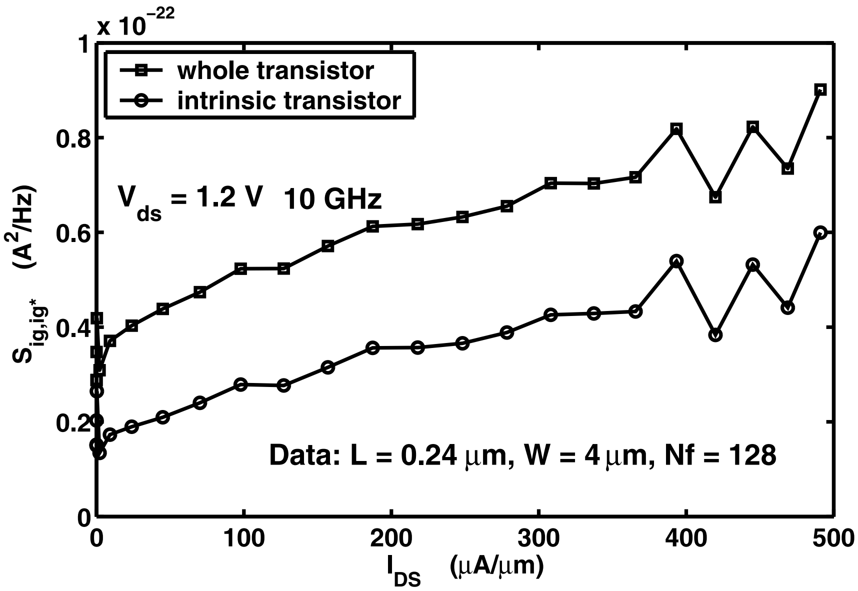

Figure 2.18: Y- noise representation input noise current for the whole and the intrinsic MOSFET transistor.

Denote Y- parameters of the output of DESSIS simulation as Y, the Z- noise representation matrix of the output of DESSIS simulation as C_Z. The chain noise representation matrix C_A is

$$C_A = T_{Z-A} \cdot C_Z \cdot T_{Z-A}^{\dagger}, \tag{2.124}$$

and T_{Z-A} is given by Table 2.1:

$$T_{Z-A} = \begin{bmatrix} 1 & -A_{12} \\ 0 & -A_{21} \end{bmatrix}, \tag{2.125}$$

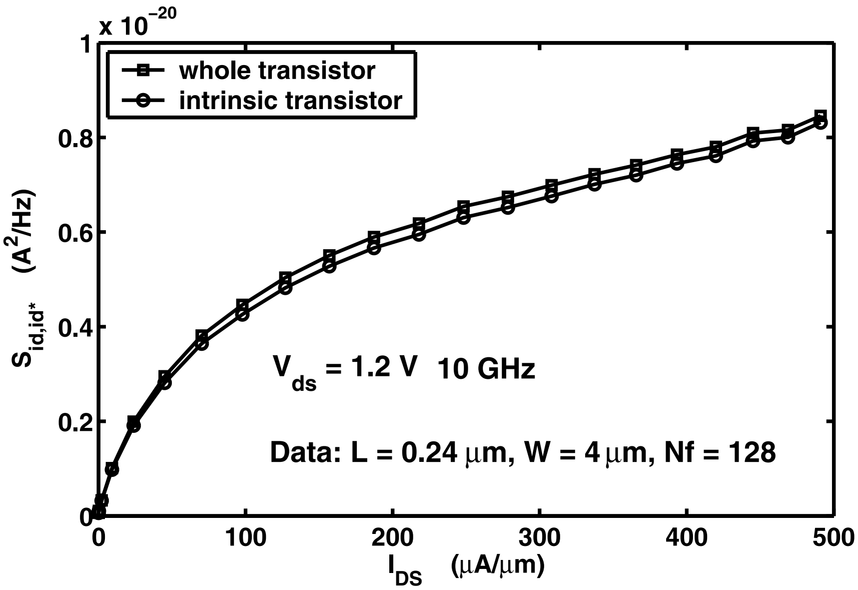

Figure 2.19: Y- noise representation output noise current for the whole and the intrinsic MOSFET transistor.

where A_{12} and A_{21} are elements of ABCD matrix A, which can be converted from Y using Table 2.2. The noise parameters NF_{min}, R_n and Y_{opt} can then be obtained using (2.24) – (8.19) directly.

Secondly, we are interested in i_b and i_c noise currents of SiGe HBT transistor. The equivalent circuit for the simulated SiGe HBT transistor is the same as Fig. 1.2 in chapter 1, which includes base resistance r_b with usual $4kTR$ thermal noise voltage, and the intrinsic transistor whose noise is described using Y- noise representation parameters S_{i_b,i_b^*}, S_{i_c,i_c^*} and S_{i_c,i_b^*}.

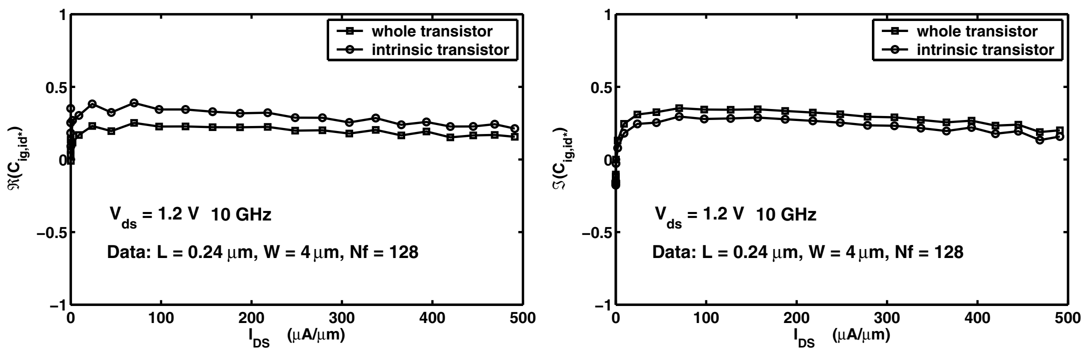

Figure 2.20: Y- noise representation correlation for the whole and the intrinsic MOSFET transistor.

Through circuit analysis, Fig. 1.2 and Fig. 2.1 show

$$\begin{pmatrix} I_1 - i_b \\ I_2 - i_c \end{pmatrix} = \begin{bmatrix} Y_{11}^{int} & Y_{12}^{int} \\ Y_{21}^{int} & Y_{22}^{int} \end{bmatrix} \cdot \begin{pmatrix} V_1 - v_b - I_1 r_b \\ V_2 \end{pmatrix}, \tag{2.126}$$

$$\begin{pmatrix} I_1 - i_a \\ I_2 \end{pmatrix} = \begin{bmatrix} Y_{11} & Y_{12} \\ Y_{21} & Y_{22} \end{bmatrix} \cdot \begin{pmatrix} V_1 - v_a \\ V_2 \end{pmatrix}. \tag{2.127}$$

Y_{11}, Y_{12}, Y_{21} and Y_{22} are Y- parameters for the whole transistor Y that includes both r_b and the intrinsic transistor. Y_{11}^{int}, Y_{12}^{int}, Y_{21}^{int} and Y_{22}^{int} are elements of the intrinsic transistor Y- parameters matrix Y_{int} . The intrinsic Y- parameters Y_{int} relates to whole Y- parameters Y as,

$$Y_{11}^{int} = \frac{Y_{11}}{1 - Y_{11} r_b}, \tag{2.128}$$

$$Y_{12}^{int} = \frac{Y_{12}}{1 - Y_{11} r_b}, \tag{2.129}$$

$$Y_{21}^{int} = \frac{Y_{21}}{1 - Y_{11} r_b}, \tag{2.130}$$

$$Y_{22}^{int} = \frac{Y_{22}}{1 - Y_{11} r_b} - \frac{r_b (Y_{11} Y_{22} - Y_{12} Y_{21})}{1 - Y_{11} r_b}. \tag{2.131}$$

From (2.126), we have,

$$I_1 = i_b + Y_{11}^{int}(V_1 - v_b) - I_1 r_b Y_{11}^{int} + Y_{12}^{int} V_2, \tag{2.132}$$

$$= \frac{i_b}{1 + Y_{11}^{int} r_b} + \frac{Y_{11}^{int}}{1 + Y_{11}^{int} r_b}(V_1 - v_b) + \frac{Y_{12}^{int}}{1 + Y_{11}^{int} r_b} V_2, \tag{2.133}$$

$$= \frac{i_b}{1 + Y_{11}^{int}} + Y_{11}(V_1 - v_b) + Y_{12} V_2, \tag{2.134}$$

and

$$I_2 = i_c + Y_{21}^{int}(V_1 - v_b - I_1 r_b) + Y_{22}^{int} V_2. \tag{2.135}$$

Substituting (2.134) in (2.135),

$$I_2 = i_c + Y_{21}^{int}(V_1 - v_b) - \frac{Y_{21}^{int} i_b r_b}{1 + Y_{11}^{int} r_b} - Y_{21}^{int} Y_{11}(V_1 - v_b) r_b - Y_{21}^{int} Y_{12} V_2 r_b + Y_{22}^{int} V_2, \tag{2.136}$$

$$= i_c + Y_{21}^{int}(1 - Y_{11} r_b)(V_1 - v_b) - Y_{21} i_b r_b + V_2(Y_{22}^{int} - Y_{12} Y_{21}^{int} r_b), \tag{2.137}$$

$$= i_c + Y_{21}(V_1 - v_b) - Y_{21} i_b r_b + V_2 \left[\frac{Y_{22}}{1 - Y_{11} r_b} - \frac{r_b(Y_{11} Y_{22} - Y_{12} Y_{21})}{1 - Y_{11} r_b} - \frac{Y_{12} Y_{21} r_b}{1 - Y_{11} r_b} \right], \tag{2.138}$$

$$= i_c + Y_{21}(V_1 - v_b) - Y_{21} i_b r_b + Y_{22} V_2. \tag{2.139}$$

From (2.127), we have,

$$I_1 = i_a + Y_{11}(V_1 - v_a) + Y_{12}V_2, \tag{2.140}$$

$$I_2 = Y_{21}(V_1 - v_a) + Y_{22}V_2. \tag{2.141}$$

(2.141)-(2.139), we have

$$v_a = v_b - \frac{i_c}{Y_{21}} + i_b r_b. \tag{2.142}$$

(2.140)-(2.134), and using the result of (2.142), we have

$$i_a = \frac{i_b}{1 + Y_{11}^{int} r_b} + Y_{11}(v_a - v_b), \tag{2.143}$$

$$= \frac{i_b}{1 + Y_{11}^{int} r_b} - \frac{Y_{11}}{Y_{21}} i_c + Y_{11} i_b r_b, \tag{2.144}$$

$$= i_b - \frac{Y_{11}}{Y_{21}} i_c. \tag{2.145}$$

Finally, Fig. 1.2 can be transformed to the form of the chain noise representation Fig. 2.1,

$$v_a = v_b + i_b r_b - \frac{1}{Y_{21}} i_c, \tag{2.146}$$

$$i_a = i_b - \frac{Y_{11}}{Y_{21}} i_c, \tag{2.147}$$

$$= i_b - \frac{i_c}{h_{21}}, \tag{2.148}$$

where

$$h_{21} = \frac{Y_{21}}{Y_{11}} = \frac{Y_{21}^{int}}{Y_{11}^{int}} = h_{21}^{int}. \tag{2.149}$$

The resulting S_{v_a,v_a^*}, S_{i_a,i_a^*} and S_{i_a,v_a^*} are

$$S_{v_a,v_a^*} = S_{v_b,v_b^*} + \frac{1}{|Y_{21}|^2} S_{i_c,i_c^*} + S_{i_b,i_b^*} r_b^2 - 2\Re(\frac{r_b}{Y_{21}} S_{i_c,i_b^*}), \tag{2.150}$$

$$S_{i_a,i_a^*} = S_{i_b,i_b^*} + \left|\frac{Y_{11}}{Y_{21}}\right|^2 S_{i_c,i_c^*} - 2\Re\left(\frac{Y_{11}}{Y_{21}} S_{i_c,i_b^*}\right), \tag{2.151}$$

$$S_{i_a,v_a^*} = \frac{Y_{11}}{|Y_{21}|^2} S_{i_c,i_c^*} + S_{i_b} r_b - \frac{1}{Y_{21}^*} S^*_{i_c,i_b^*} - \frac{r_b}{h_{21}} S_{i_c,i_b^*}. \tag{2.152}$$

On the contrary, Fig. 1.2 can be transformed from the form of the chain noise representation Fig. 2.1,

$$i_c = -Y_{21}^{internal}(v_a - v_b - i_a r_b), \tag{2.153}$$

$$= -\frac{Y_{21}}{1 - Y_{11} r_b}(v_a - v_b - i_a r_b), \tag{2.154}$$

$$i_b = i_a - Y_{11}^{internal}(v_a - v_b - i_a r_b), \tag{2.155}$$

$$= \frac{1}{1 - Y_{11} r_b} i_a - \frac{Y_{11}}{1 - Y_{11} r_b}(v_a - v_b). \tag{2.156}$$

The resulting S_{i_b,i_b^*}, S_{i_c,i_c^*} and S_{i_c,v_b^*} are

$$S_{i_b,i_b^*} = \frac{1}{|1 - Y_{11}r_b|^2}(S_{i_a,i_a^*} + |Y_{11}|^2(S_{v_a,v_a^*} - 4kTr_b) - 2\Re(Y_{11}^* S_{i_a,v_a^*})), \tag{2.157}$$

$$S_{i_c,i_c^*} = |\frac{Y_{21}}{1 - Y_{11}r_b}|^2(S_{v_a,v_a^*} - 4kTr_b + S_{i_a,i_a^*}r_b^2 - 2r_b\Re S_{i_a,v_a^*}), \tag{2.158}$$

$$S_{i_c,i_b^*} = \frac{1}{|1 - Y_{11}r_b|^2}(Y_{21}r_bS_{i_a,i_a^*} + Y_{21}Y_{11}^*(S_{v_a,v_a^*} - 4kTr_b) - Y_{21}S_{i_a,v_a^*}^* - Y_{21}Y_{11}^*r_bS_{i_a,v_a^*}). \tag{2.159}$$

The base resistance r_b for each bias is determined using semi-circle fitting method [46]. Plot $\Im(h_{11})$ versus $\Re(h_{11})$, fit the data using a semi-circle, r_b is determined using the high frequency intercept with the $\Re(h_{11})$ axis. Using (2.157) – (2.159), the i_b and i_c noise currents of SiGe HBT transistor are thus obtained.

Fig. 2.21 and Fig. 2.22 shows Y- noise current sources for the whole transistor and the intrinsic transistor for DESSIS simulation results of 8HP 0.12×1 μm^2 SiGe HBT transistor at 40 GHz. Both the input noise current and output noise current become less for the intrinsic device. The absolute value of Y- noise representation correlation decreases after de-embedding to the intrinsic device.

2.6 Importance of Terminal Series Resistances to Noise parameters

The gate electrode resistance R_g for MOSFET transistors, or the base resistance r_b for SiGe HBT transistors is the input series resistance to the intrinsic device. The input series resistance is the most important for noise parameters, since its thermal noise contribution is amplified by the two-port network. On the contrary, the output series resistance is the least important for

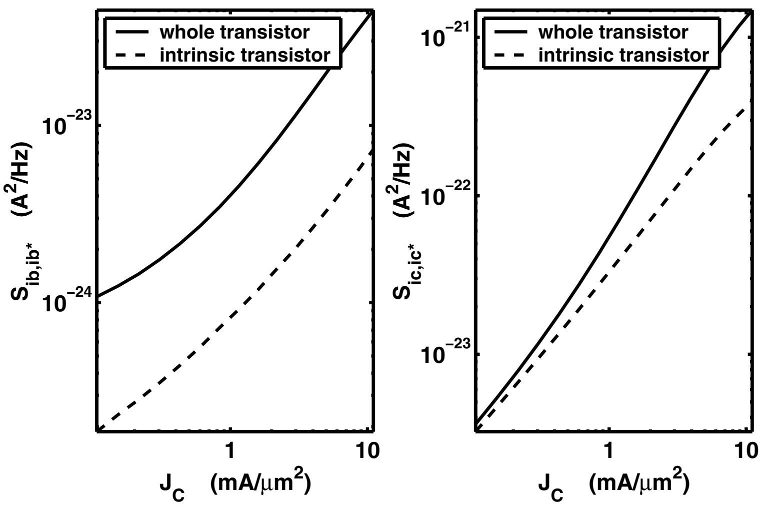

Figure 2.21: Y- noise representation input and output noise currents for the whole and the intrinsic SiGe HBT transistor.

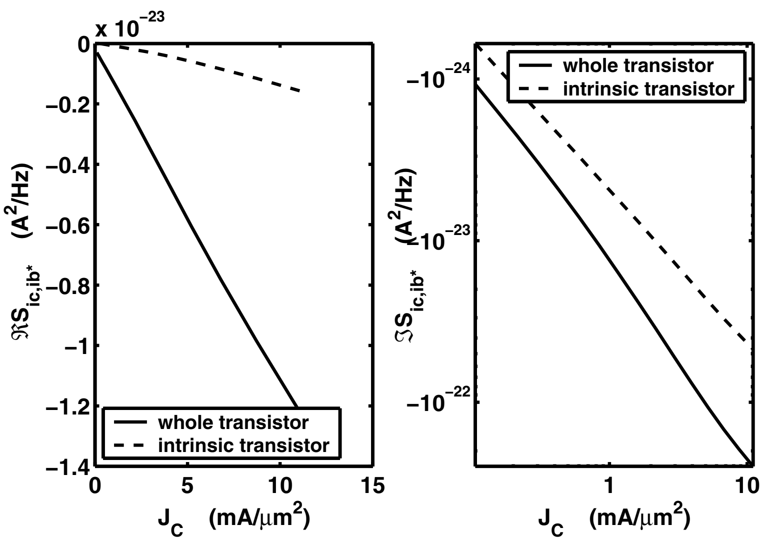

Figure 2.22: Y- noise representation correlation for the whole and the intrinsic SiGe HBT transistor.

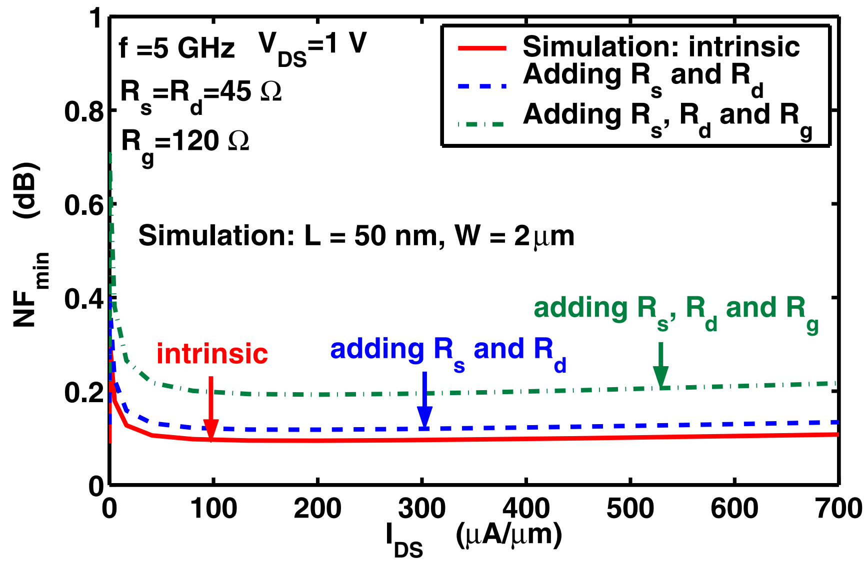

Figure 2.23: NF_{min} vs I_{DS} with and without R_g, R_s and R_d at 5 GHz.

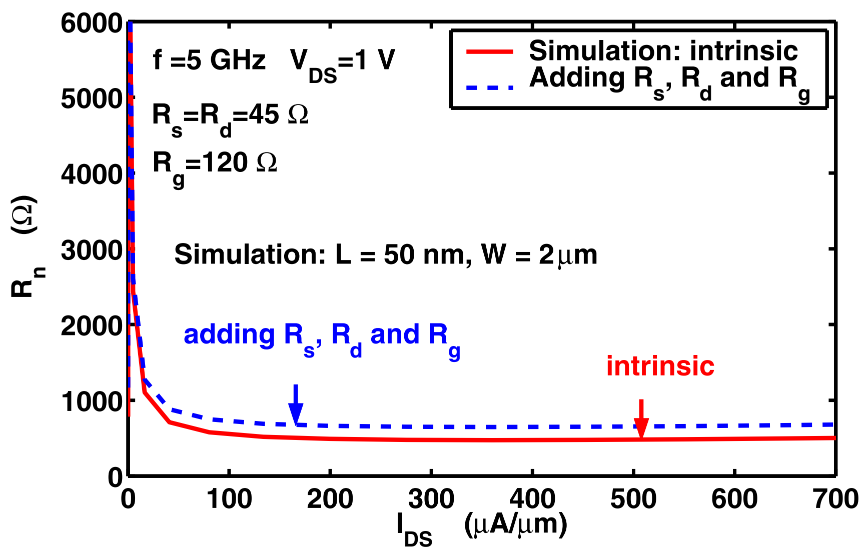

Figure 2.24: R_n vs $I_{DS}$with and without R_g, R_s and R_d at 5 GHz.

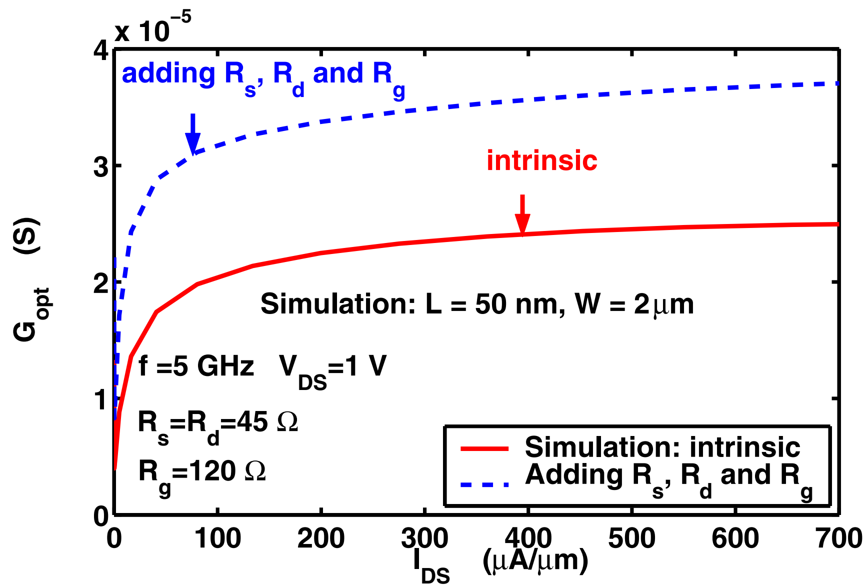

Figure 2.25: G_{opt} vs I_{DS} with and without R_g, R_s and R_d at 5 GHz.

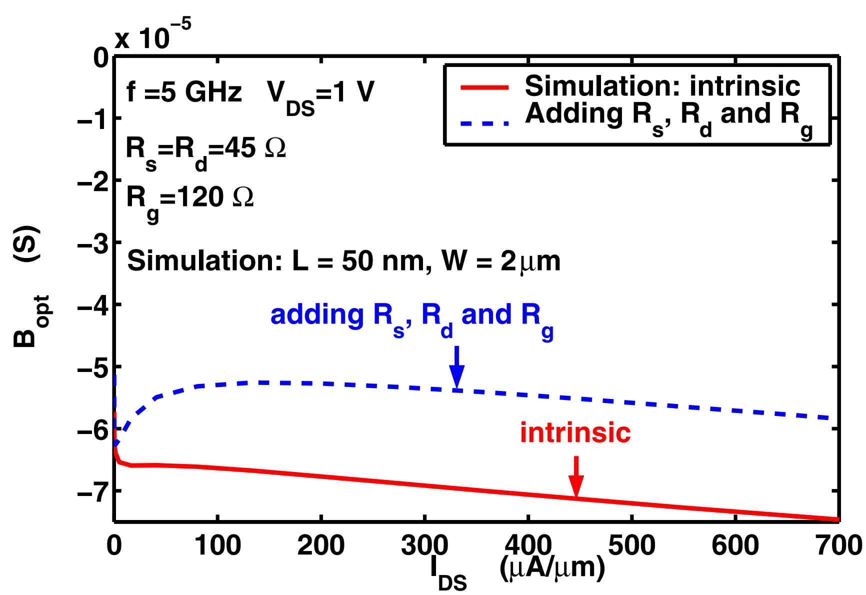

Figure 2.26: B_{opt} vs I_{DS} with and without R_g, R_s and R_d at 5 GHz.

noise parameters. The drain electrode resistance R_d for MOSFET transistors and the collector resistance r_c for SiGe HBT transistors are the output series resistance to the intrinsic device.

The source electrode resistance R_s for MOSFET transistors, or the emitter resistance r_e for SiGe HBT transistors, contributes thermal noise to the input terminal, the output terminal, and their correlation. Therefore they are less important for noise parameters compared to the input series resistance.

Fig. 2.23 shows NF_{min} simulated at 5 GHz versus I_{DS}. We find that R_s is the major reason for the increase of NF_{min} compared to the intrinsic NF_{min}, yet it is a function of the R_g and R_s values. Fig. 2.24 shows R_n vs I_{DS}, and Fig. 2.25 and Fig. 2.26 show G_{opt} and B_{opt} vs I_{DS} at 5 GHz.

2.7 Summary

Different noise representations for a linear noisy two-port network are introduced. The transformation matrices to other noise representations are given for ABCD-, Y-, Z-, and H-noise representations. Techniques of adding or de-embedding a passive component to a linear two-port network are discussed. Noise sources de-embedding for both MOSFET and SiGe HBT are given for repeatedly use in later chapters.

CHAPTER 3

MICROSCOPIC NOISE CONTRIBUTIONS

This chapter presents a new technique of simulating the spatial distribution of microscopic noise contribution to the input noise current, voltage, and their correlation. The technique is demonstrated on a 50 GHz SiGe HBT. A strong "noise crowding" effect is observed in the spatial distribution of noise concentrations due to base majority holes. The spatial distributions by base majority holes, base minority electrons, and emitter minority holes are analyzed, and compared to the compact noise model. This technique is also applied to a 120 GHz MOSFET transistor. The spatial distribution of drain noise current, gate noise current, and their correlation are analyzed.

3.1 Introduction

One of the key concerns in optimizing SiGe HBTs is to minimize noise, which requires methods of simulating transistor noise parameters for a given device design. One method is to simulate transistor s-parameters, extract parameters of an equivalent circuit, and then calculate the noise parameters using a circuit-level transistor noise model [47]. The accuracy of this method is limited by the accuracy of the transistor noise model used. The other method is microscopic noise simulation. The terminal voltage noise is obtained by summing the responses of the terminal voltage to carrier velocity fluctuations, and hence current density fluctuations at each grid cell, which is the basic element for equation solutions, using Shockley's impedance field approach [48], which has recently become available in TCAD tools. The results of microscopic noise simulation are typically given by the spatial distribution of either the open circuit noise voltages or the short circuit noise currents. For comparison with measurements, however, the input noise current i_a and the input noise voltage v_a for a chain representation shown in Fig. 2.1 in chapter 2 are the most convenient [47] [10]. The spectral densities of i_a, v_a and i_a, v_a^* directly relate to circuit-level noise parameters: minimum noise figure NF_{min}, noise resistance R_n, and the optimal source admittance Y_{opt} by (2.24) – (8.19) in chapter 2.

This chapter presents a new technique of simulating the spatial distribution of microscopic noise contributions to the input noise current, voltage and their correlation, and results obtained on a 50 GHz SiGe HBT technology [49]. The technique facilities the identification of major noise sources within the transistor physical structure, leading to device-level optimization, such as doping profile, Ge profile, and/or device layout, with respect to the noise parameters.

3.2 Microscopic Noise Simulation

Shockley's impedance field approach is illustrated in Fig. 3.1 [48]. Velocity fluctuation (thermal agitation of carriers) causes current density fluctuation $\delta I_{n/p}(r)$. Current density fluctuations at each location propagate towards the contact through $Z_{n/p}(r, r_{Contact})$. Noise voltage fluctuation results at each contact with $\delta V(r_{Contact})$ [45].

The local noise source C_{S_i} are proportional to carrier density and diffusivity,

$$C_{S_i}^n = 4qnD_n, \tag{3.1}$$

$$C_{S_i}^p = 4qpD_p, \tag{3.2}$$

where superscripts ^{n} and ^{p} denote electron and hole respectively. C_{S_i} has a unit of A^2/Hz/cm^3. n and p are electron and hole concentrations. D_n and D_p are electron and hole diffusivity, respectively. The impedance field $\widetilde{Z}(r, r_{Contact})$ from local noise source to terminal noise voltage

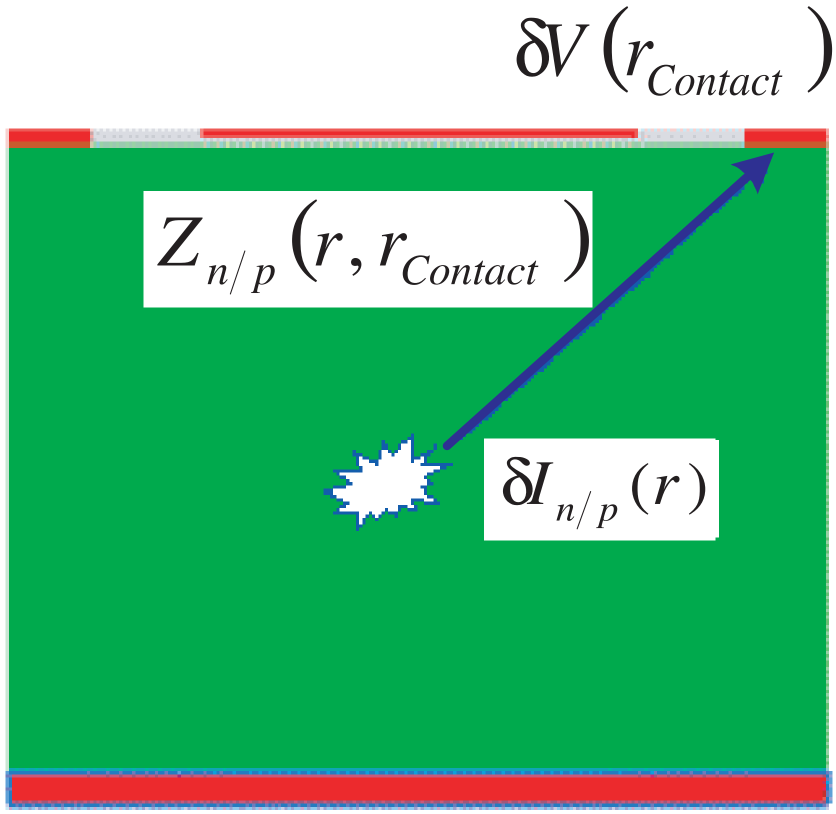

Figure 3.1: Impedance field method

is,

$$\widetilde{Z}_n(r, r_{Contact}) = \frac{1}{q}\Delta_r Z_n(r, r_{Contact}), \tag{3.3}$$

$$\widetilde{Z}_p(r, r_{Contact}) = \frac{1}{q}\Delta_r Z_p(r, r_{Contact}), \tag{3.4}$$

where subscripts $_n$ and $_p$ denote electron and hole respectively. $|\widetilde{Z}_n(r, r_{Contact})|^2$ and $|\widetilde{Z}_p(r, r_{Contact})|^2$ have a unit of V^2/A^2.

The terminal noise voltage power spectral density is obtained by integrating the "noise concentration" over the device volume,

$$S_v = \int_\Omega C_{S_v} d\Omega, \tag{3.5}$$

$$= \int_\Omega C^n_{S_v} d\Omega + \int_\Omega C^p_{S_v} d\Omega, \tag{3.6}$$

$$C^n_{S_v} = \widetilde{Z}_n(r, r_{Contact}) C^n_{S_i} \widetilde{Z}^*_n(r, r_{Contact}), \tag{3.7}$$

$$C^p_{S_v} = \widetilde{Z}_p(r, r_{Contact}) C^p_{S_i} \widetilde{Z}^*_p(r, r_{Contact}), \tag{3.8}$$

where C_{S_v} is the "concentration," or volume density of S_v, and has a unit of $\mathrm{V}^2/\mathrm{Hz/cm}^3$.

3.3 New Technique: Microscopic Noise Contribution of Chain Noise Representation Parameters

Consider the transistor as a noisy linear two port. The open circuit noise voltage parameters are obtained by integrating the "noise concentration" over the device volume

$$S_n = \int_\Omega C_{S_n} d\Omega, \tag{3.9}$$

where n is v_1, v_1^*, v_2, v_2^*, or v_1, v_2^*. For instance, $C_{S_{v_1,v_1^*}}$ is the "concentration," or volume density of S_{v_1,v_1^*}, and has a unit of $\mathrm{V}^2/\mathrm{Hz/cm}^3$. $C_{S_{v_1,v_1^*}}$, $C_{S_{v_2,v_2^*}}$ and $C_{S_{v_1,v_2^*}}$ are solved in TCAD tools including DESSIS [45] and TAURUS [44]. In principle, the boundary conditions can be modified to directly solve for the "concentration" of the chain representation noise parameters S_{v_a,v_a^*}, S_{i_a,i_a^*} and S_{i_a,v_a^*}. This, however, has not been implemented in TCAD tools. We propose here an alternative that uses postprocessing of $C_{S_{v_1,v_1^*}}$, $C_{S_{v_2,v_2^*}}$ and $C_{S_{v_1,v_2^*}}$, and requires no code development by TCAD vendors. The impedance representation noise parameters S_{v_1,v_1^*}, S_{v_2,v_2^*} and S_{v_1,v_2^*} can be transformed to the chain representation noise parameters S_{v_a,v_a^*}, S_{i_a,i_a^*} and S_{i_a,v_a^*} using transformation matrix in Table 2.1 in chapter 2 [43],

$$C_A = T_{Z-A} \cdot C_Z \cdot T_{Z-A}^{\dagger}, \tag{3.10}$$

$$\begin{bmatrix} S_{v_a,v_a^*} & S_{v_a,i_a^*} \\ S_{i_a,v_a^*} & S_{i_a,i_a^*} \end{bmatrix} = T_{Z-A} \cdot \begin{bmatrix} S_{v_1,v_1^*} & S_{v_1,v_2^*} \\ S_{v_2,v_1^*} & S_{v_2,v_2^*} \end{bmatrix} \cdot T_{Z-A}^{\dagger}, \tag{3.11}$$

and

$$T_{Z-A} = \begin{bmatrix} 1 & -A_{11} \\ 0 & -A_{21} \end{bmatrix}, \tag{3.12}$$

where A_{11} and A_{21} are elements of the ABCD parameter matrix A.

An inspection of (3.11) shows that the transform is *linear*. Substituting S_{v_1,v_1^*}, S_{v_2,v_2^*} and S_{v_1,v_2^*} expressed in the integral form of (3.9) into (3.11), the concentration of the chain representation noise parameters, $C_{S_{v_a,v_a^*}}$, $C_{S_{i_a,i_a^*}}$, and $C_{S_{i_a,v_a^*}}$ are obtained as

$$\begin{bmatrix} C_{S_{v_a,v_a^*}} & C_{S_{v_a,i_a^*}} \\ C_{S_{i_a,v_a^*}} & C_{S_{i_a,i_a^*}} \end{bmatrix} = T_{Z-A} \cdot \begin{bmatrix} C_{S_{v_1,v_1^*}} & C_{S_{v_1,v_2^*}} \\ C_{S_{v_2,v_1^*}} & C_{S_{v_2,v_2^*}} \end{bmatrix} \cdot T_{Z-A}^{\dagger}. \tag{3.13}$$

Integration of $C_{S_{v_a,v_a^*}}$, $C_{S_{i_a,i_a^*}}$, and $C_{S_{i_a,v_a^*}}$ over the whole device gives the transistor S_{v_a,v_a^*}, S_{i_a,i_a^*} and S_{i_a,v_a^*}, respectively.

3.4 Spatial Distribution of Microscopic Noise Contributions in RF SiGe HBT Transistor

The technique is applied to noise analysis of a 50 GHz SiGe HBT [49]. DESSIS from ISE is used for noise simulation. The device structure is constructed based on device layout. The doping and Ge profiles were determined using SIMS. A set of physical models suitable for HBT simulation were selected, and the model coefficients were calibrated to reproduce the measured $dc\ I - V$ characteristics and high frequency s-parameters. The carrier noise temperature is assumed to be the same as the lattice temperature. The DESSIS simulation input deck and TECPLOT mcr file can be found in B.1 in Appendix B.

3.4.1 Input Noise Voltage S_{v_a,v_a^*}

Fig. 3.2 shows the spatial distribution of the input noise voltage concentration, $C_{S_{v_a,v_a^*}}$. The transistor is biased at a relatively low J_C of 0.1 mA$/\mu$m^2, and the operating frequency is 2 GHz. Observe that $C_{S_{v_a,v_a^*}}$ is the highest in the SiGe base, indicating that transistor S_{v_a,v_a^*} mainly comes from the SiGe base. This provides guidelines to development of better circuit-level transistor noise model. That is, the noise sources originate from the EB junction.

To identify the individual contributions from electrons and holes, the spatial distributions of the $C_{S_{v_a,v_a^*}}$ due to electrons and holes are plotted in Figs. 3.3 and 3.4, respectively. It can be seen that the electron contributions mainly come from the minority electrons in the base, and the hole contributions mainly come from the majority holes in the base. The $C_{S_{v_a,v_a^*}}$ due to electrons is nearly uniform along the x-direction inside the neutral base. However, the $C_{S_{v_a,v_a^*}}$ due to holes is highly nonuniform along the x-direction, indicating a strong "noise crowding" effect. The $C_{S_{v_a,v_a^*}}$ due to holes decreases from the emitter periphery towards the emitter center. The overall $C_{S_{v_a,v_a^*}}$

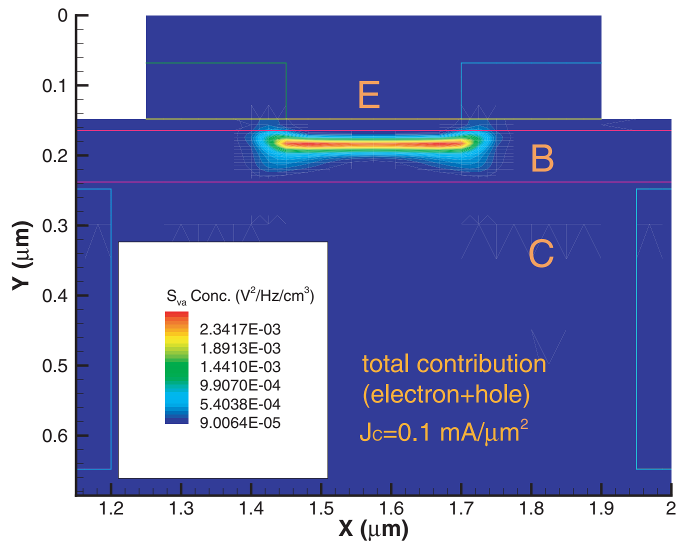

Figure 3.2: 2D distribution of the total noise concentration $C_{S_{v_a,v_a^*}}$ at 2 GHz. J_C=0.1 mA/μm^2.

is relatively uniform along the emitter width direction, simply because the electron contribution dominates (73%).

However, as J_C increases to 0.5 mA/μm^2, the hole contribution to $C_{S_{v_a,v_a^*}}$ becomes more dominant, and counts for 60% of the total S_{v_a,v_a^*}. This results in considerable crowding of the total $C_{S_{v_a}}$, as shown in Fig. 3.5. Interestingly, the electron contribution to $C_{S_{v_a,v_a^*}}$ remains uniform laterally inside the neutral base, despite the higher J_C and hence more severe *dc* and *ac* current crowding effect. The crowding in the hole contribution becomes stronger as J_C increases.

A logical and interesting question is how the microscopic noise simulation results compare to circuit-level compact noise modeling results. We consider here the SPICE noise model used in [47] and [10] as introduced in chapter 1. The base current shot noise $2qI_B$, the collector current shot noise $2qI_C$, and the thermal noise $4kTr_b$ are accounted for using the equivalent circuit shown in Fig. 1.4. The compact noise model is lumped in nature, and does not take into

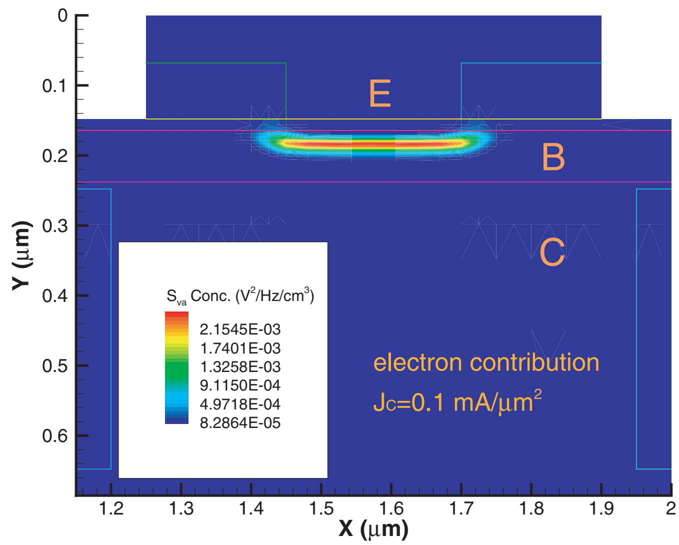

Figure 3.3: 2D distribution of electron noise concentration $C_{S_{v_a,v_a^*}}$ at 2 GHz. J_C=0.1 mA/μm^2.

account distributive effects. Roughly speaking, the $2qI_C$ collector current shot noise results from minority electrons in the base, the $2qI_B$ base current shot noise results from minority holes in the emitters [50], and the $4kTr_b$ base resistance thermal noise results from the majority holes in the neutral base. S_{v_a,v_a^*} is then obtained by taking SPICE model equations (1.11) – (1.13) into (2.150) derived in chapter 2 [47] [12],

$$S_{v_a,v_a^*} = \frac{2qI_C}{|Y_{21}|^2} + 2qI_B r_b^2 + 4kTr_b, \tag{3.14}$$

Qualitatively, the compact model captures the two major contributors to S_{v_a,v_a^*}, base majority holes, and base minority electrons. Furthermore, the simulated majority hole contribution is equal to $4kTr_b$, provided that r_b is extracted from h_{11} [46]. However, the electron contribution, $2qI_C/|Y_{21}|^2$, differs from microscopic results by 16% at J_C=0.1 mA/μm^2, and 7% at J_C=0.5 mA/μm^2. This is clearly caused by the lumped nature of the compact noise model, which cannot

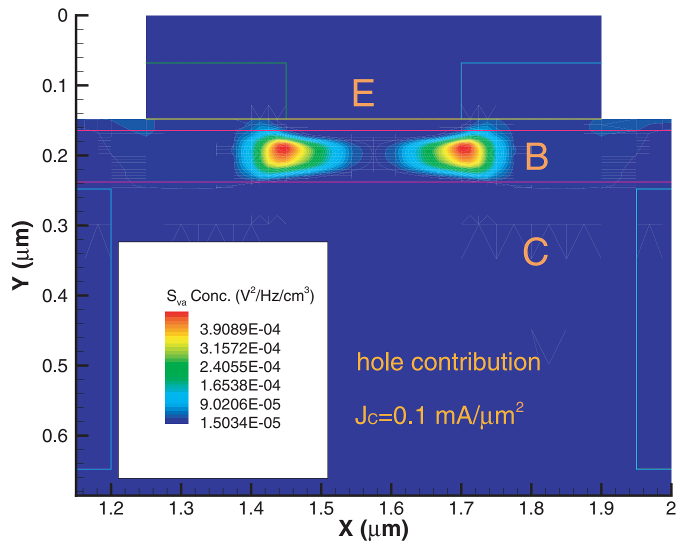

Figure 3.4: 2D distribution of hole noise concentration $C_{S_{v_a,v_a^*}}$ at 2 GHz. J_C=0.1 mA/μm^2.

take into account 2D distributive effect. The results suggest that 2D distributive effect should be modeled to obtain more accurate S_{v_a,v_a^*}.

3.4.2 Input Noise Current S_{i_a,i_a^*}

Fig. 3.6 – Fig. 3.8 show the spatial distribution of $C_{S_{i_a,i_a^*}}$, as well as the individual contributions from electrons and holes, respectively. J_C=0.1 mA/μm^2. Most of the electron contribution comes from the base minority electrons. While for the hole contribution, both the emitter minority holes and the base majority holes are important. The hole contribution to S_{i_a,i_a^*} increases from 63% to 81% of the total S_{i_a,i_a^*} as J_C increases from 0.1 to 0.5 mA/μm^2. S_{i_a,i_a^*} is given by taking SPICE model equations (1.11) – (1.13) into (2.151) [47] [12],

$$S_{i_a,i_a^*} = 2qI_B + \frac{2qI_C}{|h_{21}|^2}, \tag{3.15}$$

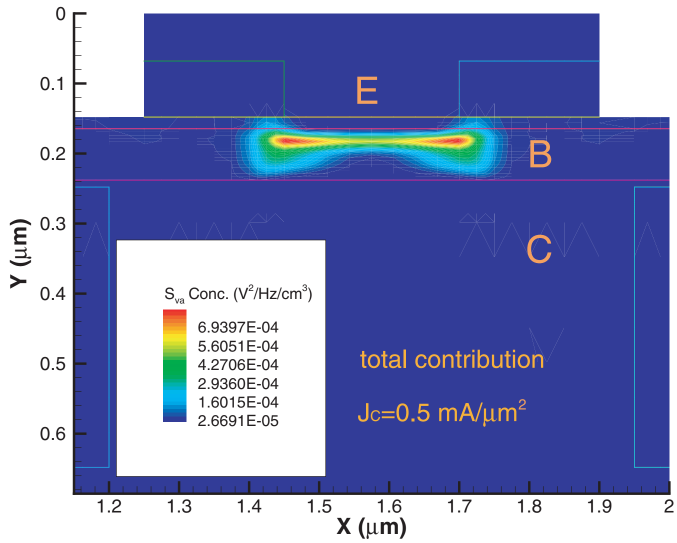

Figure 3.5: 2D distribution of the total noise concentration $C_{S_{v_a,v_a^*}}$ at 2 GHz. J_C=0.5 mA/μm^2.

Observe that the compact model does not have any contribution from the majority holes in the base, which is significant according to noise simulation results. On the other hand, the simulated electron contribution to S_{i_a,i_a^*}, is well predicted by $2qI_C/|h_{21}|^2$, within 5% accuracy. The hole contribution to S_{i_a,i_a^*}, however, is overestimated by $2qI_B$ by as high as 16% at J_C=0.5 mA/μm^2.

3.4.3 Input Noise Voltage and Current Correlation S_{i_a,v_a^*}

Fig. 3.9 shows the real part of $C_{S_{i_a,v_a^*}}$ at $J_C = 0.1$ mA/μm^2. The simulation results show that the electron contribution mainly comes from the base minority electrons, and the hole contribution mainly comes from the emitter minority holes. Fig. 3.10 shows the imaginary part of $C_{S_{i_a,v_a^*}}$. Its electron contribution also mainly comes from the base minority electrons. The hole contribution, however, mainly comes from the base majority holes and shows a strong "noise crowding"

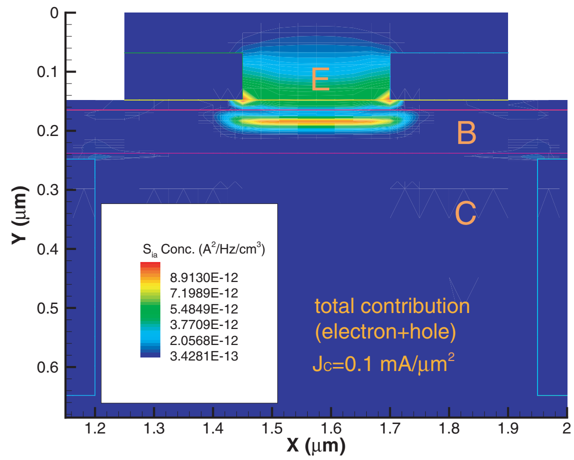

Figure 3.6: 2D distribution of noise concentration $C_{S_{i_a,i_a^*}}$ at 2 GHz. J_C=0.1 mA/μm^2.

effect. However, the total $C_{S_{i_a,v_a^*}}$ is dominated by the base electron contribution, which counts for 87% of the total $\Re(S_{i_a,v_a^*})$ and 95% of the total $\Im(S_{i_a,v_a^*})$. As J_C increases to 0.5 mA/μm^2, the electron contribution for $C_{S_{i_a,v_a^*}}$ becomes less dominant, and counts for 63% of the total $\Re(S_{i_a,v_a^*})$ and 81% of the total $\Im(S_{i_a,v_a^*})$.

The input noise voltage and current correlation S_{i_a,v_a^*} is predicted by taking SPICE model equations (1.11) – (1.13) into (2.152) [47] [12],

$$S_{i_a,v_a^*} = 2qI_C \frac{Y_{11}}{|Y_{21}|^2} + 2qI_B r_b, \tag{3.16}$$

Note that the compact model does not have any hole contribution at all, which can be important according to noise simulation. For $\Re(S_{i_a,v_a^*})$, the electron contribution predicted by (3.16) deviates from noise simulation by 14% at J_C=0.1 mA/μm^2, and by 4% at J_C = 0.5 mA/μm^2. For $\Im(S_{i_a v_a^*})$, the deviation is 9% and 69% at J_C = 0.1 and 0.5 mAμm^2, respectively. A significant

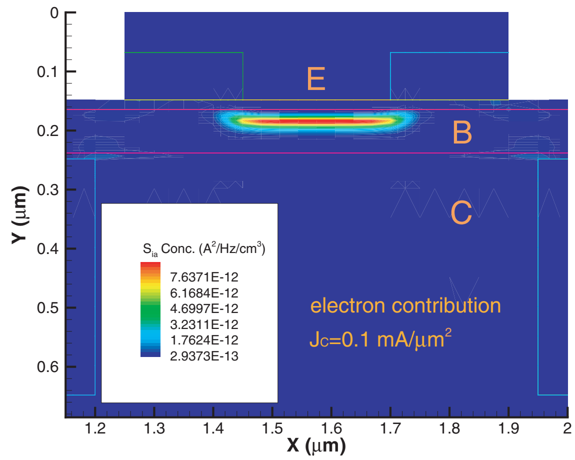

Figure 3.7: 2D distribution of electron contribution to noise concentration $C_{S_{i_a,i_a^*}}$ at 2 GHz. J_C=0.1 mA/μm^2.

source of deviation is due to the hole contribution, which does not exist in the compact model, but can become important at higher J_C.

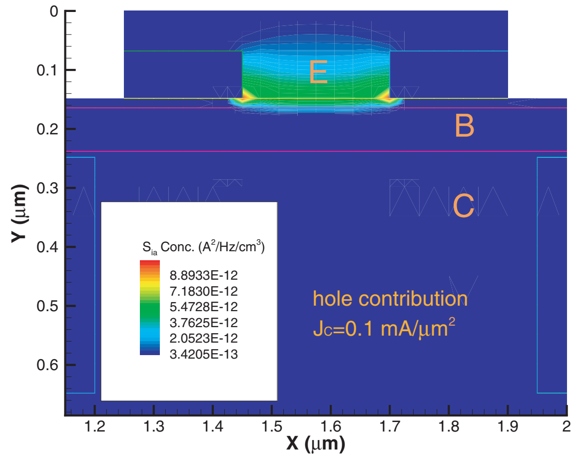

Figure 3.8: 2D distribution of hole contribution to noise concentration $C_{S_{i_a,i_a^*}}$ at 2 GHz. J_C=0.1 mA/μm^2.

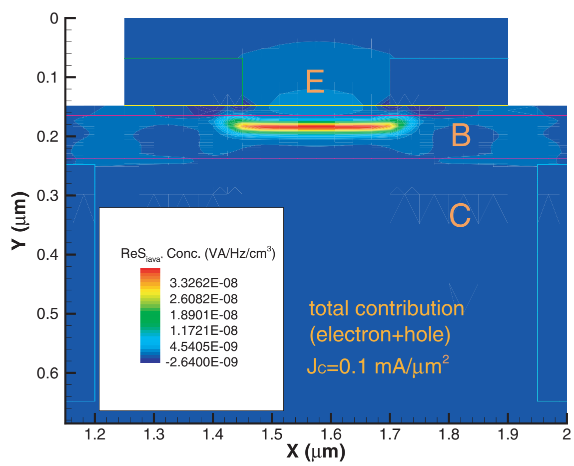

Figure 3.9: 2D distribution of the total noise concentration $\Re(C_{S_{i_a,v_a^*}})$ at 2 GHz. J_C=0.1 mA/μm^2.

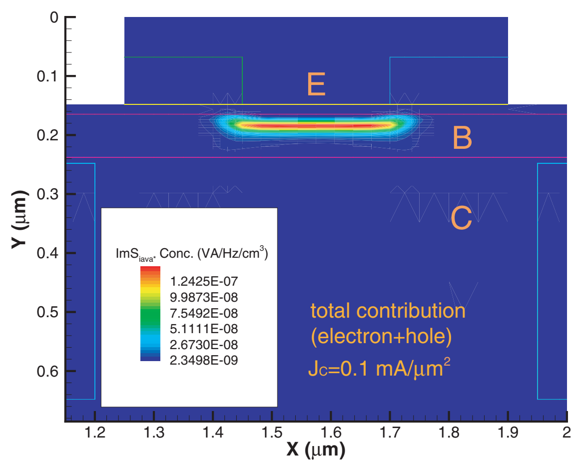

Figure 3.10: 2D distribution of the total noise concentration $\Im(C_{S_{i_a,v_a^*}})$ at 2 GHz. J_C=0.1 mA/μm^2.

3.5 Spatial Distribution of Microscopic Noise Contributions in RF MOSFET Transistor

The technique is applied to noise analysis of a 50nm L_{eff} MOSFET transistor. The device structure is constructed based on reported 90 nm CMOS literature and the ITRS roadmap. *dc* $I-V$, Y-parameters, and noise parameters are simulated using hydrodynamic transport models. The simulator used is DESSIS 9.0 from ISE [45]. The Lombardi surface mobility model and the default carrier energy relaxation time is used. The simulated $I-V$ and g_m characteristics are comparable to reported data on 90 nm CMOS devices with similar structures. The transistor has a 70 nm poly gate length, a 46 nm metallurgical channel length, and an effective oxide thickness of 1.2 nm. The channel doping is retrograded from the surface toward the bulk, and halos are used for suppressing short channel effect.

Different from section 3.4, the new technique is applied to obtain the noise concentration of Y-noise representation parameters including gate noise current S_{i_g,i_g^*}, drain noise current S_{i_d,i_d^*}, and their correlation S_{i_g,i_d^*}. The impedance representation noise parameters S_{v_1,v_1^*}, S_{v_2,v_2^*} and S_{v_1,v_2^*} can be transformed to the Y -noise representation parameters S_{i_g,i_g^*}, S_{i_d,i_d^*} and S_{i_g,i_d^*} using transformation matrix in Table 2.1 in chapter 2 [43],

$$C_Y = T_{Z-Y} \cdot C_Z \cdot T_{Z-Y}^{\dagger}, \tag{3.17}$$

$$\begin{bmatrix} S_{i_g,i_g^*} & S_{i_g,i_d^*} \\ S_{i_d,i_g^*} & S_{i_d,i_d^*} \end{bmatrix} = T_{Z-Y} \cdot \begin{bmatrix} S_{v_1,v_1^*} & S_{v_1,v_2^*} \\ S_{v_2,v_1^*} & S_{v_2,v_2^*} \end{bmatrix} \cdot T_{Z-Y}^{\dagger}, \tag{3.18}$$

and

$$T_{Z-Y} = \begin{bmatrix} Y_{11} & Y_{12} \\ Y_{21} & Y_{22} \end{bmatrix}, \tag{3.19}$$

where Y_{11}, Y_{12}, Y_{21} and Y_{22} are elements of the Y parameter matrix Y.

An inspection of (3.18) shows that the transform is *linear*. Substituting S_{v_1,v_1^*}, S_{v_2,v_2^*} and S_{v_1,v_2^*} expressed in the integral form of (3.9) into (3.18), the concentration of the chain representation noise parameters, $C_{S_{i_g,i_g^*}}$, $C_{S_{i_d,i_d^*}}$, and $C_{S_{i_g,v_d^*}}$ are obtained as

$$\begin{bmatrix} C_{S_{i_g,i_g^*}} & C_{S_{i_g,i_d^*}} \\ C_{S_{i_d,i_g^*}} & C_{S_{i_d,i_d^*}} \end{bmatrix} = T_{Z-Y} \cdot \begin{bmatrix} C_{S_{v_1,v_1^*}} & C_{S_{v_1,v_2^*}} \\ C_{S_{v_2,v_1^*}} & C_{S_{v_2,v_2^*}} \end{bmatrix} \cdot T_{Z-Y}^{\dagger}. \tag{3.20}$$

Integration of $C_{S_{i_g,i_g^*}}$, $C_{S_{i_d,i_d^*}}$, and $C_{S_{i_g,v_d^*}}$ over the whole device gives the transistor S_{i_g,i_g^*}, S_{i_d,i_d^*} and S_{i_g,i_d^*}, respectively.

3.5.1 Gate Noise Current S_{i_g,i_g^*}

Fig. 3.11 and Fig. 3.12 show the spatial distribution of $C_{S_{i_g,i_g^*}}$ at 5 GHz. V_{ds} = 1 V and V_{gs} = 0.5 V and 1 V. $C_{S_{i_g,i_g^*}}$ is the highest near the source side under the gate, and increases with increasing V_{gs}.

3.5.2 Drain Noise Current S_{i_d,i_d^*}

Fig. 3.13 and Fig. 3.14 show the spatial distribution of $C_{S_{i_d,i_d^*}}$ at 5 GHz. V_{ds} = 1 V and V_{gs} = 0.5 V and 1 V. Similar to $C_{S_{i_g,i_g^*}}$, $C_{S_{i_d,i_d^*}}$ is the highest near the source side under the gate. Moreover, another peak value of $C_{S_{i_d,i_d^*}}$ occurs near the interface of the bulk and the source. $C_{S_{i_d,i_d^*}}$ increases with increasing V_{gs}.

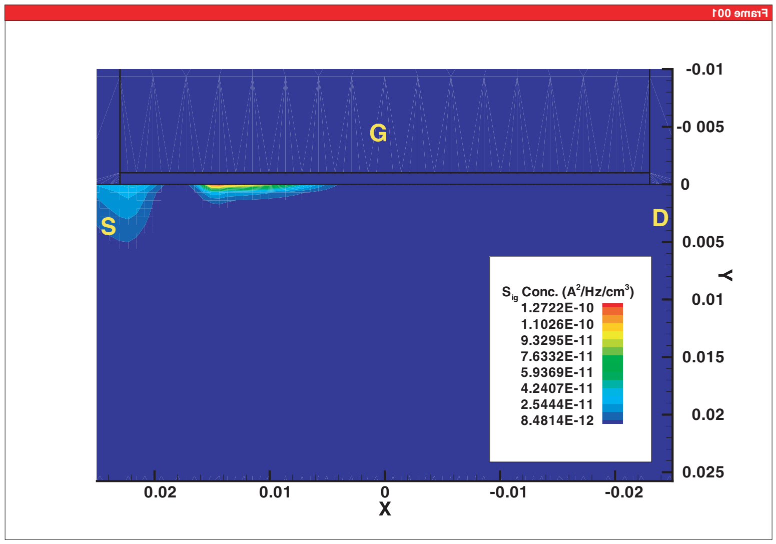

Figure 3.11: 2-D gate noise current concentration $C_{S_{i_g,i_g^*}}$ at 5 GHz. V_{ds} = 1 V. V_{gs} = 0.5 V.

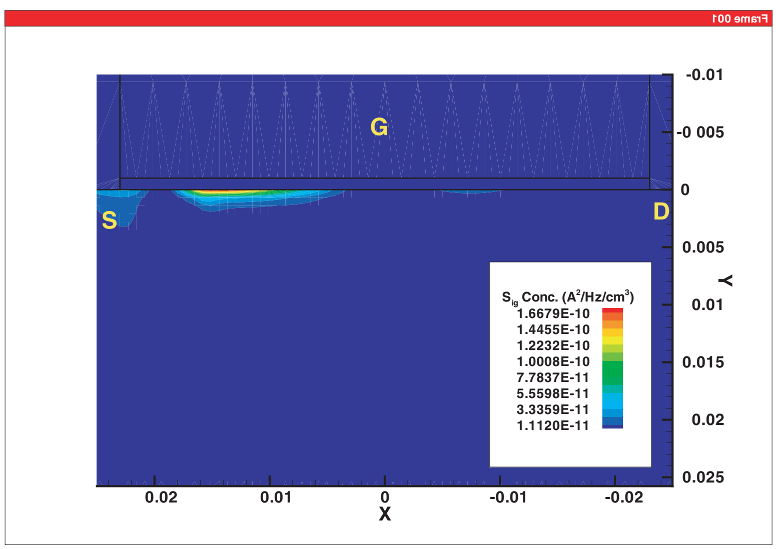

Figure 3.12: 2-D gate noise current concentration $C_{S_{i_g,i_g^*}}$ at 5 GHz. V_{ds} = 1 V. V_{gs} = 1 V.

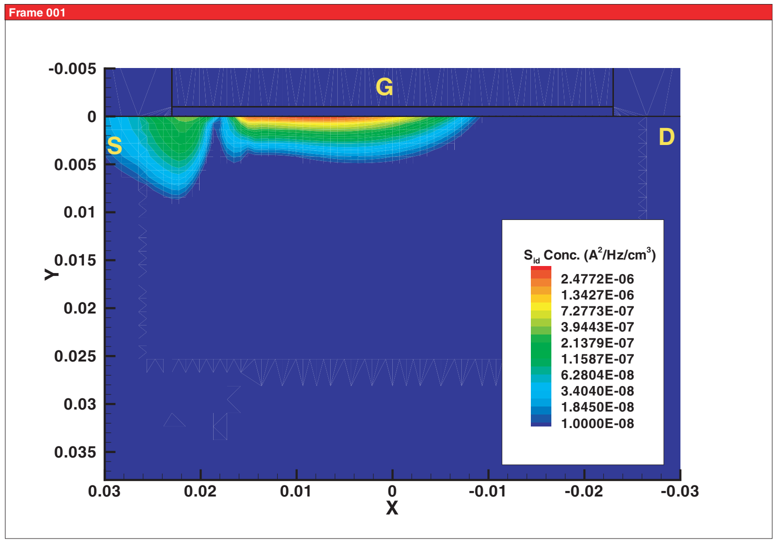

Figure 3.13: 2-D drain noise current concentration $C_{S_{i_d,i_d^*}}$ at 5 GHz. V_{ds} = 1 V. V_{gs} = 0.5 V.

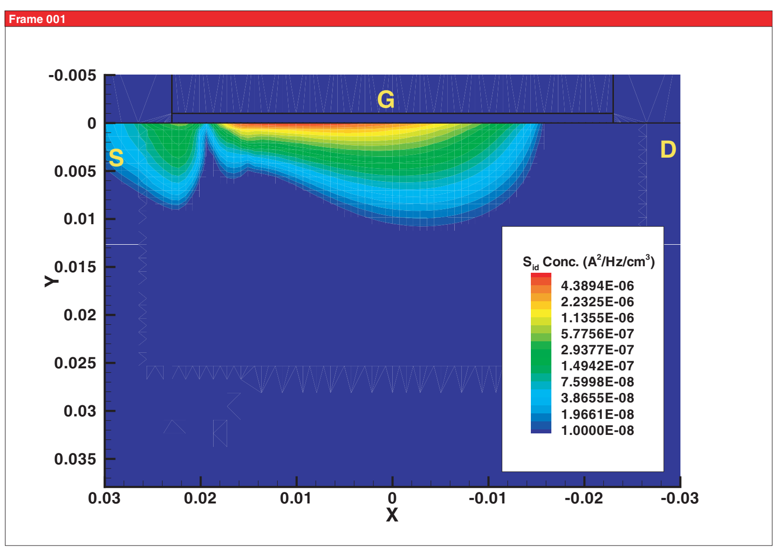

Figure 3.14: 2-D drain noise current concentration $C_{S_{i_d,i_d^*}}$ at 5 GHz. V_{ds} = 1 V. V_{gs} = 1 V.

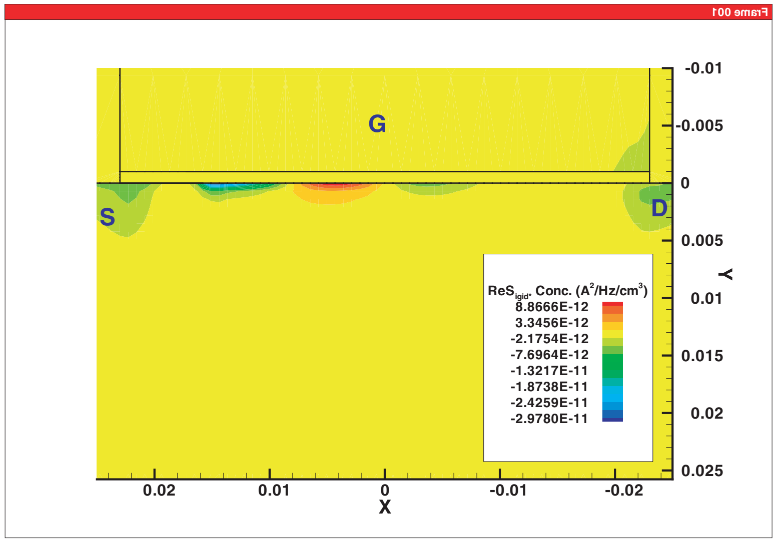

Figure 3.15: 2-D real part of noise current correlation concentration $\Re(C_{S_{i_g,i_d^*}})$ at 5 GHz. V_{ds} = 1 V. V_{gs} = 0.5 V.

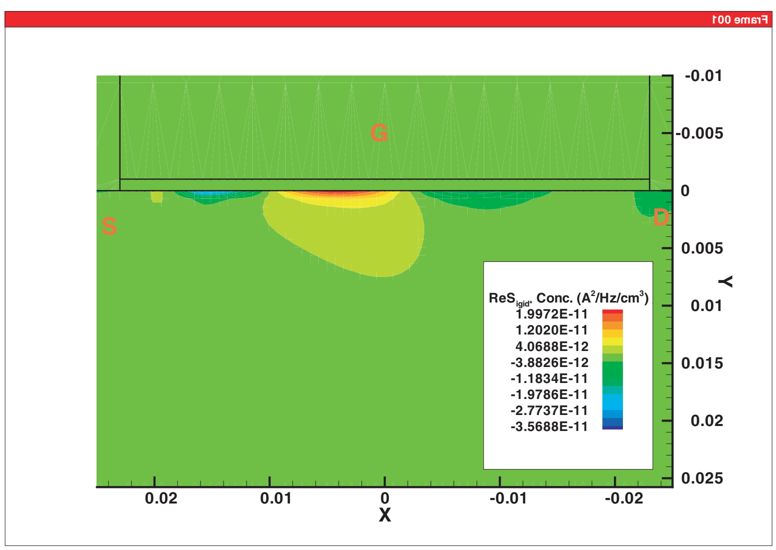

Figure 3.16: 2-D real part of noise current correlation concentration $\Re(C_{S_{i_g,i_d^*}})$ at 5 GHz. V_{ds} = 1 V. V_{gs} = 1 V.

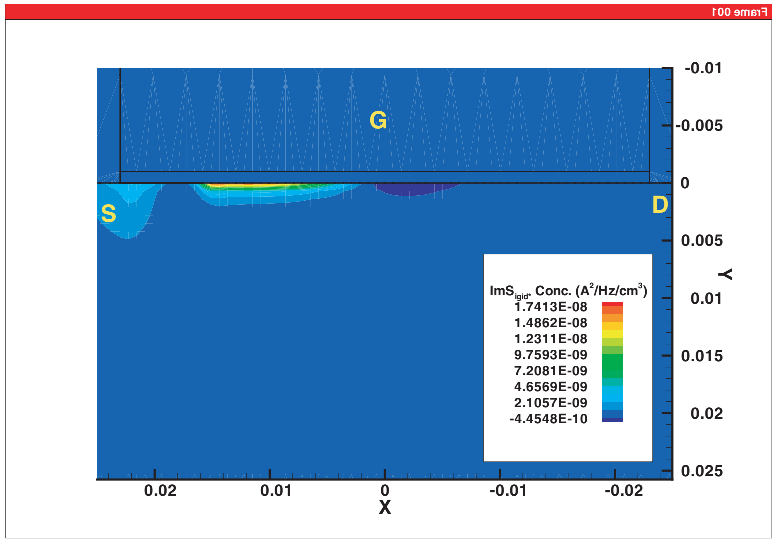

Figure 3.17: 2-D imaginary part of noise current correlation concentration $\Im(C_{S_{i_g,i_d^*}})$ at 5 GHz. $V_{ds} = 1$ V. $V_{gs} = 0.5$ V.

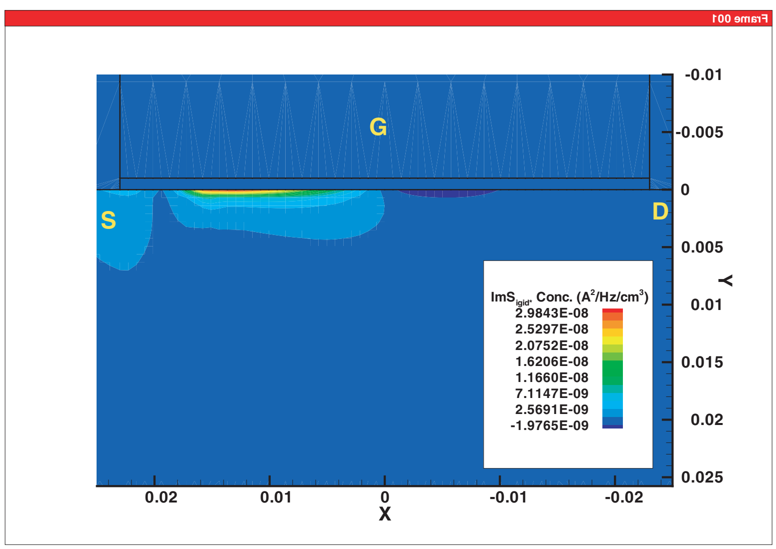

Figure 3.18: 2-D imaginary part of noise current correlation concentration $\Im(C_{S_{i_g,i_d^*}})$ at 5 GHz. $V_{ds} = 1$ V. $V_{gs} = 1$ V.

3.5.3 Drain and Gate Noise Current Correlation S_{i_g,i_d^*}

Fig. 3.15 – Fig. 3.18 show the spatial distribution of $\Re(C_{S_{i_g,i_d^*}})$ and $\Im(C_{S_{i_g,i_d^*}})$ at 5 GHz. V_{ds} = 1 V and V_{gs} = 0.5 V and 1 V. $\Re(C_{S_{i_g,i_d^*}})$ is quite small compared to $\Im(C_{S_{i_g,i_d^*}})$. The overall integration of $\Re(C_{S_{i_g,i_d^*}})$ is negative for both V_{gs}'. $\Im(C_{S_{i_g,i_d^*}})$ is the highest near the source side under the gate. Another peak value of $\Im(C_{S_{i_g,i_d^*}})$ occurs near the interface of the bulk and the source. $\Im(C_{S_{i_d,i_d^*}})$ increases with increases with increasing V_{gs}.

3.6 Summary

We have presented a new technique of simulating the spatial distribution of microscopic noise contribution to the input noise current, voltage, as well as their cross-correlations. The technique is first demonstrated on a 50 GHz SiGe HBT. The spatial contributions by base majority holes, base minority electrons, and emitter minority holes are analyzed, and compared to results from a compact noise model. A strong crowding effect is observed in the spatial distribution of noise concentrations due to base majority holes. The results suggest that 2D distributive effect needs to be taken into account in future compact noise model development.

The technique is also applied to a 46 nm L_{eff} MOSFET transistor. The spatial distribution of the Y- noise representation parameters $C_{S_{i_g,i_g^*}}$, $C_{S_{i_d,i_d^*}}$, $\Re(C_{S_{i_g,i_d^*}})$ and $\Im(C_{S_{i_g,i_d^*}})$ are analyzed. The region under the gate near the source side is the most important for all of the Y- noise representation parameters.

CHAPTER 4

BIPOLAR NOISE MODELING

This chapter examines bipolar transistor noise modeling and noise physics using microscopic noise simulation. Transistor terminal current and voltage noises resulting from velocity fluctuations of electrons and holes in the base, emitter, collector, and substrate are simulated using a new technique, and compared with modeling results. Major physics noise sources in bipolar transistor are qualitatively identified. The relevant importance as well as model-simulation discrepancy is analyzed for each physical noise source. The results are then used to propose a new noise model.

4.1 Introduction

Mixed-signal and RFIC design demands compact transistor models that can accurately model not only the *dc* and *ac* parameters, but also transistor noise parameters, including minimum noise figure NF_{min}, optimal source (noise matching) admittance Y_{opt}, and noise resistance R_n. NF_{min}, Y_{opt} and R_n are fundamentally determined by the input noise voltage and current for the chain representation of a noisy linear two-port, as shown in Fig. 2.1 in chapter 2. Fig. 1.4 in chapter 1 shows the essence of SPICE noise modeling in major CAD tools. The noise physics accounted for include: base resistance thermal noise, base current shot noise, and collector current shot noise, all of which are essentially macroscopic approximations of the microscopic *diffusion* noise due to velocity fluctuations of electrons and holes. Fig. 4.1 shows the chain noise parameters comparison of measured data from IBM and compact noise model at $J_C = 0.01$ mA$/\mu$m^2. The compact noise modeling is good for low current density. The accuracy of such compact noise modeling, however, becomes worse at higher current densities required for high speed [3]. Fig. 4.2 shows the chain noise parameters comparison of measured data and compact noise model at J_C = 0.63 mA/μm^2. The compact model deviates from the measured data, and the difference increases dramatically with increasing frequency. An improvement on the compact noise model becomes necessary for high current density and high frequency.

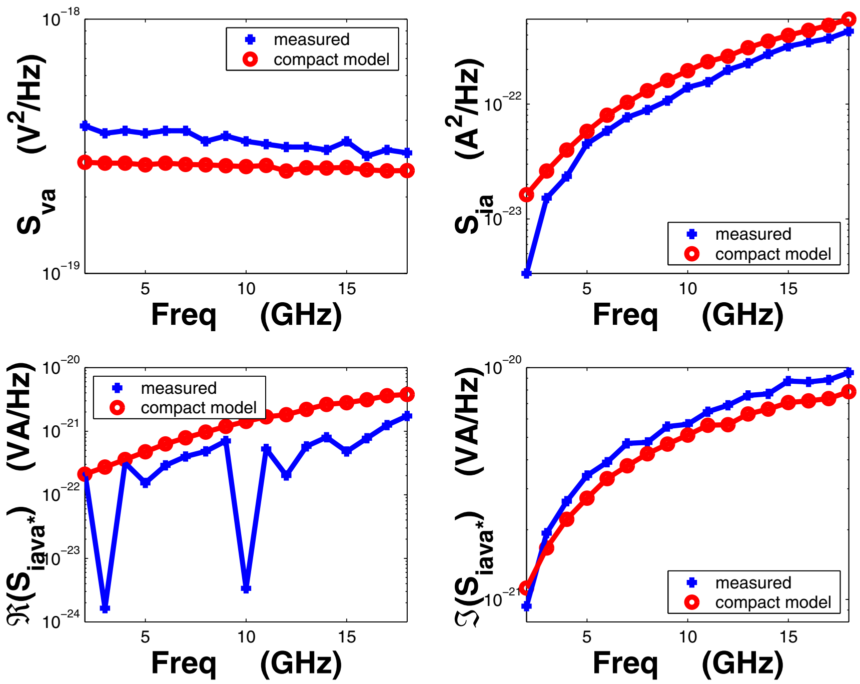

Figure 4.1: Chain noise parameter: measured vs compact model. J_C=0.01 mA/μm^2.

However, measured data itself cannot give us an efficient way to improve the compact noise model, in the reason that the measured data cannot give us detailed information about different noise sources in the device. Microscopic noise simulation available in recent years makes it possible to have a close look of device noise from the structure level. By comparing the chain noise parameters at high J_C of 0.65 mA/μm^2, as shown in Fig. 4.3, we observed that

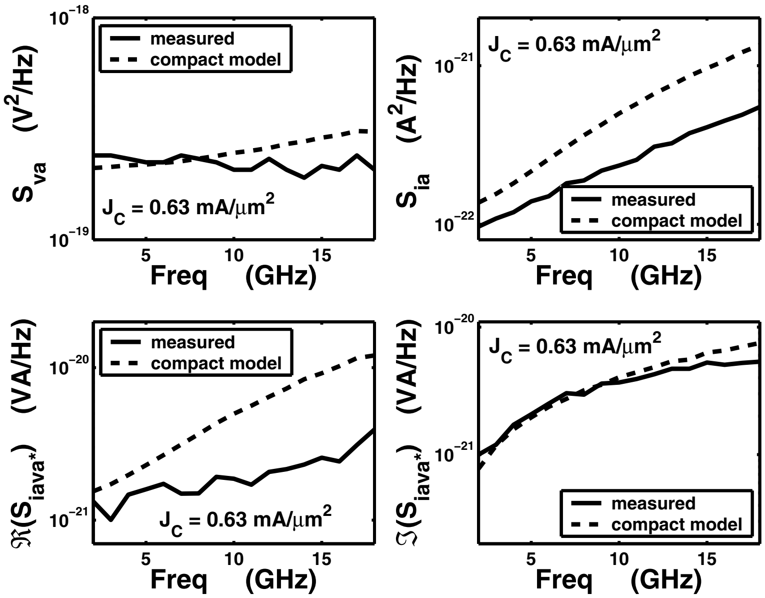

Figure 4.2: Chain noise parameter: measured v.s. compact model, J_C=0.63 mA$/\mu$m^2.

the simulation result complies to the measured data with a much better trend, which makes it feasible to examine the compact noise model with the microscopic noise simulation results.

By means of microscopic noise simulation and the technique in chapter 3, this chapter examines the noise physics accounted for in the noise model. Regional contribution analysis are performed to verify the origins of noise in the device and compared to compact noise model, and resulted from an effort to improve bipolar transistor noise modeling.

4.2 Technical Approach

4.2.1 Microscopic Input Noise Concentration

In microscopic noise simulation, the two-port open circuit noise voltage parameters S_{v_1,v_1^*}, S_{v_2,v_2^*} and S_{v_1,v_2^*} are obtained by integrating the "noise concentration" $C_{S_{v_1,v_1^*}}$, $C_{S_{v_2,v_2^*}}$, and $C_{S_{v_1,v_2^*}}$

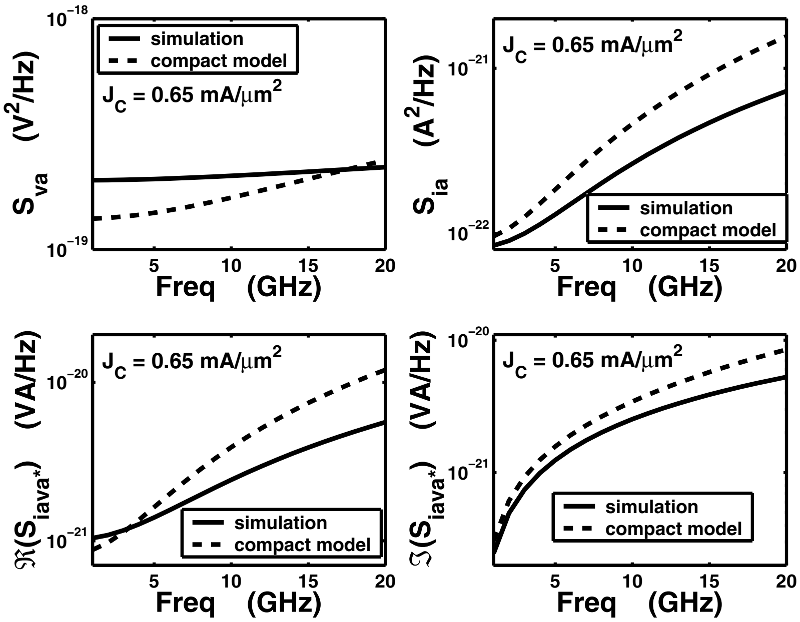

Figure 4.3: Chain noise parameter: simulation v.s. compact model, J_C=0.65 mA/μm^2..

over the device volume. $C_{S_{v_1,v_1^*}}$, $C_{S_{v_2,v_2^*}}$, and $C_{S_{v_1,v_2^*}}$ are solved in TCAD tools, including TAURUS [44] and DESSIS [45]. Each noise concentration consists of an electron contribution and a hole contribution, which account for electron and hole velocity fluctuations, respectively,

$$\begin{bmatrix} C_{S_{v_1,v_1^*}} & C_{S_{v_1,v_2^*}} \\ C_{S_{v_2,v_1^*}} & C_{S_{v_2,v_2^*}} \end{bmatrix} = \begin{bmatrix} C^e_{S_{v_1,v_1^*}} & C^e_{S_{v_1,v_2^*}} \\ C^e_{S_{v_2,v_1^*}} & C^e_{S_{v_2,v_2^*}} \end{bmatrix} + \begin{bmatrix} C^h_{S_{v_1,v_1^*}} & C^h_{S_{v_1,v_2^*}} \\ C^h_{S_{v_2,v_1^*}} & C^h_{S_{v_2,v_2^*}} \end{bmatrix}, \tag{4.1}$$

where superscripts ^{e} and ^{h} stand for electron and hole contributions, respectively. The "noise concentration" for the chain representation, $C_{S_{i_a,i_a^*}}$, $C_{S_{v_a,v_a^*}}$, and $C_{S_{i_a,v_a^*}}$ and their electron and hold contributions can then be obtained using the technique proposed in chapter 3 [51].

$$\begin{bmatrix} C_{S_{v_a,v_a^*}} & C_{S_{v_a,i_a^*}} \\ C_{S_{i_a,v_a^*}} & C_{S_{i_a,i_a^*}} \end{bmatrix} = \begin{bmatrix} C^e_{S_{v_a,v_a^*}} & C^e_{S_{v_a,i_a^*}} \\ C^e_{S_{i_a,v_a^*}} & C^e_{S_{i_a,i_a^*}} \end{bmatrix} + \begin{bmatrix} C^h_{S_{v_a,v_a^*}} & C^h_{S_{v_a,i_a^*}} \\ C^h_{S_{i_a,v_a^*}} & C^h_{S_{i_a,i_a^*}} \end{bmatrix}, \tag{4.2}$$

$$\begin{bmatrix} C^e_{S_{v_a,v_a^*}} & C^e_{S_{v_a,i_a^*}} \\ C^e_{S_{i_a,v_a^*}} & C^e_{S_{i_a,i_a^*}} \end{bmatrix} = T_{Z-A} \cdot \begin{bmatrix} C^e_{S_{v_1,v_1^*}} & C^e_{S_{v_1,v_2^*}} \\ C^e_{S_{v_2,v_1^*}} & C^e_{S_{v_2,v_2^*}} \end{bmatrix} \cdot T^\dagger_{Z-A}, \tag{4.3}$$

$$\begin{bmatrix} C^h_{S_{v_a,v_a^*}} & C^h_{S_{v_a,i_a^*}} \\ C^h_{S_{i_a,v_a^*}} & C^h_{S_{i_a,i_a^*}} \end{bmatrix} = T_{Z-A} \cdot \begin{bmatrix} C^h_{S_{v_1,v_1^*}} & C^h_{S_{v_1,v_2^*}} \\ C^h_{S_{v_2,v_1^*}} & C^h_{S_{v_2,v_2^*}} \end{bmatrix} \cdot T^\dagger_{Z-A}, \tag{4.4}$$

where T_{Z-A} is the transform matrix from Z- noise representation to chain noise representation as in (3.12). Integration of $C_{S_{i_a,i_a^*}}$, $C_{S_{v_a,v_a^*}}$, and $C_{S_{i_a,v_a^*}}$ over the whole device gives transistor S_{i_a,i_a^*}, S_{v_a,v_a^*} and S_{i_a,v_a^*}. The electron and hole contributions of S_{i_a,i_a^*}, S_{v_a,v_a^*} and S_{i_a,v_a^*} are obtained similarly.

4.2.2 Macroscopic Input Noise

Through noise circuit analysis, Fig. 1.4 can be transformed to the form of Fig. 2.1 by (3.14), (3.15), and (3.16) derived in chapter 3 [12]. The resulting S_{v_a,v_a^*}, S_{i_a,i_a^*} and S_{i_a,v_a^*} are

$$S_{v_a,v_a^*} = \frac{2qI_C}{|Y_{21}|^2} + 2qI_B r_b^2 + 4kTr_b, \tag{4.5}$$

$$S_{i_a,i_a^*} = 2qI_B + \frac{2qI_C}{|h_{21}|^2}, \tag{4.6}$$

$$S_{i_a,v_a^*} = 2qI_C \frac{Y_{11}}{|Y_{21}|^2} + 2qI_B r_b, \tag{4.7}$$

where $h_{21} = Y_{21}/Y_{11}$. The Y parameters are for the whole transistor that includes both r_b and the intrinsic transistor.

4.2.3 Microscopic and Macroscopic Connections

Physically speaking, the $4kTr_b$ terms in the model equations account for velocity fluctuations of holes in the base. One can therefore compare the $4kTr_b$ related terms in the model equations with the integration of the hole contribution of the noise concentration in the base. Similarly, the $2qI_B$ terms account for emitter minority hole velocity fluctuation, and the $2qI_C$ terms account for base minority electron velocity fluctuation [50]. Thus, connections between compact noise model and microscopic noise simulation can be established for S_{v_a,v_a^*}, S_{i_a,i_a^*} and S_{i_a,v_a^*}, as shown in Table 4.1. Here the superscripts ^{e} and ^{h} stand for electron and hole contributions, respectively.

	Model	Simulation
$S^e_{v_a,v_a^*}$	$2qI_C/\lvert Y_{21}\rvert^2$	$\int_{base} C^e_{S_{v_a,v_a^*}} d\Omega$
$S^h_{v_a,v_a^*}$	$2qI_B r_b^2$	$\int_{emitter} C^h_{S_{v_a,v_a^*}} d\Omega$
	$4kTr_b$	$\int_{base} C^h_{S_{v_a,v_a^*}} d\Omega$
$S^e_{i_a,i_a^*}$	$2qI_C/\lvert h_{21}\rvert^2$	$\int_{base} C^e_{S_{i_a,i_a^*}} d\Omega$
$S^h_{i_a,i_a^*}$	$2qI_B$	$\int_{emitter} C^h_{S_{i_a,i_a^*}} d\Omega$
$S^e_{i_a,v_a^*}$	$2qI_C Y_{11}/\lvert Y_{21}\rvert^2$	$\int_{base} C^e_{S_{i_a,v_a^*}} d\Omega$
$S^h_{i_a,v_a^*}$	$2qI_B r_b$	$\int_{emitter} C^h_{S_{i_a,v_a^*}} d\Omega$

Table 4.1: Connections between noise modeling and simulation for S_{v_a,v_a^*}, S_{i_a,i_a^*} and S_{i_a,v_a^*}.

4.3 Chain Representation Parameters

Noise simulation is performed for a 50 GHz SiGe HBT from 1 to 20 GHz using DESSIS [49]. The emitter area A_E=0.5×1μm^2. The doping and Ge profiles were determined using SIMS. A set of physical models suitable for HBT simulation were selected, and the model coefficients were calibrated to reproduce measured dc $I-V$ characteristics and high frequency s-parameters. The carrier noise temperature is assumed to be the same as the lattice temperature. The simulated $C_{S_{v_1,v_1^*}}$, $C_{S_{v_2,v_2^*}}$, and $C_{S_{v_1,v_2^*}}$ are converted to $C_{S_{i_a,i_a^*}}$, $C_{S_{v_a,v_a^*}}$, and $C_{S_{i_a,v_a^*}}$ using (3.13). Their electron and hole contributions are converted using (4.3) and (4.4). We now examine the modeling results using the simulation results as a reference. No attempt is made to "tune" the noise simulation to match measured noise data, which will require careful de-embedding of parasitics not included in the simulated structure. The simulated bias and frequency dependences, however, still qualitatively match measured data, for all noise parameters.

4.3.1 S_{v_a,v_a^*}, S_{i_a,i_a^*} and S_{i_a,v_a^*}

Fig. 4.4 (a) compares the modeled and simulated S_{v_a,v_a^*}, $S^e_{v_a,v_a^*}$ and $S^h_{v_a,v_a^*}$ for J_C=0.01 mA/μm^2. The electron contribution $S^e_{v_a,v_a^*}$ dominates over the hole contribution $S^h_{v_a,v_a^*}$. Note that the model slightly underestimates $S^e_{v_a,v_a^*}$, and significantly underestimates $S^h_{v_a,v_a^*}$. The simulated $S^e_{v_a,v_a^*}$ and $S^h_{v_a,v_a^*}$ are both frequency dependent. Despite inaccurate modeling of $S^h_{v_a,v_a^*}$, the total S_{v_a,v_a^*} is well modeled, because of the dominance of $S^e_{v_a,v_a^*}$. At a higher J_C of 0.65 mA/μm^2, however, the hole contribution dominates over the electron contribution, as shown in Fig. 4.4 (b). An inspection of Figs. 4.4 (a) and (b) immediately shows that with increasing J_C, $S^e_{v_a,v_a^*}$ decreases, while $S^h_{v_a,v_a^*}$ stays about the same. The model underestimates $S^h_{v_a,v_a^*}$, and overestimates $S^e_{v_a,v_a^*}$. Observe that the simulated $S^h_{v_a,v_a^*}$ is frequency dependent, while the modeled $S^h_{v_a,v_a^*}$ ($4kTr_b$) is frequency independent.

Noise concentration contours at 2 GHz are shown for $C^e_{S_{v_a,v_a^*}}$ and $C^h_{S_{v_a,v_a^*}}$ in Figs. 4.5 and 4.6, respectively. J_C=0.65 mA/μm^2. Observe that both $C^e_{S_{v_a,v_a^*}}$ and $C^h_{S_{v_a,v_a^*}}$ are the highest in the SiGe base, indicating that transistor S_{v_a,v_a^*} mainly comes from the SiGe base. This provides guidelines to future noise model development, that is, the transistor noise mainly originates from

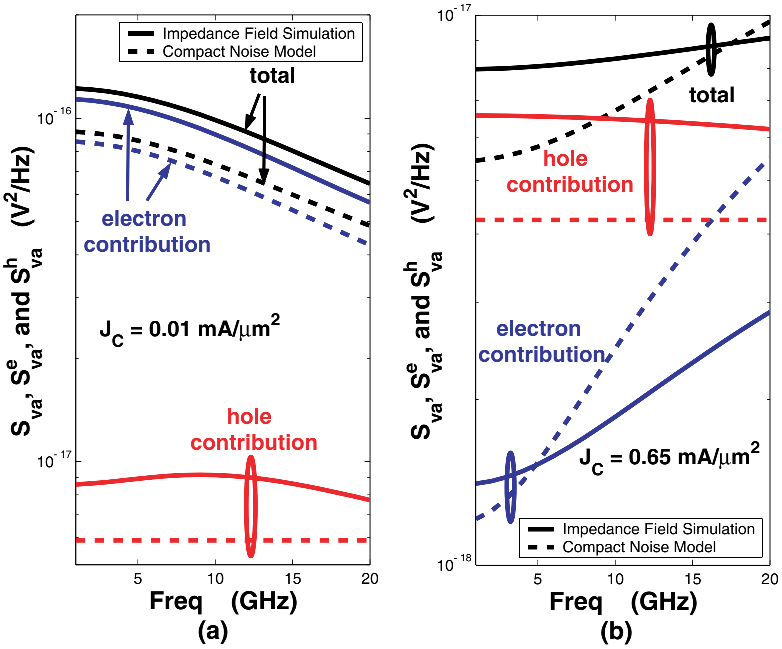

Figure 4.4: S_{v_a,v_a^*}, $S^e_{v_a,v_a^*}$, and $S^h_{v_a,v_a^*}$ vs frequency at (a) J_C=0.01 mA/μm^2. (b) J_C=0.65 mA/μm^2.

the EB junction. This contradicts the conventional wisdom that the collector current shot noise originates from passage of electrons through the reverse biased CB junction. In the intrinsic base, and along the x-direction, $C^e_{S_{v_a,v_a^*}}$ is uniform, while $C^h_{S_{v_a,v_a^*}}$ is highly nonuniform, and shows a strong "base noise crowding" effect.

Fig. 4.7 (a) shows the integrals of $C^e_{S_{v_a,v_a^*}}$ in the base, emitter, collector, and p-substrate, together with the $2qI_C$ related term in the model. J_C=0.65 mA/μm^2. Note that the model accounts for only the base contribution, which is reasonable, since the simulated base electron contribution overwhelmingly dominates over other electron contributions. The $2qI_C$ description, however, overestimates $S^e_{v_a,v_a^*}$, and thus a better description is required. Fig. 4.7 (b) shows the integrals of $C^h_{S_{v_a,v_a^*}}$ in the base, emitter, collector, and p-substrate. Also shown are the $2qI_B$

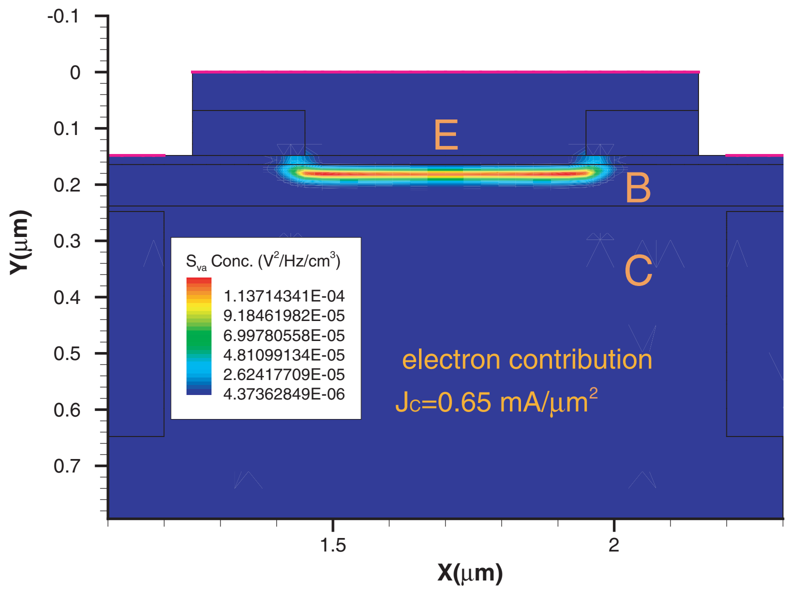

Figure 4.5: 2D distribution of $C^e_{S_{v_a,v_a^*}}$ at 2 GHz, J_C=0.65 mA/μm^2.

(emitter holes) and $4kTr_b$ (base holes) related terms accounted for in the model. The collector and substrate hole noises are indeed negligible. The noise from the base majority holes dominates over the noise from the emitter minority holes. The base majority hole noise contribution is more than predicted by $4kTr_b$, and frequency dependent as well. The noise from the emitter minority holes increases with frequency, and is underestimated by $2qI_B$ related term.

Fig. 4.8 (a) compares modeled and simulated S_{i_a,i_a^*}, $S^e_{i_a,i_a^*}$, and $S^h_{i_a,i_a^*}$ for J_C=0.01 mA/μm^2. $S^e_{i_a,i_a^*}$ increases with frequency and is slightly underestimated by the model. $S^h_{i_a,i_a^*}$ increases dramatically with frequency, and is significantly underestimated. At a higher J_C of 0.65 mA/μm^2, however, the $S^e_{i_a,i_a^*}$ discrepancy between model and simulation becomes much more pronounced,

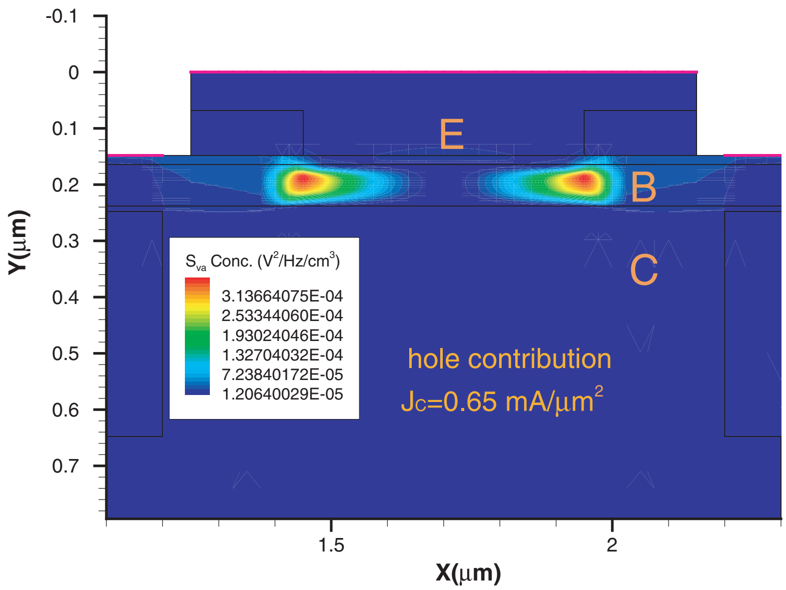

Figure 4.6: 2D distribution of $C^h_{S_{v_a,v_a^*}}$ at 2 GHz, J_C=0.65 mA/μm^2.

as shown in Fig. 4.8 (b). Thus, for S_{i_a,i_a^*}, $2qI_C$ is not a good description for base minority electron noise. Like for $S^h_{v_a,v_a^*}$, the frequency dependence for $S^h_{i_a,i_a^*}$ is not accounted for in the model. $S^h_{i_a,i_a^*}$ dominates at lower frequencies, while $S^e_{i_a,i_a^*}$ becomes dominant at higher frequencies.

Fig. 4.9 (a) shows the integrals of $C^e_{S_{i_a,i_a^*}}$ in the base, emitter, collector, and p-substrate. J_C=0.65 mA/μm^2. The model only accounts for the base electron contribution, a $2qI_C/|h_{21}|^2$ term. Like for other noise parameters, the base minority electron contribution for $S^e_{i_a,i_a^*}$ is poorly modeled by the $2qI_C$ related term. Fig. 4.9 (b) shows the regional contributions of $S^h_{i_a,i_a^*}$. The model accounts for only the emitter hole contribution through the $2qI_B$ term. Even though the collector and substrate hole contributions are indeed negligible, the base hole contribution is not negligible at higher frequencies. This emitter contribution constitutes the main discrepancy for the total $S^h_{i_a,i_a^*}$ between modeling and simulation, and shows frequency dependence.

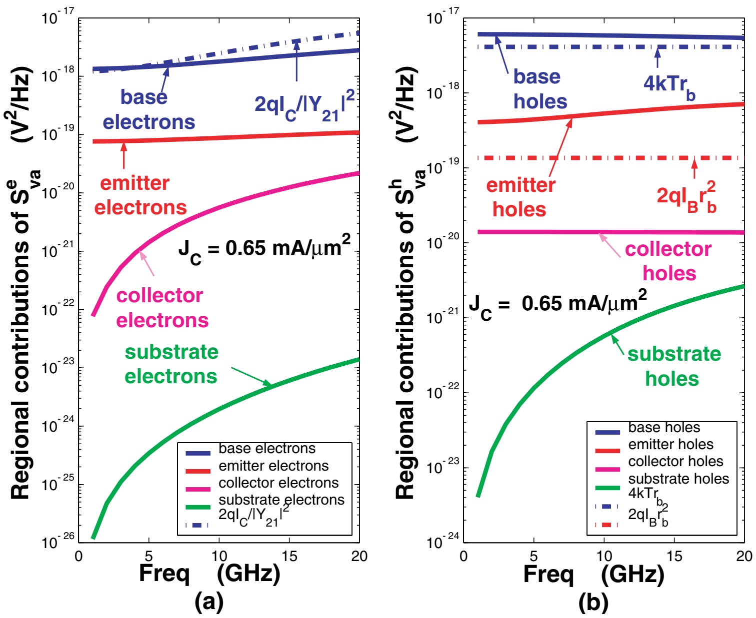

Figure 4.7: Regional contributions of $S^e_{v_a,v_a^*}$ (a) and $S^h_{v_a,v_a^*}$ (b) at J_C=0.65 mA/μm^2.

Similar analysis is performed for S_{i_a,v_a^*}. The results also show that the noise from the base minority electrons is poorly described by the model. Similar problems exist with $4kTr_b$ description of the base hole noise, and $2qI_C$ description of the base minority electron noise.

4.3.2 NF_{min}, Y_{opt} and R_n

NF_{min}, Y_{opt} and R_n are obtained from S_{v_a,v_a^*}, S_{i_a,i_a^*} and S_{i_a,v_a^*} by (2.24) – (8.19) derived in chapter 2 [11].

To compare the impact of electron and hole noise on circuit-level noise parameters, we examine NF^e_{min} and NF^h_{min}, defined as the NF_{min} that the transistor would have when only electron velocity or only hole velocity fluctuates, respectively. NF^e_{min} is obtained by substituting $S^e_{v_a,v_a^*}$, $S^e_{i_a,i_a^*}$ and $S^e_{i_a,v_a^*}$ into (2.24). NF^h_{min} is obtained similarly. Since NF_{min} is not a linear function

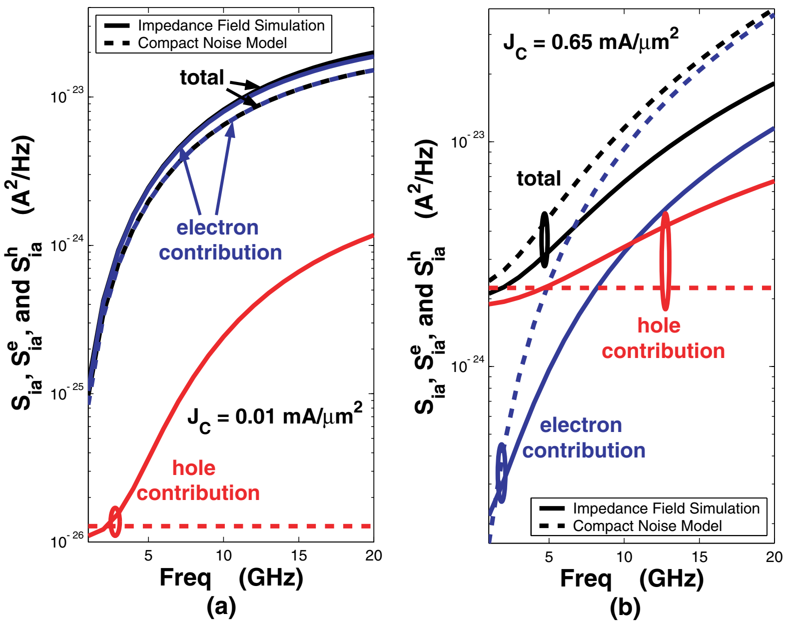

Figure 4.8: S_{i_a,i_a^*}, $S^e_{i_a,i_a^*}$, and $S^h_{i_a,i_a^*}$ vs frequency at (a) J_C=0.01 mA/μm^2. (b) J_C=0.65 mA/μm^2.

of S_{v_a,v_a^*}, S_{i_a,i_a^*} and S_{i_a,v_a^*}, $NF_{min} \neq NF^e_{min} + NF^h_{min}$. Y^e_{opt} is similarly defined and obtained from substituting $S^e_{v_a,v_a^*}$, $S^e_{i_a,i_a^*}$ and $S^e_{i_a,v_a^*}$ into (8.18) and (8.19). Like NF_{min}, $Y_{opt} \neq Y^e_{opt} + Y^h_{opt}$.

Since $R_n = S_{v_a,v_a^*}/4kT$, which is a linear function, $R_n = R^e_n + R^h_n$. The problems with S_{v_a,v_a^*} modeling directly translate into R_n inaccuracy as shown in Fig. 4.10 (a). At low J_C, NF_{min} and NF^e_{min} are well described by the model since S_{v_a,v_a^*}, S_{i_a,i_a^*} and S_{i_a,v_a^*} are well modeled at this bias. At high J_C, which is shown in Fig. 4.10 (b), however, they are both overestimated, and the discrepancies increase dramatically with frequency. NF^h_{min} is poorly modeled at high J_C. Note that the frequency dependence of NF^h_{min} is not modeled.

Similarly, Y_{opt} is well modeled at low bias. However, at J_C=0.65 mA/μm^2, neither Y_{opt} nor Y^e_{opt} or Y^h_{opt} is well modeled, as shown in Figs. 4.11 (a) and (b). The discrepancies increase with frequency. Again, the frequency dependence of Y^h_{opt} is not accounted for by the model. The

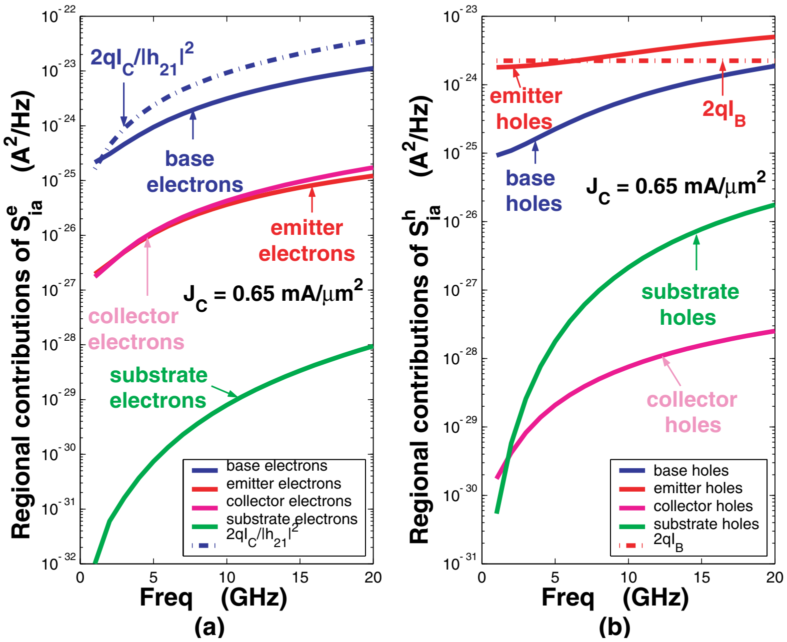

Figure 4.9: Regional contribution of $S^e_{i_a,i_a^*}$ (a) and $S^h_{i_a,i_a^*}$ (b) at J_C=0.65 mA/μm^2.

discrepancies of R_n, NF_{min} and Y_{opt} are all fundamentally caused by the inaccurate modeling of S_{v_a,v_a^*}, S_{i_a,i_a^*} and S_{i_a,v_a^*}. In particular, the description of base minority electron noise using $2qI_C$ is clearly responsible for the inaccuracy of the electron contributions, and the description of base majority hole noise using $4kTr_b$ is responsible for the inaccuracy of the hole contributions.

4.4 Intrinsic Base and Collector Noise

As we have discussed above, the main noise sources are from base electrons, base holes, and emitter holes. The integrations of $C^e_{S_{v_a,v_a^*}}$, $C^e_{S_{i_a,i_a^*}}$ and $C^e_{S_{i_a,v_a^*}}$ in base region are transformed to intrinsic transistor $S^{BE}_{i_b,i_b^*}$, $S^{BE}_{i_c,i_c^*}$ and $S^{BE}_{i_c,i_b^*}$ by (2.157), (2.158) and (2.159) derived in chapter 2. The superscript BE represents the contribution from base electrons. Similarly, we obtain intrinsic

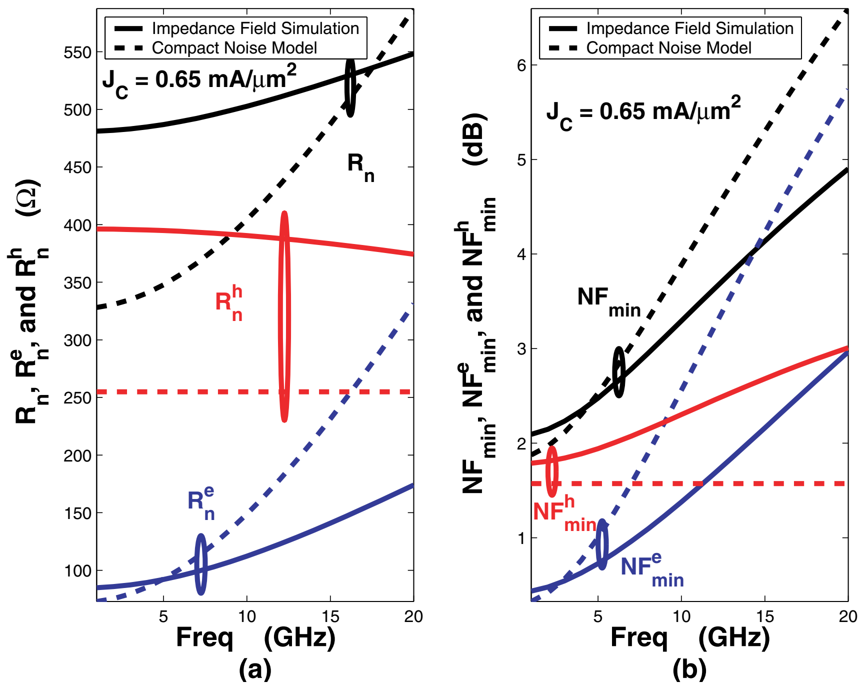

Figure 4.10: (a) R_n, and (b) NF_{min} vs frequency. J_C=0.65 mA/μm^2.

transistor S_{i_b,i_b^*}, S_{i_c,i_c^*} and S_{i_c,i_b^*} from base holes with superscript BH and from emitter holes with superscript EH. In the compact model, $S^{EH}_{i_b,i_b^*}$ is modeled as $2qI_B$, S_{i_b,i_b^*} from base region are not counted for. $S^{BE}_{i_c,i_c^*}$ is modeled as $2qI_C$, S_{i_c,i_c^*} from base and emitter holes are not modeled. S_{i_b,i_b^*} and S_{i_c,i_c^*} are not correlated to each other. Thus the connections between compact noise model and microscopic noise simulation can be established for S_{i_b,i_b^*}, S_{i_c,i_c^*} and S_{i_c,i_b^*} as shown in Table 4.2. Y_{11}^{int}, Y_{12}^{int}, Y_{21}^{int} and Y_{22}^{int} are elements of intrinsic transistor Y parameter matrix Y_{int}.

	S_{i_b,i_b^*}	S_{i_c,i_c^*}	S_{i_c,i_b^*}
SPICE model	$2qI_B$	$2qI_C$	0
van Vliet model	$4kT\Re Y_{11}^{int} - 2qI_B$	$4kT\Re Y_{22}^{int} + 2qI_C$	$2kT(Y_{21}^{int} + Y_{12}^{int*}) - 2qI_C$

Table 4.2: SPICE model and van Vliet model for intrinsic transistor S_{i_b,i_b^*}, S_{i_c,i_c^*} and S_{i_c,i_b^*}.

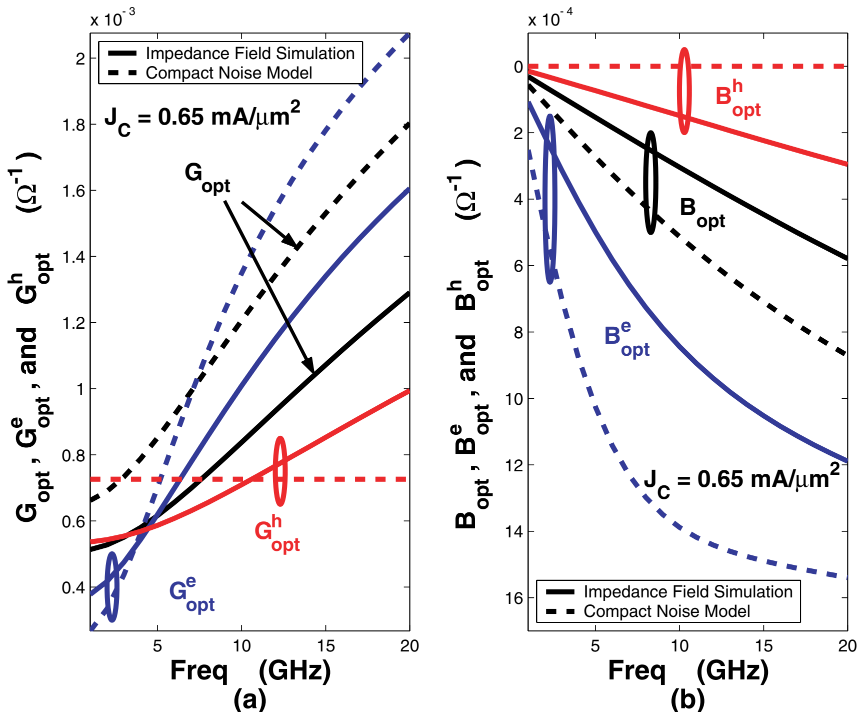

Figure 4.11: (a) G_{opt}, and (b) B_{opt} vs frequency. J_C=0.65 mA/μm^2.

Fig. 4.12 (a) shows S_{i_b,i_b^*} and its contributions $S^{BE}_{i_b,i_b^*}$, $S^{BH}_{i_b,i_b^*}$ and $S^{EH}_{i_b,i_b^*}$, respectively at a low J_C of 0.01 mA/μm^2. S_{i_b,i_b^*} is dominated by $S^{EH}_{i_b,i_b^*}$ and well modeled by $2qI_B$ at low frequency. However, as frequency increases, $S^{BE}_{i_b,i_b^*}$ and $S^{BH}_{i_b,i_b^*}$ increases dramatically and become dominant. Moreover, $S^{EH}_{i_b,i_b^*}$ increases with frequency and can not be well modeled by $2qI_B$ at high frequencies. Fig. 4.12 (b) shows S_{i_b,i_b^*} and its contributions at a higher bias of J_C=0.65 mA/μm^2. Similarly, S_{i_b,i_b^*} is dominated by emitter holes at lower frequencies and by base electrons and holes, which are not counted for in the compact noise model, at higher frequencies. This suggests that the compact noise model for S_{i_b,i_b^*} should be improved by grasping the frequency dependence at high frequency range for both high and low J_C's.

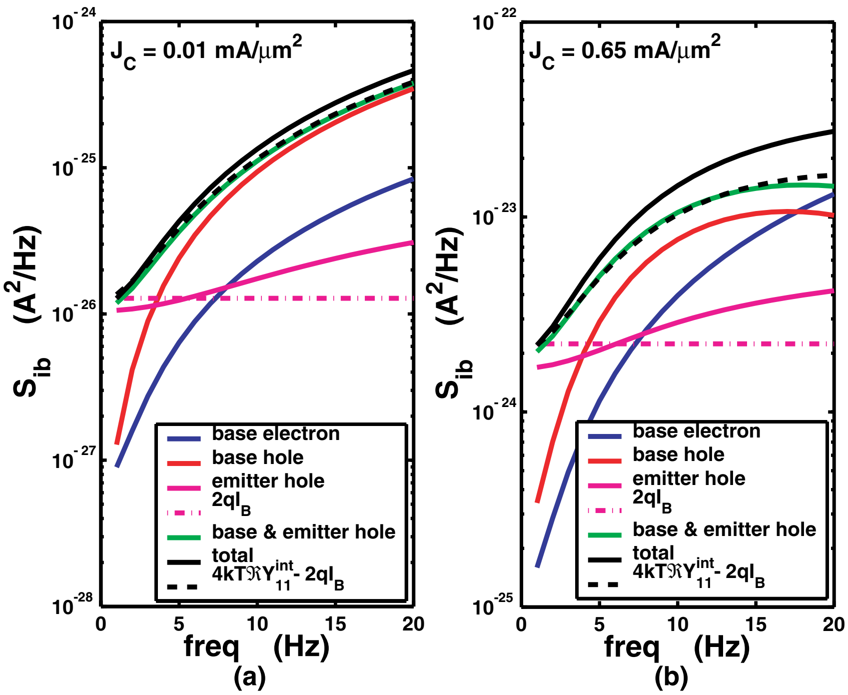

Figure 4.12: Regional contributions of internal input noise current S_{i_b,i_b^*} (a) J_C=0.01 mA/μm^2. (b) J_C=0.65 mA/μm^2.

Besides the compact noise model, the simulated intrinsic transistor input and output noise currents are also compared with van Vliet noise model as introduced in chapter 1 [13]. The van Vliet model equations are given in (1.14), (1.15), and (1.16).

Fig. 4.12 shows that $4kT\Re(Y_{11}^{int}) - 2qI_B$ grasp the frequency dependence at both low and high J_C's. However, it is more close to the overall hole contribution $S_{i_b,i_b^*}^{EH} + S_{i_b,i_b^*}^{EH}$ than for the total S_{i_b,i_b^*}. The base electron contribution $S_{i_b,i_b^*}^{EH}$ is only important at high J_C, yet there has not been a good model for it.

Fig. 4.13 (a) shows S_{i_c,i_c^*} and its contributions from base electrons, base holes and emitter holes at J_C=0.01 mA/μm^2. At this bias, S_{i_c,i_c^*} is dominated by base electrons, which is slightly underestimated by $2qI_C$. As J_C increases to 0.65 mA/μm^2 as shown in Fig. 4.13 (b), contribution from base holes becomes comparable to that from base electrons, and both of them are decreasing with frequency. Contribution from emitter holes is totally negligible at both biases. Apparently, S_{i_c,i_c^*} which is modeled by base minority electrons complies with simulation results well at low bias. However, at high bias, noise from majority carriers in the base plays an important role and makes total S_{i_c,i_c^*} deviates from $2qI_C$. This *deviation* was also claimed at high bias in [52]. However, [52] made the wrong comparison. It compared $2qI_C$ with the output noise current of the whole transistor, that can be expressed as,

$$S_{i_2,i_2^*} = 2qI_C + 4kTr_b|Y_{21}|^2 + 2qI_Br_b|Y_{21}|^2, \tag{4.8}$$

which has already included the hole contribution as shown in Fig. 4.14. Moreover, in low injection the *apparent* deviation from the compact model for drift diffusion noise in low bias as claimed in [52] is not observed in our study.

Similar to S_{i_b,i_b^*} analysis, comparison of S_{i_c,i_c^*} and $4kT\Re Y_{22}^{int} + 2qI_C$ is also shown in Fig. 4.13. the van Vliet model does not show any improvement to the frequency dependence of $S_{i_c,i_c^*}^{BE}$. Further, the base hole contribution $S_{i_c,i_c^*}^{BH}$ needs to be modeled at high J_C. The emitter hole contribution $S_{i_c,i_c^*}^{EH}$ is negligible at both biases.

Fig. 4.15 and Fig. 4.16 shows the correlation term S_{i_c,i_b^*} at low and high J_C, respectively. In the compact noise model S_{i_c,i_c^*} and S_{i_b,i_b^*} have no correlation. The simulation result, however, Fig. 4.15 shows that S_{i_c,i_b^*} is negligible at low frequency but noneligible at high frequency at low J_C. $\Re S_{i_c,i_b^*}$ is positive and slightly dominated by $\Re S_{i_c,i_b^*}^{BH}$ over $\Re S_{i_c,i_b^*}^{BE}$, which has a negative sign. $\Im S_{i_c,i_b^*}$ and its contributions are all negative. $\Im S_{i_c,i_b^*}^{BE}$ slightly dominates over $\Im S_{i_c,i_b^*}^{BH}$. $S_{i_c,i_b^*}^{EH}$ is negligible. At high J_C, as shown in Fig. 4.16, S_{i_c,i_b^*} can not be neglected for the whole frequency

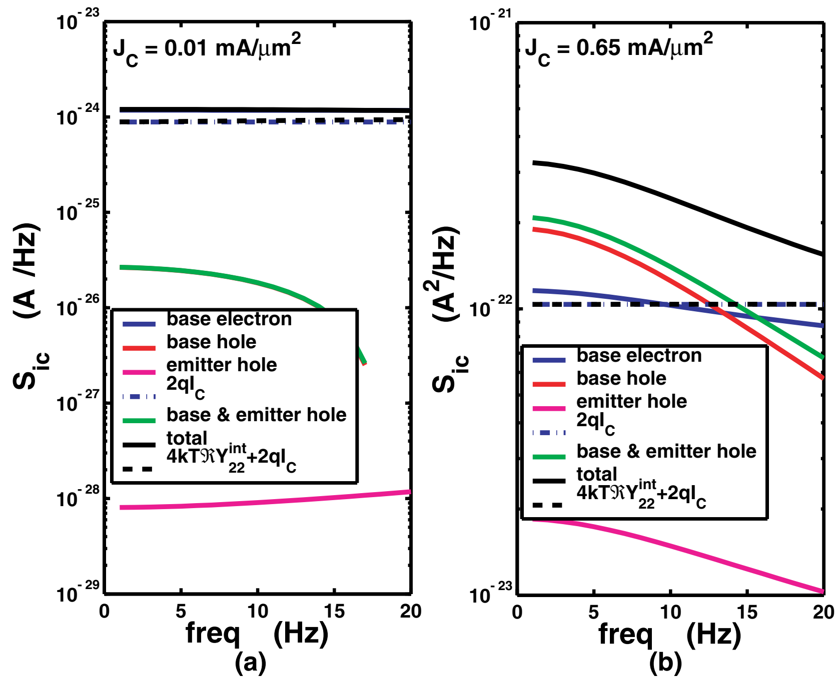

Figure 4.13: Regional contributions of internal output noise current S_{i_c,i_c^*} (a) J_C=0.01 mA/μm^2. (b) J_C=0.65 mA/μm^2.

span. Both $\Re S_{i_c,i_b^*}$ and $\Im S_{i_c,i_b^*}$ are dominated by their base hole contribution at low frequency. $S^{BH}_{i_c,i_b^*}$ and $S^{BE}_{i_c,i_b^*}$ are comparable at high frequencies. $S^{EH}_{i_c,i_b^*}$ can still be neglected.

Comparison of S_{i_c,i_b^*} and $2kT(Y_{21}^{int}+Y_{12}^{int*})-2qI_C$ is also shown in Fig. 4.15 and Fig. 4.16. At low bias, the van Vliet model grasps the frequency dependence of S_{i_c,i_b^*}, yet slightly underestimates both the real and the imaginary part. Its imaginary part is more close to $\Im S^{BE}_{i_c,i_b^*}$. At high bias, however, the van Vliet model deviated from S_{i_c,i_b^*} a lot. Hence, compared to compact noise model, [13] has its advantage of better frequency dependence description at low J_C, where minority carrier noise dominates. However, as J_C increases, where majority carrier noise becomes comparable to minority carrier noise, [13] does not do a better job than the compact noise model.

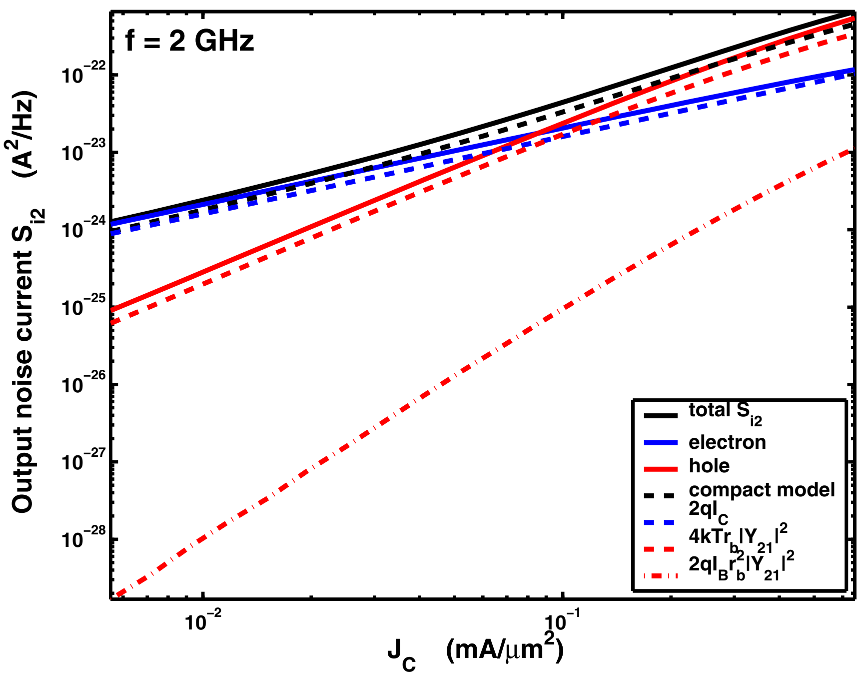

Figure 4.14: Output noise current of whole transistor S_{i_2,i_2^*} at 2 GHz.

4.5 Summary

We have examined bipolar transistor noise modeling for each physical noise source using microscopic noise simulation. Regional analysis is performed for the chain representation noise parameters. The base majority hole noise contribution is shown to be larger than modeled using $4kTr_b$ and frequency dependent for all noise parameters. The $2qI_B$ related terms underestimates the emitter hole noise, especially for higher frequencies. The base minority electron contribution is poorly modeled by the $2qI_C$ related terms for all noise parameters, particularly for higher J_C required for high speed. Further, regional analysis for intrinsic transistor input and output noise current is performed. The input noise current consists not only the emitter hole contribution corresponding to $2qI_B$, but also the base electron and hole contribution which are frequency

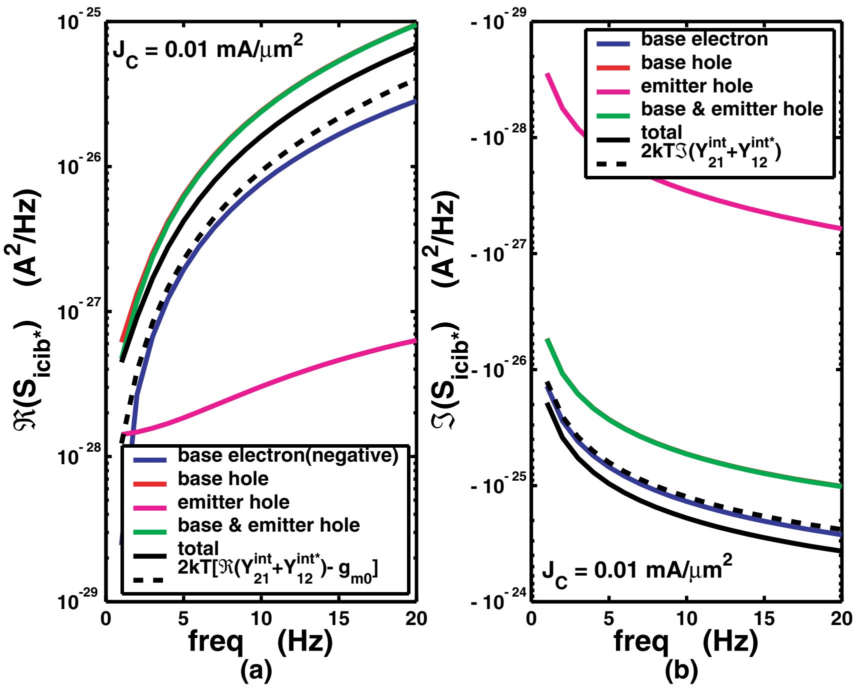

Figure 4.15: Regional contributions of internal noise current correlation S_{i_c,i_b^*}. J_C=0.01 mA/μm^2. (a) $\Re S_{i_c,i_b^*}$. (b) $\Im S_{i_c,i_b^*}$.

dependent and should be counted for especially at high frequencies. At higher J_C, the output noise current consists not only the base electron contribution corresponding to $2qI_C$, but also the base hole contribution that not counted for in the compact noise model. Moreover, the frequency dependence of base electron contribution is not described. The correlation term which is not modeled in the compact noise model should be considered for higher J_C and higher frequency.

This chapter also compared the intrinsic transistor input and output noise current with a noise model that derived from the transport theory of density fluctuations that applies to three dimensional device. The comparison shows that this model has a better description of frequency

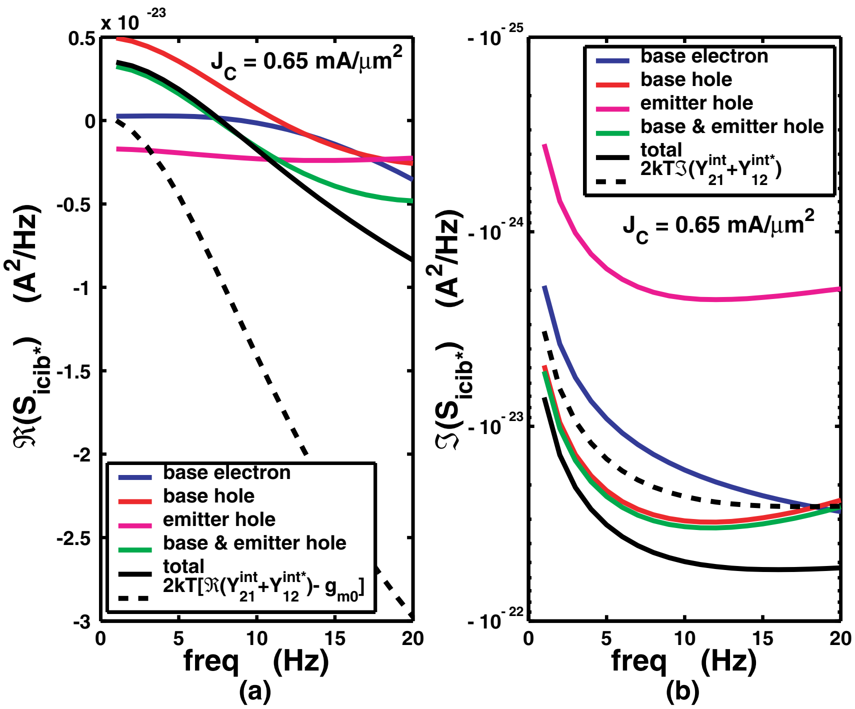

Figure 4.16: Regional contributions of internal noise current correlation S_{i_c,i_b^*}. J_C=0.65 mA/μm^2. (a) $\Re S_{i_c,i_b^*}$. (b) $\Im S_{i_c,i_b^*}$.

dependence than the compact noise model at low bias. However, as for higher J_C, it has no advantage over the compact noise model.

CHAPTER 5

SIGE PROFILE OPTIMIZATION FOR LOW NOISE

This chapter explores the RF noise physics and SiGe profile optimization for low noise using microscopic noise simulation. A higher Ge gradient in a noise critical region near the EB junction reduces impedance field and hence minimum noise figure. A higher Ge gradient near the EB junction, together with an unconventional Ge retrograding in the base to keep total Ge content below stability, when optimized, can lead to significant noise improvement without sacrificing peak f_T and without any significant high injection f_T rolloff degradation.

5.1 Introduction

RF noise is an important aspect of RF devices as it sets the sensitivity of a wireless receiver. At a given technology generation, the base resistance is primarily limited by the maximum amount of base dopants that can be kept in place after device fabrication, and hence limited by thermal cycle. SiGe profile, however, can be optimized to reduce minimum noise figure [53] [54]. In previous work, the profile optimization was made by simulating device y-parameters, and then calculating the minimum noise figure NF_{min} using a set of approximate noise modeling equations [54] [55]. Those equations rely on simplified equivalent circuit, and simplified noise source description, which become less valid at higher RF frequencies [12], particularly for scaled devices with higher speed. In some cases, unphysical noise results are obtained, preventing a meaningful optimization.

The purpose of this work is to investigate SiGe HBT noise physics and related SiGe profile optimization using a more physical approach – microscopic noise simulation. Using techniques described in chapter 3, we can calculate the transistor equivalent input noise current or voltage as integration of their corresponding noise concentration, in the same way the total number of electrons is calculated as integration of electron concentration. This enables us to examine how SiGe profile affects the input noise current or voltage, the noise concentration profile, the local noise source, as well as the propagation of local noise source towards the input, which we address below. The results are then used to optimize SiGe profile for low noise under constant SiGe film stability constraint. We use here a hypothetical SiGe HBT structure similar to those 200 GHz HBTs reported in the literature [56] [57].

5.2 SiGe Profile Impact

From the power spectral densities of the input noise current, voltage, and their correlation as S_{i_a,i_a^*}, S_{v_a,v_a^*} and S_{i_a,v_a^*}, the minimum noise figure NF_{min}, the noise resistance R_n, and optimum source admittance Y_{opt} are given (2.24) – (8.19) in chapter 2. We first examine how SiGe profile affects NF_{min}, S_{v_a,v_a^*}, S_{i_a,i_a^*}, $\Re(S_{i_a,v_a^*})$ and $\Im(S_{i_a,v_a^*})$ using two "conventional" sample SiGe profiles shown in Fig. 5.1 (a). Profile I has a constant Ge gradient in the base. Compared to profile I, profile II has a higher Ge gradient near the EB junction, but a flat Ge fraction near the CB junction to not create any Ge retrograding inside the base. Profile II has 33% more total Ge. Noise simulations are then performed using DESSIS [45], from 1 to 60 GHz, across a wide bias range. Energy balance equations are solved to account for non-equilibrium transport in these scaled devices. The DESSIS simulation input deck and MATLAB programming are given in B.2 and B.3 in Appendix B.

Fig. 5.1 (b) shows the Gummel curves of the two profiles. The base current density J_B is the same for both profiles, as expected, because of identical emitter structure. Profile II gives higher collector current density J_C, and hence higher β. f_T is also slightly higher for profile II, as shown in Fig. 5.2. A peak f_T over 200 GHz is reached at $J_C = 10$ mA/μm^2. Fig. 5.3 shows NF_{min} versus J_C at 40 GHz. A clear improvement of NF_{min} can be observed for profile II. G_{opt} is less for profile II. Profile I and II have similar R_n and B_{opt}.

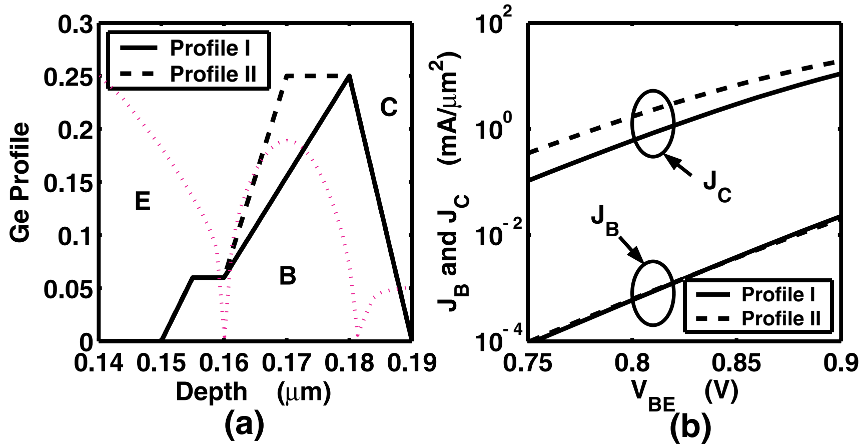

Figure 5.1: (a) Ge profile I and II. (b) Gummel curves for profile I and II.

5.2.1 Distributive Transit Time Analysis

Distributive transit time analysis as a function of J_C are performed to find out the reason of f_T improvement. Details of distributive transit time analysis can be found in [10]. The spatial distribution of the total transit time is simulated, in terms of the so called differential transit time τ_{diff}. In an ideal 1-D bipolar transistor, at any position x, $\tau_{diff}(x) \cdot \Delta x$ represents the local contribution to the total transit time due to minority carrier charge storage from depth x to $(x + \Delta x)$. τ_{diff} has a unit of ps/μm, and its integration from emitter to collector gives the total transit time τ_{ec} [10]. The cutoff frequency f_T is related to τ_{ec} by $f_T = 1/2\pi\tau_{ec}$.

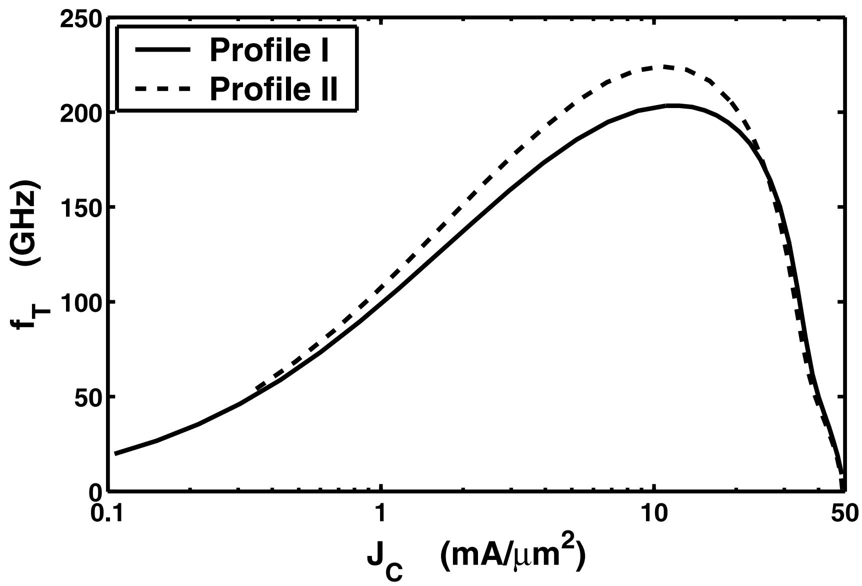

Figure 5.2: f_T vs J_C for Ge profile I and II.

Fig. 5.4 shows the simulated differential transit time τ_{diff} profile for Ge profile I and II for $J_C = 2$ mA$/\mu$m^2. The τ_{diff} profile improvement of Ge profile II over profile I mainly lies in the emitter and the base. Since the emitter of profile I and II are the same, the improvement of τ_{diff} of profile II in the emitter is the result of improved *dc* current gain β, which is induced by the additional Ge in the base of profile II. The improvement of τ_{diff} of profile II in the base is the result of the enhanced Ge gradient of profile II near the emitter-base junction. However, this improvement is slightly alleviated by the additional τ_{diff} induced by the Ge grading transition of profile II [58].

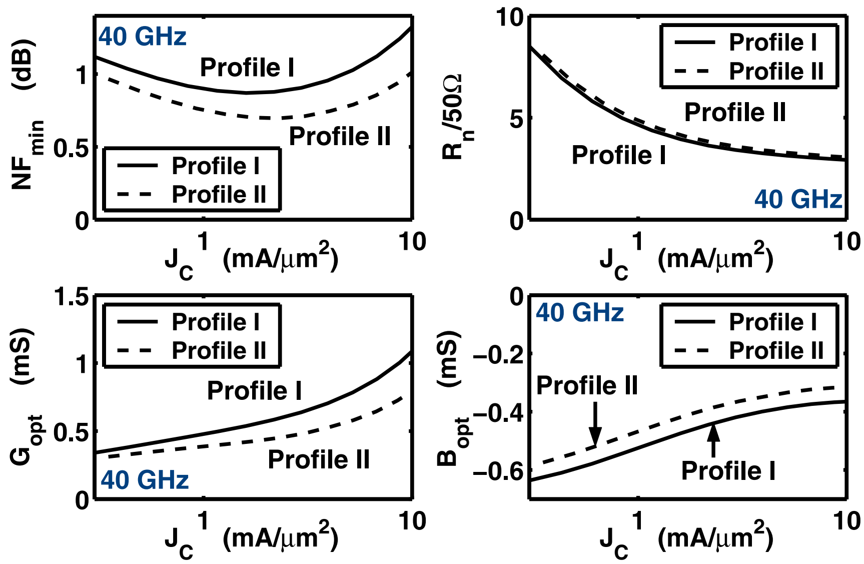

Figure 5.3: Noise parameters vs J_C for profile I and II at 40 GHz.

5.2.2 Input Noise Voltage and Current

As NF_{min} is determined by S_{i_a,i_a^*}, S_{v_a,v_a^*}, and the real and imaginary parts of S_{i_a,v_a^*}, as shown in (2.24) in chapter 2, we compare S_{i_a,i_a^*}, S_{v_a,v_a^*}, and real and imaginary parts of S_{i_a,v_a^*} for the two profiles in Fig. 5.5, as a function of J_C, at 40 GHz. The comparisons are similar at other frequencies. Note that the input noise voltage S_{v_a,v_a^*} and the imaginary part of the correlation $\Im(S_{i_a,v_a^*})$ are approximately the same for both profiles in the whole bias range. This explains similar R_n and B_{opt} for profile I and II from (8.17) and (8.19) in chapter 2. The input noise current S_{i_a,i_a^*}, and the real part of the correlation $\Re(S_{i_a,v_a^*})$, however, are much lower for profile II. It is not clear if the S_{i_a,i_a^*} reduction or the $\Re(S_{i_a,v_a^*})$ reduction, or both, is responsible for the NF_{min} reduction in profile II. To find this out, we plot the two terms of $F_{min} - 1$ in Fig. 5.6. An inspection of (2.24) immediately shows that the first term is determined by S_{i_a,i_a^*}, S_{v_a,v_a^*} and

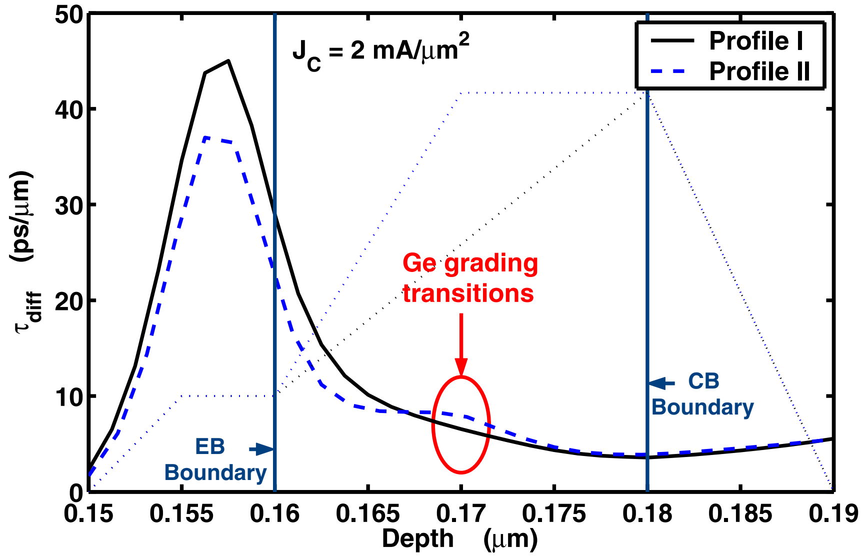

Figure 5.4: 1-D center cut of τ_{diff} for profile I and II. $J_C = 2$ mA$/\mu$m^2.

$\Im(S_{i_a,v_a^*})$, while the second term is determined by $\Re(S_{i_a,v_a^*})$. The first term clearly dominates over the second term. Because S_{v_a,v_a^*} and $\Im(S_{i_a,v_a^*})$ are the same for both profiles, the smaller input noise current S_{i_a,i_a^*} is the primary reason for the NF_{min} reduction in profile II. Similarly, we find S_{i_a,i_a^*} is the primary reason for reduction of G_{opt} in profile II from (8.18) in chapter 2. This suggests that we can focus on S_{i_a,i_a^*} in understanding the impact of SiGe profile on NF_{min}.

5.3 New Approach: Regional Electron and Hole Contributions

Fig. 5.7 shows the regional contributions of S_{v_a,v_a^*}. "*base, n*" and "*base, p*" denote base electron and hole contributions, respectively. "*emitter, n*" is used to denote emitter electron contribution. The collector contribution is negligible. S_{v_a,v_a^*} is dominated by base electron contribution at low J_C, and dominated by base hole contribution at J_C higher than 2 mA$/\mu$m^2. The base hole contribution is pretty much determined by the base doping, and does not change much

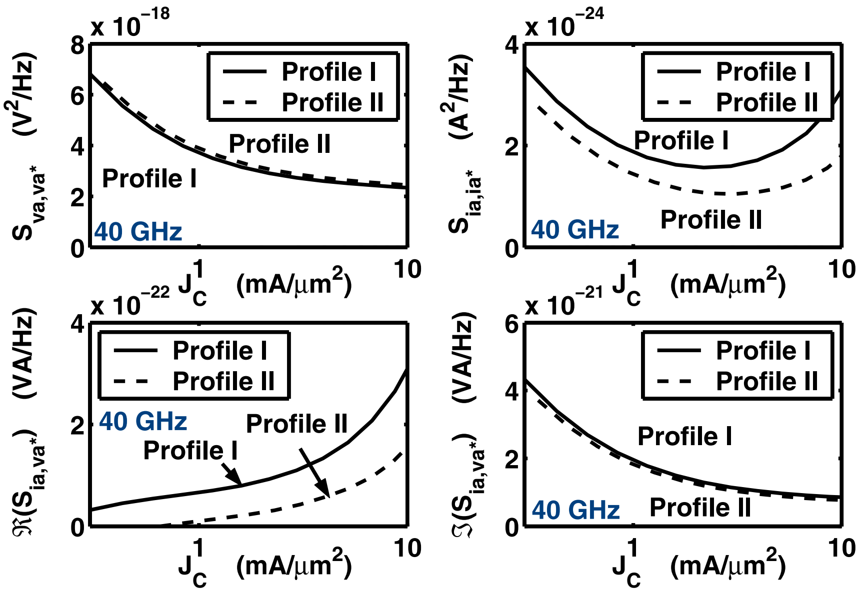

Figure 5.5: S_{i_a,i_a^*}, S_{v_a,v_a^*} and their correlation vs J_C. $f = 40$ GHz.

with bias. The base electron contributions of S_{v_a,v_a^*} for profile I and II are approximately the same, despite the Ge profile difference. This is qualitatively consistent with first order noise models [54].

Fig. 5.8 shows the regional contributions of S_{i_a,i_a^*}. At lower and moderate J_C's where NF_{min} is low, S_{i_a,i_a^*} is dominated by the base electron contribution, which is responsible for the reduction of S_{i_a,i_a^*} for profile II. At lower J_C, the emitter hole contribution of S_{i_a,i_a^*} is negligible because of the high β, unlike in the 50 GHz HBTs discussed in [55]. Thus, the higher β and hence smaller $2qI_B$ is not the reason for the reduced S_{i_a,i_a^*} in profile II at lower J_C. At higher J_C near peak f_T, however, the emitter hole contribution becomes comparable to the base electron contribution. The base hole contribution of S_{i_a,i_a^*} also comes into the picture at high J_C. The base hole contributions of S_{i_a,i_a^*} are almost the same for the two profiles. The main reason for

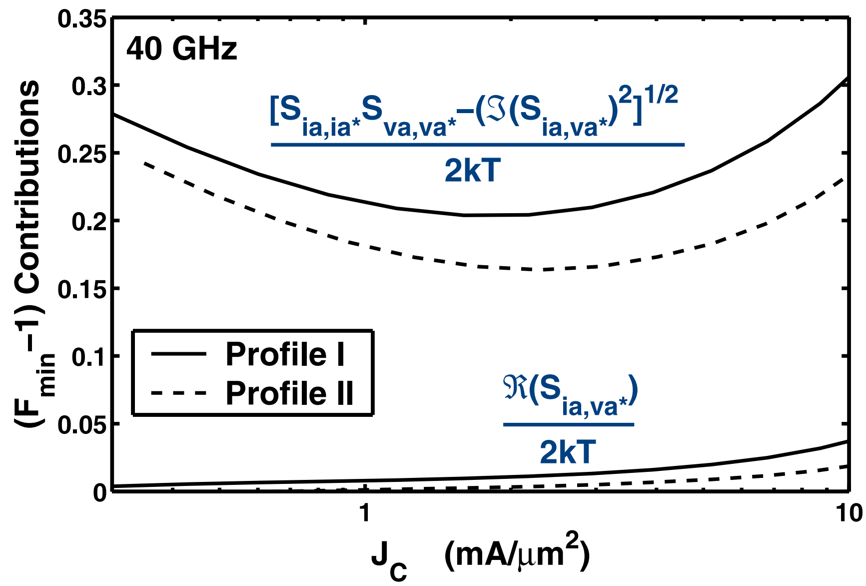

Figure 5.6: $(F_{min} - 1)$ contributions. $f = 40$ GHz.

the better noise performance of profile II at low J_C of interest to low noise is thus the smaller base electron contribution of S_{i_a,i_a^*}.

5.3.1 Noise Critical Region and Ge Profile Impact

We now analyze the spatial distribution of the noise concentration for S_{i_a,i_a^*} due to electrons and holes. Using techniques in chapter 3, S_{i_a,i_a^*} is the volume integration of the input noise current noise concentration $C_{S_{i_a,i_a^*}}$, which has electron contribution $C^n_{S_{i_a,i_a^*}}$ and hole contribution

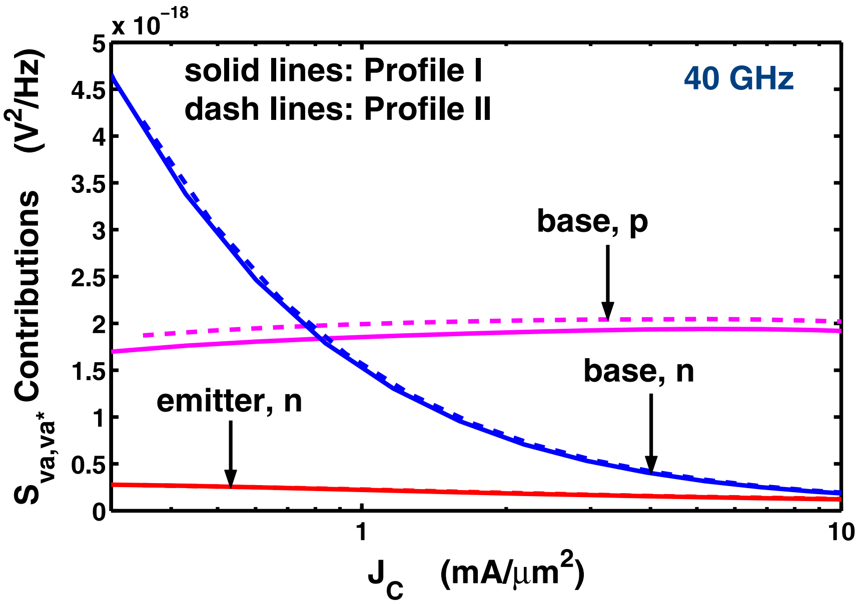

Figure 5.7: Comparison of Regional contributions of S_{v_a,v_a^*}. f=40 GHz.

$C^h_{S_{i_a,i_a^*}}$,

$$S_{i_a,i_a^*} = \int_\Omega C_{S_{i_a,i_a^*}} d\Omega, \tag{5.1}$$

$$= \int_\Omega C^n_{S_{i_a,i_a^*}} dV + \int_V C^p_{S_{i_a,i_a^*}} d\Omega, \tag{5.2}$$

$$C_{S_{i_a,i_a^*}} = C^n_{S_{i_a,i_a^*}} + C^p_{S_{i_a,i_a^*}}. \tag{5.3}$$

The input noise current noise concentration has a unit of A^2/Hz/cm^3. Fig. 5.9 (a) shows the 1-D center cut of the input noise current noise concentrations due to electrons and holes, $C^n_{S_{i_a,i_a^*}}$ and $C^p_{S_{i_a,i_a^*}}$. Integration of $C^n_{S_{i_a,i_a^*}}$ over volume gives the total input noise current due to electrons. Similarly, the integration of $C^p_{S_{i_a,i_a^*}}$ over volume gives the total input noise current due to holes. $J_C = 2$ mA$/\mu$m^2, frequency is 40 GHz. First, the electron contribution dominates over the hole

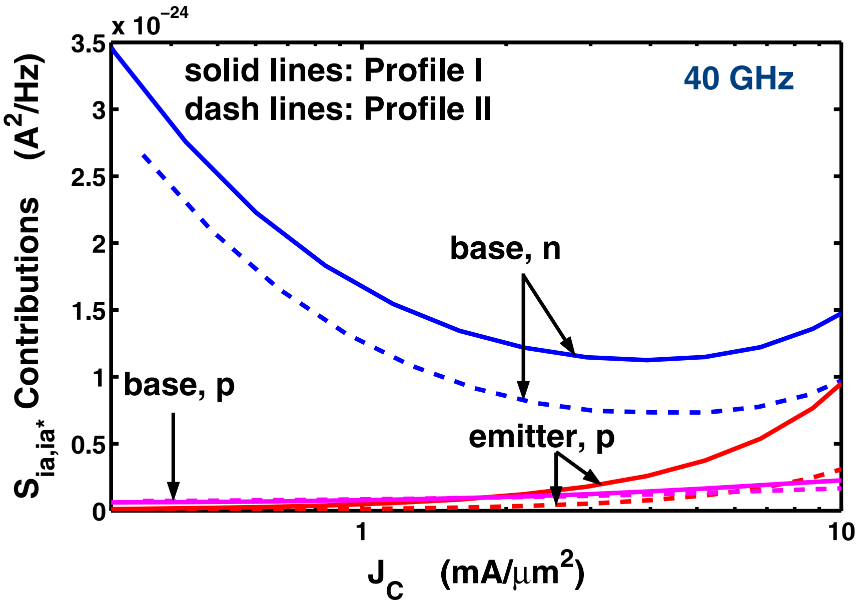

Figure 5.8: Comparison of Regional contributions of S_{i_a,i_a^*}. f=40 GHz.

contribution. It is clear that most of the input noise current comes from near the EB junction, where $C^n_{S_{i_a,i_a^*}}$ is highest. The primary reason for the smaller S_{i_a,i_a^*} of profile II is its smaller $C^n_{S_{i_a,i_a^*}}$ near the EB junction.

The noise concentration is given by the product of a local noise source which is proportional to carrier density, and the impedance field, which describes noise propagation,

$$C^n_{S_{i_a,i_a^*}} = C^n_{S_i} |G_{n,i_a}|^2, \tag{5.4}$$

$$C^p_{S_{i_a,i_a^*}} = C^p_{S_i} |G_{p,i_a}|^2, \tag{5.5}$$

where $|G_{n,i_a}|^2$ and $|G_{p,i_a}|^2$ are the electron and hole impedance field from local noise source to input noise current concentration, respectively, with a unit of A^2/A^2. Fig. 5.9 (b) shows 1-D center cut of local electron noise current source $C^n_{S_i}$, and the electron impedance field $|G_{n,i_a}|^2$. The $C^n_{S_{i_a,i_a^*}}$ difference between the two profiles is clearly dominated by the difference in impedance field, rather than the local noise source. The fundamental reason for the smaller S_{i_a,i_a^*} and NF_{min} in profile II is thus the reduced base impedance field, which means less noise current produced at the transistor input (base) for the same amount of local current density fluctuations. Observe that the high impedance field occurs over 10 nm at the beginning of the neutral base, where Ge ramps up for both profiles. The higher Ge gradient in profile II in this "noise critical" region clearly has led to S_{i_a,i_a^*} and NF_{min} reduction. To not have any retrograding of Ge in the base, Ge fraction is kept constant after the Ge peak in profile II, leading to more total Ge, which is undesired from a SiGe film stability standpoint. A logical question is if the benefit of reduced impedance field over the 10 nm "noise critical" region can be maintained if Ge is retrograded after the peak to keep the total Ge content the same. This is indeed the case, and can be used for SiGe profile optimization at constant stability.

5.4 Optimization Under Constant Stability

We now increase the Ge gradient in the noise critical region where the impedance field for input noise current is high, while keeping the total Ge content the same to maintain SiGe film stability. Inevitably, for sufficiently high peak Ge, we are forced to have Ge retrograding in the base, which is usually avoided in conventional SiGe profile design, as the retrograding can introduce a retarding field. Inspection of simulation details, however, shows that a retrograding of Ge can indeed be used in the later part of the base, near the CB junction, without degrading

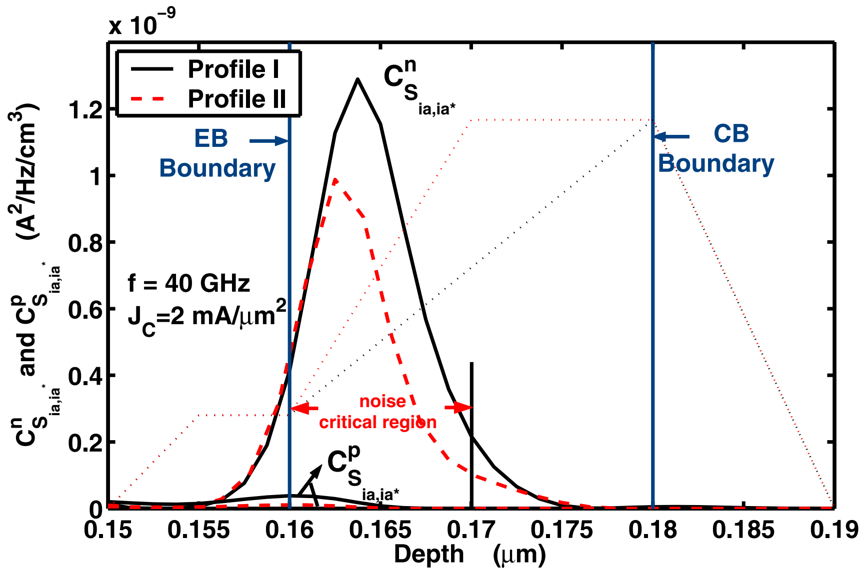

Figure 5.9: 1-D center cut of $C^n_{S_{i_a,i_a^*}}$ and $C^p_{S_{i_a,i_a^*}}$ for Ge profile I and II. $J_C = 2$ mA$/\mu$m^2. $f = 40$ GHz.

f_T if designed properly. The falloff of p-type base doping near the CB junction helps in part as it generates an accelerating field. In this case, profile III has a slightly higher peak Ge fraction. An optimized profile example using Ge retrograding in the base is given in Fig. 5.11 (a) – profile III, together with the reference profile – profile I.

Fig. 5.11 (b) compares the Gummel curves of profile I, II and III. J_B is the same, and J_C is higher for the optimized profile III. Despite the Ge retrograding in the later part of the base, profile III shows a higher peak f_T than profile I, as shown in Fig. 5.12. The f_T rolloff, however, occurs at a slightly lower J_C. The rolloff slope for profile III is similar to that for profile I, because the smaller Ge retrograding gradient partially offsets the "earlier" retrograding, an effect different from the SiGe profile design tradeoff discussed in [55]. Fig. 5.13 shows 1-D center cut of τ_{diff} for profile I, II and III at $J_C = 2$ mA$/\mu$m^2.

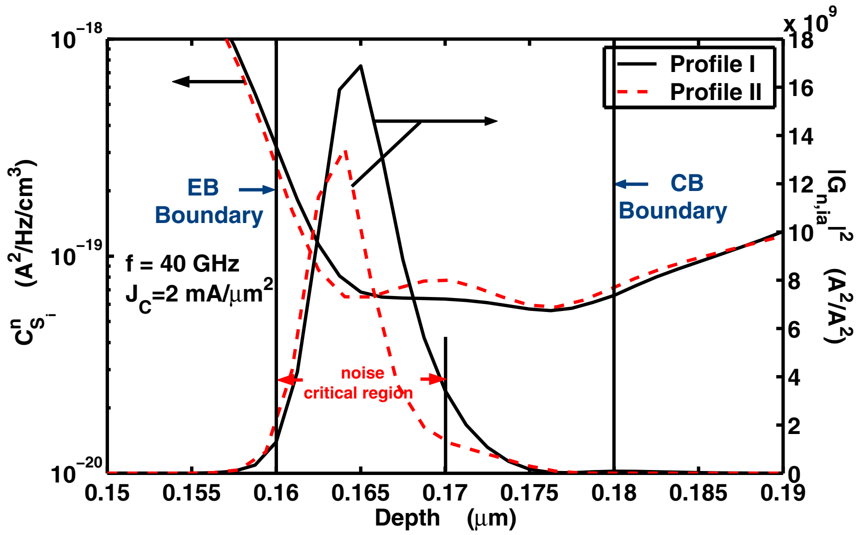

Figure 5.10: 1-D center cut of $C^n_{S_i}$ and $|G_{n,i_a}|^2$ for profile I and II. $J_C = 2$ mA/μm^2. $f = 40$ GHz.

Fig. 5.14 shows 1-D center cut of electron and hole noise concentrations of S_{i_a,i_a^*}. Profile III shows lower $C^n_{S_{i_a,i_a^*}}$ than profile I in the "noise critical" region, despite the Ge retrograding in the base required for stability, due to reduced impedance field. In terms of reducing the input noise current, Profile III is as effective as profile II, which is over stability limit, and does not have Ge retrograding in the base.

Fig. 5.15 shows NF_{min}–J_C for profile I, II and III at 10 GHz and 60 GHz. Fig. 5.16 shows NF_{min} versus frequency for profile I, II and III at $J_C = 2$ and 10 mA/μm^2. The overall noise improvement is about the same as that achieved by profile II, which has 33 % more total Ge and is over stability limit. With profile III, we have increased f_T, β and decreased NF_{min} without sacrificing SiGe film stability. The high injection f_T rolloff degradation has been kept minimum by minimizing the gradient of Ge retrograding.

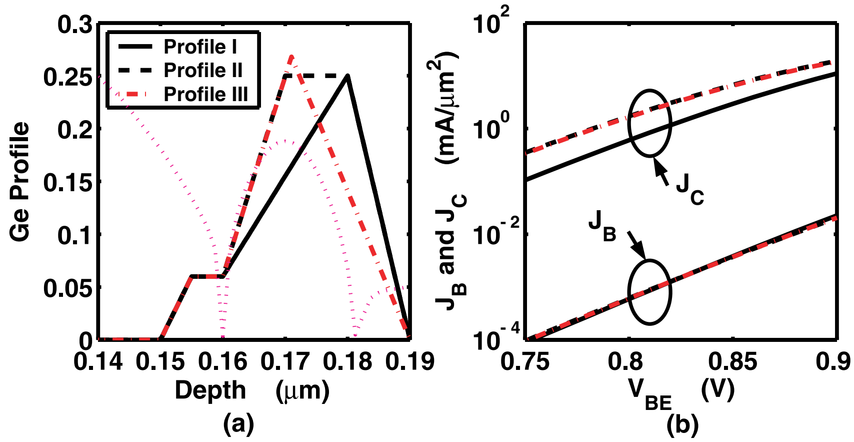

Figure 5.11: (a) Constant stability Ge profiles: profile I, II and III. (b) Gummel curves for profile I, II and III.

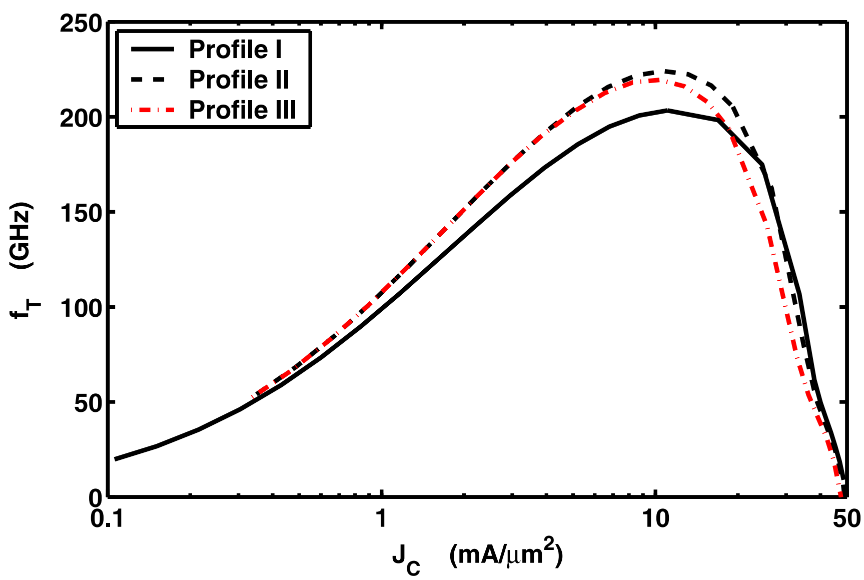

Figure 5.12: f_T vs J_C for profile I, II and III.

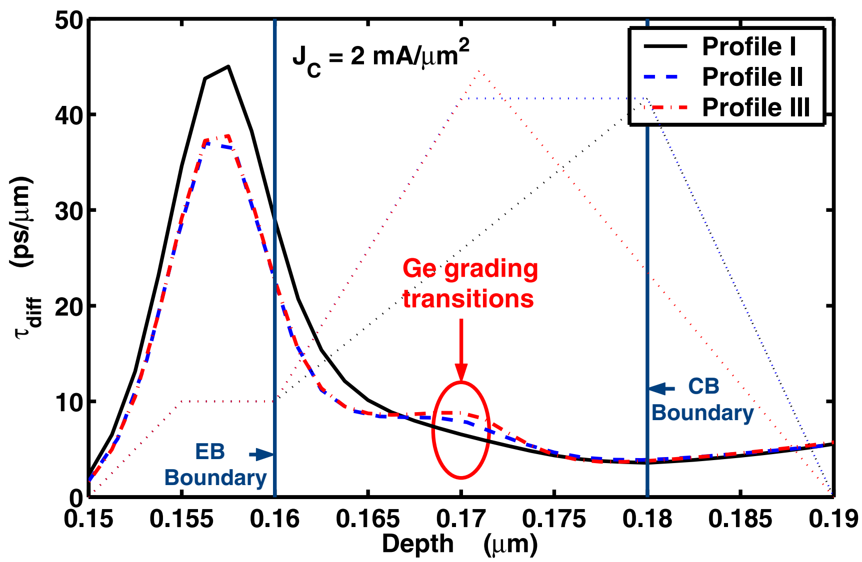

Figure 5.13: 1-D center cut of τ_{diff} for profile I, II and III. $J_C = 2$ mA/μm^2.

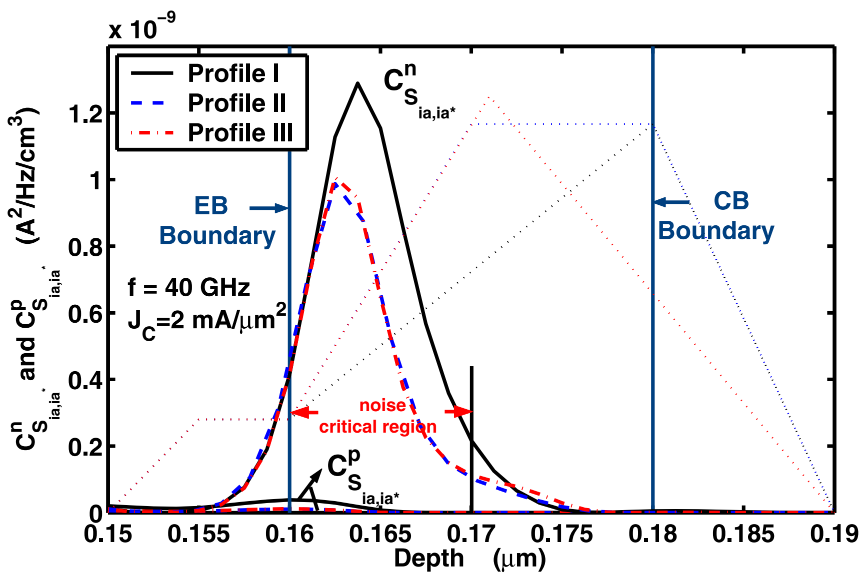

Figure 5.14: 1-D center cut of $C^n_{S_{i_a,i_a^*}}$ and $C^p_{S_{i_a,i_a^*}}$ for profile I, II and III. $f = 40$ GHz. $J_C = 2$ mA/μm^2.

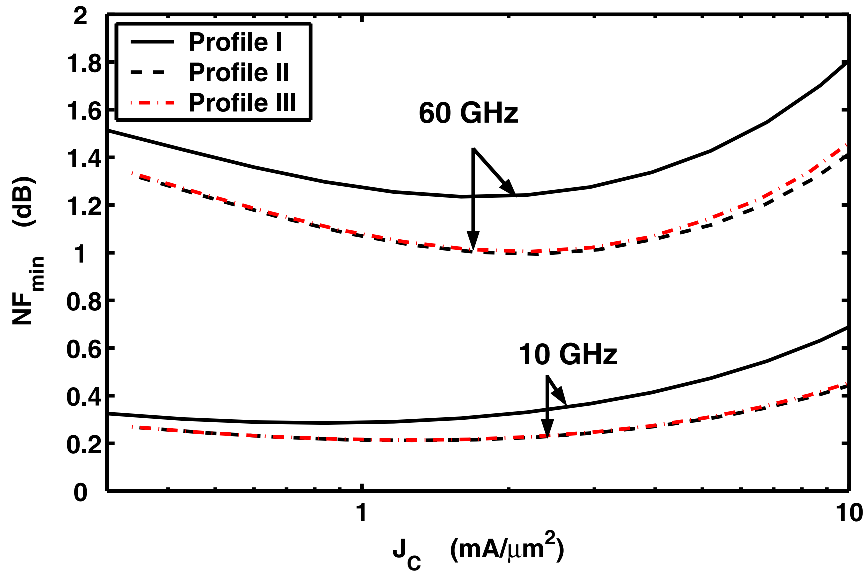

Figure 5.15: NF_{min} vs J_C at 10 and 60 GHz.

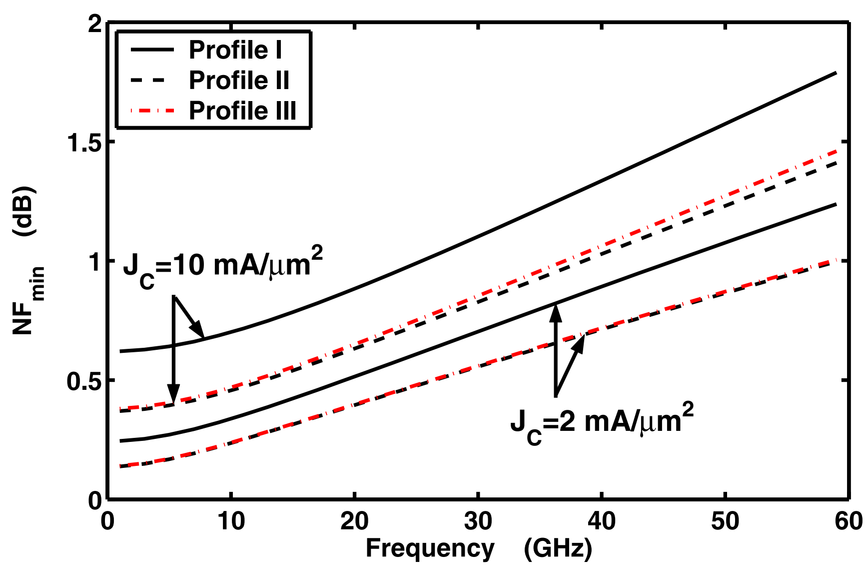

Figure 5.16: NF_{min} vs frequency at $J_C = 2$ and 10 mA$/\mu$m^2.

5.5 Summary

We have explored RF noise physics in advanced SiGe HBTs using microscopic noise simulation. We have shown that SiGe profile primarily affects the minimum noise figure through the input noise current, and identified the small region near the EB junction as where most of the input noise current originates. A higher Ge gradient in this region helps reducing the impedance field for the input noise current. At constant SiGe film stability, increasing the Ge gradient in the noise critical region ultimately necessitates retrograding of Ge inside the neutral base, and the gradient of such Ge retrograding needs to be optimized within stability limit to minimize high injection f_T rolloff degradation. An example of successful SiGe profile optimization using unconventional Ge retrograding inside the base has been presented.

CHAPTER 6

MODELING OF INTRINSIC NOISE IN CMOS

In this chapter, RF noise of 50 nm L_{eff} CMOS is simulated using hydrodynamic noise simulation. Intrinsic noise sources for the Y- and H- noise representations are examined and models of intrinsic noise sources are proposed. The relations between the Y- and H- noise representations for MOSFETs are examined, and the importance of correlation for both representations is quantified. The theoretical values of H- noise representation model parameters are derived for the first time for long channel devices. The H- noise representation correlation is shown theoretically to have a zero imaginary part. The H- noise representation has the inherent advantage of a more negligible correlation, which makes circuit design and simulation easier.

The H-representation noise sources are experimentally extracted using noise parameters measured on 0.25 μm RF CMOS devices. A simple yet effective model is proposed to model the H-representation noise sources as a function of bias. Excellent modeling results are achieved for all of the noise parameters up to 26 GHz, at all biases.

6.1 Introduction

Recent CMOS scaling has led to significant RF performance improvement. One of the major concerns is RF noise. A popular noise representation for MOSFET is the Y-representation, which describes the short-circuit input and output noise currents, i_g and i_d, as shown in Fig. 1.9 in section 1.4.1. For GaAs MESFETs and HEMTs, however, the H-representation is more popular, and is represented by the Pospieszalski model [27], as shown in Fig. 1.14 in section 1.4.2.

This chapter first investigates the RF noise performance of 50 nm L_{eff} CMOS transistors using hydrodynamic microscopic noise simulation [59]. The simulation results are then used to analyze the intrinsic noise sources for the Y- noise representation and the H- noise representation. This chapter will show that the Y- representation noise sources can be modeled using the Y-parameters, and the H-representation noise sources can be modeled using the H-parameters. We will also show that the correlation between noise sources has negligible impact on transistor noise parameters for both noise representations. This chapter further examines the relationships between MOSFET Y- and H- noise representations, and derives a set of theoretical equations for conversion between the two noise models described above. The theoretical values of H- representation model parameters are derived for the first time for long channel devices. The H- noise representation correlation is shown theoretically to have a zero imaginary part. We further show that the H- noise representation has the inherent advantage of a more negligible correlation for noise parameter modeling.

6.2 Technical Approach

The device structure is constructed based on reported 90 nm CMOS literature and the ITRS roadmap. DC $I-V$, y-parameters, and noise parameters are simulated using hydrodynamic transport models. The simulator used is DESSIS 9.0 from ISE [45]. The Lombardi surface mobility model and the default carrier energy relaxation time is used. The simulated $I-V$ and g_m characteristics are comparable to reported data on 90 nm CMOS devices with similar structures. The simulations are performed from 1 to 40 GHz. The transistor has a 70 nm poly gate length, a 50 nm metallurgical channel length, and an effective oxide thickness of 1.2 nm. The channel doping is retrograded from the surface toward the bulk, and halos are used for suppressing short channel effect. Due to a limitation of the simulator in handling terminal resistances during noise simulation, only the intrinsic device is simulated. The terminal resistances are then added to the intrinsic device through standard linear noise circuit analysis. The error introduced is quite small when compared to self-consistent mixed-mode device and circuit simulation results. The DESSIS simulation input deck and MATLAB Programming are given in Appendix C.

6.3 Simulation Results

6.3.1 DC $I - V$ Curves

Fig. 6.1 shows I_{DS} and g_m vs V_{gs} at V_{ds} = 1 V. $I_{D,sat}$ = 1341 μA/μm at V_{gs} = 1 V. Fig. 6.2 shows the output curves for V_{gs} = 0.1 – 1 V, with step of 0.1 V.

6.3.2 Noise Parameters

Fig. 6.3 shows NF_{min} simulated at 5 GHz versus I_{DS}. The simulation is performed for a 2 μm wide finger. The r_g value is estimated assuming double side gate contact, and a gate sheet resistance of 16 $\Omega/\Box$, which gives 40 Ω lateral resistance. We assume an additional 80 Ω for other gate resistance components. r_s=r_d=45 Ω for W = 2 μm is from the ITRS roadmap for 90 nm CMOS (which have L_{eff} between 50 and 70 nm) [60]. Experimental measurement of deep submicron CMOS noise has proven challenging, which is certainly the case for 90 nm CMOS processes with below 1 dB NF_{min}. The measured NF_{min} for an experimental 90 nm CMOS [8] is plotted for comparison. The simulated NF_{min} is still below measurement data. The electrical channel length difference between the simulated and experimental structures, models of mobility and microscopic noise source density, uncertainty in terminal resistances and other parasitics in the test structure could all contribute to the simulation-data discrepancy. We note

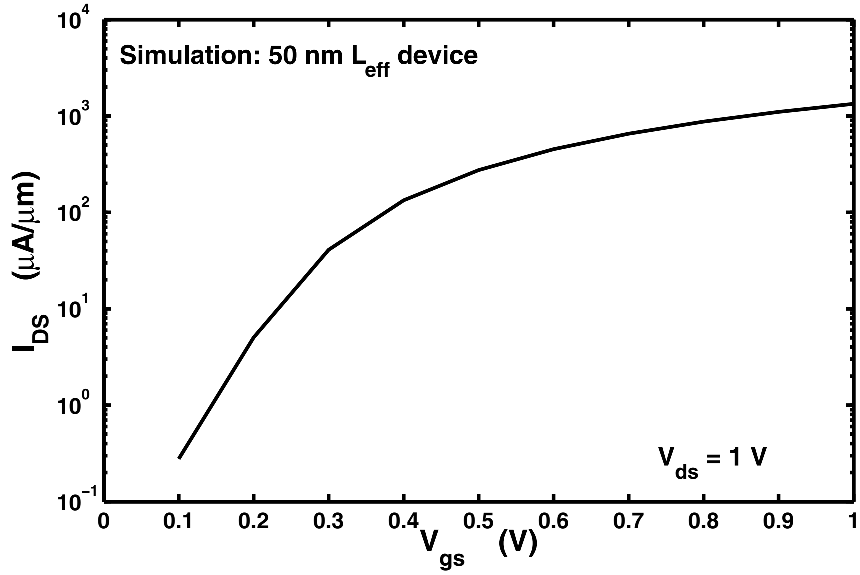

(a)

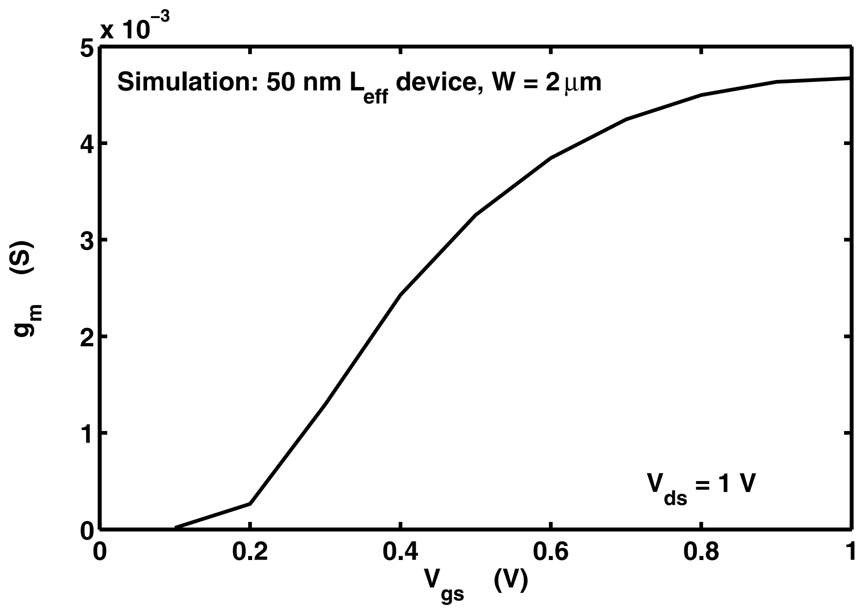

(b)

Figure 6.1: (a) I_{DS}, and (b) g_m vs V_{gs} at $V_{ds} = 1$ V.

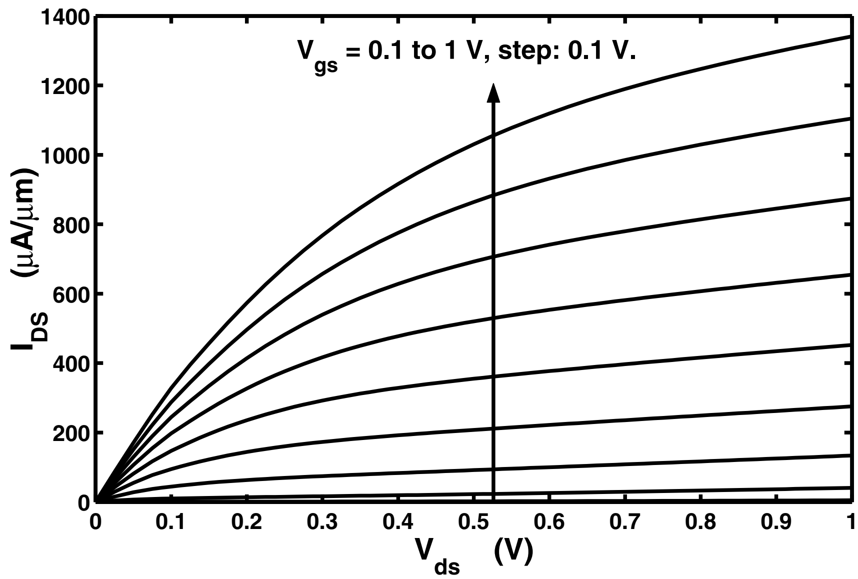

Figure 6.2: Output Curve

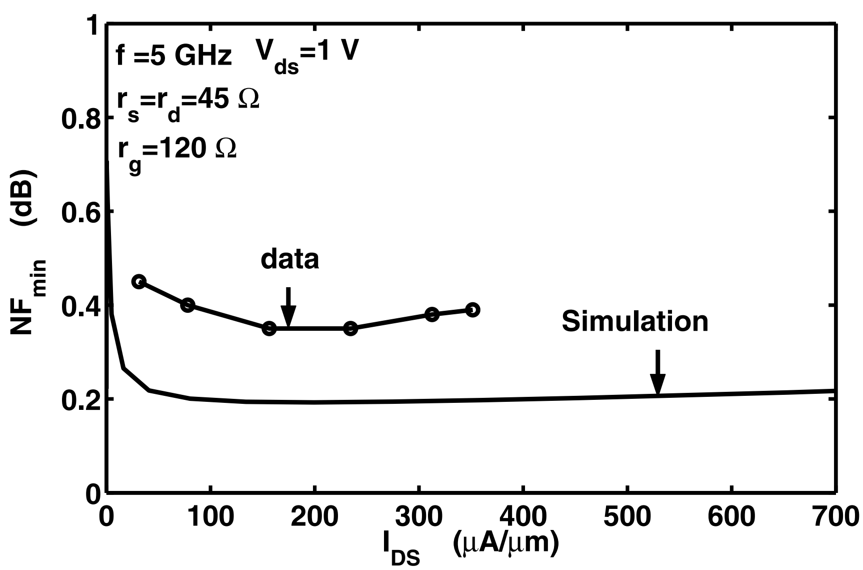

Figure 6.3: Simulation vs data reported in [8]: NF_{min} at 5 GHz vs I_{DS}.

that the measured NF_{min} is dependent on the number of gate fingers [8], which is not the case for an ideal transistor. This may be another source of data-simulation discrepancy.

According to Fig. 6.3, the minimum of NF_{min} occurs when I_{DS} is 100-200 μA/μm, which corresponds to moderate inversion operation, where the cutoff frequency f_T is rising rapidly and near the peak (Fig. 6.4). The overall I_{DS} dependence of NF_{min} is weak once moderate inversion occurs. For low-noise amplifiers, the combination of a low NF_{min} and a high f_T at low I_{DS} is desirable from a power consumption standpoint. Fig. 6.5 and Fig. 6.6 shows G_{opt} and B_{opt} at 5 GHz vs I_{DS} and Fig. 6.7 shows R_n at 5 GHz vs I_{DS}. Scaling enables high f_T in the moderate inversion region, and thus lower power CMOS LNA design.

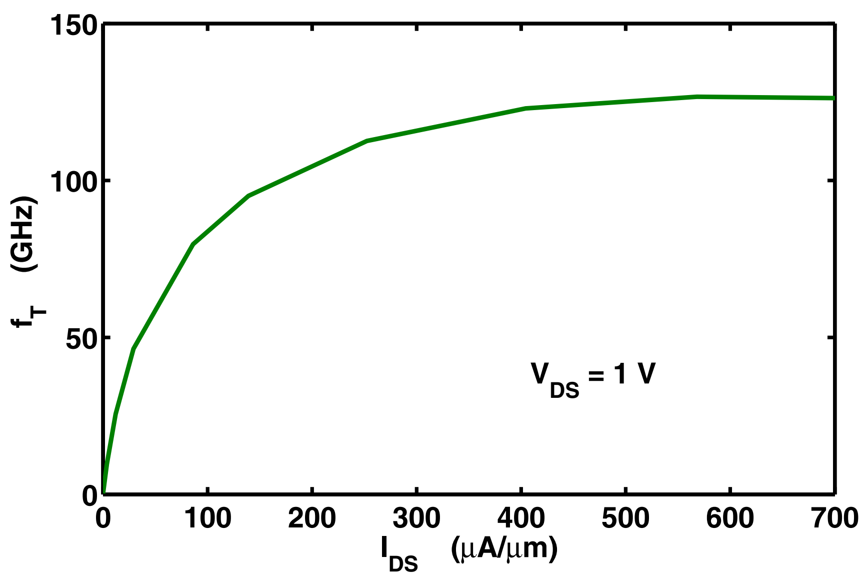

Figure 6.4: f_T vs I_{DS}.

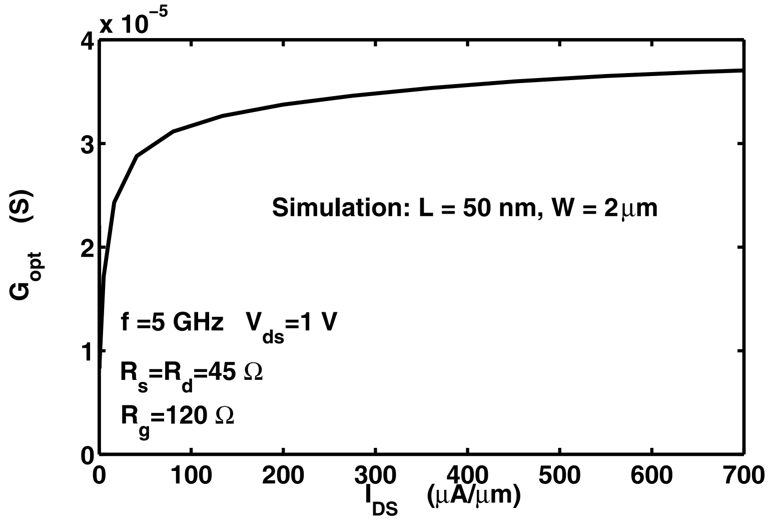

Figure 6.5: G_{opt} vs I_{DS}.

6.4 Intrinsic Noise Sources and Modeling

In general, two correlated noise sources are required to fully describe the noise behavior of any linear noisy two port. For each linear two port parameter set (e.g. Y, Z, H, and ABCD), there is a corresponding set of noise sources. The two noise sources (voltages, currents or a combination) are in general frequency and bias dependent.

6.4.1 Y-representation Noise Sources

We first consider the noise sources for the Y-parameter set, the gate and drain current noises. Fig. 6.8 shows S_{i_d,i_d^*} versus frequency. S_{i_d,i_d^*} is normalized by $4kTg_m$ as opposed to $4kTg_{d0}$, as it is more relevant for circuit design. S_{i_d,i_d^*} is nearly frequency independent for frequencies below f_T. At low I_{DS} where LNAs are biased, $S_{i_d,i_d^*}/4kTg_m$ is not too much greater than its long channel theoretical value $(2/3)$.

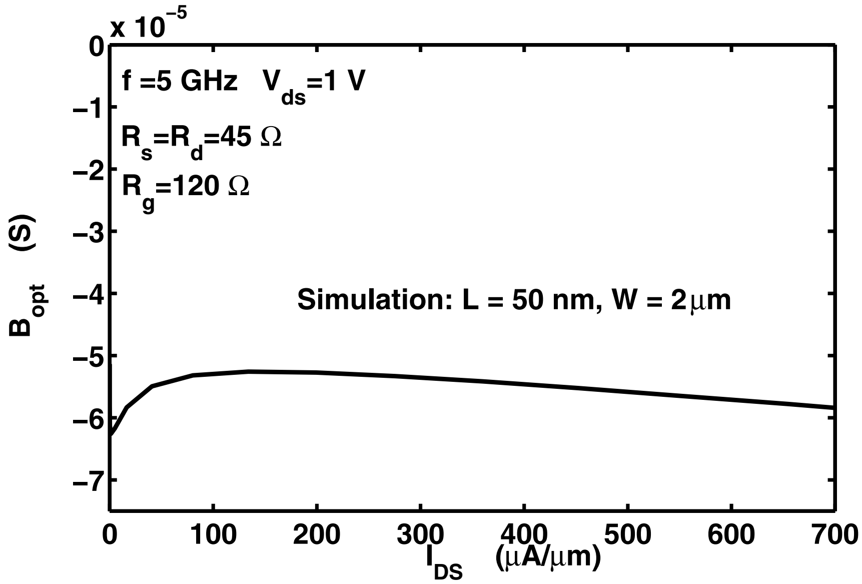

Figure 6.6: B_{opt} vs I_{DS}.

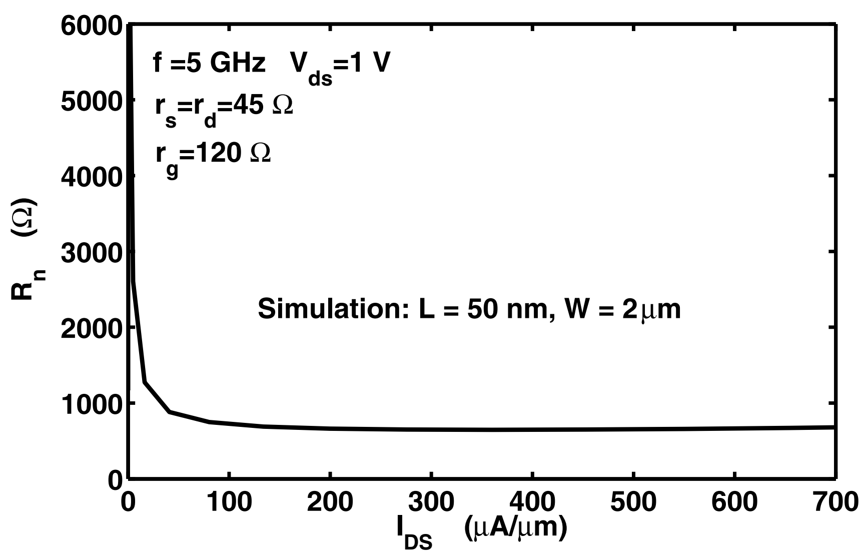

Figure 6.7: R_n vs I_{DS}.

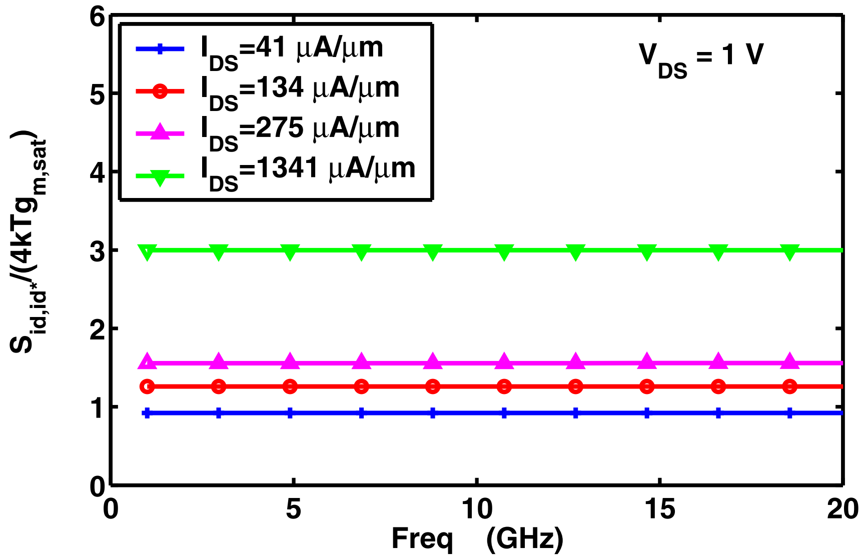

Figure 6.8: $S_{i_d,i_d^*}/[4kTg_m]$ vs frequency.

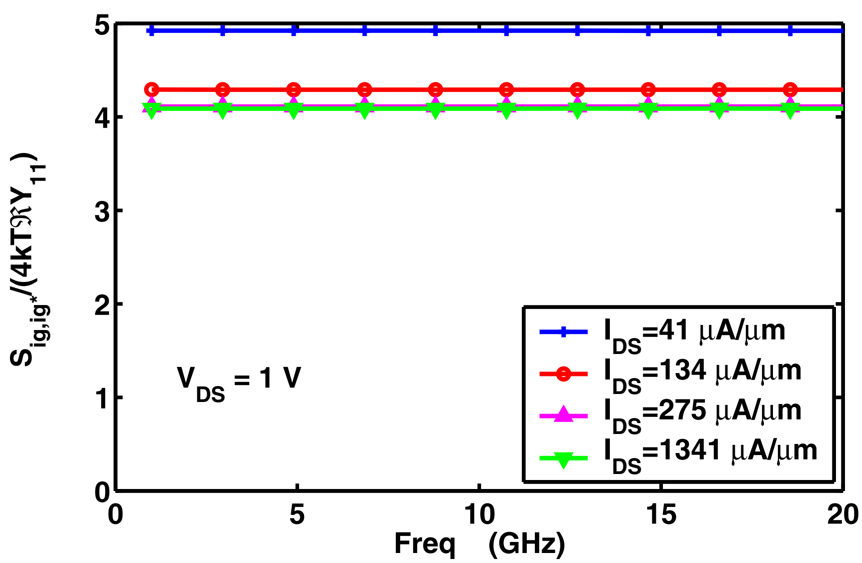

Figure 6.9: $S_{i_g,i_g^*}/[4kT\Re(Y_{11})]$ vs frequency.

Fig. 6.9 shows S_{i_g,i_g^*} normalized by $4kT\Re(Y_{11})$ versus frequency. $S_{i_g,i_g^*}/[4kT\Re(Y_{11})]$ is frequency independent, as found in long channel devices. The value of $S_{i_g,i_g^*}/[4kT\Re(Y_{11})]$ is close to 4 at lower I_{DS} of interest to LNAs.

The normalized correlation $c \equiv S_{i_g,i_d^*}/\sqrt{S_{i_g,i_g^*}S_{i_d,i_d^*}}$ shows a negligible real part, as found in long channel devices (Fig. 6.10). The imaginary part of c is nearly frequency independent.

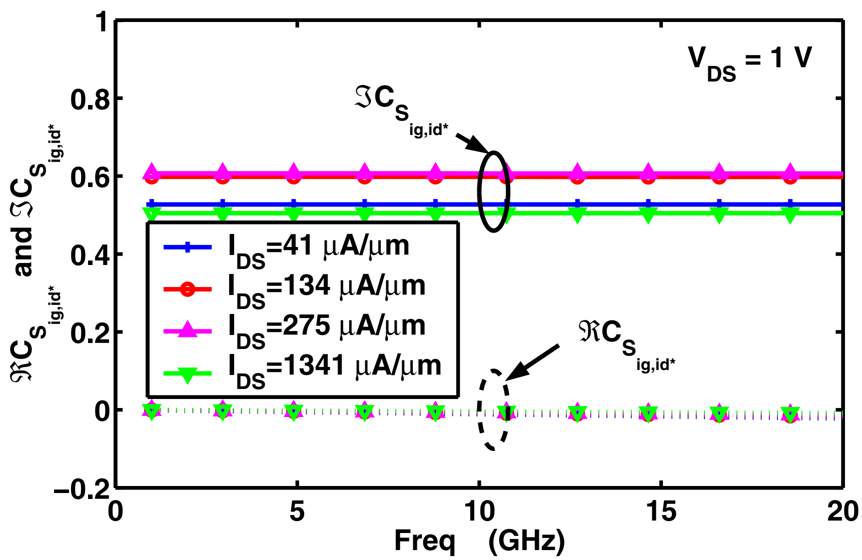

Figure 6.10: Normalized correlation c vs frequency.

A simplified yet accurate model for noise sources is desired for circuit design and circuit simulation. We have shown that S_{i_d,i_d^*} and S_{i_g,i_g^*} can be readily modeled using g_m and Y_{11} in these 50 nm L_{eff} devices, with simple coefficients that are constant for a given bias. The remaining question is the correlation, which cannot be handled by certain simulators like SPICE. This correlation can not be neglected for practical purposes in 50 nm L_{eff} CMOS. Figs. 6.11 and 6.12 show the NF_{min}, R_n and Y_{opt} simulated with and without the correlation. From 10 – 20 GHz, for all biases of interest, the difference between the noise parameters obtained with and without the correlation is noticeable except for R_n.

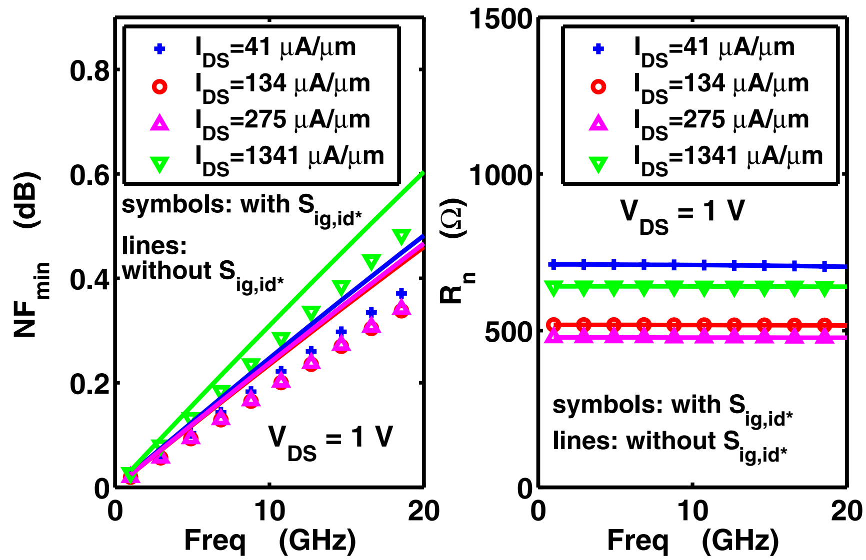

Figure 6.11: NF_{min} and R_n vs frequency, with and without correlation.

6.4.2 H-representation Noise Sources

A linear noisy two port can also be described using the H-parameter set, which involves an input noise voltage and an output noise current, which are denoted as v_h and i_h. Note that i_h is different from the i_d discussed above (the output noise current for Y-representation). Even though the H-representation was not given in the original noise representation standards [43], it has been successfully used for noise modeling of GaAs MESFETs and HEMTs. The Pospieszalski noise model [27] falls into this category, which further assumed that v_h and i_h are uncorrelated.

Through circuit analysis, we convert the noise sources from Y- noise representation to H-noise representation. Fig. 6.13 shows S_{v_h,v_h^*} versus frequency. In Pospieszalski's model, it was

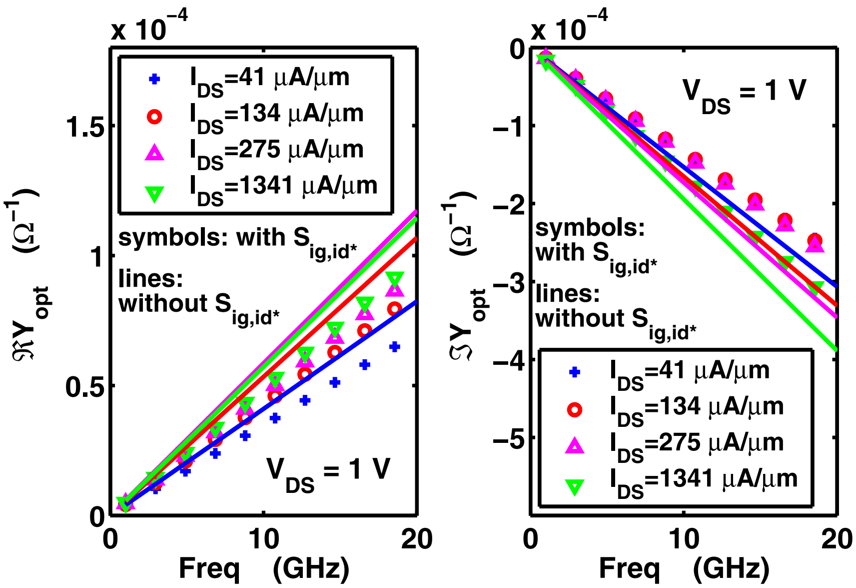

Figure 6.12: Y_{opt} vs frequency, with and without correlation.

assumed that S_{v_h,v_h^*} is proportional to the NQS channel resistance r_{nqs}, and therefore frequency independent. Note that S_{v_h,v_h^*} is frequency independent as shown in Fig. 6.13, which complies with the assumption in Pospieszalski's model.

S_{v_h,v_h^*} normalized by $4kT\Re(h_{11})$ is shown in Fig. 6.14. This provides a natural way of modeling S_{v_h,v_h^*} as long as the small signal model can correctly model h_{11}. We only need to model the $S_{v_h,v_h^*}/[4kT\Re(h_{11})]$ ratio, which is a constant for a given bias. $S_{v_h,v_h^*}/[4kT\Re(h_{11})] \approx 5$ at lower I_{DS}, and decreases with increasing I_{DS} as shown in Fig. 6.15.

Fig. 6.16 shows $S_{i_h,i_h^*}/[4kT\Re(g_m)]$ vs frequency, which is nearly frequency independent. Fig. 6.17 shows the correlation between v_h and i_h. Compared to the Y-representation, the correlation for the H-representation is much weaker for *all* of the biases and frequencies. In this

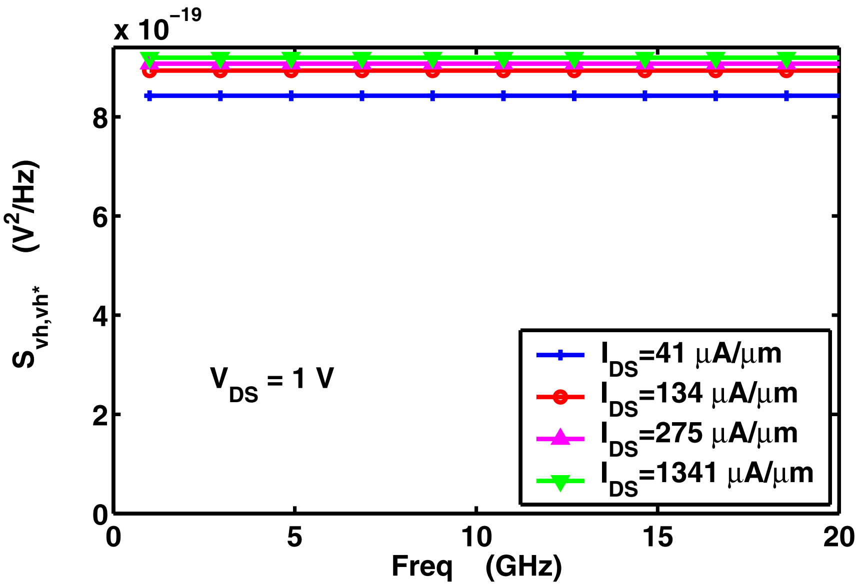

Figure 6.13: S_{v_h,v_h^*} vs frequency.

sense, the H-representation is a better choice, comparing to the correlation for Y-representation is large and non-negligible.

The NF_{min}, R_n and Y_{opt} are calculated with and without the correlation for comparison. For all practical purposes, the impact of the correlation on NF_{min}, R_n and $\Im(Y_{opt})$ is negligible, as shown in Figs. 6.18. The $\Re(Y_{opt})$ shows a visible but small sensitivity to the correlation. This suggests a new path to compact modeling of noise sources in 50 nm L_{eff} based on h_{11} and g_m. Only two parameters are needed for modeling noise at each bias, the ratio of $S_{v_h,v_h^*}/[4kT\Re(h_{11})]$.

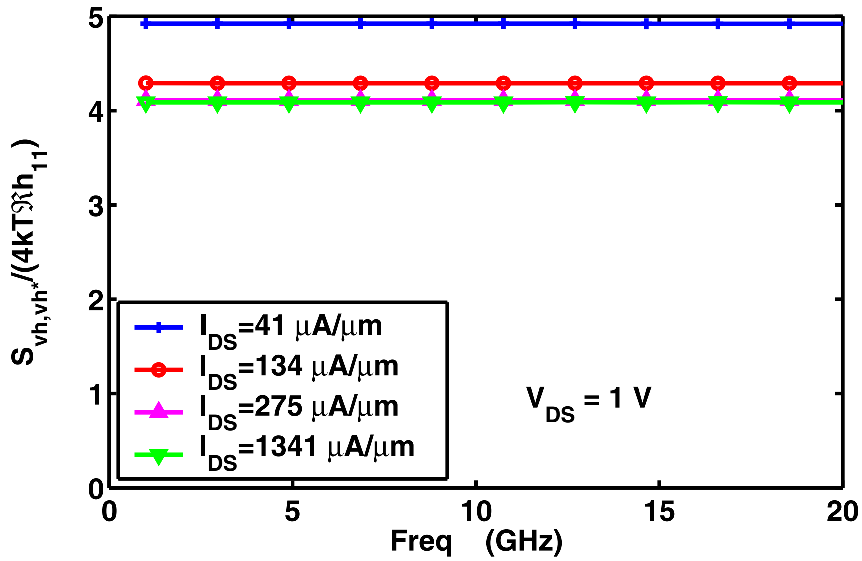

Figure 6.14: $S_{v_h,v_h^*}/[4kT\Re(h_{11})]$ vs frequency.

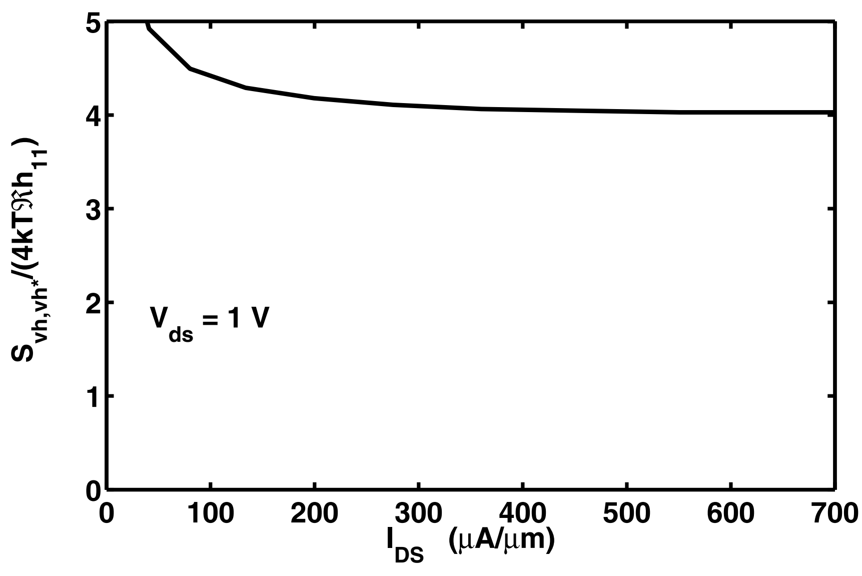

Figure 6.15: $S_{v_h,v_h^*}/[4kT\Re(h_{11})]$ vs I_{DS}.

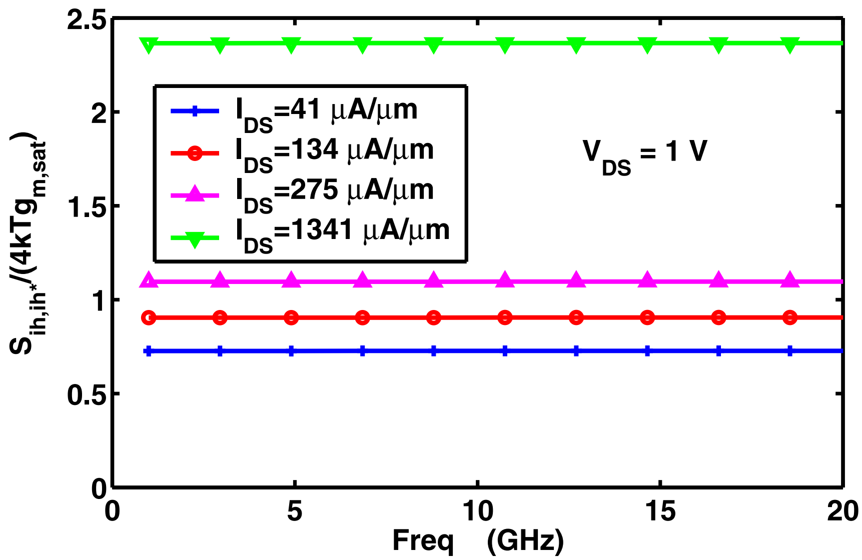

Figure 6.16: S_{i_h,i_h^*} vs frequency.

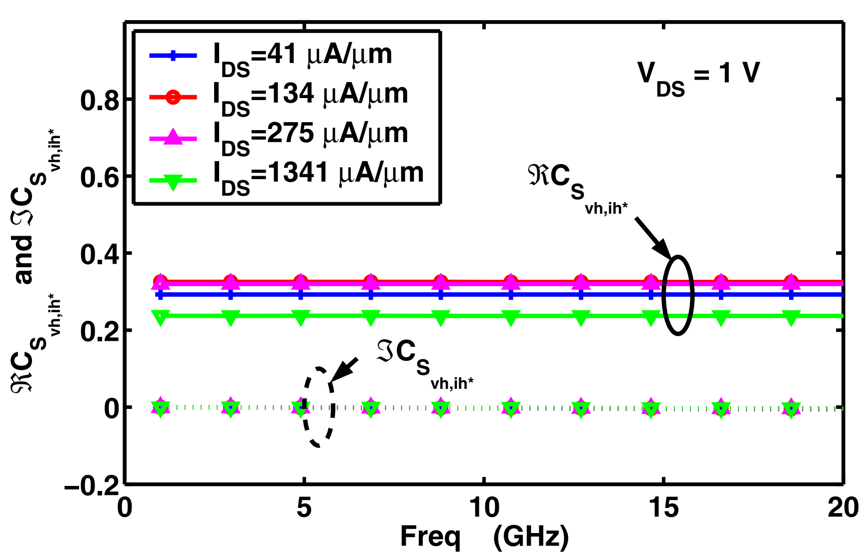

Figure 6.17: Correlation of H-representation noise sources vs frequency.

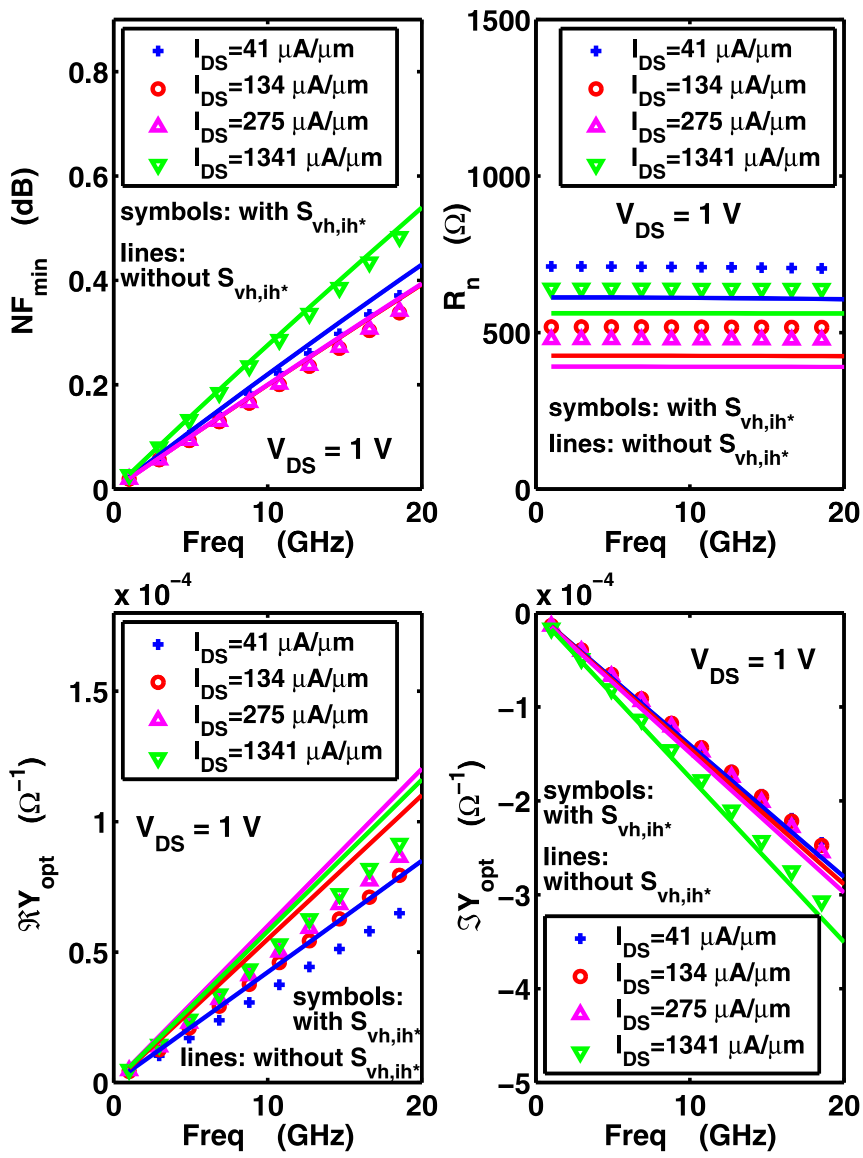

Figure 6.18: NF_{min}, R_n and Y_{opt} with and without correlation between v_h and i_h.

6.5 Relations Between Y- and H- Noise Representations in MOSFETs

As discussed above, the widely used van der Ziel model [15] describes i_g, i_d and their correlation for a MOSFET operated in the saturation region as:

$$S_{i_g,i_g^*} = 4kT\alpha_{i_g}\Re(Y_{11}), \tag{6.1}$$

$$S_{i_d,i_d^*} = 4kT\gamma_{i_d}g_m, \tag{6.2}$$

$$c_Y \triangleq \frac{S_{i_g,i_d^*}}{\sqrt{S_{i_g,i_g^*}S_{i_d,i_d^*}}} = y + jx, \tag{6.3}$$

where α_{i_g}, γ_{i_d}, and normalized correlation term c_Y are model parameters. Depending on preference, the zero V_{ds} output conductance g_{d0} is sometimes used instead of g_m in (6.2). For long channel devices, $\alpha_{i_g} = 4/3$, $\gamma_{i_d} = 2/3$, and $c_Y = j0.4$ ($y = 0$, $x = 0.4$). For short channel devices, these parameters become bias dependent and deviate from their long channel values, and there do not exist general expressions for these parameters. However, these parameters remain frequency independent, and the correlation c_Y remains imaginary only, or $y = 0$, because of the capacitive nature of the channel to gate coupling.

The H- noise representation describe the transistor noise with the An input noise voltage v_h and an output noise current i_h. Note that i_h is different from the i_d discussed above. Even though it has been argued in [61] and [62] that the H- noise representation is inherently unsuitable for MOSFETs, H- noise representation has been successfully applied the H-representation to noise modeling in 50 nm MOSFETs using DESSIS simulation, as discussed in previous section in this chapter [63]. The H- noise representation was further shown to have the advantage of having a negligible correlation term, which is significant for circuit design [63]. A model for v_h and i_h

was also proposed [63]:

$$S_{v_h,v_h^*} = 4kT\alpha_{v_h}\Re(h_{11}) \tag{6.4}$$

$$S_{i_h,i_h^*} = 4kT\gamma_{i_h}g_m \tag{6.5}$$

$$c_H \triangleq \frac{S_{v_h,i_h^*}}{\sqrt{S_{v_h,v_h^*}S_{i_h,i_h^*}}} = a + jb, \tag{6.6}$$

where α_{v_h}, γ_{i_h}, and c_H are bias dependent but frequency independent model parameters in general. It was also observed that c_H is largely real, and more negligible than c_Y for noise parameters. The reasons for the observations, however, were not understood.

6.5.1 Relations Between Y- and H- Noise Representation Coefficients

Consider the simplified small signal equivalent circuit in Fig. 6.19 for a MOSFET operating in saturation region. R_{gs} is the Non-Quasi-Static (NQS) channel resistance, which can be related to g_m through $R_{gs} = 1/(\psi g_m)$. $\psi = 5$ for long channel. An inspection of Fig. 6.19 shows $\Re(h_{11}) = R_{gs}$, where $\Re$ stands for taking the real part. The Y-parameter matrix is given by

$$Y = \begin{bmatrix} j\frac{\omega C_{gs}}{A} + \frac{\omega^2 C_{gs}^2 R_{gs}}{A} & 0 \\ g_m & 0 \end{bmatrix}, \tag{6.7}$$

where

$$A = 1 + \omega^2 C_{gs}^2 R_{gs}^2 = 1 + \left(\frac{\omega}{\psi\omega_T}\right)^2, \tag{6.8}$$

here $\omega_T = g_m/C_{gs}$. In practice, $\omega << \psi\omega_T$, thus $A \approx 1$ and

$$Y_{11} \approx \omega^2 C_{gs}^2 R_{gs} + j\omega C_{gs}. \tag{6.9}$$

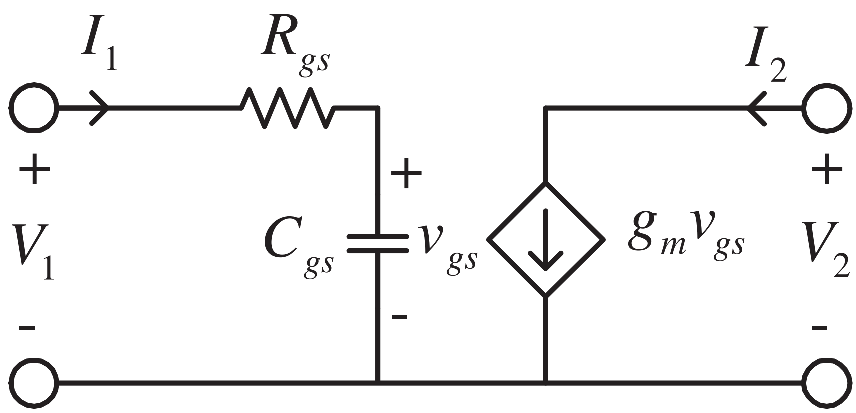

Figure 6.19: Small signal equivalent circuit for intrinsic MOSFET.

Substituting (6.9) into (6.1),

$$S_{i_g,i_g^*} = 4kT\theta_{i_g} g_m \left(\frac{\omega}{\omega_T}\right)^2, \tag{6.10}$$

where $\theta_{i_g} = \alpha_{i_g}/\psi$. With $R_{gs} = 1/(\psi g_m)$, (6.4) becomes:

$$S_{v_h,v_h^*} = 4kT\alpha_{v_h}\frac{1}{\psi g_m} = 4kT\theta_{v_h}\frac{1}{g_m}, \tag{6.11}$$

where $\theta_{v_h} = \alpha_{v_h}/\psi$.

Using two port noise circuit analysis, we have derived equations for conversions between the two representations. Substituting (6.7), and (6.1) – (6.3) into (2.69) – (2.71) in section 2.1.4, we have

$$
\begin{aligned}
S_{v_h,v_h^*} &= 4kT\theta\frac{1}{g_m}, && (6.12)\\
S_{i_h,i_h^*} &= 4kTg_m\left(\theta+\gamma_{i_d}-2x\sqrt{\theta\gamma_{i_d}}\right), && (6.13)\\
&= 4kT\gamma_{i_h}g_m,\\
S_{v_h,i_h^*} &= 4kT(\theta-x\sqrt{\theta\gamma_{i_d}})+jy\cdot 4kT\sqrt{\theta\gamma_{i_d}}. && (6.14)
\end{aligned}
$$

The normalized H-representation correlation c^H is defined by,

$$
\begin{aligned}
c_H &\triangleq \frac{S_{v_h,i_h^*}}{\sqrt{S_{v_h,v_h^*}S_{i_h,i_h^*}}} && (6.15)\\
&= a+jb, && (6.16)
\end{aligned}
$$

and a and b are obtained by,

$$
\begin{aligned}
a &= \Re(c_H) = \frac{\sqrt{\theta}-x\sqrt{\gamma_{i_d}}}{\sqrt{\theta+\gamma_{i_d}-2x\sqrt{\theta\gamma_{i_d}}}}, && (6.17)\\
b &= \Im(c_H) = y\cdot\frac{\sqrt{\gamma_{i_d}}}{\sqrt{\theta+\gamma_{i_d}-2x\sqrt{\theta\gamma_{i_d}}}}. && (6.18)
\end{aligned}
$$

Therefore given Y- noise representation model parameters α_{i_g}, γ_{i_d} and $c_Y = y + jx$, the H- noise representation model parameters are obtained as:

$$
\begin{aligned}
\alpha_{v_h} &= \alpha_{i_g}, && (6.19)\\
\gamma_{i_h} &= \theta_{i_g}+\gamma_{i_d}-2x\sqrt{\theta_{i_g}\gamma_{i_d}}, && (6.20)
\end{aligned}
$$

$$a = \frac{\sqrt{\theta_{i_g}} - x\sqrt{\gamma_{i_d}}}{\sqrt{\theta_{i_g} + \gamma_{i_d} - 2x\sqrt{\theta_{i_g}\gamma_{i_d}}}}, \tag{6.21}$$

$$b = \frac{y\sqrt{\gamma_{i_d}}}{\sqrt{\theta_{i_g} + \gamma_{i_d} - 2x\sqrt{\theta_{i_g}\gamma_{i_d}}}}. \tag{6.22}$$

Since y, the real part of c_Y, is 0 physically due to capacitive gate to channel coupling, $b = 0$, meaning that the corresponding *H- noise representation correlation is purely real*. As $\alpha_{i_g} = \alpha_{v_h}$, we have $\theta_{i_g} = \theta_{v_h}$. From now on, we will use α and θ for convenience.

For long channel device, $\alpha_{v_h} = 4/3$, $\gamma_{i_h} = 0.6$, which is less than $\gamma_{i_d} = 2/3$, $a = 0.2458$, which is smaller than $x = 0.4$, and $b = 0$.

Similarly, substituting (6.7), and (6.4) – (6.6) into (2.66) – (2.68) in section 2.1.4, we have,

$$S_{i_g,i_g^*} = \left(\frac{\omega}{\omega_T}\right)^2 \cdot 4kT\theta g_m \tag{6.23}$$

$$S_{i_d,i_d^*} = 4kTg_m\left(\gamma_{i_h} + \theta - 2a\sqrt{\gamma_{i_h}\theta}\right), \tag{6.24}$$

$$= 4kT\gamma_{i_d}g_m,$$

$$S_{i_g,i_d^*} = j\frac{\omega}{\omega_T} \cdot 4kT\theta g_m\left[\left(1 - a\sqrt{\frac{\gamma_{i_h}}{\theta}}\right) - jb\sqrt{\frac{\gamma_{i_h}}{\theta}}\right]. \tag{6.25}$$

The normalized correlation c_Y is obtained by,

$$c_Y \triangleq \frac{S_{i_g,i_d^*}}{\sqrt{S_{i_g,i_g^*}S_{i_d,i_d^*}}} \tag{6.26}$$

$$= y + jx, \tag{6.27}$$

and x and y are obtained by

$$x = \Im(c_Y) = \frac{\sqrt{\theta} - a\sqrt{\gamma^{ih}}}{\sqrt{\gamma^{ih} + \theta - 2a\sqrt{\gamma^{ih}\theta}}}, \tag{6.28}$$

$$y = \Re(c_Y) = b\frac{\sqrt{\gamma^{ih}}}{\sqrt{\gamma^{ih} + \theta - 2a\sqrt{\gamma^{ih}\theta}}}. \tag{6.29}$$

Therefore, given H- noise representation parameters, Y- noise representation parameters can be obtained by

$$\alpha_{i_g} = \alpha_{v_h}, \tag{6.30}$$

$$\gamma_{i_d} = \gamma_{i_h} + \theta - 2a\sqrt{\gamma_{i_h}\theta}, \tag{6.31}$$

$$x = \frac{\sqrt{\theta} - a\sqrt{\gamma_{i_h}}}{\sqrt{\gamma_{i_h} + \theta - 2a\sqrt{\gamma_{i_h}\theta}}}, \tag{6.32}$$

$$y = \frac{b\sqrt{\gamma_{i_h}}}{\sqrt{\gamma_{i_h} + \theta - 2a\sqrt{\gamma_{i_h}\theta}}}. \tag{6.33}$$

Even if $c_H = 0$ ($a = 0$, $b = 0$), meaning zero correlation for the H- noise representation, c_Y still has an imaginary part according to (6.32) and (6.33)

$$c_Y|_{c_H=0} = y + jx = j\sqrt{\frac{\theta}{\gamma_{i_h} + \theta}}. \tag{6.34}$$

6.5.2 Noise Parameters

We now examine the importance of correlation for noise parameter modeling, for Y- and H- noise representations. The minimum noise figure NF_{min}, the noise resistance R_n, the real and imaginary part of the optimal source admittance G_{opt} and B_{opt}, are directly determined by the chain noise representation parameters S_{v_a,v_a^*}, S_{i_a,i_a^*} and S_{i_a,v_a^*} [11]. We now derive the chain noise parameters S_{v_a,v_a^*}, S_{i_a,i_a^*} and S_{i_a,v_a^*} using Y- and H- noise representation model parameters.

Substituting (6.1) - (6.3) into (2.43), (2.44), and (2.45) in section 2.1.2, the chain noise parameters S_{v_a,v_a^*}, S_{i_a,i_a^*} and S_{i_a,v_a^*} can be obtained using Y-representation model parameters by

$$S_{v_a,v_a^*} = \frac{1}{|Y_{21}|^2} S_{i_d,i_d^*}, \tag{6.35}$$

$$= 4kT \frac{1}{g_m} \gamma_{i_d}, \tag{6.36}$$

$$S_{i_a,i_a^*} = S_{i_g,i_g^*} + \left| \frac{Y_{11}}{Y_{21}} \right|^2 S_{i_d,i_d^*} - 2\Re \left(\frac{Y_{11}^*}{Y_{21}^*} S_{i_g,i_d^*} \right), \tag{6.37}$$

$$= 4kT g_m \left(\frac{\omega}{\omega_T} \right)^2 \left(\gamma_{i_d} + \theta - 2x\sqrt{\gamma_{i_d}\theta} \right), \tag{6.38}$$

$$S_{i_a,v_a^*} = \frac{Y_{11}}{|Y_{21}|^2} S_{i_d,i_d^*} - \frac{1}{Y_{21}^*} S_{i_g,i_d^*}, \tag{6.39}$$

$$= j4kT \frac{\omega}{\omega_T} \left(\gamma_{i_d} - x\sqrt{\gamma_{i_d}\theta} \right). \tag{6.40}$$

Substituting (6.30) - (6.33) into (6.36), (6.38), and (6.40), the chain noise parameters S_{v_a,v_a^*}, S_{i_a,i_a^*} and S_{i_a,v_a^*} can be obtained using H-representation model parameters as well

$$S_{v_a,v_a^*} = 4kT \frac{1}{g_m} \left(\gamma_{i_h} + \theta - 2a\sqrt{\gamma_{i_h}\theta} \right), \tag{6.41}$$

$$S_{i_a,i_a^*} = 4kT g_m \left(\frac{\omega}{\omega_T} \right)^2 \gamma_{i_h}, \tag{6.42}$$

$$S_{i_a,v_a^*} = j4kT \frac{\omega}{\omega_T} \left(\gamma_{i_h} - a\sqrt{\gamma_{i_h}\theta} \right). \tag{6.43}$$

Substituting (6.36), (6.38), and (6.40) in (2.24) – (8.19) in section 2.1.1, the minimum noise figure NF_{min}, the noise resistance R_n, the real and imaginary part of the optimal source admittance G_{opt} and B_{opt}, are derived using Y- noise representation coefficients θ, γ_{i_d}, and x,

$$NF_{min} = 10\log_{10}\left(1 + 2\frac{\omega}{\omega_T}\sqrt{(1-x^2)\gamma_{i_d}\theta}\right), \tag{6.44}$$

$$R_n = \frac{\gamma_{i_d}}{g_m}, \tag{6.45}$$

$$G_{opt} = g_m\frac{\omega}{\omega_T}\sqrt{(1-x^2)\frac{\theta}{\gamma_{i_d}}}, \tag{6.46}$$

$$B_{opt} = -g_m\frac{\omega}{\omega_T}\frac{\gamma_{i_d} - x\sqrt{\theta\gamma_{i_d}}}{\gamma^{id}}. \tag{6.47}$$

Substituting (6.41), (6.42), and (6.43) in (2.24) – (8.19) in section 2.1.1, NF_{min}, R_n, G_{opt} and B_{opt} are also derived using H- noise representation coefficients θ, γ_{i_h}, and a,

$$NF_{min} = 10\log_{10}\left(1 + 2\frac{\omega}{\omega_T}\sqrt{(1-a^2)\gamma_{i_h}\theta}\right). \tag{6.48}$$

$$R_n = \frac{\gamma_{i_h} + \theta - 2a\sqrt{\gamma_{i_h}\theta}}{g_m}, \tag{6.49}$$

$$G_{opt} = g_m\frac{\omega}{\omega_T}\frac{\sqrt{(1-a^2)\gamma_{i_h}\theta}}{\gamma^{ih} + \theta - 2a\sqrt{\gamma_{i_h}\theta}}, \tag{6.50}$$

$$B_{opt} = -g_m\frac{\omega}{\omega_T}\frac{\gamma_{i_h} - a\sqrt{\theta\gamma_{i_h}}}{\gamma^{ih} + \theta - 2a\sqrt{\gamma_{i_h}\theta}}. \tag{6.51}$$

6.6 Importance of Correlations

We now examine the importance of Y- and H- noise representation correlations to noise parameters NF_{min}, R_n, G_{opt} and B_{opt}. By neglecting c_Y or c_H, (6.44) and (6.48) reduce to

$$NF_{min}|_{c_Y=0} = 10\log_{10}\left(1 + 2\frac{\omega}{\omega_T}\sqrt{\gamma_{i_d}\theta}\right), \tag{6.52}$$

$$NF_{min}|_{c_H=0} = 10\log_{10}\left(1 + 2\frac{\omega}{\omega_T}\sqrt{\gamma_{i_h}\theta}\right). \tag{6.53}$$

Neglecting the correlation term will cause overestimation of NF_{min} for both Y- and H-representation. Since

$$x^2\gamma_{i_d}\theta - a^2\gamma_{i_h}\theta = (\gamma_{i_d} - \gamma_{i_h})\theta, \tag{6.54}$$

and γ_{i_d} is normally greater than γ_{i_h}, c_H is more negligible than c_Y for NF_{min}.

By neglecting c_Y or c_H, (6.45) and (6.49) reduce to

$$R_n|_{c_Y=0} = R_n, \tag{6.55}$$

$$R_n|_{c_H=0} = \frac{\gamma_{i_h} + \theta}{g_m}. \tag{6.56}$$

R_n does not change when neglecting c_Y, i.e., $R_n|_{x=0} = R_n$. An inspection of (6.31) shows that $\gamma_{i_h} + \theta - \gamma_{i_d} = 2a\sqrt{\gamma_{ih}\theta}$. Normally $a > 0$, hence $R_n|_{c_H=0} > R_n$, therefore neglecting c_H will overestimate R_n.

By neglecting c_Y or c_H, (6.46) and (6.50) reduce to

$$G_{opt}|_{x=0} = g_m\frac{\omega}{\omega_T}\sqrt{\frac{\theta}{\gamma_{i_d}}}, \tag{6.57}$$

$$G_{opt}|_{a=0} = g_m\frac{\omega}{\omega_T}\frac{\sqrt{\gamma_{i_h}\theta}}{\gamma_{i_h} + \theta}. \tag{6.58}$$

$G_{opt}|_{x=0}$ overestimates G_{opt}. Since

$$\frac{G_{opt}|_{x=0}}{G_{opt}|_{a=0}} = \frac{\gamma_{i_h} + \theta}{\sqrt{\gamma_{i_h}(\gamma_{i_h} + \theta - 2a\sqrt{\gamma_{i_h}\theta})}}, \tag{6.59}$$

and,

$$(\gamma_{i_h}+\theta)^2-[\gamma_{i_h}(\gamma_{i_h}+\theta-2a\sqrt{\gamma_{i_h}\theta})]=\theta^2+\theta\gamma_{i_h}+2a\gamma_{i_h}\sqrt{\gamma_{i_h}\theta}, \tag{6.60}$$

$$>0, \tag{6.61}$$

we conclude that $G_{opt}|_{x=0} > G_{opt}|_{a=0}$. However, it is hard to determine the relationship between $G_{opt}|_{a=0}$ and G_{opt} theoretically.

By neglecting c_Y or c_H, (6.47) and (6.51) reduce to

$$B_{opt}|_{x=0} = -g_m\frac{\omega}{\omega_T}, \tag{6.62}$$

$$B_{opt}|_{a=0} = -g_m\frac{\omega}{\omega_T}\frac{\gamma_{i_h}}{\gamma_{i_h}+\theta}. \tag{6.63}$$

An inspection of (6.47), (6.62) shows that $B_{opt}|_{x=0}$ underestimates B_{opt}. Moreover, an inspection of (6.62) and (6.63) shows that $B_{opt}|_{x=0} < B_{opt}|_{a=0}$. Comparing (6.51) and (6.63), we found that

$$B_{opt}|_{a=0} - B_{opt} = \frac{a(\gamma_{i_h}-\theta)\sqrt{\gamma_{i_h}\theta}}{(\gamma_{i_h}+\theta)(\gamma_{i_h}+\theta-2a\sqrt{\gamma_{i_h}\theta})}. \tag{6.64}$$

Therefore the difference between $B_{opt}|_{a=0}$ and B_{opt} determined by $\gamma_{i_h}-\theta$.

It is sufficient to simply define the induced errors by neglecting c_Y and c_H for NF_{min}, R_n, G_{opt} and B_{opt} to discuss the importance of Y- and H- noise representation correlations to the noise parameters. Since NF_{min} is already in dB, we define the induced error of neglecting Y- and H- noise presentation correlations c_Y and c_H for NF_{min} as

$$\Delta NF_{min}|_{c_{Y/H}=0} = NF_{min}|_{c_{Y/H}=0} - NF_{min}. \tag{6.65}$$

ΔNF_{min} is both frequency and bias dependent. ΔR_n, the induced error of neglecting c_Y and c_H for R_n, is defined as,

$$\Delta R_n|_{c_{Y/H}=0} = R_n|_{c_{Y/H}=0} - R_n. \tag{6.66}$$

An inspection of (6.45), (6.49) and (6.66) shows that the error percentage term $\Delta R_n/R_n$ does not depend on frequency. Similarly, ΔG_{opt} and ΔB_{opt}, the induced errors of neglecting c_Y and c_H for G_{opt} and B_{opt}, are defined as,

$$\Delta G_{opt}|_{c_{Y/H}=0} = G_{opt}|_{c_{Y/H}=0} - G_{opt}, \tag{6.67}$$

$$\Delta B_{opt}|_{c_{Y/H}=0} = B_{opt}|_{c_{Y/H}=0} - B_{opt}. \tag{6.68}$$

An inspection of (6.46) and (6.47) shows that the error percentage terms $\Delta G_{opt}/G_{opt}$ and $\Delta B_{opt}/B_{opt}$ do not depend on frequency, although G_{opt} and B_{opt} are proportional to frequency.

We now consider the 50 nm L_{eff} NMOS intrinsic device used in this chapter [63]. The small signal MOSFET model parameters are extracted, and used for deembedding to obtain the noise parameters of the intrinsic MOSFET shown in Fig. 6.19. Model parameters for both representations are extracted and used to verify the analytical conversion equations derived.

Fig. 6.20 quantifies the importance of c_H and c_Y to $NF_{min}$by plotting ΔNF_{min} vs frequency for both representations. I_{DS} = 41, 134, 275 and 1341 μA/μm are used, which covers the whole bias range of interest. With increasing I_{DS}, α decreases from 4.83 to 4.07, ψ decreases from 6.81 to 4.76, θ increases from 0.71 to 0.86, and γ_{i_d} increases from 0.86 to 2.86. The correlation term x ranges from 0.52 to 0.63. Accordingly, a decreases from 0.4 to 0.04, indicating c_H becomes more negligible as bias increases. γ_{i_h} increases from 0.70 to 2.08. For all biases and frequencies of interest, neglecting c_H results in little error in NF_{min} for all the biases and frequencies.

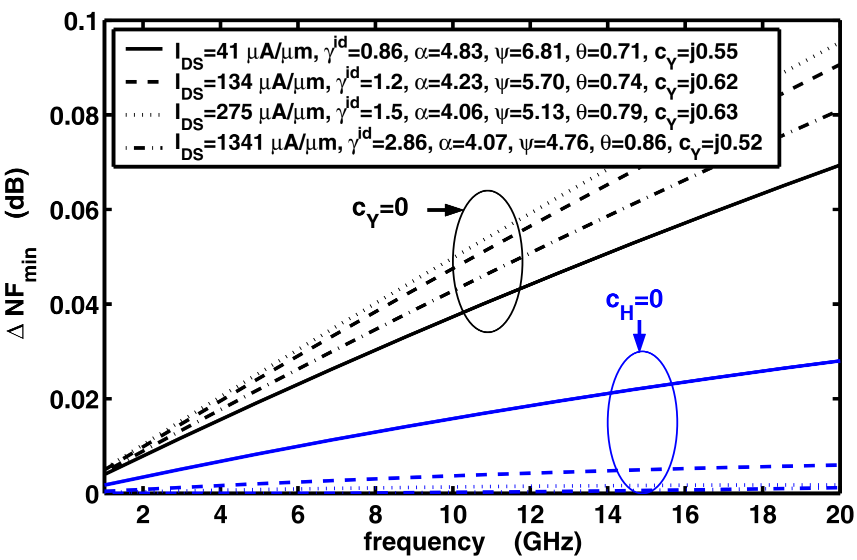

Figure 6.20: Importance of H- and Y- noise representation correlations: ΔNF_{min} vs frequency for 50nm NMOS.

Since R_n does not change with frequency, Fig. 6.21 quantifies the importance of c_H and c_Y to R_n by plotting the error percentage term $\Delta R_n/R_n$ vs I_{DS} for both representations at 5 GHz. An inspection of (6.45) shows that neglecting c_Y has no change on R_n, i.e., $\Delta R_n|_{c_Y=0}/R_n = 0$, as shown Fig. 6.21. Therefore, Y-noise representation is a better choice for R_n. $\Delta R_n|_{c_H=0}/R_n >$ 1, indicates that neglecting c_H overestimates R_n. Moreover $\Delta R_n|_{c_H=0}/R_n$ decreases as bias increases. It shows that c_H is still negligible at higher biases for R_n.

Similarly, Fig. 6.22 and Fig. 6.23 quantify the importance of c_H and c_Y to G_{opt} and B_{opt} by plotting the error percentage terms $\Delta G_{opt}/G_{opt}$ and $\Delta B_{opt}/B_{opt}$ vs I_{DS} for both representations.

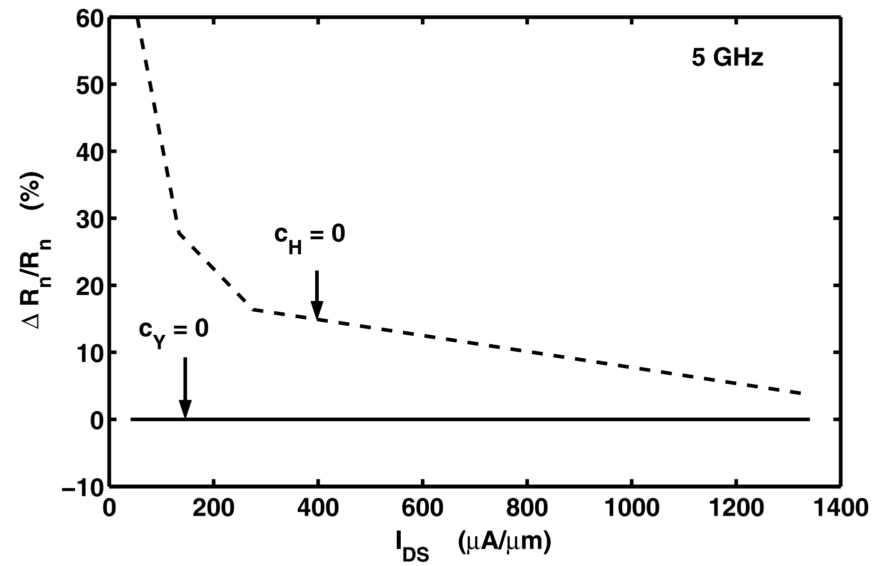

Figure 6.21: Importance of H- and Y- noise representation correlations: $\Delta R_n/R_n$ vs I_{DS} for 50nm NMOS.

Frequency is 5 GHz. Fig. 6.22 shows that c_Y is not negligible for all biases for G_{opt}. c_H becomes negligible as bias increases. At bias of interest $I_{DS} = 400$ μA/μm, the induced error for neglecting c_H is around 10%. Therefore, H- noise representation is still a good choice at higher biases for G_{opt}. Fig. 6.23 shows that the induced error for neglecting c_H is practically zero for all biases. Therefore H- noise representation is a better choice for B_{opt}.

6.7 Extraction and Modeling of H-Representation RF Noise Sources in CMOS

It has been shown using microscopic noise simulation and simple equivalent circuit derivation that the H-representation provides certain advantages such as frequency independent noise sources and negligible correlation [63], thus making easier noise analysis for circuit designers and noise modeling for device modelers. In this section, we present experimental extraction and

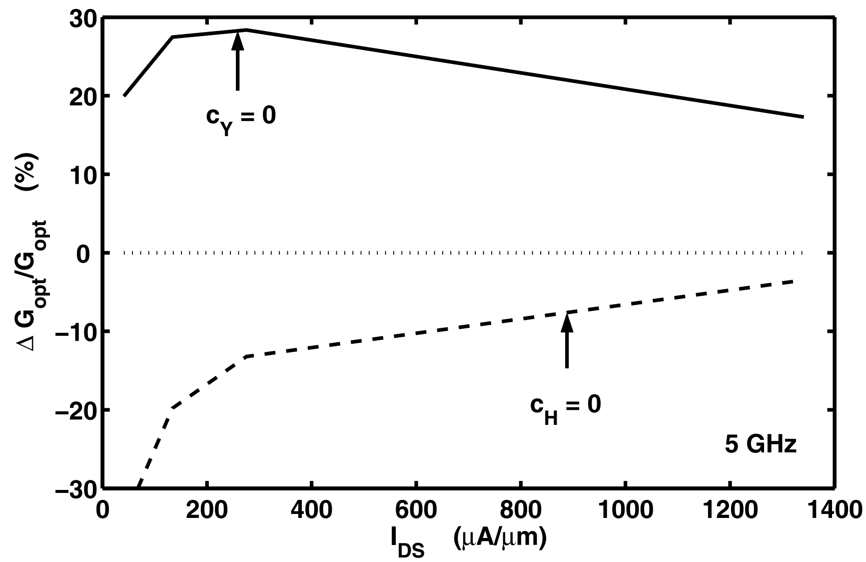

Figure 6.22: Importance of H- and Y- noise representation correlations: $\Delta G_{opt}/G_{opt}$ vs I_{DS} for 50nm NMOS.

modeling of the H-representation noise sources in a 0.25 μm RF CMOS process. This section will show that the extracted input noise voltage and output noise current can be successfully modeled as simple functions of the channel resistance and transconductance respectively. The parameters of these functions can be related to the biasing current and voltage in a straightforward manner. The new model yields excellent agreement with measured noise data, for all of the noise parameters, including NF_{min}, Y_{opt}, and R_n, from 2 – 26 GHz, across a wide bias range.

6.7.1 Experimental Extraction

Noise parameters are measured on wafer from 2–26 GHz, using an ATN NP5 system. Open and short de-embedding are performed for both Y-parameters and noise parameters to move

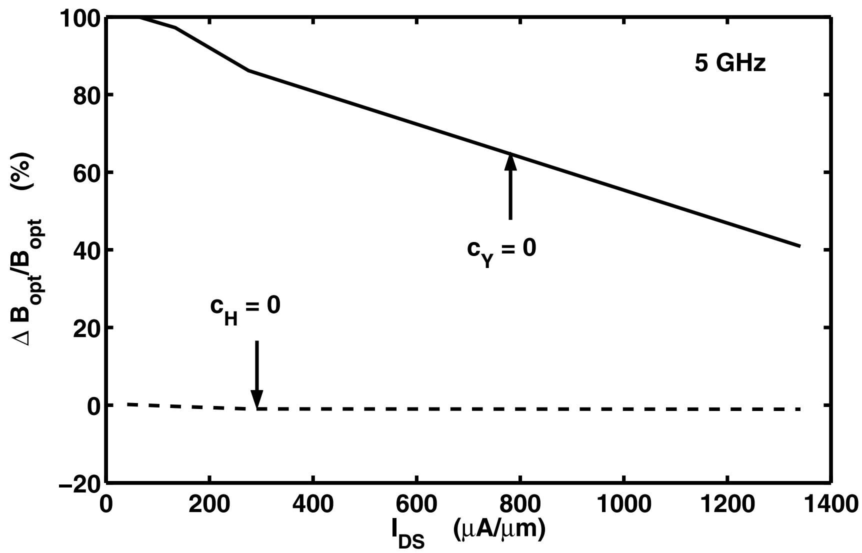

Figure 6.23: Importance of H- and Y- noise representation correlations: $\Delta B_{opt}/B_{opt}$ vs I_{DS} for 50nm NMOS.

the reference plane to the device terminals using techniques in section 2.4. The resulting Y-parameters and noise parameters are for the transistor, the equivalent circuit of which is shown in Fig. 6.24. The equivalent circuit parameters are extracted using the method described in [9]. Here we choose to define v_h and i_h as the H-representation input noise voltage and output noise current for the level II block shown in Fig. 6.24. The level II block consists of $R_g s$, C_{gs}, the g_m controlled source and $g_d s$, and is the core part for noise modeling. The level I block is defined as the combination of the level II block with C_{gd}, R_{gd}, C_{db} and R_{db}. Next we need to extract the power spectral densities (PSD) of v_h, i_h, and their correlation, which we denote as $S^{II}_{v_h,v_h^*}$, $S^{II}_{i_h,i_h^*}$, and $S^{II}_{v_h,i_h^*}$. They can also be written using matrix notation as:

$$C_{H_{II}} \triangleq \begin{bmatrix} S^{II}_{v_h,v_h^*} & S^{II}_{v_h,i_h^*} \\ S^{II}_{i_h,v_h^*} & S^{II}_{i_h,i_h^*} \end{bmatrix}, \tag{6.69}$$

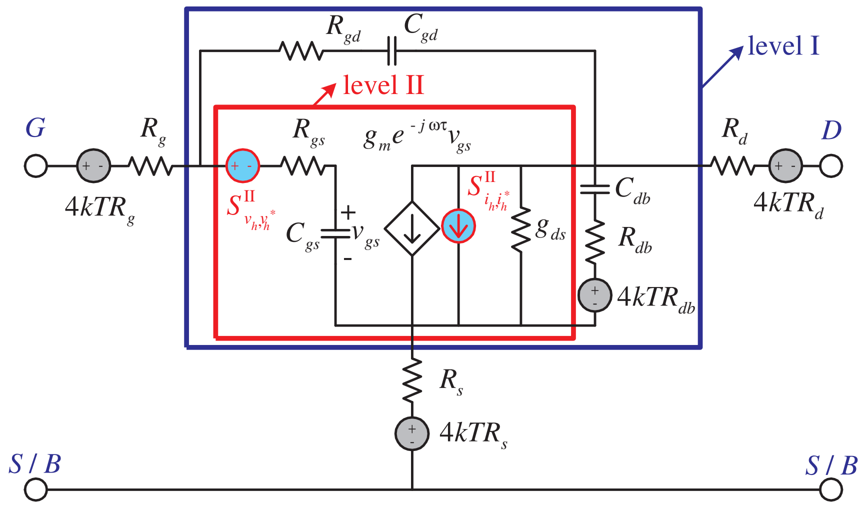

Figure 6.24: The small signal equivalent circuit model used with H-representation noise sources.

where $C_{H_{II}}$ is also referred to as the H-representation noise matrix for the level II block.

The Y- noise representation parameters matrix for block II, $C_{Y_{II}}$, with elements $S^{II}_{i_g,i_g^*}$, $S^{II}_{i_d,i_d^*}$, and $S^{II}_{i_g,i_d^*}$, are obtained using techniques in section 2.5.1. Next, we transform Y- noise representation matrix $C_{Y_{II}}$ to H- noise representation matrix $C_{H_{II}}$ using transform matrix in Table 2.1:

$$C_{H_{II}} = T_{Y-H} \cdot C_{Y_{II}} \cdot T^{\dagger}_{Y-H} \tag{6.70}$$

$$T_{Y-H} = \begin{bmatrix} -h^{II}_{11} & 0 \\ -h^{II}_{21} & 1 \end{bmatrix}. \tag{6.71}$$

6.7.2 Noise Source Modeling

The above extraction is applied to a 128 finger device from a 0.25 μm RF CMOS process measured in IBM. The designed length is 0.24 μm. The device width is W = 4 μm to minimize gate resistance. Fig. 6.25 shows the measured and modeled Y-parameters versus frequency at

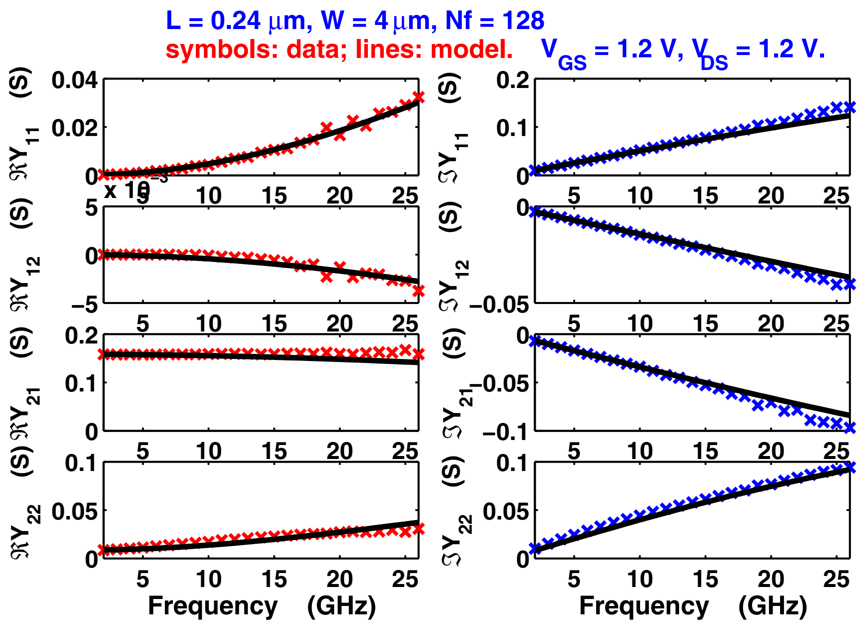

Figure 6.25: Data-model comparison of Y-parameter vs frequency at $V_{GS} = 1.2$ V. $V_{DS} = 1.2$ V.

$V_{GS} = 1.2$ V and $V_{DS} = 1.2$ V. All of the Y-parameters are well modeled. Fig. 6.26 shows the Y-parameters at 10 GHz as a function of V_{GS}. The biasing current dependence is well modeled too.

Using the equivalent circuit parameters extracted, the Y-parameters and H-parameters for all the blocks can be calculated using straightforward linear circuit analysis. The H-representation noise matrix is then extracted using the procedures described in section 6.7.1. Fig. 6.27 shows the extracted S_{v_h,v_h^*} and S_{i_h,i_h^*} as a function of frequency. $V_{GS} = 1.2$ V, and $V_{DS} = 1.2$ V. For modeling purpose, we have normalized $S^{II}_{v_h,v_h^*}$ by $4kTR_{gs}$, and normalized $S^{II}_{i_h,i_h^*}$ by $4kTg_m$. Observe that S_{v_h,v_h^*} and S_{i_h,i_h^*} are both frequency *independent*, which simplifies modeling. Thus, for a given bias, we can define two coefficients α and β as follows:

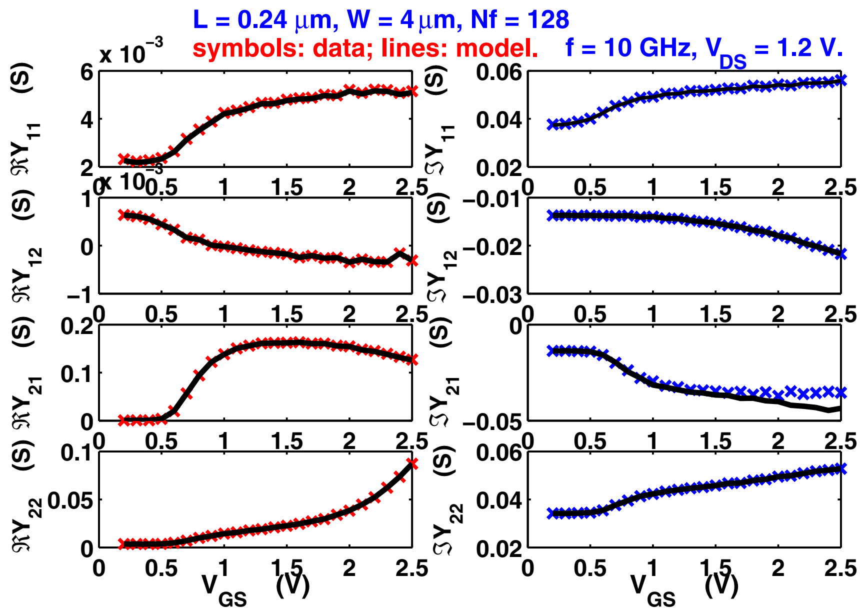

Figure 6.26: Data-model comparison of Y-parameter at $f = 10$ GHz. $V_{DS} = 1.2$ V.

$$S^{II}_{v_h,v_h^*} \stackrel{\triangle}{=} 4kT\alpha R_{gs}, \tag{6.72}$$

$$S^{II}_{i_h,i_h^*} \stackrel{\triangle}{=} 4kT\gamma_{i_h} g_m, \tag{6.73}$$

where we express S_{v_h,v_h^*} using R_{gs}, and S_{i_h,i_h^*} using g_m. The α and γ_{i_h} coefficients can then be extracted for each bias, and modeled as a function of bias, as detailed below.

Fig. 6.28 shows real and imaginary parts of the correlation. The normalized correlation coefficient is plotted. The normalized correlation coefficient is defined by $C^{II}_{v_h,i_h*} \stackrel{\triangle}{=} S^{II}_{v_h,i_h^*}/\sqrt{S^{II}_{v_h,v_h^*} S^{II}_{i_h,i_h^*}}$. Overall, the correlation is small. We have compared the noise parameters calculated with and

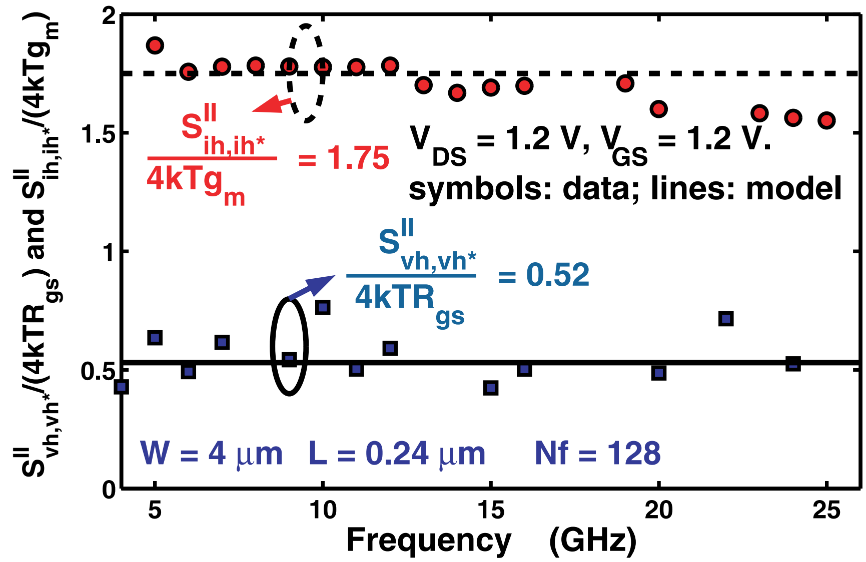

Figure 6.27: $S^{II}_{v_h,v_h^*}/(4kTR_{gs})$ and $S^{II}_{i_h,i_h^*}/(4kTg_m)$ (symbols) vs frequency. V_{GS} = 1.2 V. V_{DS} = 1.2 V.

without the correlation, and observed negligible difference. This is consistent with previous microscopic noise simulation results [63]. We will thus neglect the correlation in the discussions that follow.

Fig. 6.29 (a) shows the modeled and extracted NF_{min} and R_n at V_{GS} = 1.2 V and V_{DS} =1.2 V. Fig. 6.29 (b) shows the corresponding real and imaginary parts of Y_{opt}. The correlation $S^{II}_{v_h,i_h^*}$ is assumed to be zero in the modeling. R_n, NF_{min}, both real and imaginary parts of Y_{opt} are well fitted up to 26 GHz.

Fig. 6.30 shows extracted α and γ_{i_h} as a function of V_{GS}. For device modeling, we need to model α and γ_{i_h} as a function of bias. An inspection of experimental extraction data shows that the bias dependence of α and γ_{i_h} can be modeled through V_{GS} and I_{DS} using the following

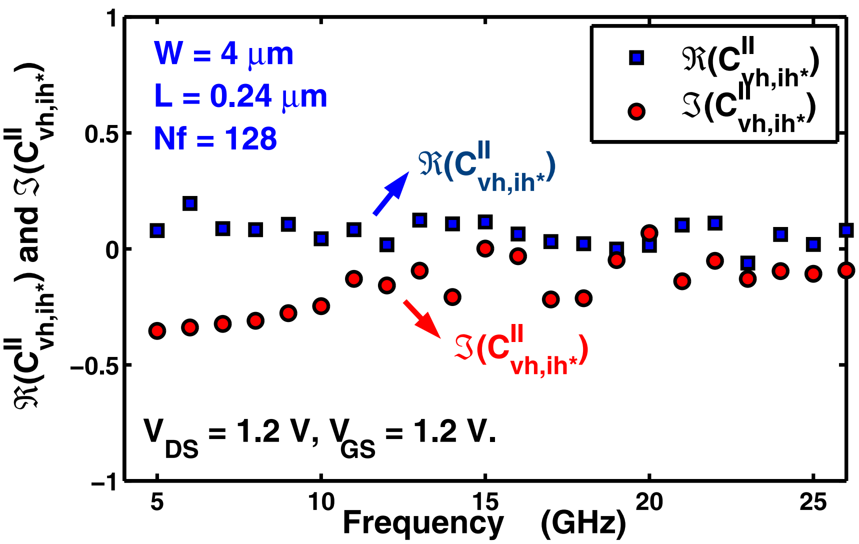

Figure 6.28: $C^{II}_{v_h,i_h^*}$ vs frequency, V_{GS} = 1.2 V. V_{DS} = 1.2 V.

proposed equations:

$$\alpha = \alpha_0 + \alpha_1 \cdot I_{DS}, \tag{6.74}$$

and

$$\gamma_{i_h} = \gamma_{i_h,0} + \gamma_{i_h,1} \cdot V_{GS} + \gamma_{i_h,2} \cdot {V_{GS}}^2, \tag{6.75}$$

where α_0, α_1, $\gamma_{i_h,0}$, $\gamma_{i_h,1}$ and $\gamma_{i_h,2}$ are technology dependent parameters and can be easily determined once noise parameters are extracted. I_{DS} has a unit of μA/μm. From noise physics, we expect these parameters to be independent of channel width, but dependent on channel length and oxide thickness. For the device used at V_{ds} = 1.2 V, $\alpha_0 = 0.4068$, $\alpha_1 = 0.0011$, $\gamma_{i_h,0} = 0.1774$,

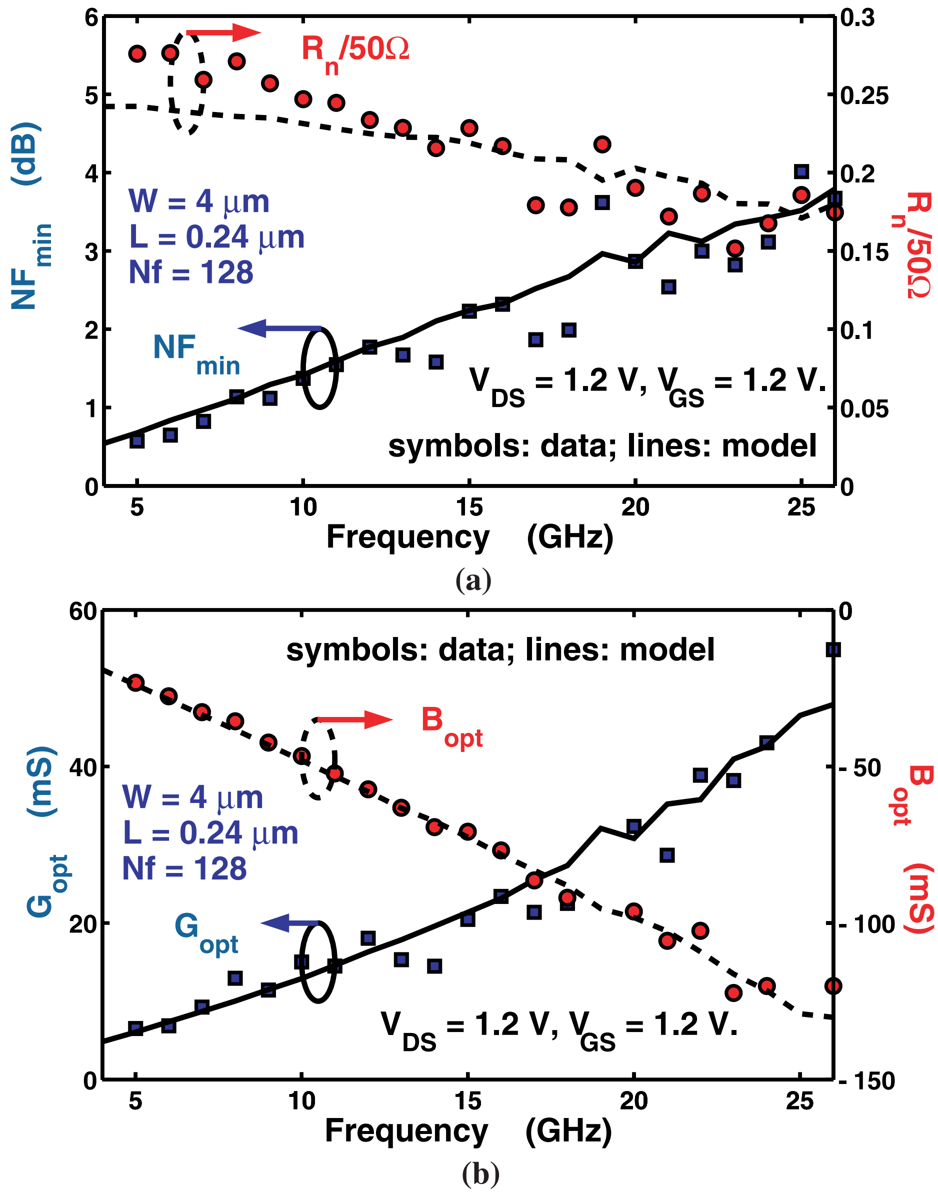

Figure 6.29: (a) NF_{min} and R_n vs frequency; (b) real and imaginary parts of Y_{opt} vs frequency. $S^{II}_{v_h,i_h^*} = 0$. $V_{GS} = 1.2$ V. $\alpha = 0.6$, $\gamma_{i_h} = 1.75$. $V_{DS} = 1.2$ V.

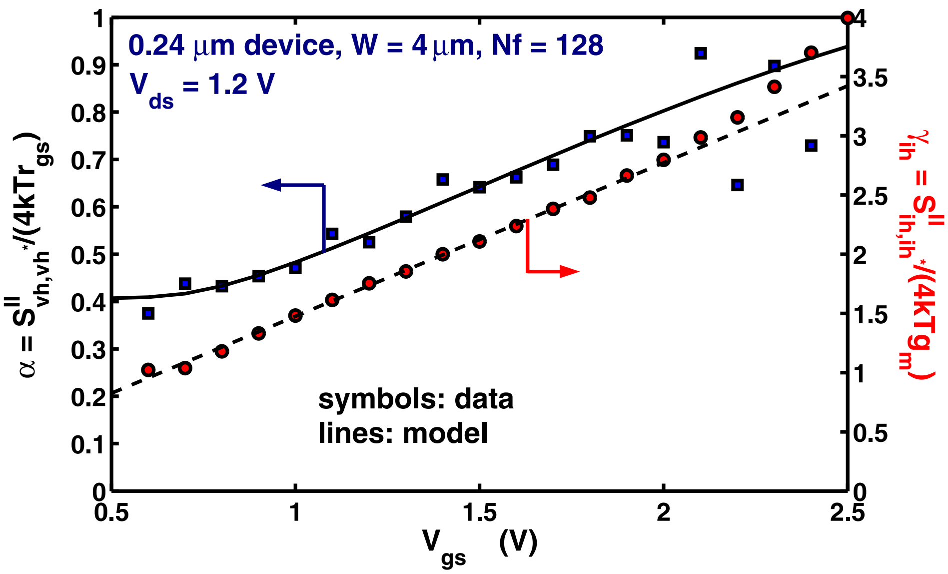

Figure 6.30: $\alpha = S^{II}_{v_h,v_h^*}/(4kTR_{gs})$ and $\gamma_{i_h} = S^{II}_{i_h,i_h^*}/(4kTg_m)$ vs V_{GS}. Symbols are extracted values, lines are model results.

$\gamma_{i_h,1} = 1.2974$, and $\gamma_{i_h,2} = 0$. The α and γ_{i_h} calculated using (6.74) and (6.75) fit the extracted data well, as shown in Fig. 6.30.

Note that α, the $S^{II}_{v_h,v_h^*}/(4kTR_{gs})$ ratio, is nearly flat at V_{GS} slightly above V_{th}, then increases with increasing V_{GS}. However, the $S^{II}_{v_h,v_h^*}/(4kTR_{gs})$ ratio is less than 1 for most biases. This is different from noise simulation results using Shockley's impedance field theory [63], which show that α is larger than 1. On the other hand, γ_{i_h}, the $S^{II}_{i_h,i_h^*}/(4kTg_m)$ ratio, increases with increasing bias, which agrees with simulation [63].

Fig. 6.31 (a) shows the measured and modeled NF_{min} and R_n versus I_{DS} at 10 GHz. Fig. 6.31 (b) shows real and imaginary parts of Y_{opt} versus I_{DS} at 10 GHz. $V_{DS} = 1.2$ V. The correlation $S^{II}_{v_h,i_h^*}$ is neglected. Excellent fitting is achieved for all of the noise parameters across the whole biasing current range.

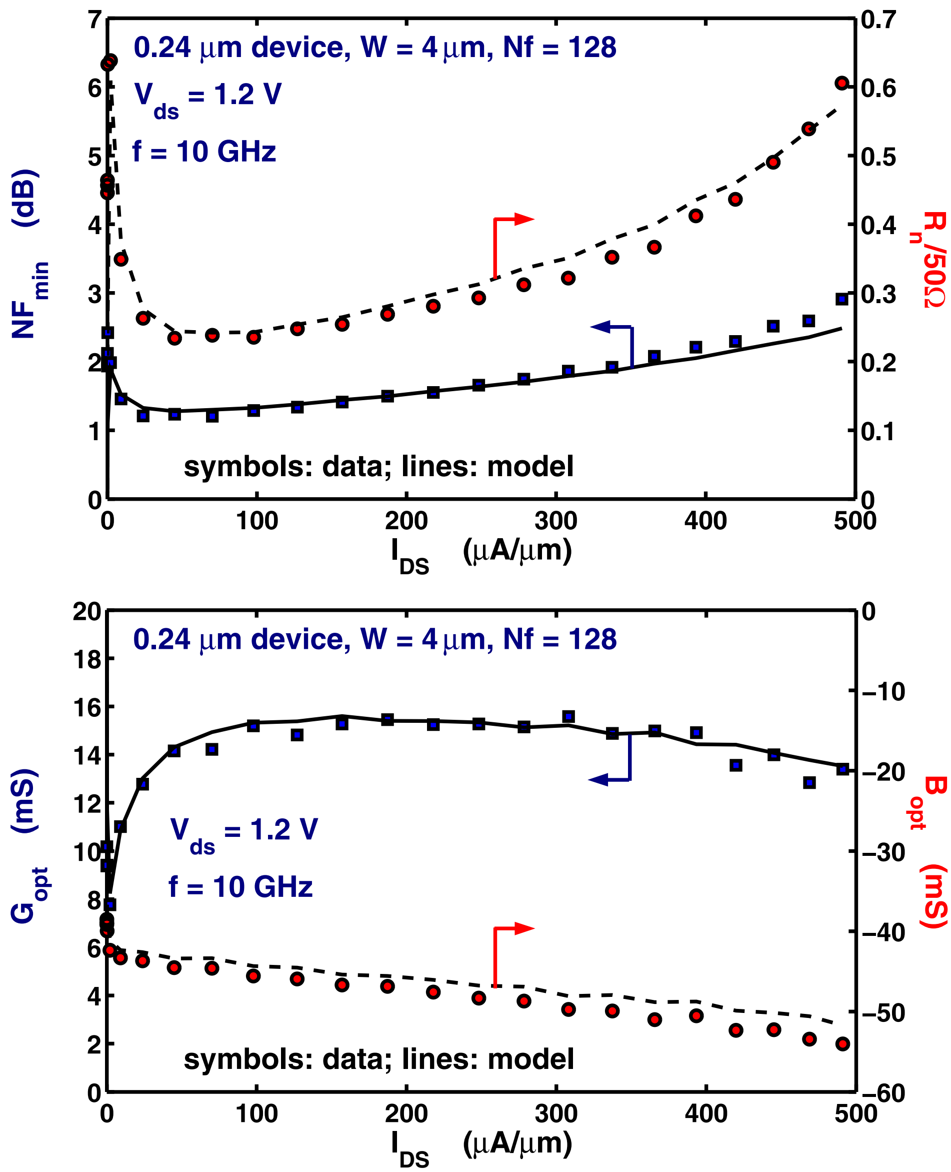

(a)

(b)

Figure 6.31: (a) NF_{min} and R_n vs I_{DS}; (b): real and imaginary parts of Y_{opt} vs I_{DS}. f = 10 GHz. V_{DS} = 1.2 V.

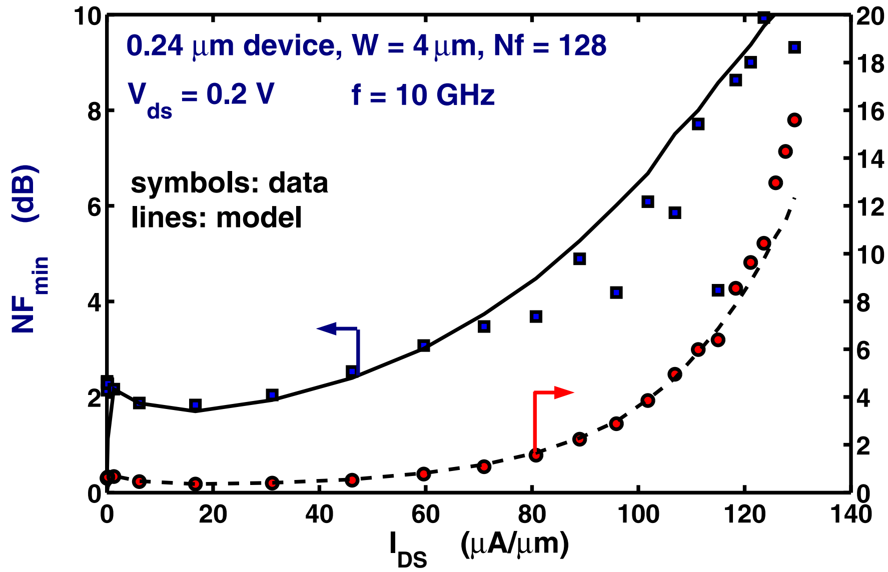

(a)

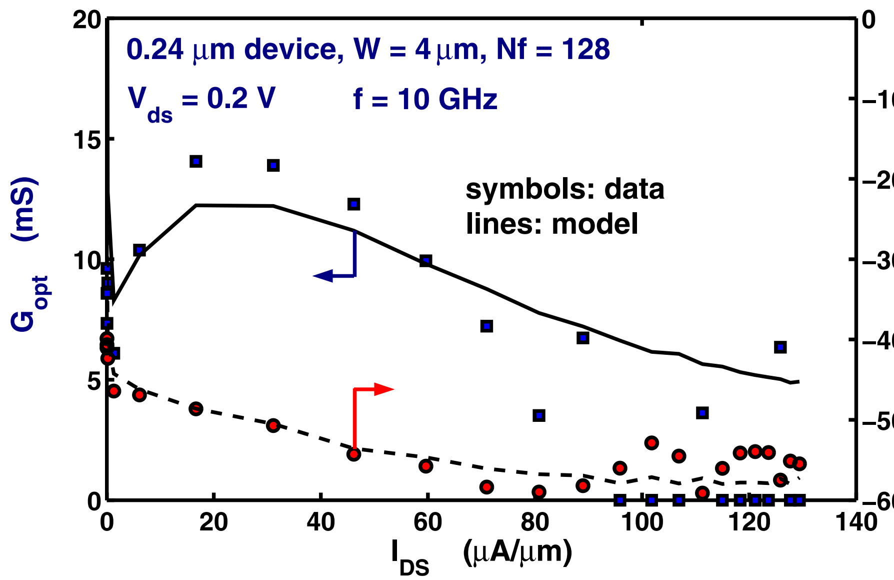

(b)

Figure 6.32: (a) NF_{min} and R_n vs I_{DS}; (b) real and imaginary parts of Y_{opt} vs I_{DS}. $f = 10$ GHz. $V_{DS} = 0.2$ V.

A logical question is if the α and γ_{i_h} equations proposed apply to all of the V_{DS}. In our measurements, V_{GS} is swept at $V_{DS} = 0.2$ and 1.2 V. The resulting α_0, α_1, $\gamma_{i_h,0}$, $\gamma_{i_h,1}$ and $\gamma_{i_h,2}$ from the two different V_{DS} are different for the devices used. It is possible that the α and γ_{i_h} equations proposed here may be less valid for another RF CMOS process, and new equations will need to be developed using extracted data.

Fig. 6.32 (a) shows data-model comparison of NF_{min} and R_n vs I_{DS} at 10 GHz for a $V_{DS} =$ 0.2 V. Fig. 6.32 (b) shows real and imaginary parts of Y_{opt} vs I_{DS}. The $\alpha_0 = 0.4068$, $\alpha_1 = 0$, $\gamma_{i_h,0} = 8.0535$, $\gamma_{i_h,1} = -19.5941$ and $\gamma_{i_h,2} = 13.9161$ are extracted from $V_{ds} = 0.2$ V. $\gamma_{i_h,0}$ and $\gamma_{i_h,2}$ increases with decreasing V_{ds}, while $\gamma_{i_h,1}$ decreases with decreasing V_{ds}. The model fits the data very well without introducing additional equations.

6.8 Summary

We have presented microscopic RF noise simulation results on 50 nm L_{eff} CMOS devices, and examined the compact modeling of intrinsic noise sources for both the Y-representation and the H-representation. The correlation is shown to be smaller for the H-representation than for the Y-representation. For practical biasing currents and frequencies, the correlation is negligible for H-representation. Models for the noise sources are suggested.

Furthermore, we have examined the relations between the Y- and H-noise representations for MOSFETs, and quantified the importance of correlation for both representations. The theoretical values of α_{v_h}, γ_{i_h} and c_H are derived for the first time for long channel devices, $\alpha_{v_h} = 4/3$, $\gamma_{i_h} = 0.6$, $a = 0.2458$, and $b = 0$. c_H is shown theoretically to have a zero imaginary part. We further show that Y-representation is a better choice for R_n, and the H-representation has the inherent advantage of a more negligible correlation for NF_{min}, G_{opt}, and B_{opt}. Overall, the importance of correlation is much more negligible for H-representation than for Y-representation. This makes circuit design and simulation easier.

We have presented experimental extraction and modeling of H-representation noise sources in a 0.25 μm RF CMOS process. Excellent agreement is achieved between modeled and measured noise data, including all noise parameters, for V_{ds} = 0.2 and 1.2 V, from 2 to 26 GHz. The results suggest a new path to RF CMOS noise modeling.

CHAPTER 7

EFFECTIVE GATE RESISTANCE MODELING

Since R_g is important especially for short channel devices, accurate extraction of R_g plays a big role in compact noise modeling of modern CMOS. This chapter explains the frequency and bias dependence of the effective gate resistance (real part of h_{11}) by considering the effect of gate-to-body capacitance, gate to source/drain overlap capacitances, fringing capacitances, and Non-Quasi-Static (NQS) effect. A new method of separating the physical gate resistance and the NQS channel resistance is proposed. Separating the gate-to-source parasitic capacitances from the gate-to-source inversion capacitance is found to be necessary for accurate modeling of all of the Y-parameters.

7.1 Introduction

Accurate extraction of effective gate resistance $R_{g,eff}$ is important for RF CMOS modeling, particularly in noise modeling [64] [65] [66]. The effective gate resistance $R_{g,eff}$ often refers to the sum of the gate electrode resistance R_g and the Non-Quasi-Static (NQS) channel resistance R_{nqs}, as shown in the small signal equivalent circuit in Fig. 7.1. R_g does not depend on bias or frequency, while R_{nqs} depends on bias [67].

Using the equivalent circuit in Fig. 7.1 , $R_{g,eff} = R_g + R_{nqs}$ is often extracted from the real part of h_{11} $(= 1/Y_{11})$ [64], which we denote as $\Re(h_{11})$. Here $\Re$ stands for the real part. The source and drain series resistances R_s and R_d can be de-embedded using values determined from dc I-V data. The extracted $R_{g,eff}$ should be independent of frequency, and decrease with increasing V_{gs}. However, as we show below, measured $\Re(h_{11})$ can be strongly frequency dependent,

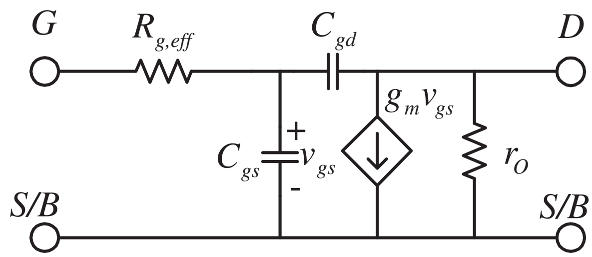

Figure 7.1: MOSFET small signal equivalent circuit model.

and does not decrease with V_{gs}. This was also observed in [68], where $\Re(h_{11})$ of experimental data is strongly frequency dependent from 1 to 4 GHz, particularly at V_{gs} slightly above threshold voltage, where low-noise amplifiers are biased. Interestingly, the frequency dependence of $\Re(h_{11})$ is much weaker at both V_{gs} values well below V_{th} and V_{gs} values well above V_{th}. Furthermore, $\Re(h_{11})$ is lowest at V_{gs} values well below V_{th} and well above V_{th}, but highest at moderate V_{gs} values. These abnormal bias and frequency dependences of $\Re(h_{11})$ cannot be explained by the simple small signal equivalent circuit model in Fig. 7.1.

Fig. 7.2 shows the measured frequency dependence of $\Re(h_{11})$ for a 0.18μm single-ended gate contact CMOS device. Standard open/short de-embedding are performed on the S-parameters measured using an HP8510C vector network analyzer from 2-20 GHz for a wide bias range. The standard open/short de-embedding is a sufficient de-embedding method for a frequency range of 2-20 GHz [69]. The channel width W is 10 μm. The number of fingers Nf is 8. Fig. 7.3 shows the bias dependence of $\Re(h_{11})$. $\Re(h_{11})$ increases with I_{DS} at lower biases, but decreases with I_{DS} at higher biases. Moreover, the frequency dependence of $\Re(h_{11})$ is the strongest at the bias corresponding to the $\Re(h_{11})$ peaks in Fig. 7.2 . This abnormal bias frequency dependence of $\Re(h_{11})$ has also been observed for devices with Nf = 16 and 32. However, only the device with $Nf = 8$ is shown in this chapter as an example. The physical R_g extracted decreases with increasing Nf, as expected.

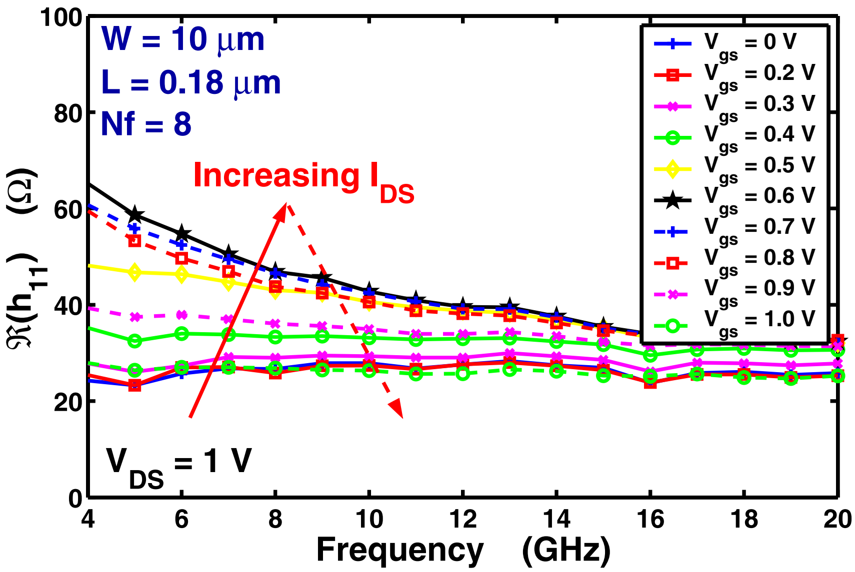

Figure 7.2: $\Re(h_{11})$ vs frequency for 0.18 μm CMOS device, $W = 10\mu$m, $Nf = 8$. V_{ds}=1 V.

Using the small signal model described in Fig. 7.1, we cannot obtain decent data-model fitting, since the real part of h_{11} is independent of frequency. One possible way of producing a frequency dependent $\Re(h_{11})$ is to separate R_g and R_{nqs} using the small signal equivalent circuit model in [9], which is shown in Fig. 7.4. However, the data-model comparison using the extraction method in [9], as shown in Fig. 7.5, shows that this model cannot yield a good fit of the data either. The main difficulty is that C_{gd} is the primary reason for the frequency dependence of $\Re(h_{11})$, while the value of C_{gd} is determined mainly by Y_{12}, where Y_{12} is an element of Y-parameter matrix for the whole device.

This chapter explains the above *anomalous* frequency and bias dependence of $\Re(h_{11})$ in saturation region where $V_{ds} > V_{d,sat}$ by including gate-to-body capacitance C_{gb}, the gate to

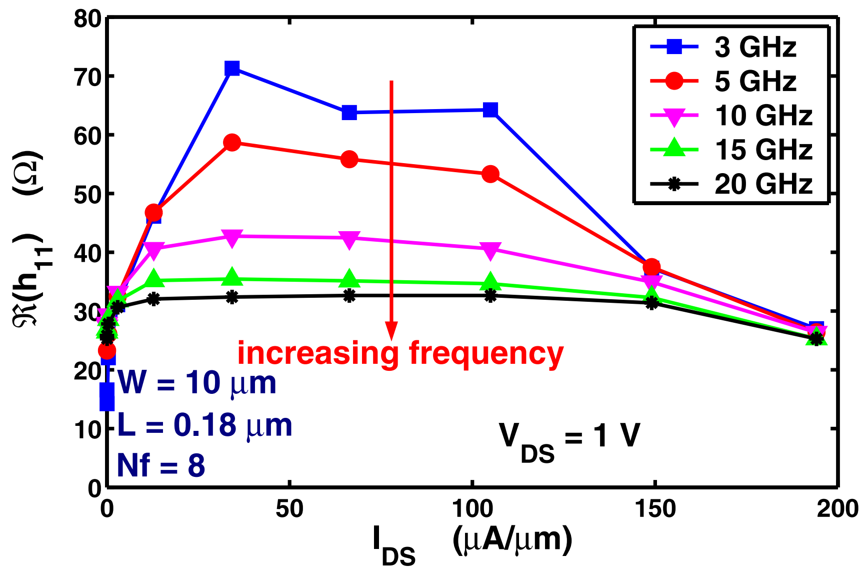

Figure 7.3: $\Re(h_{11})$ vs I_{DS} for 0.18 μm CMOS device, $W = 10\mu$m, $Nf = 8$. V_{ds}=1 V.

source/drain overlap capacitance $C_{ov,s}$ and $C_{ov,d}$, and the gate to source/drain fringing capacitance C_{fs} and C_{fd} according to the equivalent circuit shown in Fig. 7.6. Note that R_{nqs} is part of the intrinsic transistor, and R_{nqs} can also be used to model gate induced noise [63]. From a noise standpoint, R_g has the noise power spectral density of $4kTR$, while the noise associated with R_{nqs} is described by the induced gate noise current. The bulk resistance component in series with C_{gb} becomes important only when C_{gb} well dominates over other parasitic capacitances, which is not the case from our extraction. Furthermore, this substrate resistance component is fairly independent of gate biases, and thus cannot explain the observed behavior. Based on these considerations, we will neglect the R_{sub} component in series with C_{gb}, and will only consider the substrate resistance component in series with the drain-substrate junction. This method of describing gate resistance is similar to but different from the gate resistance option 3 in BSIM4 [5]. The key difference is that the gate to body capacitance is placed directly between the G and B, as

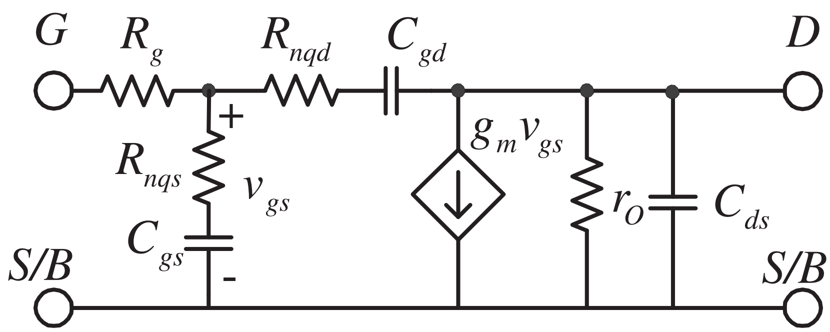

Figure 7.4: CMOS small signal model in [9].

opposed to between G' and B. The gate-to-body capacitance charging occurs through movement of majority carriers in the bulk, and thus does not experience the non-quasi-static delay due to inversion charge formation in the channel. Another difference is that the controling voltage of the transconductance is the total voltage across the R_{nqs} and C_{gs}, and the transconductance term is $g_m/(1 + j\omega\tau)$, which accounts for output NQS and charge partition effects [18]. C_{db} is the drain-to-body junction capacitance , and C_{sub} is the substrate capacitance.

7.2 h_{11} model

Fig. 7.7 shows the equivalent circuit for the h_{11} derivation, which is obtained by shorting the output of the circuit in Fig. 7.6. R_{nqd} is negligible for the device used. R_{nqs}, which is used to describe the NQS effect in the channel, decreases with increasing V_{gs}. C_{gs} is the inversion charge capacitance that increases with V_{gs} normally, and slightly decreases with V_{gs} due to the polysilicon-gate depletion effect [70] [71]. C_p is the combination of the source side peripheral capacitance $C_{peri,s}$ and the drain side peripheral capacitance $C_{peri,d}$. $C_{peri,s}$ includes

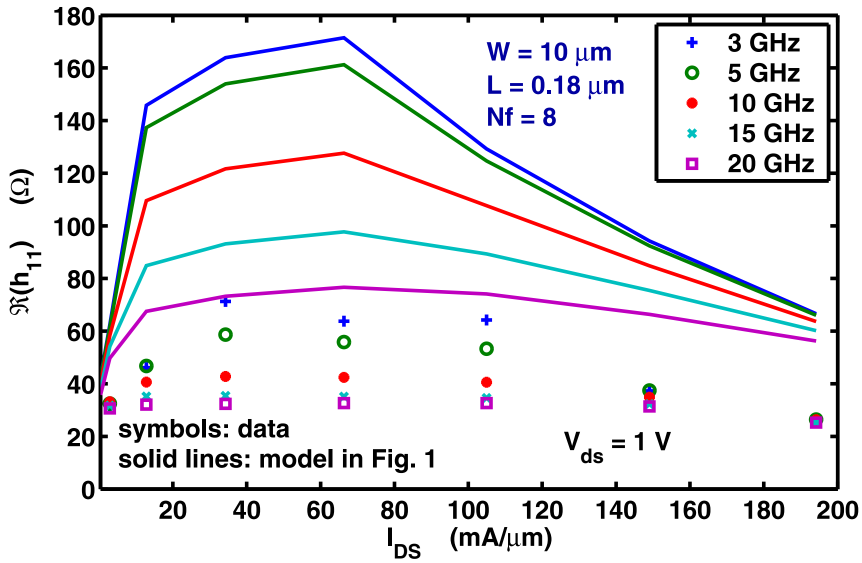

Figure 7.5: Data-model comparison of $\Re(h_{11})$ vs I_{DS} for 0.18μm CMOS device, $W = 10\mu$m, $Nf = 8$, using the small signal model in Fig. 7.4. V_{ds}=1 V.

gate-to-body capacitance C_{gb}, gate-to-source overlap capacitance $C_{ov,s}$, and gate-to-source fringing capacitance C_{fs}. $C_{peri,d}$ includes gate-to-drain overlap capacitance $C_{ov,d}$, and gate-to-drain fringing capacitance C_{fd},

$$C_p = C_{peri,s} + C_{peri,d}, \tag{7.1}$$

$$C_{peri,s} = C_{gb} + C_{ov,s} + C_{fs}, \tag{7.2}$$

$$C_{peri,d} = C_{ov,d} + C_{fd}. \tag{7.3}$$

The gate-to-drain capacitance C_{gd} is negligible in the saturation region. The source/drain series resistances R_s and R_d can be extracted from dc I-V data, and de-embedded. R_s and R_d are negligible for the devices used.

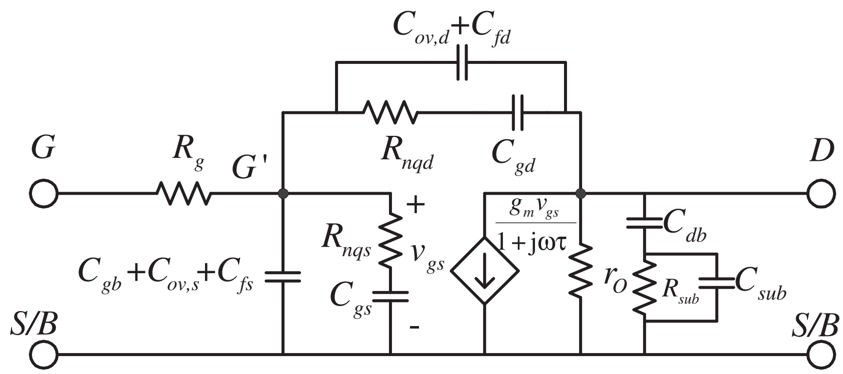

Figure 7.6: A more complete MOSFET small signal model.

An inspection of Fig. 7.7 gives the intrinsic h_{11} as

$$h_{11}^{intr} = R_{nqs} + \frac{1}{j\omega C_{gs}}, \tag{7.4}$$

the real part of which is simply a frequency independent R_{nqs}, at least to first order, which decreases with increasing V_{gs}.

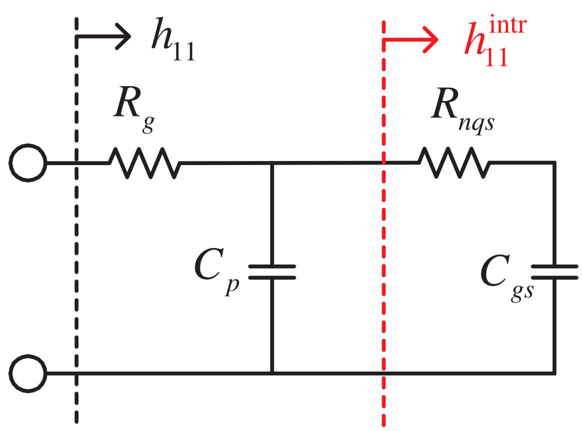

Figure 7.7: h_{11} derivation illustration.

h_{11} is given by

$$h_{11} = R_g + \frac{1}{j\omega C_p + \frac{1}{R_{nqs} + \frac{1}{j\omega C_{gs}}}}. \tag{7.5}$$

The real and imaginary parts of h_{11} are

$$\Re(h_{11}) = R_g + \frac{R_{nqs}}{\left(1 + \frac{C_p}{C_{gs}}\right)^2 + (\omega C_p R_{nqs})^2}, \tag{7.6}$$

$$\Im(h_{11}) = -\frac{\left(1 + \frac{C_p}{C_{gs}}\right) + \omega^2 C_{gs} C_p R_{nqs}^2}{\left(1 + \frac{C_p}{C_{gs}}\right)^2 + \omega^2 C_p^2 R_{nqs}^2} \cdot \frac{1}{\omega C_{gs}}. \tag{7.7}$$

For convenience, we define a threshold frequency ω_1 as

$$\omega_1^2 = \frac{1}{10 R_{nqs}^2 (C_p // C_{gs})^2}, \tag{7.8}$$

and another threshold frequency ω_2 as

$$\omega_2 = 10\omega_1. \tag{7.9}$$

If $\omega < \omega_1$, or $\omega^2 R_{nqs}^2 C_p^2 << (1 + \frac{C_p}{C_{gs}})^2$, (7.6) reduces to

$$\Re(h_{11}) = R_g + \frac{R_{nqs}}{\left(1 + \frac{C_p}{C_{gs}}\right)^2}, \tag{7.10}$$

where $(\Re(h_{11}) - R_g)$ is independent of frequency. Here we denote the $(\Re(h_{11}) - R_g)$ value at zero frequency as R_1,

$$R_1 = (\Re(h_{11}) - R_g)|_{\omega=0} = \frac{R_{nqs}}{\left(1 + \frac{C_p}{C_{gs}}\right)^2} \tag{7.11}$$

If $\omega^2 R_{nqs}^2 C_p^2 >> (1 + \frac{C_p}{C_{gs}})^2$, or $\omega > \omega_2$, (7.6) and (7.7) reduce to

$$\Re(h_{11}) = R_g + \frac{1}{\omega^2 C_p^2 R_{nqs}}, \tag{7.12}$$

where $(\Re(h_{11}) - R_g)$ is proportional to $1/\omega^2$.

Since R_g is independent of frequency and bias, the frequency dependence of $\Re(h_{11})$ directly comes from the term $(\Re(h_{11}) - R_g)$. However, the frequency dependence of $\Re(h_{11})$ depends not only on the frequency dependence of $(\Re(h_{11}) - R_g)$, but also on the relative importance of $(\Re(h_{11}) - R_g)$ compared to R_g. If R_g is much greater than the change of $(\Re(h_{11}) - R_g)$ over the used frequency range, a relatively constant $\Re(h_{11})$ can still be obtained.

The frequency dependence of $(\Re(h_{11}) - R_g)$ is illustrated in Fig. 7.8 and Fig. 7.9 in logarithm and linear scales for both x and y axes, respectively. If the working frequency range lies below ω_1, $(\Re(h_{11}) - R_g)$ is nearly a constant equal to R_1 according to (7.10), and independent of frequency. If the working frequency range lies between ω_1 and ω_2, the frequency dependence of $(\Re(h_{11}) - R_g)$ is the most obvious on a linear scale, decreasing from $0.9R_1$ at ω_1 to $0.1R_1$ at ω_2. If the working frequency range lies above ω_2, $(\Re(h_{11}) - R_g)$ becomes inversely proportional to ω^2, and decreases rapidly from $0.1R_1$ at ω_2 towards zero. When the working frequency range is fixed, the decrease of ω_1 to ω_1' will result in more frequencies lying between ω_1' and ω_2', as shown in Fig. 7.10. At the same time, (7.11) can be rewritten in terms of ω_1 as,

$$R_1 = \frac{1}{10\omega_1^2} \cdot C_p^2 R_{nqs}. \tag{7.13}$$

Compared to $C_p^2 R_{nqs}$, $\frac{1}{10\omega_1^2}$ is the dominant term for R_1. Hence, R_1 can be considered inversely proportional to the threshold frequency ω_1^2. Therefore, as ω_1 decreases to ω_1', R_1 increases as shown in Fig. 7.10. As a result, in the working frequency range, $(\Re(h_{11}) - R_g)$ becomes more frequency dependent, and vice versa.

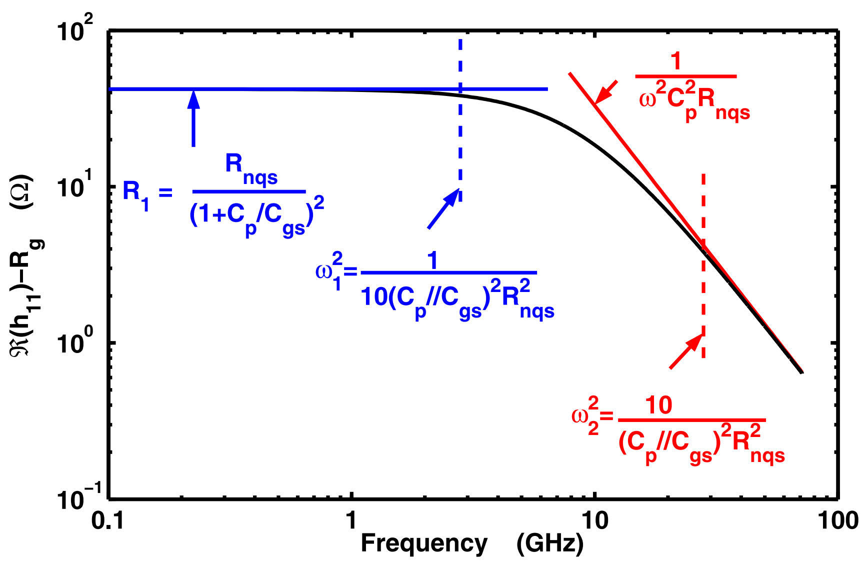

Figure 7.8: Frequency dependence of $(\Re(h_{11}) - R_g)$ in logarithm scale.

If $R_{nqs}(C_p//C_{gs})$ increases with increasing V_{gs}, ω_1 will decrease with increasing V_{gs}. As a result, $(\Re(h_{11}) - R_g)$ becomes more frequency dependent with increasing V_{gs}. On the other hand, if $R_{nqs}(C_p//C_{gs})$ decreases with increasing V_{gs}, ω_1 will increase with increasing V_{gs}. As

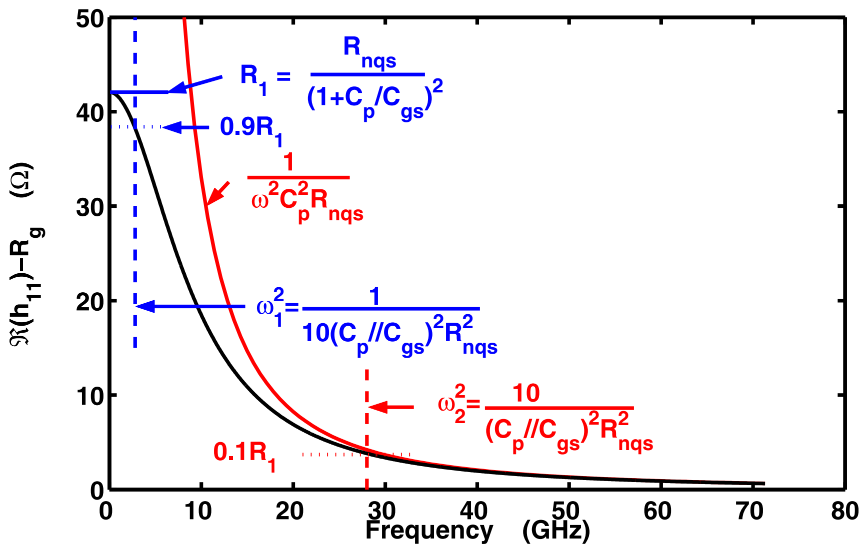

Figure 7.9: Frequency dependence of $(\Re(h_{11}) - R_g)$ in linear scale.

a result, $(\Re(h_{11}) - R_g)$ becomes less frequency dependent with increasing V_{gs}. Next, we extract equivalent parameters, and use the extraction results to understand the observed $\Re(h_{11})$ behavior.

7.3 Parameter Extraction

We extract R_g, C_p, R_{nqs} and C_{gs} through the following steps.

1. Determine an initial guess of R_g using semi-circle fitting.

   Plot $\Im(h_{11})$ versus $\Re(h_{11})$, fit the data using a semi-circle, the high frequency intercept with the $\Re(h_{11})$ axis is used as an initial guess of R_g. This is the same as the extraction of base resistance in bipolar devices [46].

2. Determine initial guesses of C_p, C_{gs} and R_{nqs} as follows.

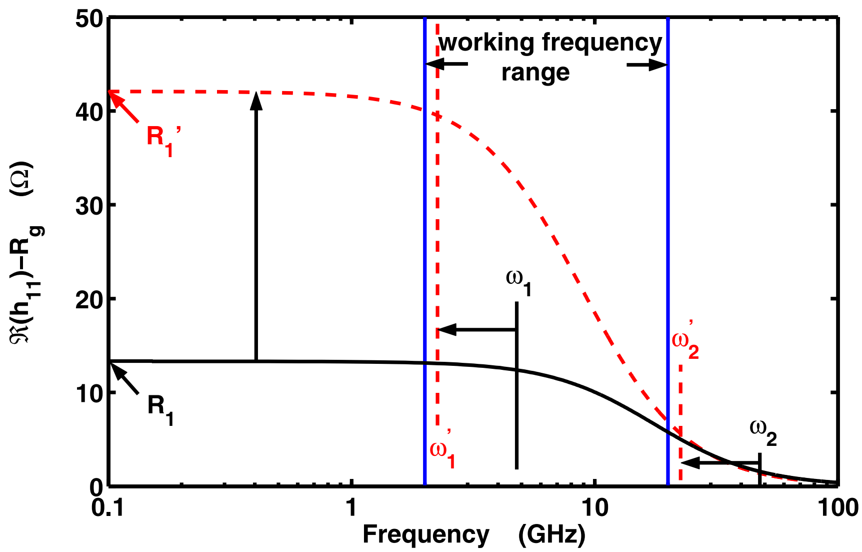

Figure 7.10: Influence of ω_1 on the frequency dependence of $(\Re(h_{11}) - R_g)$.

From (7.6), we have,

$$\frac{1}{\Re(h_{11}) - R_g} = p_2 + \omega^2 \cdot p_1, \tag{7.14}$$

$$p_1 = C_p^2 R_{nqs}, \tag{7.15}$$

$$p_2 = \frac{\left(1 + \frac{C_p}{C_{gs}}\right)^2}{R_{nqs}}. \tag{7.16}$$

Moreover, from (7.6) and (7.7), we have,

$$-\frac{\omega \Im(h_{11})}{\Re(h11) - R_g} = q_2 + \omega^2 \cdot q_1, \tag{7.17}$$

$$q_1 = C_p R_{nqs}, \tag{7.18}$$

$$q_2 = \frac{1 + \frac{C_p}{C_{gs}}}{C_{gs} R_{nqs}}. \tag{7.19}$$

p_1 and p_2 can be extracted using $\frac{1}{\Re(h_{11})-R_g}$ vs ω^2 plot, and q_1 and q_2 can be extracted using $-\frac{\omega\Im(h_{11})}{\Re(h11)-R_g}$ vs ω^2 plot at each bias, as shown in Fig. 7.11.

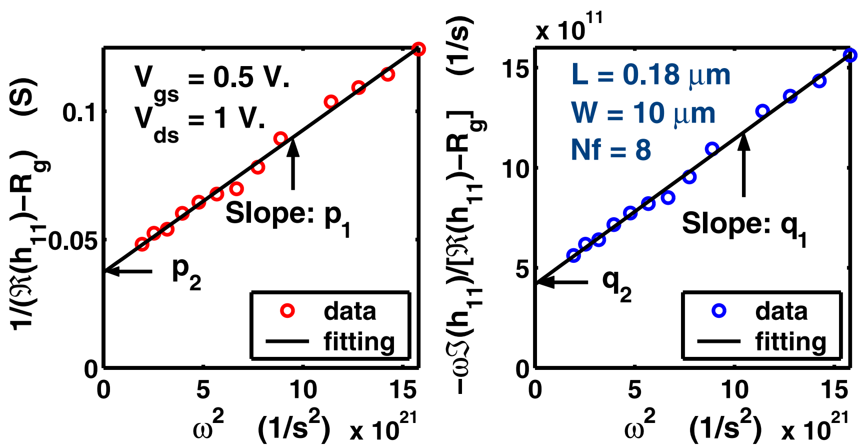

Figure 7.11: Extraction of p_1, p_2, q_1 and q_2 at V_{gs} = 0.5 V for 0.18 μm device, W=10 μm, Nf = 8.

From (7.15), (7.16), (7.18), and (7.19), we can solve for C_p, R_{nqs} and C_{gs} as,

$$C_p = \frac{p_1}{q_1}, \tag{7.20}$$

$$R_{nqs} = \frac{q_1^2}{p_1}, \tag{7.21}$$

$$C_{gs} = \frac{1+\sqrt{1+4q_1q_2}}{2q_1^2q_2} \cdot p_1. \tag{7.22}$$

These are our initial guesses of C_p, R_{nqs} and C_{gs}.

3. The C_p, R_{nqs} and C_{gs} values are refined by fitting $\Re(h_{11})$ and $\Im(h_{11})$ versus frequency for each bias. Here the least mean square error method is used for numerical optimization.

4. $(C_{ov,d} + C_{fd})$ is estimated from the intrinsic Y_{12}, Y_{12}^{intr}, by

$$C_{ov,d} + C_{fd} = -\frac{\Im(Y_{12}^{intr})}{\omega}. \tag{7.23}$$

$(C_{gb} + C_{ov,s} + C_{fs})$ is then determined using (7.1) as

$$(C_{gb} + C_{ov,s} + C_{fs}) = C_p - (C_{ov,d} + C_{fd}). \tag{7.24}$$

Fig. 7.12 shows the extracted capacitances for the same device used in Fig. 7.2 including C_p, C_{gs}, $C_{peri,s}$, and $C_{peri,d}$ versus V_{gs}. The gate electrode resistance R_g is 25 Ω. For the Nf = 16 and 32 devices, R_g = 13 and 7 Ω. Fig. 7.12 also shows the extracted R_{nqs} versus V_{gs}. C_{gs} increases with increasing V_{gs} at first, then decreases with increasing V_{gs} after 0.8 V due to the polysilicon-gate depletion effect [70] [71]. C_p increases with increasing V_{gs}. $C_{peri,d}$ is almost independent of bias, while $C_{peri,s}$ increases with increasing bias. R_{nqs} decreases with increasing V_{gs}, as expected. Assuming the drain and source-side overlap and fringing capacitances are approximately symmetric, C_{gb} can be roughly estimated by $(C_{peri,s} - C_{peri,d})$. C_{gb} is much smaller than $C_{peri,d}$ at lower V_{gs}, increases with V_{gs}, and saturates at high V_{gs}, as expected.

Fig. 7.13 shows ω_1, ω_2 and R_1 vs V_{gs} calculated using (7.8), (7.9) and (7.11). For most biases, the measured frequency range of 2-20 GHz lies between ω_1 and ω_2. As V_{gs} increases, ω_1 begins to decrease first, at the same time, R_1 begins to increase, for reasons detailed in Section 7.2, indicating that $(\Re(h_{11}) - R_g)$ becomes more frequency dependent. ω_1 reaches the lowest point at V_{gs} = 0.6 V, corresponding to the most frequency dependent $\Re(h_{11})$ curve in Fig. 7.2. After that, ω_1 begins to increase while R_1 begins to decrease as V_{gs} increases. Correspondingly, $(\Re(h_{11}) - R_g)$ becomes less frequency dependent again at higher biases.

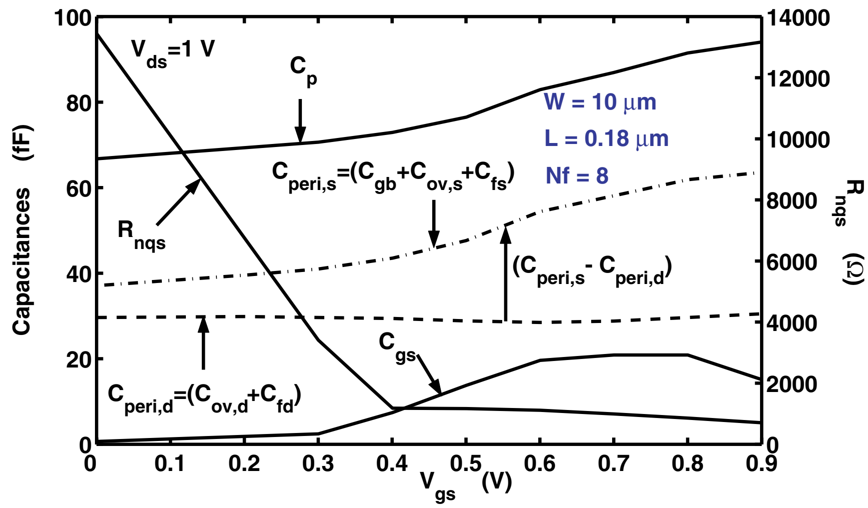

Figure 7.12: Extracted capacitances C_p, $C_{peri,s}$, $C_{peri,d}$, and C_{gs}, and extracted R_{nqs} vs V_{gs} for 0.18 μm device, W=10 μm, Nf = 8.

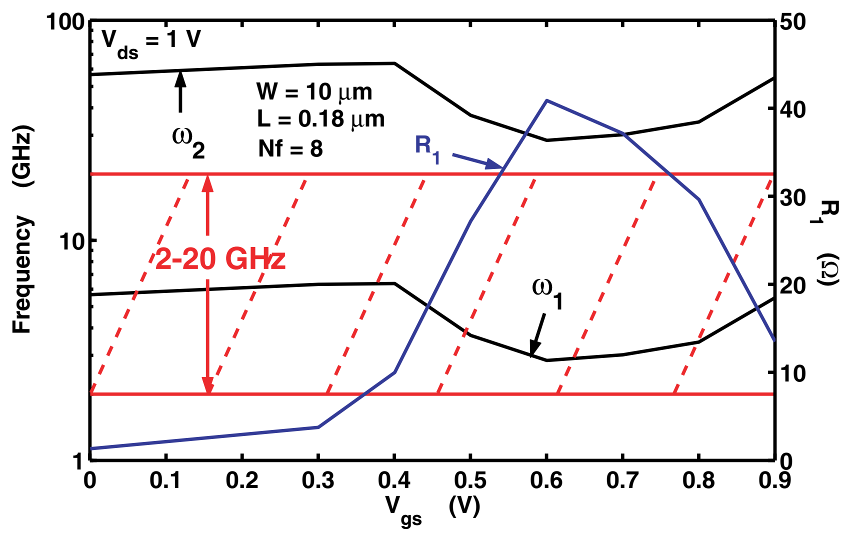

Figure 7.13: ω_1, ω_2 and R_1 vs V_{gs} for 0.18 μm device. W = 10 μm, Nf = 8.

7.4 Results and Discussion

Fig. 7.14 compares the modeled and measured $\Re(h_{11})$ at several biases as a function of frequency. The model captures the frequency dependence of the measured $\Re(h_{11})$ quite well. At lower $V_{gs} = 0.4$ V, $R_{nqs} = 1178\ \Omega$, the inversion capacitance $C_{gs} = 7.4\ f$F is much smaller than $C_p = 73\ f$F, i.e. $C_{gs} << C_p$. The threshold frequency $\omega_1 = 6.4$ GHz, $\omega_2 = 64$ GHz and $R_1 = 10\ \Omega$. Hence, for a frequency range of 2 GHz to 20 GHz, most of the frequencies lie between ω_1 and ω_2, but close to ω_1. Accordingly, $(\Re(h_{11}) - R_g)$ decreases from 9 Ω at 4 GHz to 5 Ω at 20 GHz, as shown in Fig. 7.15. Compared to $R_g = 25\ \Omega$, the 4 Ω decrease of $(\Re(h_{11}) - R_g)$ is negligible. $\Re(h_{11})$ shows only a slight decrease with increasing frequency as can be seen from Fig. 7.14.

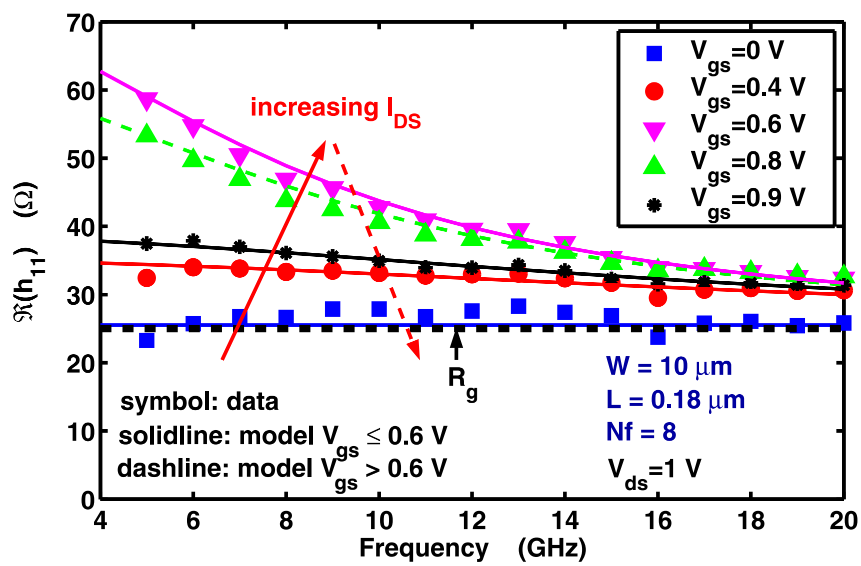

Figure 7.14: $\Re(h_{11})$ vs frequency. Symbols are measurement data. Lines are modeling results.

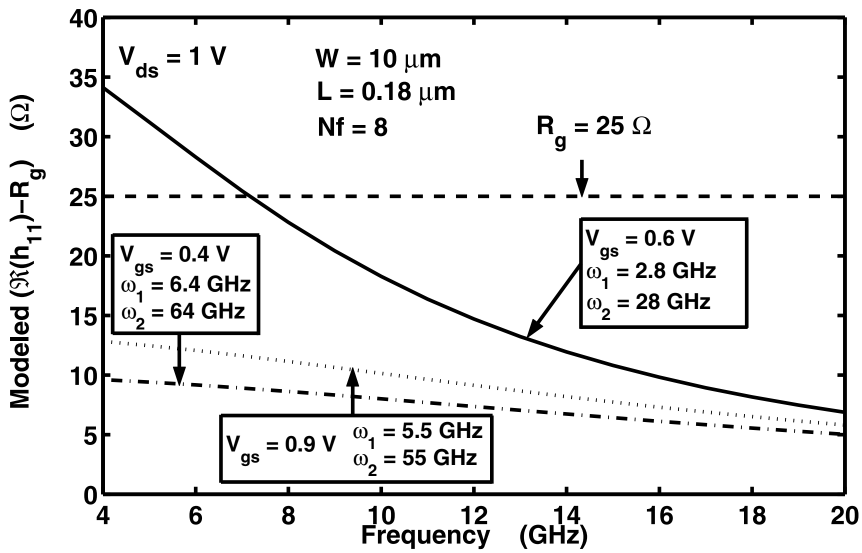

Figure 7.15: Modeled ($\Re(h_{11}) - R_g$) vs frequency for 0.18 μm device. $W = 10$ μm, $Nf = 8$. $V_{gs} = 0.4$, 0.6, and 0.9 V.

At medium $V_{gs} = 0.6$ V, $R_{nqs} = 1116$ Ω, $C_p = 83$ fF, and $C_{gs} = 20$ fF, C_{gs} is comparable to C_p. Compared to $V_{gs} = 0.4$ V, ω_1 decreases to 2.8 GHz, ω_2 decreases to 28 GHz, while R_1 increases to 41 Ω. Hence, for a frequency range of 2 GHz to 20 GHz, most of the frequencies lie between ω_1 and ω_2, and the frequency dependence is the most obvious. ($\Re(h_{11}) - R_g$) decreases from 40 Ω at 4 GHz, to 7 Ω at 20 GHz, as shown in Fig. 7.15. As $R_g = 25$ Ω, the overall $\Re(h_{11})$ shows an obvious decrease from 65 Ω at 4 GHz to 32 Ω at 20 GHz as can be seen from Fig. 7.14.

At a higher V_{gs} of 0.9 V, $R_{nqs} = 703$ Ω, $C_p = 94$ fF, and $C_{gs} = 15$ fF, C_{gs} is comparable to C_p. Compared to $V_{gs} = 0.6$ V, ω_1 increases to 5.5 GHz, ω_2 increases to 55 GHz, and R_1 decreases to 13.5 Ω. Hence, most of the frequencies (2-20 GHz) lie close to ω_1. ($\Re(h_{11}) - R_g$) becomes less frequency dependent, and decreases from 13 Ω at 4 GHz to 6 Ω at 20 GHz, as shown in Fig. 7.15. As $R_g = 25\ \Omega$, $\Re(h_{11})$ slightly decreases from 38 Ω at 4 GHz to 31 Ω at 20 GHz as can be seen from Fig. 7.14.

Fig. 7.16 compares the modeled and measured $\Re(h_{11})$ at several frequencies as a function of I_{DS}. The model captures the bias dependence of the measured $\Re(h_{11})$ quite well. At 3 GHz, which is close to the ω_1 for most biases, (7.10) holds. At lower V_{gs}, where $C_p >> C_{gs}$, (7.10) reduces to

$$\Re(h_{11}) = R_g + \frac{R_{nqs}C_{gs}^2}{C_p^2}. \tag{7.25}$$

The bias dependence of $\Re(h_{11})$ is complicated and not necessarily monotonic, because R_{nqs}, C_{gs} and C_p are all functions of V_{gs}. R_{nqs} decreases with increasing V_{gs} as shown in Fig. 7.12. C_{gs} increases with increasing V_{gs} at lower biases, does not change much with V_{gs} at medium biases, and slightly decreases with increasing V_{gs} at higher biases. C_p slightly increases with increasing V_{gs}. From (7.25), we observe that both the bias dependence of R_{nqs} and the bias dependence of the C_{gs}/C_p ratio contribute to the bias dependence of $\Re(h_{11})$. Fig. 7.17 shows the bias dependence of the C_{gs}/C_p ratio for the device used. C_{gs}/C_p ratio increases with bias at low V_{gs}, since the increase of C_{gs} is faster than the increase of C_p. At medium V_{gs}, the C_{gs}/C_p ratio changes slightly, since the increases of C_{gs} and C_p are about the same. At high V_{gs}, while C_{gs} decreases slightly and C_p increases slightly, the C_{gs}/C_p ratio decreases with increasing bias.

At lower V_{gs}, if R_{nqs} is the dominant changing parameter, $\Re(h_{11})$ will decrease as V_{gs} increases. If the C_{gs}/C_p ratio is the dominant changing parameter, $\Re(h_{11})$ will increase with V_{gs}. At medium V_{gs}, e.g. 0.6 to 0.8 V, where the C_{gs}/C_p ratio does not change much, and R_{nqs} decreases with V_{gs}, $\Re(h_{11})$ begins to decrease slightly with V_{gs}. At higher V_{gs}, e.g. 0.9 V, (7.25)

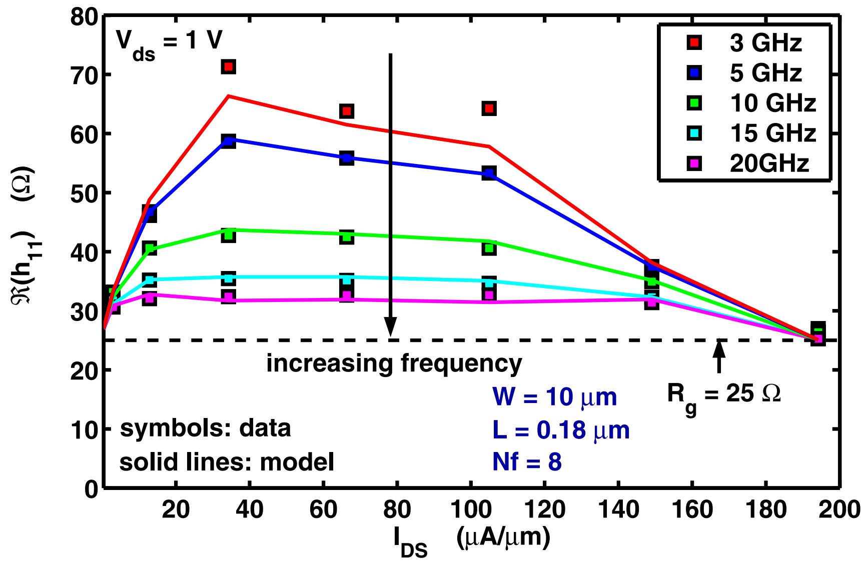

Figure 7.16: $\Re(h_{11})$ vs I_{DS}. Symbols are measurement data. Lines are modeling results.

holds. R_{nqs} as well as the C_{gs}/C_p ratio decreases as V_{gs} increases. Therefore $\Re(h_{11})$ is expected to decrease as V_{gs} increases at higher V_{gs}.

Fig. 7.18 and Fig. 7.19 shows the data-model comparison for the Y-parameters at 3 GHz, 5 GHz, 10 GHz, 15 GHz and 20 GHz. R_g and $(C_{gb} + C_{ov,s} + C_{fs})$ are de-embedded to obtain the Y-parameters of the intrinsic circuit. The parameters of the intrinsic circuit are then extracted using the method described in [9], with modifications to account for the differences in the transconductance term. The Y-parameters fit quite well using the proposed method over all biases and at all frequencies. This suggests that it is necessary to separately consider the $(C_{gb} + C_{ov,s} + C_{fs})$ and the inversion capacitance C_{gs} in order to accurately model all of the Y-parameters over all biases.

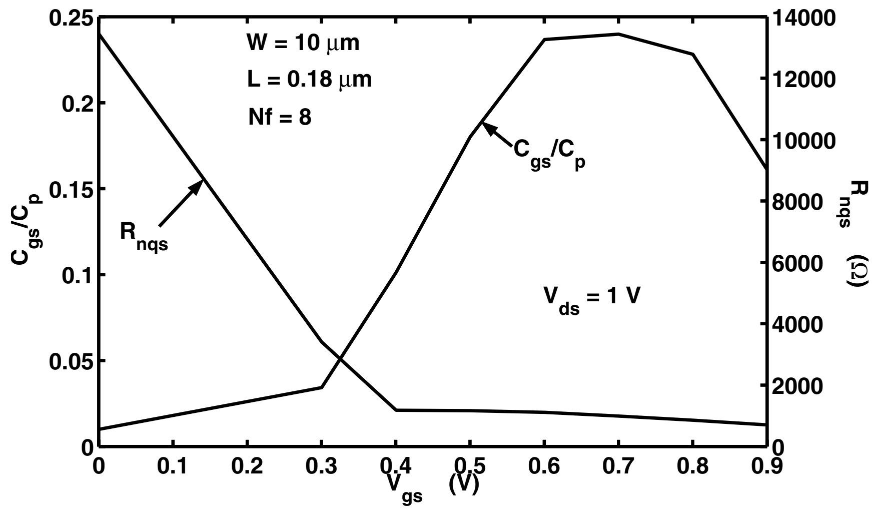

Figure 7.17: C_{gs}/C_p ratio vs V_{gs} for 0.18 μm device. $W = 10$ μm, $Nf = 8$.

7.5 Length and Width Effects

The anomalous frequency and bias dependence of $\Re(h_{11})$ also exist in devices with different channel length, as shown in Fig. 7.20. Theoretically, as channel length L decreases, R_{nqs} decreases, C_{gs} decreases, the sum of peripheral capacitances C_p does not change with L, resulting in a decrease of R_1 and an increase of ω_1, and hence less frequency dependence in the R_{nqs} related term of $\Re(h_{11})$. On the other hand, R_g has one component that increases with decreasing L, and another component that decreases with decreasing L. Therefore, the corresponding change in R_g with decreasing L depends on which component of R_g dominates. For the devices shown in Fig. 7.20, R_g is slightly lower for the device with larger L. Therefore, $\Re(h_{11})$ is less frequency dependent for the device with smaller L in Fig. 7.20.

As device width W decreases, theoretically R_{nqs} increases, however C_{gs} and C_p decrease, leading to an increase in R_1 but no change in ω_1, and hence more frequency dependence in

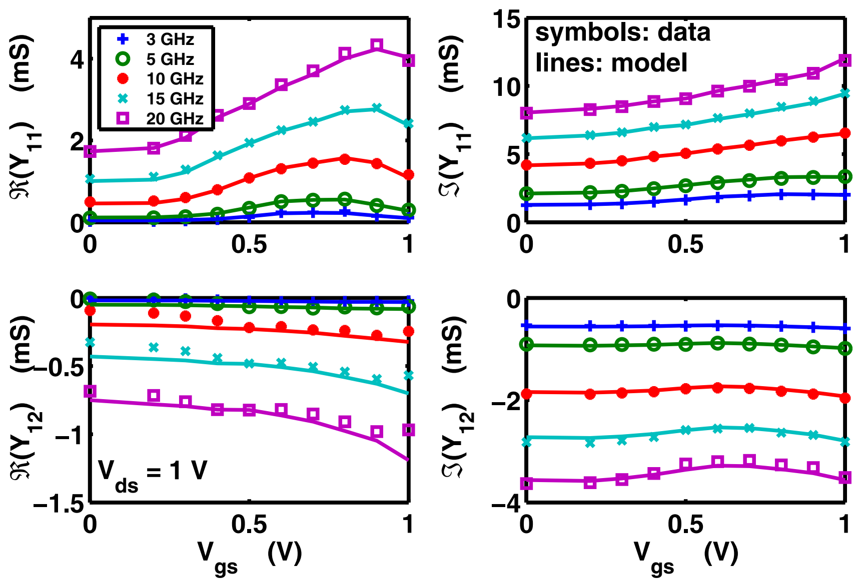

Figure 7.18: The real and imaginary parts of Y_{11} and Y_{12} vs V_{gs} for 0.18μm CMOS device. W = 10 μm, Nf = 8. Symbols are measurement data. Lines are modeling results.

the R_{nqs} related term of $\Re(h_{11})$. On the other hand, with decreasing W, one component of R_g decreases, while another component of R_g increases. Therefore, the net change in R_g with decreasing W depends on which component of R_g dominates. If the R_g increase is less than the increase of R_1 with decreasing W, or if R_g decreases with decreasing W, a stronger frequency dependence in $\Re(h_{11})$ can be expected.

As the number of fingers Nf decreases, both R_g and R_{nqs} increase, and both C_{gs} and C_p decrease, leading to an increase in R_1 but no change in ω_1, and hence a stronger frequency dependence in the R_{nqs} related term of $\Re(h_{11})$. However, theoretically R_g and R_1 increase by the same percentage with decreasing Nf, resulting in no change in the frequency dependence of $\Re(h_{11})$.

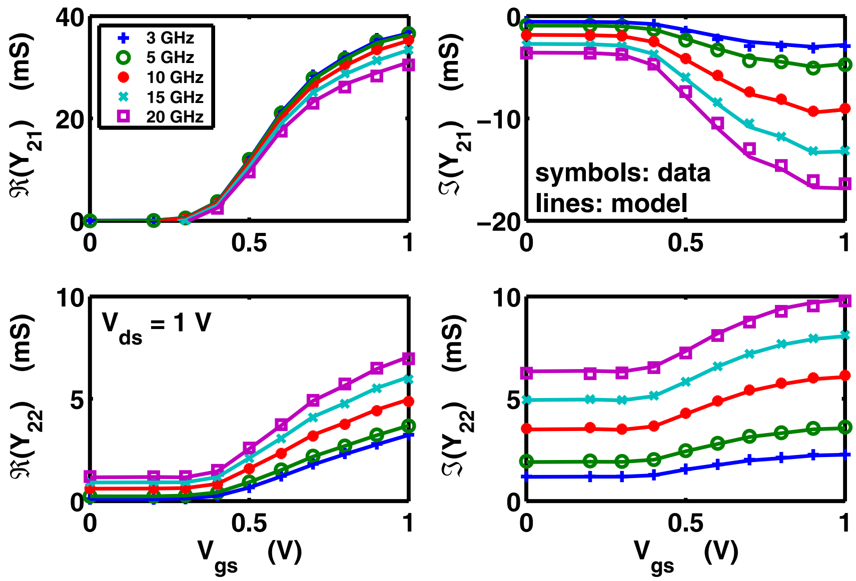

Figure 7.19: The real and imaginary parts of Y_{21} and Y_{22} vs V_{gs} for 0.18μm CMOS device. W = 10 μm, Nf = 8. Symbols are measurement data. Lines are modeling results.

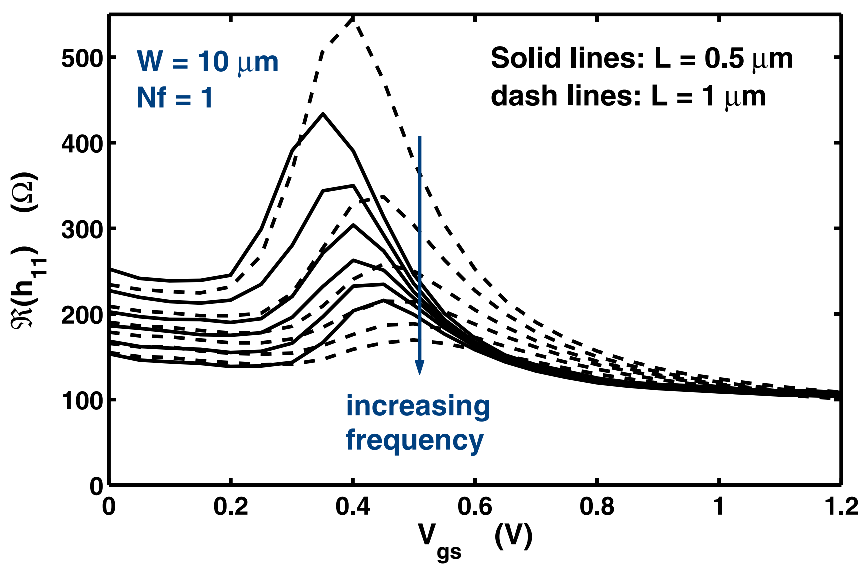

Figure 7.20: $\Re(h_{11})$ vs V_{gs} for 0.5 μm and 1 μm CMOS device. W = 10 μm, Nf = 1.

7.6 Summary

An anomalous frequency dependence and bias dependence of $\Re(h_{11})$ is observed. $\Re(h_{11})$ decreases with frequency, and increases with V_{gs} at low biases. We have shown that both the frequency dependence and bias dependence can be understood by considering the gate-to-body capacitance and the parasitic gate-to-source capacitances as capacitances in parallel with the series combination of the NQS resistance and inversion capacitance C_{gs}. A new parameter extraction method is developed to separate the physical gate resistance and the NQS channel resistance. The modeling results show excellent agreement with data, and suggest the importance of modeling NQS effect for RF CMOS even at frequencies well below f_T of the technology. The proposed model parameter extraction method can be used to facilitate MOSFET noise modeling and more accurate Y-parameter modeling over a wide bias range.

CHAPTER 8

EXCESS NOISE FACTORS AND NOISE PARAMETER EQUATIONS FOR RF CMOS

This chapter examines the differences between the g_{d0} and g_m referenced drain current excess noise factors in CMOS transistors as a function of channel length and bias. The technology scaling are discussed for 0.25 μm process measured in IBM, 0.18 μm process measured in Georgia Institute of Technology and 0.12 μm process measured in IBM. Using standard linear noisy two-port theory, a simple derivation of noise parameters is presented. The results are compared with the well known Fukui's empirical FET noise equations. Experimental data on a 0.18 μm CMOS process are measured and used to evaluate the simple model equations. New figures-of-merit for minimum noise figure is proposed. The amount of drain current noise produced to achieve one GHz f_T is shown to fundamentally determine the noise capability of the intrinsic transistor.

8.1 Introduction

CMOS has recently become a technology for implementing lost cost RF system due to its economy of scale and ability to integrate analog, digital and RF functions. For analog and RF circuits, a deeper understanding of the drain current thermal noise at both the device and circuit level is required. A primary figure-of-merit used is the so-called drain noise excess noise factor, defined as $S_{i_d,i_d^*}/4kTg_{d0}$, with g_{d0} being the output conductance at $V_{ds} = 0$ V, and S_{i_d,i_d^*} being the power spectral density (PSD) of drain current noise. As g_{d0} is used as a reference, we will refer to this as the g_{d0} referenced excess noise factor, and denote it as $\gamma_{g_{d0}}$. For circuit designers, however, the transconductance at the operating bias, g_m, is a better reference for defining excess noise factor, and we will refer to this as the g_m referenced excess noise factor, $\gamma_{g_m} = S_{i_d,i_d^*}/4kTg_m$. Here we examine the relationship between $\gamma_{g_{d0}}$ and γ_{g_m} using experimental data, particular its bias and channel length dependence.

Ultimately, from a circuit perspective, we need to establish exactly how circuit level noise parameters relate to device level parameters, including the minimum noise figure NF_{min}, the noise resistance R_n, and the noise matching source admittance Y_{opt}. Fukui's equations have been widely used in interpretation, understanding and modeling of noise properties of field-effect transistors (FETs), first in GaAs FETs and more recently in RF CMOS [34] [35] [36] [37] [38]. Based on observation of experimental noise parameter data obtained on MESFETs [31] [32] [33], Fukui first proposed a set of empirical equations for NF_{min}, R_n, and Z_{opt}. These equations involve an empirical Fukui's noise figure coefficient K_f, and other "constants." K_f has since been frequently used as a figure-of-merit for comparing the intrinsic noise performance of different technologies [34] [36]. Recently, various equations of NF_{min}, R_n and Y_{opt} have been derived based on linear two-port theories and small signal equivalent circuits [40]. In this chapter, the noise parameter equations from small signal equivalent circuit derivation are compared with empirical Fukui's equations to better understand the physical meanings of the various constants. Noise measurements are then made on a 0.18μm CMOS process for model evaluation. The results show that there does not exist a bias or channel length independent Fukui's noise figure coefficient for CMOS. The results are then used to develop new figures-of-merit for NF_{min}. Experimental data are used to demonstrate the new NF_{min} figures-of-merit.

8.2 Excess Noise Factors

The PSD of drain current noise i_d can be expressed using either $\gamma_{g_{d0}}$ or γ_{gm}

$$S_{i_d,i_d^*} = \frac{\langle i_d, i_d^* \rangle}{\Delta f} = 4kT\gamma_{g_m}g_m = 4kT\gamma_{g_{d0}}g_{d0}. \tag{8.1}$$

The two excess noise factors are related by

$$\gamma_{g_m} = \gamma_{g_{d0}}\frac{g_{d0}}{g_m}. \tag{8.2}$$

In device modeling, $\gamma_{g_{d0}}$ is often preferred because it is less bias dependent [72]. Another perhaps more important reason is that an analytical expression of $\gamma_{g_{d0}}$ is straightforward to derive using a drift-diffusion based noise source model, as was done in [15]. Given the weak bias dependence of $\gamma_{g_{d0}}$, the bias dependence of γ_{g_m} should primarily come from the ratio of g_{d0}/g_m.

Fig. 8.1 shows the measured g_{d0}/g_m ratio versus V_{gs} for different channel length from a 0.13 μm process. Similar results are obtained on 0.18 μm process. V_{ds} is chosen at 1.5 V to bias the device in saturation. Observe in Fig. 8.1 that for long channel devices, $g_{d0} = g_m$ in strong inversion (high V_{gs}), $\gamma_{g_{d0}} = \gamma_{g_m}$, and differentiating $\gamma_{g_{d0}}$ or γ_{g_m} does not make a difference.

For short channel lengths of interest, however, the g_{d0}/g_m ratio increases linearly with V_{gs}. If we assume a bias independent $\gamma_{g_{d0}}$, which remains to be verified, we should expect a strong increase of γ_{g_m} with V_{gs}. Optimal biasing and sizing for low-noise amplifier optimization under the assumption of a bias independent γ_{g_m} [40] is thus problematic.

With decreasing channel length, velocity saturation makes g_m increasingly smaller than its "long channel" behavior value, while g_{d0} does not suffer from velocity saturation and remains close to its long channel behavior, because $V_{ds} = 0$ V. The g_{d0}/g_m ratio thus increases with

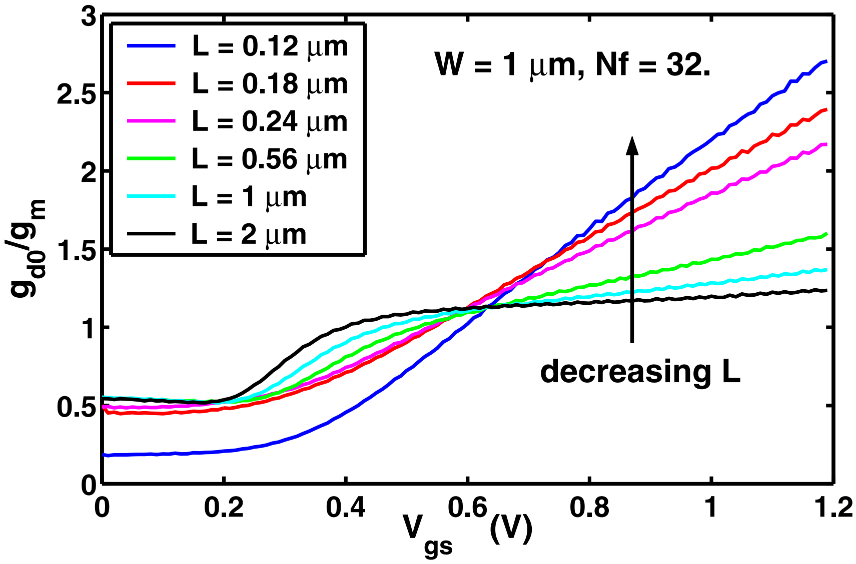

Figure 8.1: Measured ratio of g_{d0}/g_m vs V_{gs} for different channel lengths from a 0.13 μm CMOS process. $V_{ds} = 1.5$ V.

decreasing channel length. A calculation of g_{d0}/g_m using the BSIM3v3 model equation with and without velocity saturation confirms the above intuitive explanation.

Fig. 8.2 shows $\gamma_{g_{d0}}$ and γ_{g_m} extracted from noise parameter measurements for a 0.18 μm process. S-parameters and noise parameters were measured using a ATN NP-5B system on wafer from 2 to 20 GHz, using open short de-embedding. $V_{ds} = 1$ V. Gate resistance was extracted from s-parameters, and further de-embedded for calculation of S_{i_d,i_d^*}. g_m is extracted from y-parameters (converted from s-parameters), and verified to be consistent with that obtained from derivatives of $I_{ds} - V_{gs}$. g_{d0} is extracted from $I_{ds} - V_{ds}$ data, with a small V_{ds} step of 0.05 V. Devices with 8, 16 and 32 fingers were measured, and the resulting S_{i_d,i_d^*} is proportional to the number of fingers. Note that $\gamma_{g_{d0}}$ decreases slightly with increasing bias, while γ_{g_m} increases with increasing bias at a larger slope.

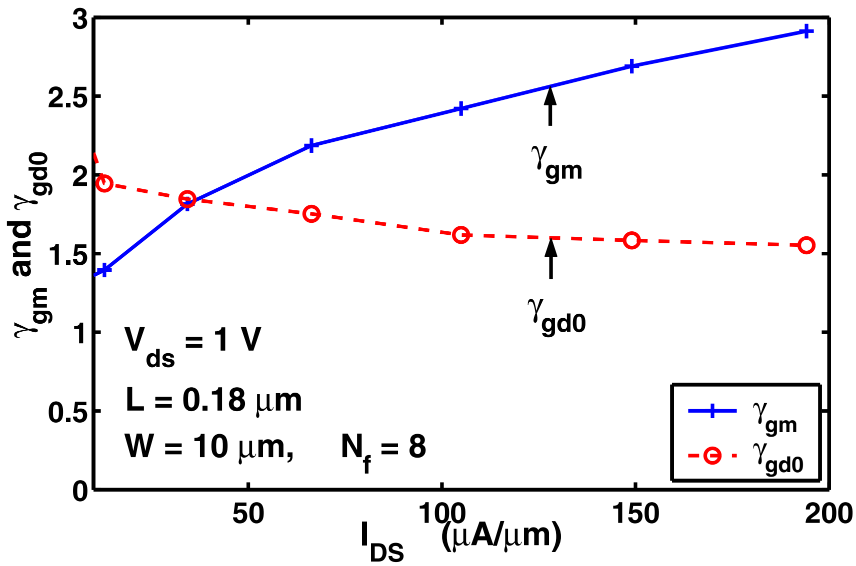

Figure 8.2: Measured $\gamma_{g_{d0}}$ and γ_{g_m} for a 0.18 μm CMOS process. V_{ds} = 1 V.

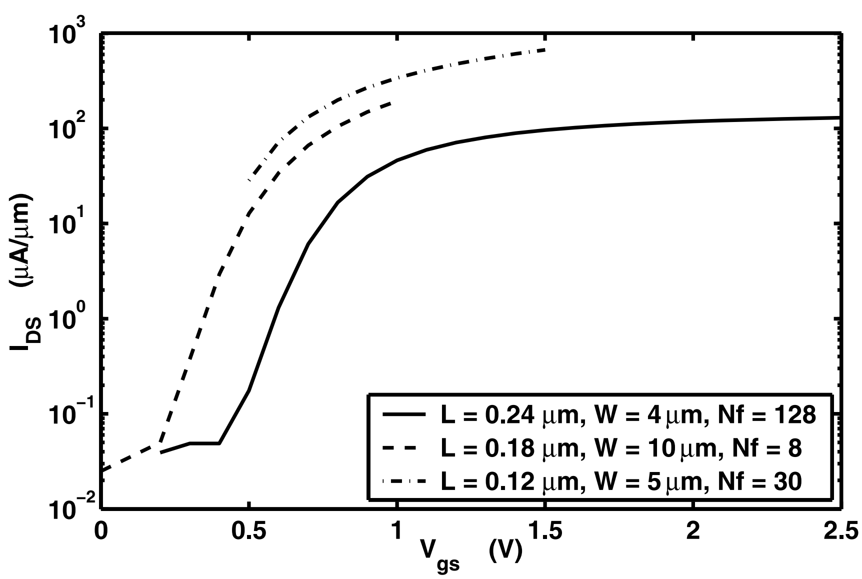

Figure 8.3: I_{DS} vs V_{gs} in saturation region for gate length of 0.24 μm, 0.18 μm, and 0.12 μm devices.

8.3 Technology Discussion of Excess Noise Factor

Fig. 8.3 shows I_{DS} vs V_{gs} in saturation region for gate length of 0.24 μm, 0.18 μm, and 0.12 μm devices. I_{DS} increases with scaling. Fig. 8.4 show cutoff frequency f_T vs I_{DS} and V_{gs}, respectively. f_T increases with decreasing gate length.

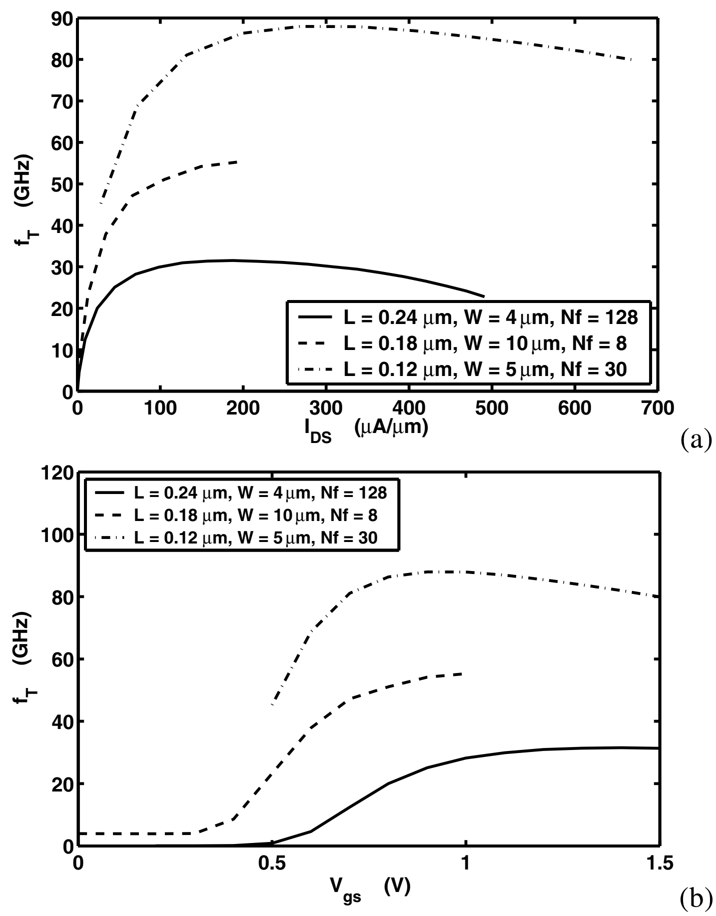

Figure 8.4: f_T vs (a) I_{DS}, and (b) V_{gs} for gate length of 0.24 μm, 0.18 μm, and 0.12 μm devices.

Fig. 8.5 (a) shows S_{i_d,i_d^*} normalized by $(W \cdot Nf)$ vs I_{DS} and S_{i_d,i_d^*} vs V_{gs} for gate length of 0.24 μm, 0.18 μm, and 0.12 μm devices, respectively. S_{i_d,i_d^*} of 0.12 μm gate length device is the highest. The normalized S_{i_d,i_d^*} increases with scaling. g_m normalized by $(W \cdot Nf)$ vs I_{DS} is shown in Fig. 8.5 (b) for gate length of 0.24 μm, 0.18 μm, and 0.12 μm devices. The normalized g_m increases with scaling.

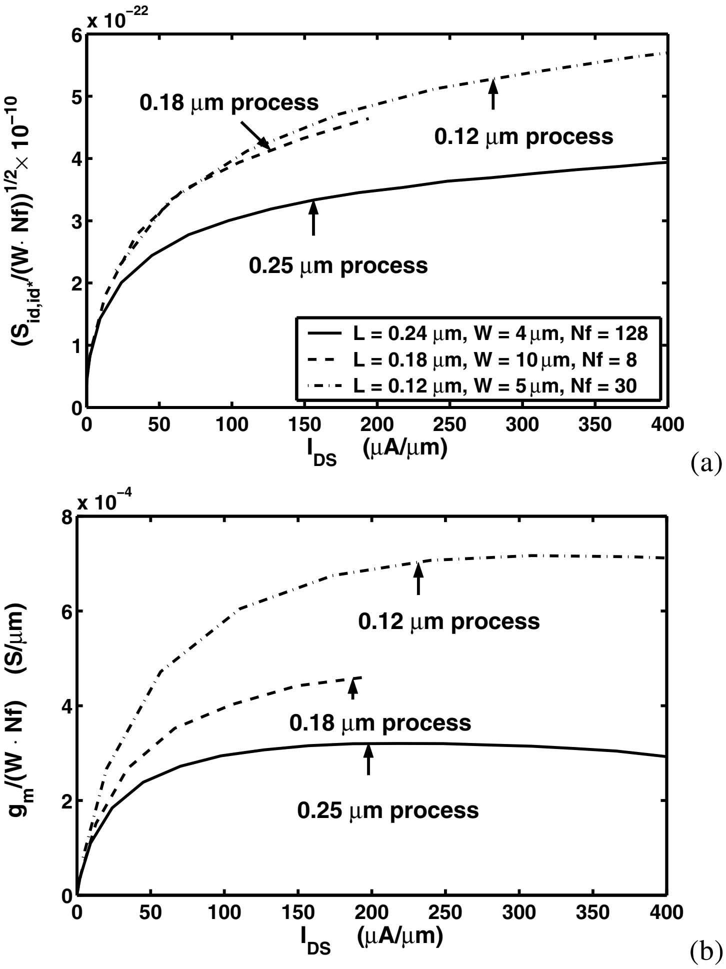

Figure 8.5: (a) S_{i_d,i_d^*}, and (b) g_m normalized by $(W \cdot Nf)$ vs I_{DS} for gate length of 0.24 μm, 0.18 μm, and 0.12 μm devices.

Fig. 8.6 shows γ_{g_m} and $\gamma_{g_{d0}}$ vs I_{DS} for gate length of 0.24 μm, 0.18 μm, and 0.12 μm devices. γ_{g_m} and $\gamma_{g_{d0}}$ do not necessarily increase or decrease with scaling, although normalized S_{i_d,i_d^*} and g_m increase with scaling as shown in Fig. 8.5.

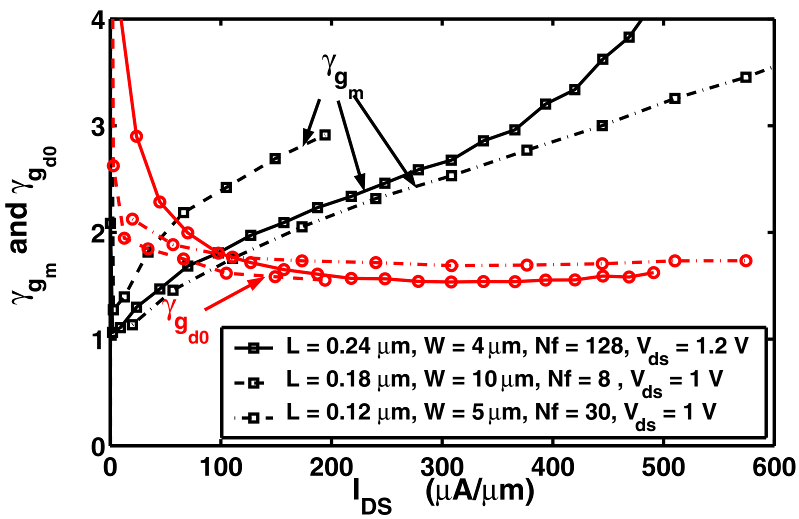

Figure 8.6: γ_{g_m} and $\gamma_{g_{d0}}$ vs I_{DS} for gate length of 0.24 μm, 0.18 μm, and 0.12 μm devices.

8.4 V_{ds} Dependence of Excess Noise Factor

Due to the limitation of measurement data, only gate length of 0.12 μm device and 0.24 μm device are discussed here.

8.4.1 0.24 μm device, W = 4 μm, Nf = 128.

Fig. 8.7 (a) shows γ_{i_d} and γ_{i_h} vs I_{DS} and V_{gs} at V_{ds} = 0.2 V and 1.2 V for 0.24 μm device. W = 4 μm, Nf = 128. γ_{i_d} is similar to but higher than γ_{i_h} for all biases. As V_{ds} increases, both γ_{i_d} and γ_{i_h} decrease. In section 6.7.1, modeling of γ_{i_h} is discussed for V_{ds} = 0.2 and 1.2 V. γ_{i_d} can be similarly modeled.

$$\gamma_{i_d} = \gamma_{i_d,0} + \gamma_{i_d,1} \cdot V_{gs} + \gamma_{i_d,2} \cdot {V_{gs}}^2, \tag{8.3}$$

$\gamma_{i_d,0} = 8.1166$, $\gamma_{i_d,1} = -19.5604$ and $\gamma_{i_d,2} = 13.7592$ for $V_{ds} = 0.2$ V, and $\gamma_{i_d,0} = 0.0810$, $\gamma_{i_d,1} = 1.4981$ and $\gamma_{i_d,2} = 0$ for $V_{ds} = 1.2$ V. Similar to analysis for γ_{i_h}, $\gamma_{i_d,0}$ and $\gamma_{i_d,2}$ increases with decreasing V_{ds}, while $\gamma_{i_d,1}$ decreases with decreasing V_{ds}.

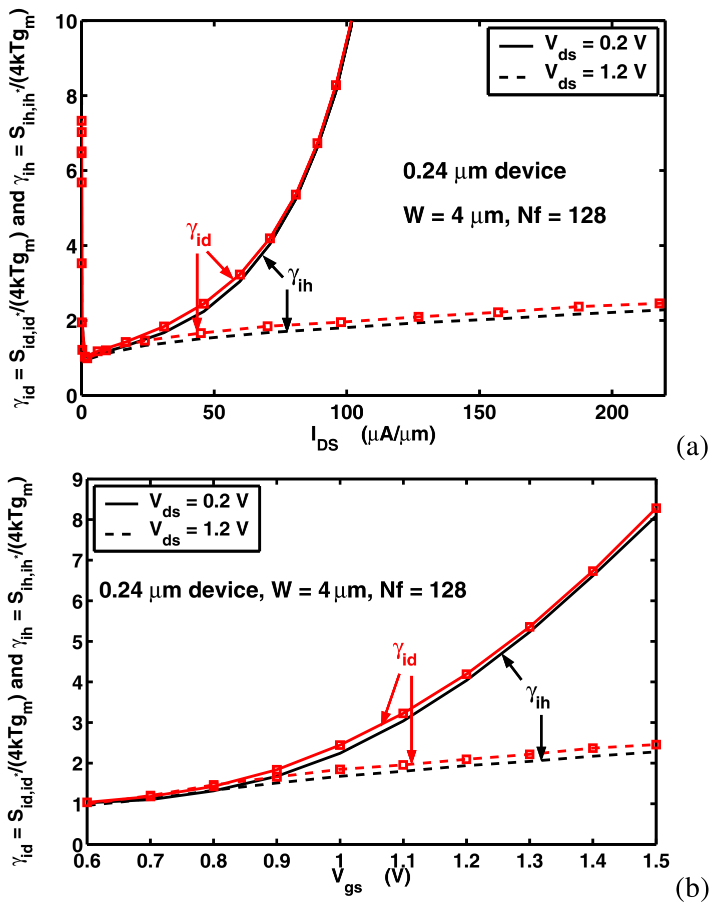

Figure 8.7: γ_{i_d} and γ_{i_h} (a) vs I_{DS}, and (b) vs V_{gs} at $V_{ds} = 0.2$ V and 1.2 V for 0.24 μm device. $W = 4$ μm, $Nf = 128$.

8.4.2 0.12 μm Device, W = 5 μm, Nf = 30.

Fig. 8.8 shows I_{DS} vs V_{gs} at $V_{ds} = 1$ V and 1.5 V for 0.12 μm device. $W = 5$ μm, $Nf = 30$. I_{DS} slightly increases with increasing V_{ds}. Fig. 8.9 shows I_{DS} vs V_{ds} at $V_{gs} = 0.7$, 1.0 and 1.5 V. I_{DS} does not increase much with increasing V_{DS} for $V_{gs} = 0.7$ and 1.0 V. For $V_{gs} = 1.5$ V, I_{DS} increases at lower V_{DS}, then saturates at higher V_{DS}.

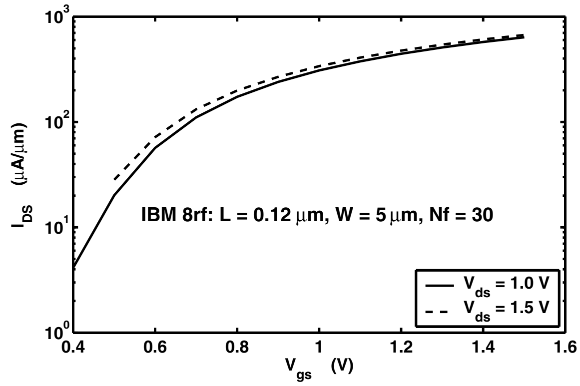

Figure 8.8: I_{DS} vs V_{gs} at $V_{ds} = 1$ V and 1.5 V for 0.12 μm device. $W = 5$ μm, $Nf = 30$.

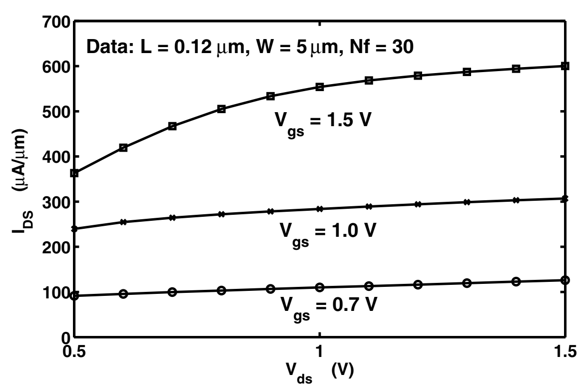

Figure 8.9: I_{DS} vs V_{ds} at $V_{gs} = 0.7$, 1.0 and 1.5 V for gate length of 0.12 μm device.

Fig. 8.10 shows the S_{i_d,i_d^*}, γ_{g_m} and $\gamma_{g_{d0}}$ vs V_{gs} at V_{ds} = 1 V and 1.5 V. Fig. 8.11 shows the S_{i_d,i_d^*}, γ_{g_m} and $\gamma_{g_{d0}}$ vs I_{DS} at V_{ds} = 1 V and 1.5 V.

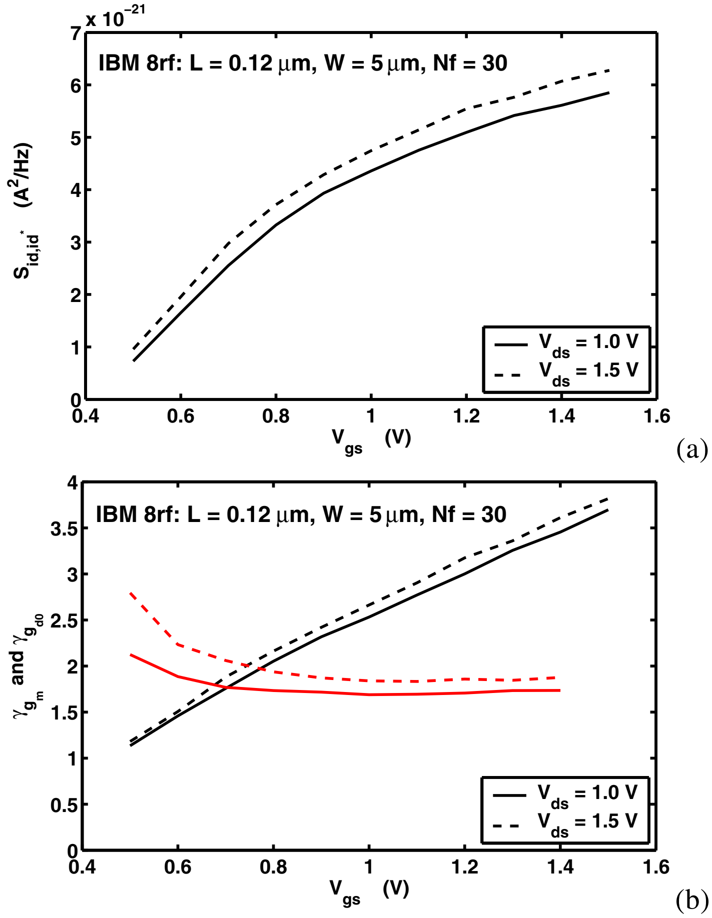

Figure 8.10: (a) S_{i_d,i_d^*}, and (b)γ_{g_m} and $\gamma_{g_{d0}}$ vs V_{gs} at V_{ds} = 1 V and 1.5 V for 0.12 μm device. W = 5 μm, Nf = 30.

Fig. 8.12 (a) shows S_{i_d,i_d^*} vs V_{ds} at V_{gs} = 0.7, 1.0 and 1.5 V. S_{i_d,i_d^*} is almost flat over V_{ds} at V_{gs} = 0.7 V. For V_{gs} = 1.0 and 1.5 V, however, S_{i_d,i_d^*} increases with increasing V_{ds}. Higher the V_{gs}, higher the slope of $S_{i_d,i_d^*} - V_{ds}$ curve. Fig. 8.12 (b) shows $\gamma_{g_{d0}}$ vs V_{ds} at V_{gs} = 0.7, 1.0 and 1.5 V for gate length of 0.12 μm device. $\gamma_{g_{d0}}$ slightly increases with increasing V_{ds}, and is the

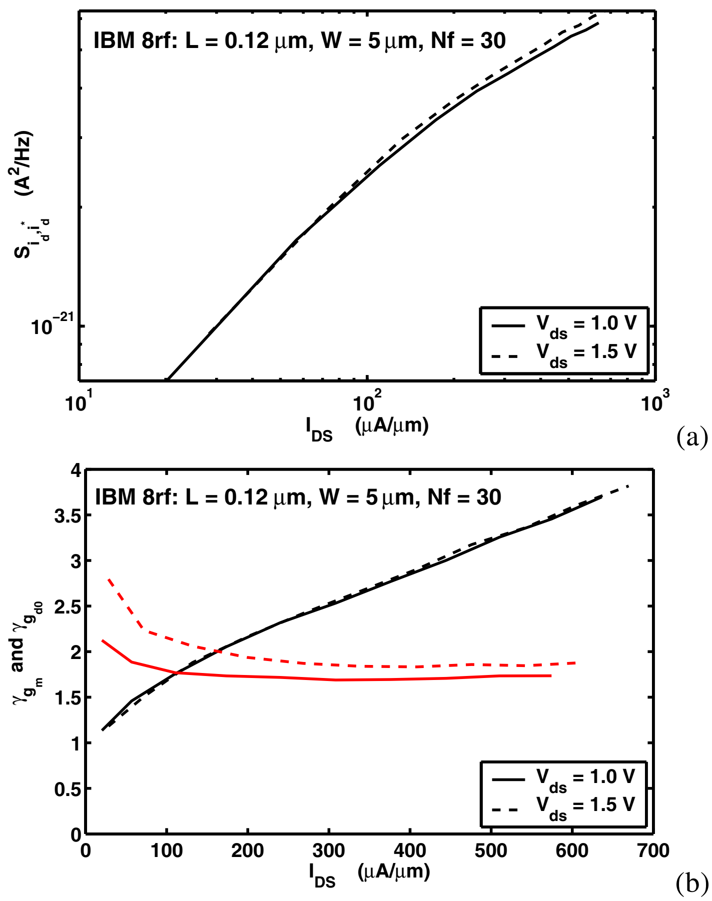

Figure 8.11: (a) S_{i_d,i_d^*}, and (b)γ_{g_m} and $\gamma_{g_{d0}}$ vs I_{DS} at V_{ds} = 1 V and 1.5 V for 0.12 μm device. W = 5 μm, Nf = 30.

lowest for V_{gs} = 1 V. Fig. 8.12 (c) shows γ_{g_m} vs V_{ds} at V_{gs} = 0.7, 1.0 and 1.5 V for gate length of 0.12 μm device. γ_{g_m} is almost flat over V_{ds} at V_{gs} = 0.7 and 1.0 V. For V_{gs} = 1.5 V, however, γ_{g_m} decreases in the linear region, then becomes flat in the saturation region.

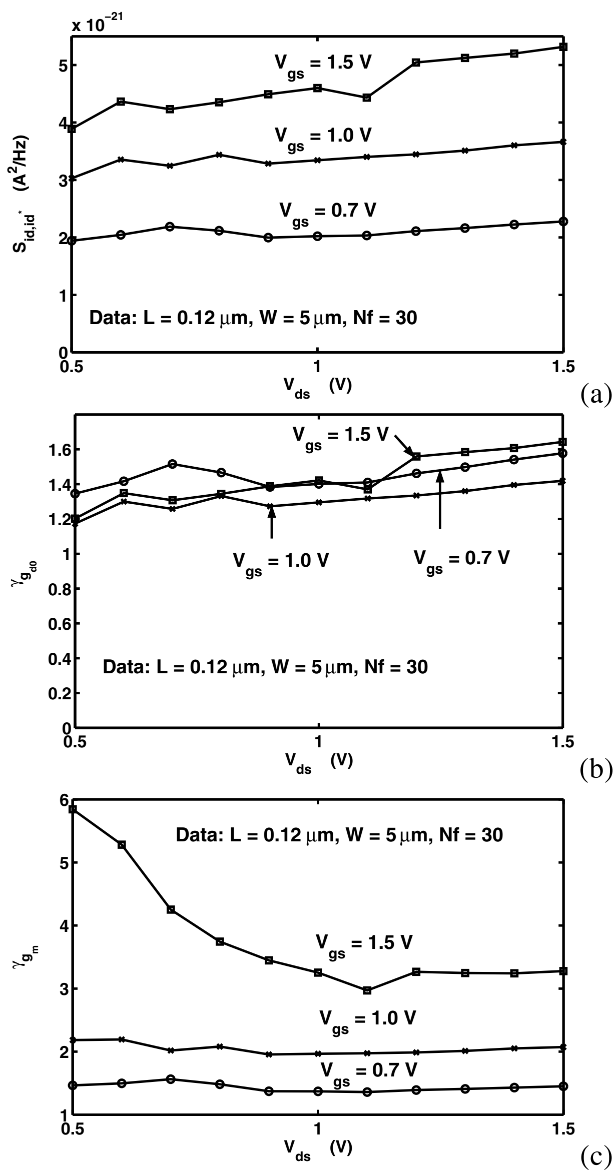

Figure 8.12: (a) S_{i_d,i_d^*}, (b) $\gamma_{g_{d0}}$, and (c) γ_{g_m} vs V_{ds} at V_{gs} = 0.7, 1.0 and 1.5 V for gate length of 0.12 μm device.

8.4.3 Simulation Results on 50 nm L_{eff} CMOS

In order to further investigate V_{ds} dependence of S_{i_d,i_d^*}, $\gamma_{g_{d0}}$, and γ_{g_m}, 50 nm L_{eff} gate length CMOS simulation results in chapter 6 are used. Fig. 8.13 shows S_{i_d,i_d^*}, $\gamma_{g_{d0}}$, and γ_{g_m} vs V_{gs} at V_{ds} = 0.1 V to 1.0 V with step of 0.1 V. S_{i_d,i_d^*} and $\gamma_{g_{d0}}$ increases with increasing V_{ds}. γ_{g_m} decreases with increasing V_{ds}.

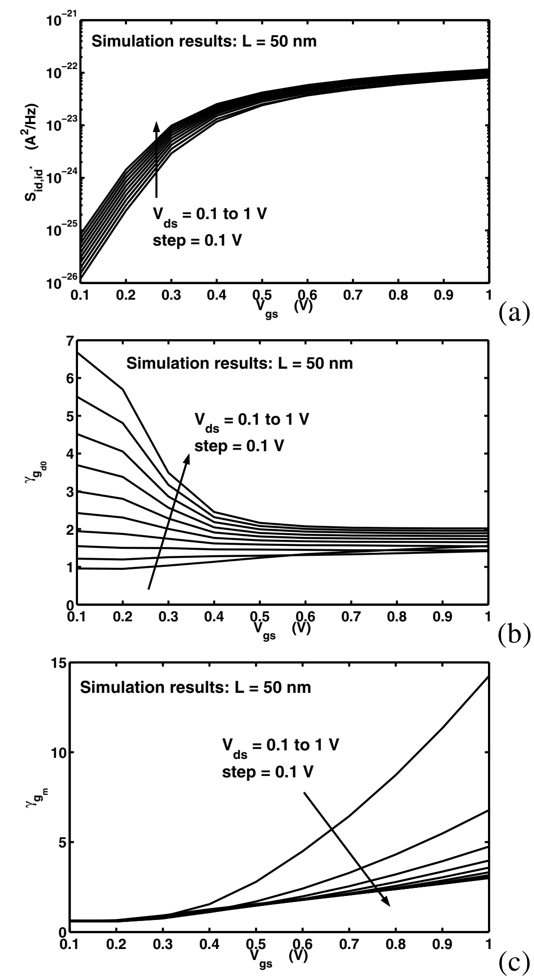

Figure 8.13: (a) S_{i_d,i_d^*}, (b) $\gamma_{g_{d0}}$, and (c) γ_{g_m} vs V_{gs} at $V_{ds} = 0.1$ V to 1.0 V with step of 0.1 V for 50 nm L_{eff} CMOS simulation.

Fig. 8.14 shows S_{i_d,i_d^*}, $\gamma_{g_{d0}}$, and γ_{g_m} vs I_{DS} at $V_{ds} = 0.1$ V to 1.0 V with step of 0.1 V. S_{i_d,i_d^*} vs I_{DS} almost does not change for V_{ds} above 0.3 V.

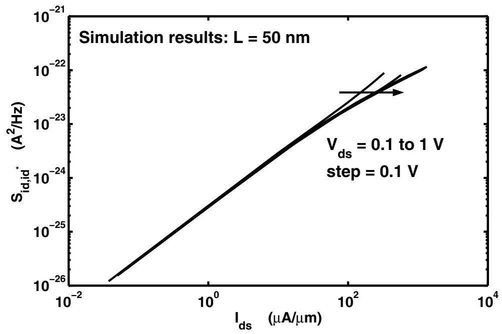

(a)

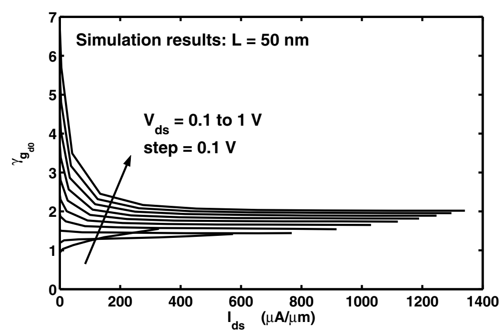

(b)

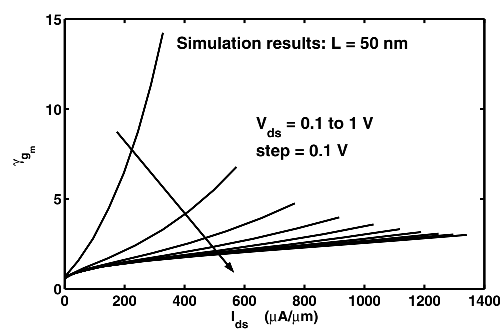

(c)

Figure 8.14: (a) S_{i_d,i_d^*}, (b) $\gamma_{g_{d0}}$, and (c) γ_{g_m} vs I_{DS} at $V_{ds} = 0.1$ V to 1.0 V with step of 0.1 V for 50 nm L_{eff} CMOS simulation.

Fig. 8.15 shows simulation-model comparison of γ_{g_m} vs I_{DS} and vs V_{gs} at $V_{ds} = 0.1$ V to 1.0 V with step of 0.1 V. γ_{g_m} is modeled using (8.3). Excellent simulation-model agreement are obtained. The V_{ds} dependence of the model parameters $\gamma_{i_d,0}$, $\gamma_{i_d,1}$ and $\gamma_{i_d,2}$ are shown in Fig. 8.16. $\gamma_{i_d,0}$ and $\gamma_{i_d,2}$ decreases as V_{ds} increases. $\gamma_{i_d,1}$ increases as V_{ds} increases. The simulation results complies with the measurement data analysis for the above 0.24 μm device.

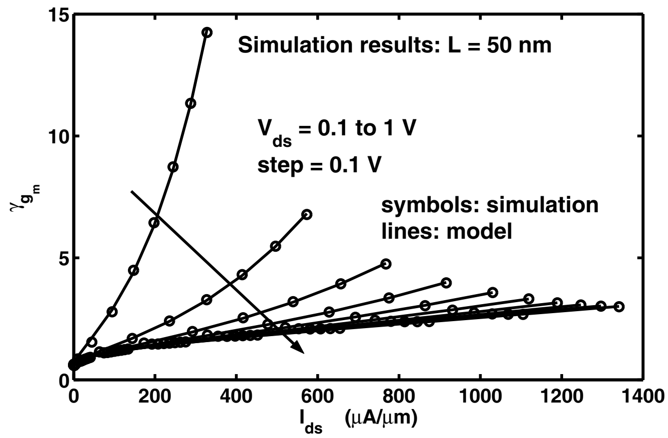

(a)

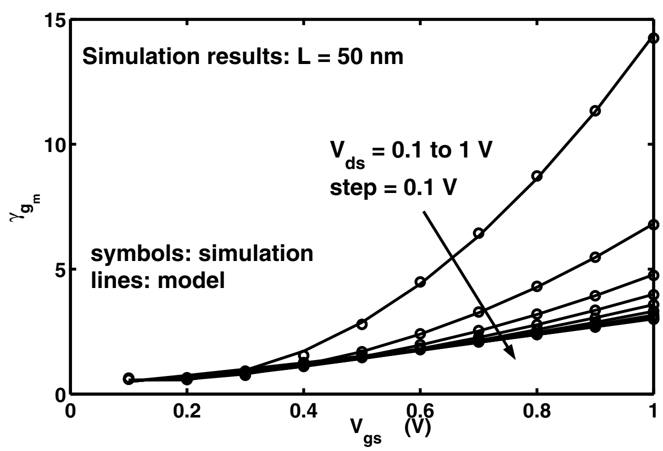

(b)

Figure 8.15: γ_{g_m} (a) vs I_{DS}, and (b) vs V_{gs} at $V_{ds} = 0.1$ V to 1.0 V with step of 0.1 V for 50 nm L_{eff} CMOS simulation.

$\gamma_{i_d,2}$, $\gamma_{i_d,1}$, and $\gamma_{i_d,0}$ can be further modeled as function of V_{ds}.

$$\gamma_{i_d,2} = 10^{[-0.4475(\log_{10} V_{ds})^4 - 1.7225(\log_{10} V_{ds})^3 - 2.5302(\log_{10} V_{ds})^2 - 2.8588(\log_{10} V_{ds}) - 0.3274]}, \quad (8.4)$$

$$\gamma_{i_d,1} = 10^{[-0.1552(\log_{10} V_{ds})^4 - 0.3067(\log_{10} V_{ds})^3 - 0.2801(\log_{10} V_{ds})^2 - 0.0093(\log_{10} V_{ds}) + 1.5063]} - 30, \quad (8.5)$$

$$\gamma_{i_d,0} = 10^{[-0.0698(\log_{10} V_{ds})^2 - 0.6374(\log_{10} V_{ds}) - 0.5782]}. \quad (8.6)$$

The calulations using model equations (8.4) – (8.6) are compared to model parameters $\gamma_{i_d,2}$, $\gamma_{i_d,1}$, and $\gamma_{i_d,0}$ in Fig. 8.16. Excellent agreement has been achieved. Therefore, γ_{g_m} at certain V_{ds} and V_{gs} can be modeled using 14 constant coefficients in (8.4) – (8.6), together with (8.3).

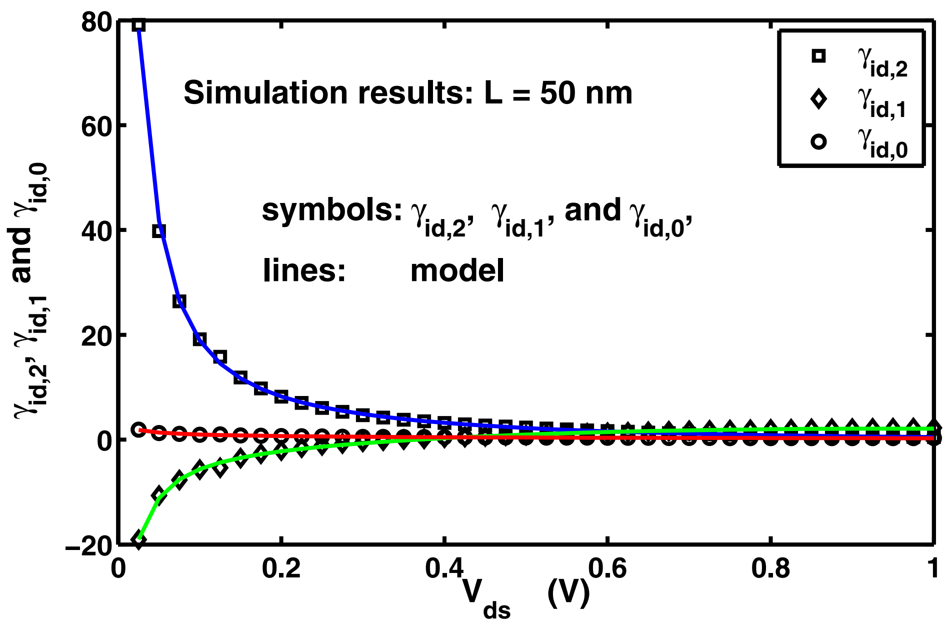

Figure 8.16: $\gamma_{i_d,0}$, $\gamma_{i_d,1}$ and $\gamma_{i_d,2}$ vs V_{ds} for 50 nm L_{eff} CMOS simulation.

8.5 Noise Parameter Equations

Fig. 8.17 shows a simplified MOSFET equivalent circuit including gate resistance noise and drain current noise. The Y matrix of the intrinsic device is denoted by Y^{intr}. We first consider only the intrinsic MOSFET without R_g, and consider only the drain current noise i_d.

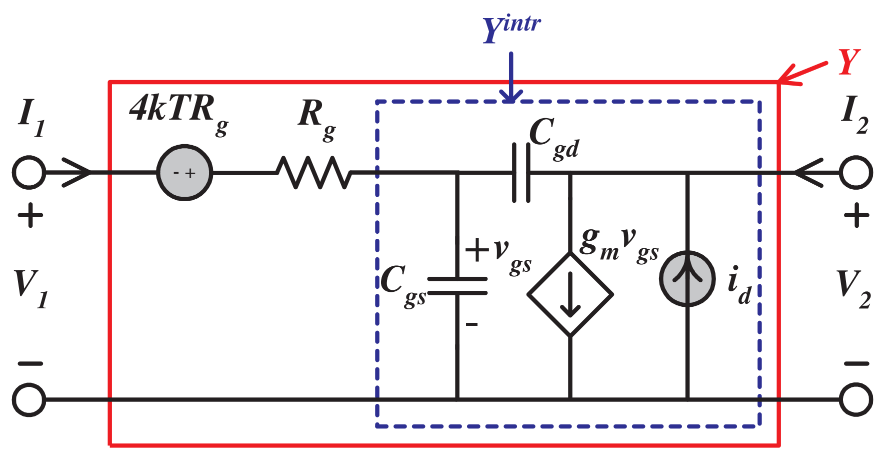

Figure 8.17: MOSFET equivalent circuit with drain current noise and gate resistance noise.

We first convert i_d into v_a and i_a, input voltage and current,

$$v_a = -\frac{i_d}{Y_{21}^{intr}}, \tag{8.7}$$

$$i_a = -\frac{i_d}{h_{21}^{intr}}. \tag{8.8}$$

For the dashed box in Fig. 8.17,

$$Y_{21}^{intr} \approx g_m, \tag{8.9}$$

$$Y_{11}^{intr} = j\omega C_i, \tag{8.10}$$

$$h_{21}^{intr} = \frac{Y_{21}^{intr}}{Y_{11}^{intr}} = \frac{g_m}{j\omega C_i} = \frac{1}{j}\frac{f_T}{f}, \tag{8.11}$$

where $C_i = C_{gs} + C_{gd}$, and f_T is cutoff frequency. The PSDs of v_a, i_a and their correlation are then obtained as

$$S_{v_a,v_a^*} = \frac{< v_a, v_a^* >}{\Delta f} = \frac{S_{i_d,i_d^*}}{|Y_{21}^{intr}|^2} \approx \frac{S_{i_d,i_d^*}}{g_m^2}, \tag{8.12}$$

$$S_{i_a,i_a^*} = \frac{< i_a, i_a^* >}{\Delta f} = \frac{S_{i_d,i_d^*}}{|h_{21}^{intr}|^2} \approx \left(\frac{f}{f_T}\right)^2 S_{i_d,i_d^*}, \tag{8.13}$$

$$S_{i_a,v_a^*} = \frac{< i_a, v_a^* >}{\Delta f} = \frac{S_{i_d,i_d^*}}{|Y_{21}^{intr}|^2} Y_{11}^{intr} \approx j\frac{f}{f_T} \cdot \frac{S_{i_d,i_d^*}}{g_m}. \tag{8.14}$$

Now we add the gate resistance as shown in Fig. 8.17. The primary effect is an increase in S_{v_a,v_a^*},

$$S_{v_a,v_a^*} \approx \frac{S_{i_d,i_d^*}}{|Y_{21}^{intr}|^2} + 4kTR_g \approx \frac{S_{i_d,i_d^*}}{g_m^2} + 4kTR_g. \tag{8.15}$$

S_{v_a,v_a^*}, S_{i_a,i_a^*}, and S_{i_a,v_a^*} can then be used to calculate NF_{min}, R_n and Y_{opt} using standard equations in [11] as

$$NF_{min} = 10\log_{10}\left(1 + \frac{f}{f_T}\sqrt{\frac{S_{i_d,i_d^*}}{kT}R_g}\right), \tag{8.16}$$

$$R_n = \frac{\gamma_{g_m}}{g_m} + R_g = \frac{S_{i_d,i_d^*}/4kT}{g_m^2} + R_g, \tag{8.17}$$

$$G_{opt} = g_m\frac{f}{f_T}\cdot\frac{\sqrt{\gamma_{g_m}g_mR_g}}{\gamma_{g_m} + g_mR_g}, \tag{8.18}$$

$$B_{opt} = -g_m\frac{f}{f_T}\cdot\frac{\gamma_{g_m}}{\gamma_{g_m} + g_mR_g}. \tag{8.19}$$

$Z_{opt} = R_{opt} + jX_{opt}$ is also calculated from $1/Y_{opt}$ as

$$R_{opt} = \frac{f_T}{f}\sqrt{\frac{R_g}{\gamma_{g_m}g_m}} = \frac{g_m}{2\pi fC_i}\frac{4kT}{S_{i_d,i_d^*}}\cdot\sqrt{R_g}, \tag{8.20}$$

$$X_{opt} = \frac{f_T}{f}\cdot\frac{1}{g_m} = \frac{1/2\pi}{fC_i}, \tag{8.21}$$

Note that γ_{g_m} appears directly in the R_n, R_{opt}, and X_{opt} expressions. We can also write the NF_{min} expression (8.16) by replacing S_{i_d,i_d^*} with $4kT\gamma_{g_m}g_m$,

$$NF_{min} = 10\log_{10}\left(1 + 2\sqrt{\gamma_{g_m}}\frac{f}{f_T}\sqrt{g_mR_g}\right). \tag{8.22}$$

8.6 Comparison with Fukui's Equations

Based on experimental data in GaAs MESFETs, Fukui proposed the following empirical equations [31] [32]

$$NF_{min} = 10\log_{10}\left(1 + K_f \frac{f}{f_T}\sqrt{g_m R_g}\right), \tag{8.23}$$

$$R_n = \frac{K_2}{g_m^2}, \tag{8.24}$$

$$R_{opt} = K_3\left(\frac{1}{4g_m} + R_g\right), \tag{8.25}$$

$$X_{opt} = \frac{K_4}{fC_{gs}}, \tag{8.26}$$

where K_f, K_2, K_3 and K_4 were proposed to be bias independent and channel length independent [31]. R_n was later modified in [33] as

$$R_n = \frac{K_2^n}{g_m}, \tag{8.27}$$

where $K_2^n = 0.8$.

An inspection of (8.23) and (8.22) immediately shows:

$$K_f = 2\sqrt{\gamma_{g_m}}, \tag{8.28}$$

which gives a meaning to Fukui's noise figure coefficient. For long channel device operating in saturation region (strong inversion), $\gamma_{g_m} = \gamma_{g_{d0}} = 2/3$ [15], and $K_f = 1.633$. This is close to the empirical $K_f = 2$ in [31] and [32], which was also proposed to be channel length independent at the minimum NF_{min} bias point [31]. This is not the case for short channel CMOS, in which

$K_f = 2\sqrt{\gamma_{g_m}}$ becomes strongly bias dependent, as shown in Fig. 8.2. The bias dependence of γ_{g_m} is primarily due to the strong bias dependence of g_{d0}/g_m in short channel devices, as was shown in Fig. 8.1. This indicates that there does not exist a bias independent or channel length independent universal Fukui's noise figure coefficient for RF CMOS. We therefore cannot use (8.23) for low-noise optimization, as was done in [31] and [40].

Comparing (8.24), (8.27) and (8.17),

$$K_2 = \frac{S_{i_d,i_d^*}}{4kT} = \gamma_{g_m} g_m, \tag{8.29}$$

$$K_2^n = \frac{S_{i_d,i_d^*}}{4kTg_m} = \gamma_{g_m} \tag{8.30}$$

for g_m related terms. The R_g term was not included in Fukui's R_n equation because of the low R_g due to the use of metal gate in MESFETs, but is important for CMOS. Clearly neither S_{i_d,i_d^*} nor γ_{g_m} is a constant. Instead, both S_{i_d,i_d^*} and γ_{g_m} should be bias and channel length dependent.

A comparison of (8.25) and (8.20) shows that the inverse frequency dependence is not considered in Fukui's R_{opt} equation. A comparison of (8.26) and (8.21) shows

$$K_4 = 1/2\pi, \tag{8.31}$$

which is indeed a constant. Note that C_{gd} was not included in (8.26). Table I summarizes the "physical meanings" of $K_1 - K_4$.

8.7 Model Validation

For validation, we compare measured and simulated noise parameters. Here we use the 8 finger device as an example. S-parameters and noise parameters are measured from 2 to 20 GHz.

Table 8.1: Comparison of Fukui empirical constants with our derivation.

	Empirical equations [31] [32]	Our derivation
NF_{min}	$K_f = 2$	$2\sqrt{\gamma_{g_m}}$
R_n	K_2 $K_2^n = 0.8$ [33] (R_g not included)	$\frac{S_{i_d,i_d^*}}{4kT} = \gamma_{g_m} g_m$ γ_{g_m} (R_g included)
R_{opt}	K_3 (f independent)	$\frac{4g_m^2\sqrt{R_g}}{2\pi f C_i \gamma_{g_m}(1+4g_m R_g)}$ (f dependent)
Z_{opt}	K_4 (C_{gd} not included)	$1/2\pi$ (C_{gd} included)

V_{ds} is fixed at 1.5V, and V_{gs} is swept. R_g, g_m, and f_T are extracted from y-parameters. The R_s and R_d extracted from dc measurements are negligibly small. S_{i_d,i_d^*} is extracted from measured NF_{min}, R_n, and Y_{opt} through standard noise de-embedding [43] [11].

For each parameter, comparisons are shown in Fig. 8.18 as a function of frequency at a fixed V_{gs} of 0.7 V, and then in Fig. 8.19 as a function of bias at a fixed frequency of 5 GHz. Good model-data correlation is achieved for both bias and frequency dependence of NF_{min}. A fairly good correlation between model and data is observed for both bias and frequency dependence of R_n. R_n is flat over frequency. With increasing V_{gs}, R_n decreases first and then stays nearly constant, as expected from (8.17). Fairly good model-data correlation is observed for both bias and frequency dependence of G_{opt}. G_{opt} is positive and linearly increases with frequency, as expected from (8.18). G_{opt} is only weakly dependent on V_{gs} after g_m and f_T reach their peaks. A larger discrepancy is observed at higher frequencies, which is related to the use of a simplified equivalent circuit model. For frequencies below 5 GHz, the intended RF design frequencies for a 0.18 μm process, the model still works reasonably well over all biases.

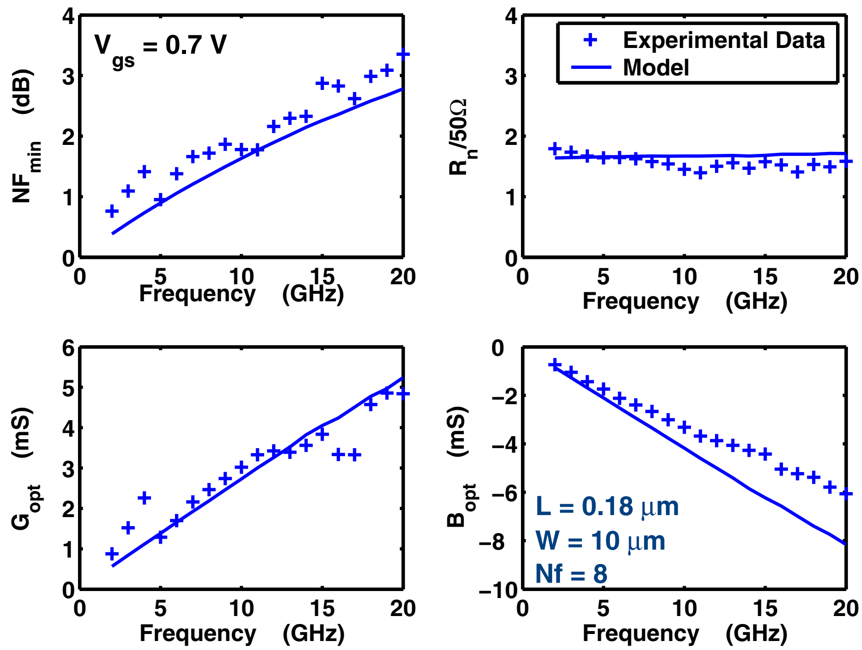

Figure 8.18: Model-data comparison of noise parameters vs frequency. $V_{gs} = 0.7$ V, $V_{ds} = 1$ V.

8.8 Figure-of-Merit for NF_{min}

An inspection of (8.16) shows that it is the absolute value of the drain current noise S_{i_d,i_d^*} that fundamentally determines NF_{min}. The Fukui's noise figure coefficient, the K_f factor, which is historically used as a figure-of-merit for comparing the noise figure capability of different technologies, is less applicable to CMOS, as it is strongly bias dependent through γ_{g_m}.

Similarly, the γ_{g_m} excess noise factor cannot be used as a figure-of-merit for measuring the minimum noise figure capability of a technology, even though it appears in (8.22). The product of γ_{g_m} and g_m simply leads us back to S_{i_d,i_d^*}. One can also decompose S_{i_d,i_d^*} into the product of $\gamma_{g_{d0}}$ and g_{d0}, however, it is the S_{i_d,i_d^*} value that matters.

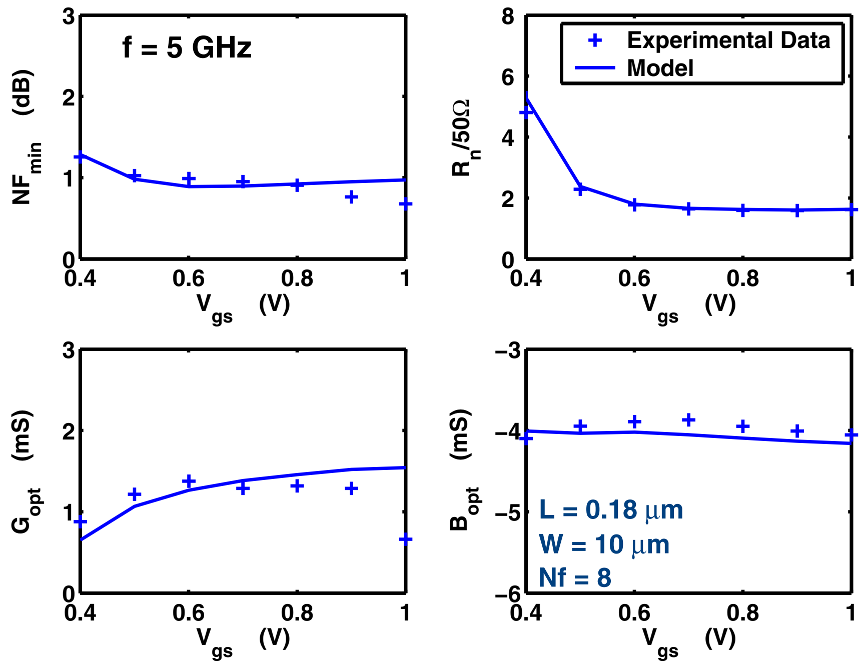

Figure 8.19: Model-data comparison of noise parameters vs V_{gs}, $f = 5$ GHz, $V_{ds} = 1$ V.

To propose a figure-of-merit for measuring the intrinsic transistor low noise capability, we rewrite (8.16) as

$$F_{min} - 1 = f \cdot K_{NF} \cdot \sqrt{\frac{W_{total} \cdot R_g}{kT}}, \tag{8.32}$$

where K_{NF} is the proposed new figure-of-merit for NF_{min}

$$K_{NF} = \frac{\sqrt{S_{i_d,i_d^*}/W_{total}}}{f_T}, \tag{8.33}$$

and W_{total} is the total device width, $W_{total} = W \times N_f$. The normalization to W_{total} is made to make K_{NF} device width independent. The $\sqrt{W_{total} R_g}$ term can be minimized through layout techniques, while the K_{NF} factor represents the noise capability of the intrinsic device, and essentially represents the amount of noise current generated in order to achieve one GHz f_T.

Fig. 8.20 show $\sqrt{S_{i_d,i_d^*}/(W \cdot N_f)}$, f_T, and the K_{NF} factor vs log scale I_{DS} and linear scale I_{DS} respectively for the 0.18 μm process. Similarly, Fig. 8.21 show $\sqrt{S_{i_d,i_d^*}/(W \cdot N_f)}$, f_T, and the K_{NF} factor vs I_{DS} for the 0.25 μm process, the 0.18 μm process, and the 0.12 μm process. Different normalizations are used to plot all quantities on the same scale. The same noise measurements were made on the 0.25 μm process and 0.12 μm process, from which S_{i_d,i_d^*} was extracted. Observe that with increasing I_{DS}, both f_T and S_{i_d,i_d^*} increase, as expected. The K_{NF} factor, which is a direct indicator of NF_{min}, decreases rapidly first as the device turns on, reaches a minimum at a moderate I_{DS} when V_{gs} is slightly above threshold voltage. This corresponds to the bias for minimum NF_{min}, at which the lowest amount of noise is generated for one GHz f_T, or the same amount of f_T is achieved with the least amount of noise.

With technology scaling, both S_{i_d,i_d^*} and f_T increase as shown in Fig. 8.22 (a) and (b). Only when the f_T increase dominates over the S_{i_d,i_d^*} increase, NF_{min} improves (decreases) with scaling. This differs from the conventional wisdom that a higher f_T in scaled device directly leads to improved NF_{min}, a result from Fukui's empirical NF_{min} equation. Fig. 8.22 (c) compares the K_{NF} factor of the 0.25 μm process, 0.18 μm process and 0.12 μm process. Indeed, the K_{NF} factor, which directly determines intrinsic device NF_{min}, decreases (improves) with technology scaling from 0.25 μm, 0.18 μm to 0.12 μm, because the f_T increase with scaling dominates the drain current noise increase with scaling. The K_{NF} factor does not include the $R_g \cdot W_{total}$ effect by design to measure only intrinsic device noise figure. The $R_g \cdot W_{total}$ term in (8.32), however, can increase with scaling in a silicided poly gate process, which may ultimately limit overall device NF_{min}, as detailed below. In order to compare technologies with different gate material or devices with different layout, we define another noise figure-of-merit to include the effect of $R_g \cdot W_{total}$,

$$K_{NF,R_g} = \frac{1}{f_T}\sqrt{\frac{S_{i_d,i_d^*}}{kT}R_g} = K_{NF}\sqrt{\frac{R_g W_{total}}{kT}}, \tag{8.34}$$

and

$$F_{min} = 1 + f \cdot K_{NF,R_g}. \tag{8.35}$$

Fig. 8.23 compares the K_{NF,R_g} of three devices, one from the 0.18 μm process with $W = 10$ μm, $N_f = 8$, and the other two from the 0.25 μm process with $W = 4$ μm, $N_f = 128$, and the 0.12 μm process with $W = 5$ μm, $N_f = 30$. Note that the gate finger width is much larger for the 0.18 μm device. $R_g \cdot W_{total}$ is 2000 $\Omega\mu m$ for the 0.18 μm device, 307.2 $\Omega\mu m$ for the 0.25 μm device, and 780 $\Omega\mu m$ for the 0.12 μm device. Even though K_{NF}, a measure of the intrinsic device noise, is smaller in the 0.18 μm device, K_{NF,R_g} and hence NF_{min} are higher in the 0.18 μm device, because of the much smaller $R_g \cdot W_{total}$. The combination of a smaller gate length L and a larger gate finger width W results in the higher $R_g \cdot W_{total}$ in the 0.18 μm device, despite reduced gate sheet resistance (10.8 $\Omega/\square$ for 0.18μm processes, 13.8 $\Omega/\square$ for 0.25 μm processes, and 11.2 $\Omega/\square$ for 0.12 μm processes). A smaller finger gate width, e.g. 2 μm, should be used to decrease K_{NF,R_g} and hence NF_{min} of the 0.18 μm device.

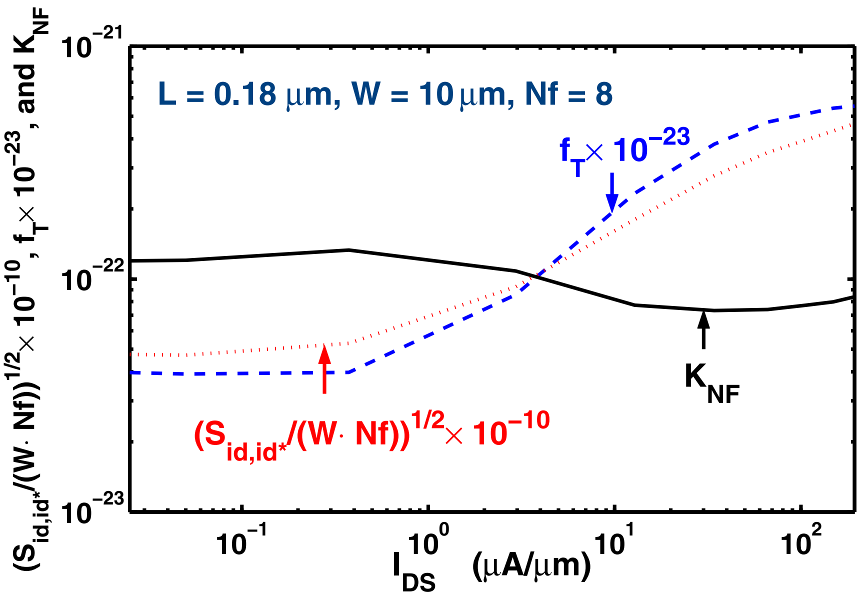

(a)

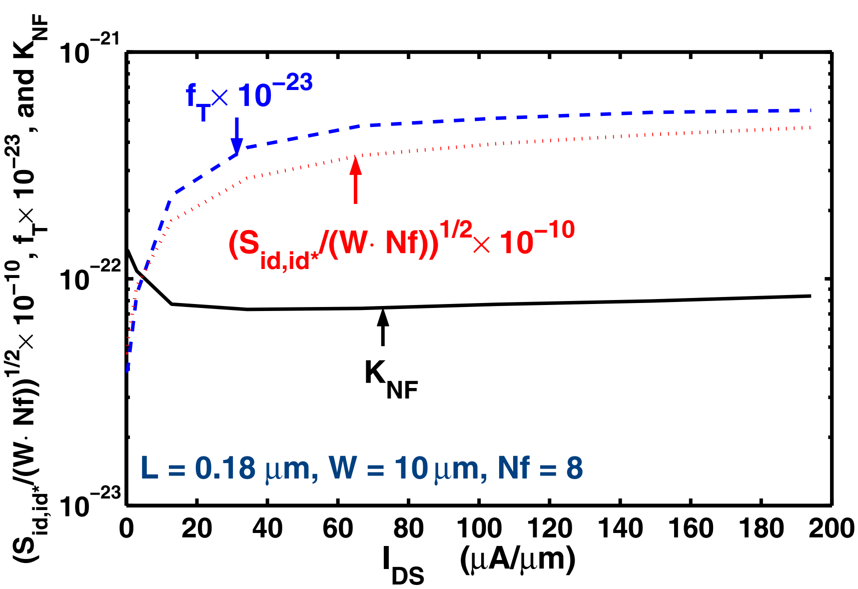

(b)

Figure 8.20: $\sqrt{S_{i_d,i_d^*}/(W \cdot N_f)}$, f_T, and K_{NF} vs (a) log scale I_{DS}, and (b) linear scale I_{DS} for the 0.18 μm process, with S_{i_d,i_d^*} in unit of A^2/Hz, W in unit of μm, f_T in unit of GHz, and K_{NF} in unit of $A/\sqrt{\mu m H z^3}$.

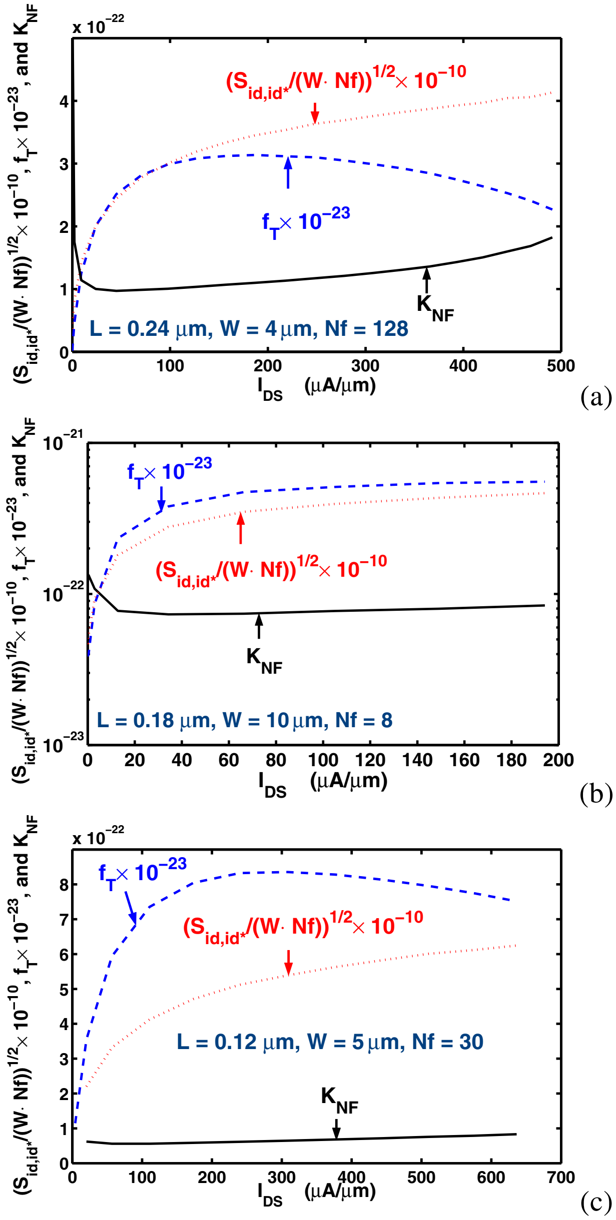

Figure 8.21: $\sqrt{S_{i_d,i_d^*}/(W \cdot N_f)}$, f_T, and K_{NF} vs I_{DS} for (a) the 0.25 μm process, (b) the 0.18 μm process, and (c) the 0.12 μm process, with S_{i_d,i_d^*} in unit of A^2/Hz, W in unit of μm, f_T in unit of GHz, and K_{NF} in unit of $A/\sqrt{\mu m Hz^3}$.

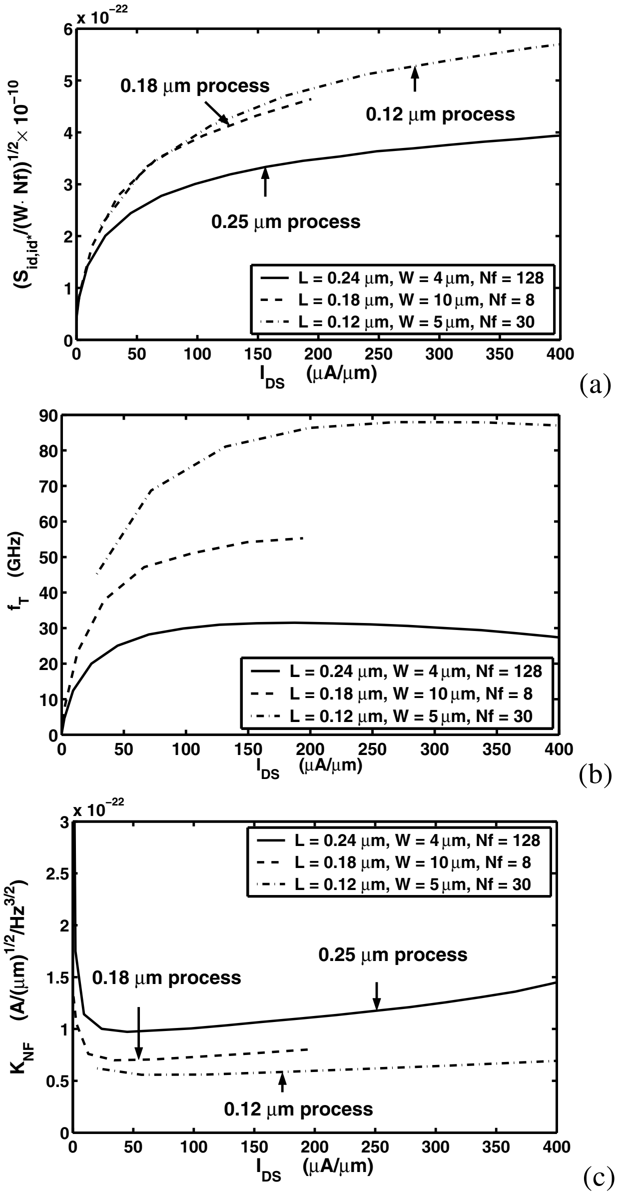

Figure 8.22: (a) $\sqrt{S_{i_d,i_d^*}/(W \cdot N_f)}$, (b) f_T, and (c) K_{NF} vs I_{DS} comparison between a 0.25 μm process, a 0.18 μm process, and a 0.12 μm process.

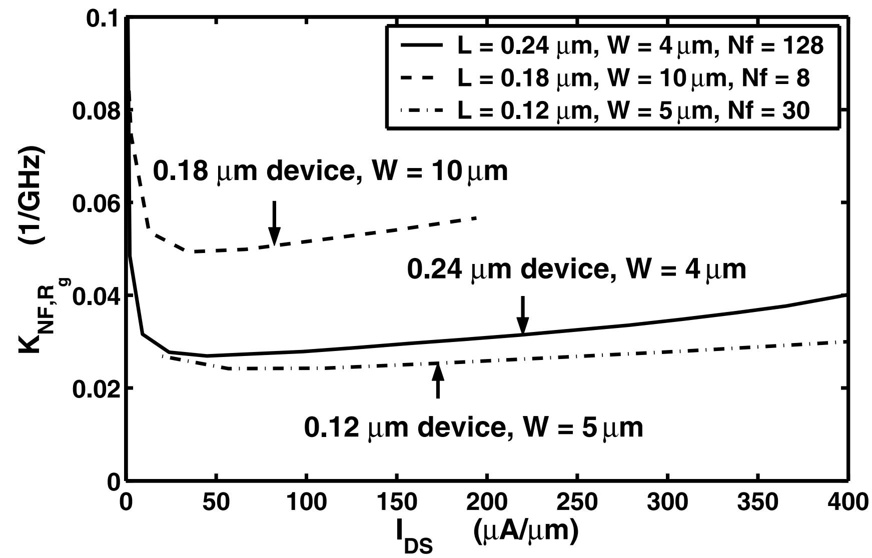

Figure 8.23: K_{NF,R_g} vs I_{DS} comparison between a 0.18 μm process device with $W = 10$ μm, a 0.25 μm process device with $W = 4$ μm, and a 0.12 μm process device with $W = 5$ μm.

8.9 Summary

The difference between g_{d0} and g_m referenced excess noise factors in CMOS transistors is examined. The technology scaling are discussed for 0.25 μm process, 0.18 μm process and 0.12 μm process. A simple set of analytical equations for NF_{min}, R_n and Y_{opt} (or Z_{opt}) is derived. The equations are compared with Fukui's empirical noise equations to identify the physical meanings of various Fukui "constants," and validated using experimental data. The results show that there does not exist a bias independent or channel length independent Fukui's coefficient for the well known NF_{min} equation. Instead, the amount of drain current noise produced to achieve one GHz f_T fundamentally determines the NF_{min} of the intrinsic device, and can be used as a figure-of-merit to better measure the intrinsic noise figure capability of a technology. With technology scaling from 0.25 μm to 0.18 μm, both f_T and drain current noise increase. The f_T increase, however, dominates over the drain current noise increase, thus improving the minimum noise figure of the intrinsic device. Another figure-of-merit is proposed to include the effect of gate resistance which facilitates layout optimization for low noise and evaluation of the relevant importance of gate resistance noise with respect to drain current noise in determining NF_{min}.

CHAPTER 9

CONCLUSIONS

In this dissertation, detailed information about RF bipolar and CMOS noise in terms of device physics were provided. To achieve these goals, this dissertation has tackled various areas including microscopic noise simulation, Ge profile optimization in SiGe HBT device, noise characterization, and compact noise modeling.

Chapter 1 gave an introduction of definitions and classifications of RF device noise and noise parameters. Review of RF bipolar and CMOS noise models and the intrinsic noise sources in RF bipolar and CMOS devices was also given in chapter 1. Different noise representations for a linear noisy two-port network were introduced in chapter 2. The transformation matrices to other noise representations were given for ABCD-, Y-, Z-, and H- noise representations. Techniques of adding or de-embedding a passive component to a linear two-port network were discussed. Noise sources de-embedding for both MOSFET and SiGe HBT were given for repeatedly use in later chapters.

In chapter 3, a new technique of simulating the spatial distribution of microscopic noise contribution to the input noise current, voltage, as well as their cross-correlations were presented. The technique was first demonstrated on a 50 GHz SiGe HBT. The spatial contributions by base majority holes, base minority electrons, and emitter minority holes were analyzed, and compared to results from a compact noise model. A strong crowding effect was observed in the spatial distribution of noise concentrations due to base majority holes. The results suggest that 2D distributive effect needs to be taken into account in future compact noise model development. The technique was also applied to a 46 nm L_{eff} MOSFET transistor. The spatial distribution of the Y- noise representation parameters $C_{S_{i_g,i_g^*}}$, $C_{S_{i_d,i_d^*}}$, $\Re(C_{S_{i_g,i_d^*}})$ and $\Im(C_{S_{i_g,i_d^*}})$ were analyzed. The region under the gate near the source side is the most important for all of the Y- noise representation parameters.

Bipolar transistor noise modeling for each physical noise source using microscopic noise simulation were examined in chapter 4. Regional analysis was performed for the chain representation noise parameters. The base majority hole noise contribution was shown to be larger than modeled using $4kTr_b$ and frequency dependent for all noise parameters. The $2qI_B$ related terms underestimates the emitter hole noise, especially for higher frequencies. The base minority electron contribution is poorly modeled by the $2qI_C$ related terms for all noise parameters, particularly for higher J_C required for high speed. Further, regional analysis for intrinsic transistor input and output noise current was performed. The input noise current consists not only the emitter hole contribution corresponding to $2qI_B$, but also the base electron and hole contribution which are frequency dependent and should be counted for especially at high frequencies. At higher J_C, the output noise current consists not only the base electron contribution corresponding to $2qI_C$, but also the base hole contribution that not counted for in the compact noise model. Moreover, the frequency dependence of base electron contribution is not described. The correlation term which is not modeled in the compact noise model should be considered for higher J_C and higher frequency. Chapter 4 also compared the intrinsic transistor input and output noise current with a noise model that derived from the transport theory of density fluctuations that applied to three dimensional device. The comparison showed that this model has a better description of frequency dependence than the compact noise model at low bias. However, as for higher J_C, it has no advantage over the compact noise model.

RF noise physics in advanced SiGe HBTs using microscopic noise simulation was explored in chapter 5. SiGe profile primarily affects the minimum noise figure through the input noise current, and identified the small region near the EB junction as where most of the input noise current originates. A higher Ge gradient in this region helps reducing the impedance field for the input noise current. At constant SiGe film stability, increasing the Ge gradient in the noise critical region ultimately necessitates retrograding of Ge inside the neutral base, and the gradient of such Ge retrograding needs to be optimized within stability limit to minimize high injection f_T rolloff degradation. An example of successful SiGe profile optimization using unconventional Ge retrograding inside the base was presented.

In chapter 6, microscopic RF noise simulation results on 50 nm L_{eff} CMOS devices were presented, and the compact modeling of intrinsic noise sources for both the Y-representation and the H-representation were examined. The correlation was shown to be smaller for the H-representation than for the Y-representation. For practical biasing currents and frequencies, the correlation is negligible for H-representation. Models for the noise sources were suggested. Furthermore, the relations between the Y- and H-noise representations for MOSFETs were examined , and the importance of correlation for both representations were quantified. The theoretical values of α_{v_h}, γ_{i_h} and c_H were derived for the first time for long channel devices, $\alpha_{v_h} = 4/3$, $\gamma_{i_h} = 0.6$, $a = 0.2458$, and $b = 0$. c_H is shown theoretically to have a zero imaginary part. It was further shown that Y-representation is a better choice for R_n, and the H-representation has the inherent advantage of a more negligible correlation for NF_{min}, G_{opt}, and B_{opt}. Overall, the importance of correlation is much more negligible for H-representation than for Y-representation. This makes circuit design and simulation easier. Chapter 6 also presented experimental extraction and modeling of H-representation noise sources in a 0.25 μm RF CMOS process. Excellent agreement was achieved between modeled and measured noise data, including all noise parameters, for the whole bias range, from 2 to 26 GHz. The results suggest a new path to RF CMOS noise modeling.

An anomalous frequency dependence and bias dependence of $\Re(h_{11})$ was observed in chapter 7. $\Re(h_{11})$ decreases with frequency, and increases with V_{gs} at low biases. It was shown that both the frequency dependence and bias dependence can be understood by considering the gate-to-body capacitance and the parasitic gate-to-source capacitances as capacitances in parallel with the series combination of the NQS resistance and inversion capacitance C_{gs}. A new parameter extraction method was developed to separate the physical gate resistance and the NQS channel resistance. The modeling results showed excellent agreement with data, and suggest the importance of modeling NQS effect for RF CMOS even at frequencies well below f_T of the technology. The proposed model parameter extraction method can be used to facilitate MOSFET noise modeling and more accurate Y-parameter modeling over a wide bias range.

The difference between g_{d0} and g_m referenced excess noise factors in CMOS transistors was examined in chapter 8. The technology scaling were discussed for 0.25 μm process, 0.18 μm process and 0.12 μm process. A simple set of analytical equations for NF_{min}, R_n and Y_{opt} (or Z_{opt}) was derived. The equations were compared with Fukui's empirical noise equations to identify the physical meanings of various Fukui "constants," and validated using experimental data. The results showed that there does not exist a bias independent or channel length independent Fukui's coefficient for the well known NF_{min} equation. Instead, the amount of drain current noise produced to achieve one GHz f_T fundamentally determines the NF_{min} of the intrinsic device, and can be used as a figure-of-merit to better measure the intrinsic noise figure capability of a technology. With technology scaling from 0.25 μm to 0.18 μm, both f_T and drain current noise increase. The f_T increase, however, dominates over the drain current noise increase, thus improving the minimum noise figure of the intrinsic device. Another figure-of-merit is proposed to include the effect of gate resistance which facilitates layout optimization for low noise and evaluation of the relevant importance of gate resistance noise with respect to drain current noise in determining NF_{min}.

BIBLIOGRAPHY

[1] J.C.J. Paasschens, "Compact modeling of the noise of a bipolar transistor under DC and AC current crowding conditions," *IEEE Transactions on Electron Devices*, vol. 51, no. 9, pp. 1483–1495, Sept. 2004.

[2] M. Rudolph, R. Doerner, L. Klapproth, and P. Heymann, "An HBT noise model valid up to transit frequency," *IEEE Electron Device Letters*, vol. 20, no. 1, pp. 24–26, Jan. 1999.

[3] G. F. Niu, J. D. Cressler, W.E. Ansley, C. Webster, and D. Harame, "A unified approach to RF and microwave noise parameter modeling in bipolar transistors," *IEEE Transactions on Electron Devices*, vol. 48, no. 11, pp. 2568–2574, Nov. 2001.

[4] A.J. Scholten, L.F. Tiemeijer, R.J. Havens, R. de Kort, R. van Langevelde, and D.B.M. Klaassen, "RF noise modeling & characterization," *2006 IEEE MTT-S International Microwave Symposium*, June 2006.

[5] Xuemei Xi, Mohan Dunga, Jin He, Weidong Liu, Kanyu M. Cao, Xiaodong Jin, Jeff J. Ou, Mansun Chan, Ali M. Niknejad, and Chenming Hu, *BSIM4 manual*, BSIM Research Group at UC Berkeley, Mar. 2004.

[6] A. Scholten, L.F. Tiemeijer, R. van Langevelde, R.J. Havens, A.T.A. Zegers-van Duijnhoven, and V.C. Venezia, "Noise modeling for RF CMOS circuit simulation," *IEEE Transactions on Electron Devices*, vol. 50, no. 3, pp. 618–632, Mar. 2003.

[7] M.C.A.M. Koolen, J.A.M. Geelen, and M.P.J.G. Versleijen, "An improved de-embedding technique for on-wafer high-frequency characterization," *Proceeding of IEEE Bipolar Circuit and Technology*, pp. 188–191, Sept. 1991.

[8] D. Becher, G. Banerjee, R. Basco, C. Hung, K. Kuhn, and Wei-Kai Shih, "Noise Performance of 90 nm CMOS Technology," *IEEE MTT-S International Microwave Symposium Digest*, pp. 17–20, June 2004.

[9] Andreas Pascht, Markus Gröing, Dirk Wiegner, and Manfred Berroth, "Small-signal and temperature noise model for MOSFETs," *IEEE Transactions on Microwave Theory and Techniques*, vol. 50, no. 8, pp. 1927–1934, Aug. 2002.

[10] J.D. Cressler and G.F. Niu, *Silicon-Germanium heterojunction bipolar transistors*, Artech House, 2003.

[11] H.A. Haus, W.R. Atkinson, W.H. Fonger, W.W. Mcleod, G.M. Branch, W.A. Harris, E.K. Stodola, W.B. Davenport Jr., S.W. Harrison, and T.E. Talpey, "Representation of noise in linear twoports," *Proceeding of IRE*, vol. 48, pp. 69–74, 1960.

[12] Yan Cui, Guofu Niu, and D.L. Harame, "An examination of bipolar transistor noise modeling and noise physics using microscopic noise simulation," *Proceeding of IEEE Bipolar/BiCMOS Circuit and Technology*, pp. 225–228, Sept. 2003.

[13] K.M. Van Vliet, "General Transistor Theory of Noise in *PN* Junction-Like Devices—I. Three-Dimensional Green's Function Formulation," *Solid-State Electronics*, vol. 15, no. 10, pp. 1033–1053, Oct. 1972.

[14] A. van der Ziel, "Thermal noise in field effect transistors," *Proc. IRE*, vol. 50, pp. 1808–1812, Aug. 1962.

[15] A. van der Ziel, *Noise in Solid-State Devices and Circuits*, John Wiley & Sons, 1986.

[16] F.M. Klaassen and J. Prins, "Thermal noise of MOS transistors," *Philips Res. Rep.*, vol. 22, pp. 505–514, 1967.

[17] A. van der Ziel, *Noise Sources, Characterization, Measurement*, Englewood Cliffs, NJ: Prentice-Hall, 1970.

[18] Yannis Tsividis, *Operation and Modeling of The CMOS Transistor*, McGraw-Hill, 2 edition, 1999.

[19] C.H. Chen and M.J. Deen, "High frequency noise of MOSFETs i modeling," *Solid State Electron*, vol. 42, pp. 2069–2081, 1998.

[20] J.C.J. Paasschens, A.J. Scholten, and R. van Langevelde, "Generalizations of the Klaassen-Prins equation for calculating the noise of semiconductor devices," *IEEE Transactions on Electron Devices*, vol. 52, pp. 2463–2472, Nov. 2005.

[21] F. Bonani and G. Ghione, *Noise in Semiconductor Devices*, Berlin, Germany: Springer-Verlag, 2001.

[22] K.M. Van Vliet, A. Friedmann, R.J.J. Zijlstra, A. Gisolf, and A. van der Ziel, "Noise in single injection diodes. I. A survey of methods," *Journal of Applied Physics*, vol. 46, pp. 1804–1813, 1975.

[23] K.M. Van Vliet, A. Friedmann, R.J.J. Zijlstra, A. Gisolf, and A. van der Ziel, "Noise in single injection diodes. II. Applications," *Journal of Applied Physics*, vol. 46, pp. 1814–1823, 1975.

[24] D.K. Ferry, J.R. Barker, and C. Jacoboni, *Physics of Nonlinear Transport in Semiconductors*, New York: Plenum, 1980.

[25] J.P. Nougier, "Fluctuations and noise of hot carriers in semiconductor materials and devices," *IEEE Transactions on Electron Devices*, vol. 41, no. 12, pp. 2035–2049, Dec. 1994.

[26] C. H. Chen and M. J. Deen, "Channel noise modeling of deep-submicron MOSFETs," *IEEE Transactions on Electron Devices*, vol. 49, no. 8, pp. 1484–1487, Aug. 2002.

[27] M. W. Pospieszalski, "Modeling of noise parameters of MESFET's and MODFET's and their frequency and temperature dependence," *IEEE Transactions on Microwave Theory and Techniques*, vol. 37, no. 9, pp. 508–509, Sept. 1989.

[28] A. Litwin, "Overlooked interfacial silicide-polysilicon gate resistance in MOS transistors," *IEEE Transactions on Electron Devices*, vol. 48, pp. 2179–2181, 2001.

[29] Takaaki Tatsumi, "Geometry Optimization of Sub-100nm Node RF CMOS Utilizing Three Dimensional TCAD Simulation," *IEEE European Solid-State Device Research Conference*, pp. 319–322, Sept. 2006.

[30] A. Scholten, L.F. Tiemeijer, R. van Langevelde, R.J. Havens, A.T.A. Zegers-van Duijnhoven, and V.C. Venezia, "Noise modeling for RF CMOS circuit simulation," *IEEE Transactions on Electron Devices*, vol. 50, no. 3, pp. 618–632, Mar. 2003.

[31] Hatsuaki Fukui, "Optimal noise figure of microwave GaAs MESFET's," *IEEE Transactions on Electron Devices*, vol. 26, no. 7, pp. 1032–1037, July 1979.

[32] Hatsuaki Fukui, "Design of microwave GaAs MESFET's for broad-band low-noise amplifiers," *IEEE Transactions on Microwave Theory and Techniques*, vol. 27, no. 7, pp. 643–650, July 1979.

[33] Hatsuaki Fukui, "Addendum to "design of microwave GaAs MESFET's for broad-band low-noise amplifiers"," *IEEE Transactions on Microwave Theory and Techniques*, vol. 29, no. 10, pp. 1119, Oct. 1981.

[34] M.C. King, M.T. Yang, C.W. Kuo, Yun Chang, and A. Chin, "RF noise scaling trend of MOSFETs from 0.5 μm to 0.13 μm technology nodes," *IEEE MTT-S International Microwave Symposium Digest*, vol. 1, pp. 9–12, June 2004.

[35] S. Tehrani, V. Nair, C. E. Weitzel, and G. Tam, "The effects of parasitic capacitance on the noise figure of MESFETs," *IEEE Transactions on Electron Devices*, vol. 35, no. 5, pp. 703–706, May 1988.

[36] C. L. Lau, M. Feng, T. R. Lepkowski, G. W. Wang, Y. Chang, and C. Ito, "Half-micrometer gate-length ion-implanted GaAs MESFET with 0.8-dB noise figure at 16 GHz," *IEEE Electron Device Letters*, vol. 10, no. 9, pp. 409–411, Sept. 1989.

[37] Lawrence E. Larson, "Silicon technology tradeoffs for radio-frequency/mixed-signal "systems-on-a-chip"," *IEEE Transactions on Electron Devices*, vol. 50, no. 3, pp. 683–699, Mar. 2003.

[38] J.-C. Guo and Y.-M. Lin, "A new lossy substrate de-embedding method for sub-100 nm RF CMOS noise extraction and modeling," *IEEE Transactions on Electron Devices*, vol. 53, no. 2, pp. 339–347, Feb. 2006.

[39] C. Enz, "An CMOS transistor model for RF IC design valid in all regions of operation," *IEEE Transactions on Microwave Theory and Techniques*, vol. 50, no. 1, pp. 342–359, Jan. 2002.

[40] Thomas H. Lee, *The Design of CMOS Radio-Frequency Integrated Circuits*, Cambridge University Press, Dec. 2003.

[41] Tajinder Manku, "Microwave CMOS–device physics and design," *IEEE Journal of Solid-State Circuits*, vol. 34, no. 3, pp. 277–285, Mar. 1999.

[42] M. Reisch, *High-Frequency Bipolar Transistors*, Springer, 2003.

[43] H. Hillbrand and P. Russer, "An efficient method for computer aided noise analysis of linear amplifier networks," *IEEE Transactions on Circuits and Systems*, vol. 23, no. 4, pp. 235–238, Apr. 1976.

[44] *TAURUS, 2-D Device Simulator*, Synopsys.

[45] *DESSIS, 2-D Device Simulator, version 9.0*, Synopsys.

[46] W.M.C. Sansen and R.G. Meyer, "Characterization and measurement of the base and emitter resistances of bipolar transistors," *IEEE Journal of Solid-State Circuits*, vol. 7, pp. 492–498, Dec. 1972.

[47] G.F. Niu, W.E. Ansley, S. Zhang, J.D. Cressler, C.S. Webster, and R.A. Groves, "Noise parameter optimization of UHV/CVD SiGe HBT's for RF and microwave applications," *IEEE Transactions on Electron Devices*, vol. 46, no. 8, pp. 1589–1598, Aug. 1999.

[48] W. Shockley, J.A. Copeland, and R.P. James, "The impedance field method of noise calculation in active semiconductor devices," in *Quantum theory of atoms, molecules, and the solid-state*. 1966, pp. 537–563, Academic Press.

[49] D.L. Harame, J.H. Comfort, J.D. Cressler, E.F. Crabbé, J.Y.-C. Sun, B.S. Meyerson, and T. Tice, "Si/SiGe epitaxial-base transistors Part *II*: process integration and analog applications," *IEEE Transactions on Electron Devices*, vol. 42, no. 3, pp. 469–482, Mar. 1995.

[50] F. Bonani, G. Ghione, M.R. Pinto, and R.K. Smith, "An efficient approach to noise analysis through multidimensional physics-based models," *IEEE Transactions on Electron Devices*, vol. 45, no. 1, pp. 261–269, Jan. 1998.

[51] Yan Cui, Guofu Niu, Yun Shi, and D.L. Harame, "Spatial distribution of microscopic noise contributions in SiGe HBT," *IEEE Topical Meeting on Silicon Monolithic Integrated Circuits in RF Systems*, pp. 170–173, Apr. 2003.

[52] Christoph Jungemann, Burkhard Neinhus, S. Decker, and Bernd Meinerzhagen, "Hierarchical 2-D DD and HD Noise Simulations of Si and SiGe Devices—Part II: Results," *IEEE Transactions on Electron Devices*, vol. 49, no. 7, pp. 1258–1264, July 2002.

[53] Guofu Niu, Shiming Zhang, J.D. Cressler, A.J. Joseph, J.S. Fairbanks, L.E. Larson, C.S. Webster, W.E. Ansley, and D.L. Harame, "SiGe profile design tradeoffs for RF circuit applications," *Technical Digest of International Electron Devices Meeting*, vol. 49, pp. 573–576, Dec. 1999.

[54] Guofu Niu, Shiming Zhang, J.D. Cressler, A.J. Joseph, J.S. Fairbanks, L.E. Larson, C.S. Webster, W.E. Ansley, and D.L. Harame, "Noise modeling and SiGe profile design tradeoffs for RF applications [HBTs]," *IEEE Transactions on Electron Devices*, vol. 47, no. 11, pp. 2037–2044, Nov. 2000.

[55] Guofu Niu, W.E. Ansley, S. Zhang, J.D. Cressler, C.S. Webster, and R.A. Groves, "Noise parameter optimization of UHV/CVD SiGe HBT's for RF and microwave applications," *IEEE Transactions on Electron Devices*, vol. 46, no. 8, pp. 1589–1598, Aug. 1999.

[56] S.J. Jeng, B. Jagannathan, J.S. Rieh, J. Johnson, K.T. Schonenberg, D. Greenberg, A. Stricker, H. Chen, M. Khater, D. Ahlgren, G. Freeman, K. Stein, and S. Subbanna, "A 210-GHz fT SiGe HBT with a non-self-aligned structure," *IEEE Electron Device Letters*, vol. 22, pp. 542–544, Nov. 2001.

[57] T.F. Meister and et. al., "SiGe bipolar technology with 3.9 ps gate delay," *Proceeding of IEEE Bipolar/BiCMOS Circuit and Technology*, pp. 103–106, Sept. 2003.

[58] Y. Cui, G. Niu, Y. Shi, C. Zhu, L. Najafizadeh, J. D. Cressler, and A. Joseph, "SiGe Profile Optimization for Improved Cryogenic Operation at High Injection," *IEEE Bipolar/BiCMOS Circuits and Technology Meeting*, Oct. 2006.

[59] C. Jungemann, B. Neinhüs, C. D. Nguyen, B. Meinerzhagen, R. W. Dutton, J. Scholten, and L. F. Tiemeijer, "Hydrodynamic Modeling of RF Noise in CMOS Devices," *Technical Digest of IEEE International Electron Devices Meeting*, pp. 803–873, Dec. 2003.

[60] *The National Technology Roadmap for Semiconductors*, Semiconductor Industry Association, 2001.

[61] Jung-Suk Goo, W. Liu, Chang-Hoon Choi, K.R. Green, Zhiping Yu, T.H. Lee, and R.W. Dutton, "The equivalence of van der Ziel and BSIM4 models in modeling the induced gate noise of MOSFETs," *Technical Digest of International Electron Devices Meeting*, pp. 811–814, Dec. 2000.

[62] Jung-Suk Goo, *High Frequency Noise in CMOS Low Noise Amplifiers*, Ph.D. Thesis, Stanford University, 2001.

[63] Guofu Niu, Yan Cui, and S. S. Taylor, "Microscopic RF noise simulation and noise source modeling in 50 nm l_{eff} CMOS," *Tech. Dig. of IEEE Topical Meeting on Silicon Monolithic Integrated Circuits in RF Systems*, pp. 123–126, 2004.

[64] Xiaodong Jin, Jia-Jiunn Ou, Chih-Hung Chen, Weidong Liu, M.J. Deen, P.R. Gray, and Chenming Hu, "An effective gate resistance model for CMOS RF and noise modeling," *Technical Digest of International Electron Devices Meeting*, pp. 961–964, Dec. 1998.

[65] Yuhua Cheng and M. Matloubian, "High frequency characterization of gate resistance in RF MOSFETs," *IEEE Electron Device Letters*, vol. 22, no. 2, pp. 98–100, Feb. 2001.

[66] T.A. Fjeldly, T. Ytterdal, and Y. Cheng, ," May 2003.

[67] Mansun Chan, Kelvin Hui, R. Neff, Chenming Hu, and Ping Keung Ko, "A relaxation time approach to model the non-quasi-static transient effects in MOSFETs," *Technical Digest of International Electron Devices Meeting*, pp. 169–172, Dec. 1994.

[68] J. Tao, A. Rezvani, and P. Findley, "RF CMOS gate resistance and noise characterization," *IEEE International Conference on Solid-State and Integrated-Circuit Technology*, vol. 1, pp. 159–162, Oct. 2004.

[69] Q. Q. Liang, J. D. Cressler, G. Niu, Y. Lu, G. Freeman, D. C. Ahlgren, R. M. Malladi, K. Newton, and D. L. Harame, "A simple four-port parasitic deembedding methodology for high-frequency scattering parameter and noise characterization of SiGe HBTs," *IEEE Transactions on Microwave Theory and Techniques*, vol. 51, no. 11, pp. 2165–2174, Nov. 2003.

[70] C.Y. Wong, J.Y.C. Sun, Y. Taur, C.S. Oh, R. Angelucci, and B. Davari, "Doping of n^+ and p^+ polysilicon in a dual-gate CMOS process," *Technical Digest of International Electron Devices Meeting*, pp. 238–241, 1988.

[71] R. Rios and N.D. Arora, "Determination of ultra-thin gate oxide thickness for CMOS structures using quantum effects," *Technical Digest of International Electron Devices Meeting*, pp. 613–616, 1994.

[72] A. Scholten, *Private communication*.

APPENDICES

Appendix A
MATLAB Programming for Open-Short Deembedding in Chapter 2

```
correction = 1;   % correction = 0: matrix operation; 1: correction

k=1.38e-23;
To=290;
T=295;
dut = load('DUT_Vgp685_Vd1p5_Fswp_DELSP');
noise = load('DUT_Vgp685_Vd1p5_Fswp_DELNP');
open = load('DUT_OPEN_840step2_SP.s2p');
short = load('DUT_SHORT_840step2_SP.s2p');

for i=1:17
% S-parameters of the device:
    fre(i)=dut(i,1);
    mag=dut(i,2);
    deg=dut(i,3)/180*pi;
    s(1,1)=mag*(cos(deg)+j*sin(deg));
    mag=dut(i,4);
    deg=dut(i,5)/180*pi;
    s(2,1)=mag*(cos(deg)+j*sin(deg));
    mag=dut(i,6);
    deg=dut(i,7)/180*pi;
    s(1,2)=mag*(cos(deg)+j*sin(deg));
    mag=dut(i,8);
    deg=dut(i,9)/180*pi;
    s(2,2)=mag*(cos(deg)+j*sin(deg));
% convert s-parameter to Y parameters
    temp=50*((1+s(1,1))*(1+s(2,2))-s(1,2)*s(2,1));
    y(1,1)=((1-s(1,1))*(1+s(2,2))+s(1,2)*s(2,1))/temp;
    y(1,2)=-2*s(1,2)/temp;
    y(2,1)=-2*s(2,1)/temp;
    y(2,2)=((1+s(1,1))*(1-s(2,2))+s(1,2)*s(2,1))/temp;
% S-parameters of the open:
    mag=open(i,2);
    deg=open(i,3)/180*pi;
    s(1,1)=mag*(cos(deg)+j*sin(deg));
    mag=open(i,4);
    deg=open(i,5)/180*pi;
    s(2,1)=mag*(cos(deg)+j*sin(deg));
```

```
    mag=open(i,6);
    deg=open(i,7)/180*pi;
    s(1,2)=mag*(cos(deg)+j*sin(deg));
    mag=open(i,8);
    deg=open(i,9)/180*pi;
    s(2,2)=mag*(cos(deg)+j*sin(deg));
% convert s-parameter to Y parameters
    temp=50*((1+s(1,1))*(1+s(2,2))-s(1,2)*s(2,1));
    y_open(1,1)=((1-s(1,1))*(1+s(2,2))+s(1,2)*s(2,1))/temp;
    y_open(1,2)=-2*s(1,2)/temp;
    y_open(2,1)=-2*s(2,1)/temp;
    y_open(2,2)=((1+s(1,1))*(1-s(2,2))+s(1,2)*s(2,1))/temp;
 % S-parameters of the Short:
    mag=short(i,2);
    deg=short(i,3)/180*pi;
    s(1,1)=mag*(cos(deg)+j*sin(deg));
    mag=short(i,4);
    deg=short(i,5)/180*pi;
    s(2,1)=mag*(cos(deg)+j*sin(deg));
    mag=short(i,6);
    deg=short(i,7)/180*pi;
    s(1,2)=mag*(cos(deg)+j*sin(deg));
    mag=short(i,8);
    deg=short(i,9)/180*pi;
    s(2,2)=mag*(cos(deg)+j*sin(deg));
% convert s-parameter to Y parameters
    temp=50*((1+s(1,1))*(1+s(2,2))-s(1,2)*s(2,1));
    y_short(1,1)=((1-s(1,1))*(1+s(2,2))+s(1,2)*s(2,1))/temp;
    y_short(1,2)=-2*s(1,2)/temp;
    y_short(2,1)=-2*s(2,1)/temp;
    y_short(2,2)=((1+s(1,1))*(1-s(2,2))+s(1,2)*s(2,1))/temp;
 % 2. read in noise parameters of DUT
    NFmin=noise(i,2);
    NFmin_old(i)=NFmin;
    NFmin=10^(NFmin/10.);
    Rn=noise(i,5)*50;
    Rn_old(i)=Rn;
    mag=noise(i,3);
    deg=noise(i,4)/180*pi;
    Gama_opt=mag*(cos(deg)+j*sin(deg));
% convert the Gama_opt to Y_opt
    Zopt=50*(1+Gama_opt)/(1.-Gama_opt);
```

```
    Yopt=1./Zopt;
    re_Yopt_old(i)=real(Yopt);
    im_Yopt_old(i)=imag(Yopt);
% 3. Caluculate correlation matrix
   Ca_dut(1,1)=Rn;
   Ca_dut(1,2)=(NFmin-1)/2-Rn*conj(Yopt);
   Ca_dut(2,1)=(NFmin-1)/2-Rn*Yopt;
   Ca_dut(2,2)=Rn*abs(Yopt)*abs(Yopt);
   Ca_dut=Ca_dut*2*k*To;
% 4. convert the Ca matrix into its Cy correlation matrix
   T_dut=[-y(1,1) , 1; -y(2,1), 0];
%-----------------------------------------------------------------------------

switch correction
case 0
   Cy_dut=T_dut*Ca_dut*(T_dut');
case 1
    % Yan's correction
   T_dut_conj_trans = T_dut';
   Cy_dut(1,1) = (abs(T_dut(1,1)))^2*Ca_dut(1,1) ...
       + (abs(T_dut(1,2)))^2*Ca_dut(2,2)...
       + 2*real(T_dut_conj_trans(1,1)*T_dut(1,2)*Ca_dut(2,1));
   Cy_dut(1,2) = T_dut(1,1)*T_dut_conj_trans(1,2)*Ca_dut(1,1)...
       +T_dut(1,2)*T_dut_conj_trans(1,2)*Ca_dut(2,1)...
       +T_dut(1,1)*T_dut_conj_trans(2,2)*Ca_dut(1,2)...
       +T_dut(1,2)*T_dut_conj_trans(2,2)*Ca_dut(2,2);
   Cy_dut(2,1) = Cy_dut(1,2)';
   Cy_dut(2,2) = (abs(T_dut(2,1)))^2*Ca_dut(1,1) ...
       + (abs(T_dut(2,2)))^2*Ca_dut(2,2)...
       + 2*real(T_dut_conj_trans(2,2)*T_dut(2,1)*Ca_dut(1,2));
end
%-----------------------------------------------------------------------------

% 5. calculate the correlation matrix [Cy_open] of the open dummy structure
   Cy_open=2*k*T*real(y_open);
% 6. subtract parallel parasitics from the Y_dut and Y_short
   yi_dut=y-y_open;
   yi_short=y_short-y_open;
% 7. deembed Cy_DUT from the parallel parasitic
   Cyi_dut=Cy_dut-Cy_open;
% 8. convert the yi_dut to Zi_dut and Yi_short to Zi_short
   temp=yi_dut(1,1)*yi_dut(2,2)-yi_dut(1,2)*yi_dut(2,1);
```

```
   Zi_dut=[yi_dut(2,2), -yi_dut(1,2); -yi_dut(2,1), yi_dut(1,1)];
   Zi_dut=Zi_dut/temp;

   temp=yi_short(1,1)*yi_short(2,2)-yi_short(1,2)*yi_short(2,1);
   Zi_short=[yi_short(2,2),-yi_short(1,2);-yi_short(2,1),yi_short(1,1)];
   Zi_short=Zi_short/temp;

% 9. convert the Cyi_dut into Czi_dut
%-----------------------------------------------------------------------------
switch correction
case 0
   Czi_dut=Zi_dut*Cyi_dut*(Zi_dut');
case 1
   %Yan's correction
   Zi_dut_conj_trans = Zi_dut';
   Czi_dut(1,1) = (abs(Zi_dut(1,1)))^2*Cyi_dut(1,1) ...
       + (abs(Zi_dut(1,2)))^2*Cyi_dut(2,2)...
       +2*real(Zi_dut_conj_trans(1,1)*Zi_dut(1,2)*Cyi_dut(2,1));
   Czi_dut(1,2) = Zi_dut(1,1)*Zi_dut_conj_trans(1,2)*Cyi_dut(1,1)...
       +Zi_dut(1,2)*Zi_dut_conj_trans(1,2)*Cyi_dut(2,1)...
       +Zi_dut(1,1)*Zi_dut_conj_trans(2,2)*Cyi_dut(1,2)...
       +Zi_dut(1,2)*Zi_dut_conj_trans(2,2)*Cyi_dut(2,2);
   Czi_dut(2,1) = Czi_dut(1,2)';
   Czi_dut(2,2) = (abs(Zi_dut(2,1)))^2*Cyi_dut(1,1) ...
       + (abs(Zi_dut(2,2)))^2*Cyi_dut(2,2)...
       + 2*real(Zi_dut_conj_trans(2,2)*Zi_dut(2,1)*Cyi_dut(1,2));
end
%-----------------------------------------------------------------------------

%10. calculate correlation matrix Czi_short after
%     deembedding parallel parasitic
   Czi_short=2*k*T*real(Zi_short);
%11. subtract series parasitics from Zi_dut to get
%    Z parameter of the intrinsic transistor
   Ztran=Zi_dut-Zi_short;
%12. De-embed Czi_dut from series parasitics to get
%     the correlation matrix Cz of the intrinsic transistor
   Cz=Czi_dut-Czi_short;
%13. convert the Ztran to its chain matrix Atrans
   Atran=[Ztran(1,1), Ztran(1,1)*Ztran(2,2)-Ztran(1,2)*Ztran(2,1);
             1, Ztran(2,2)];
   Atran=Atran/Ztran(2,1);
```

```
%14. Transform Cz to Ca
   Ta=[1, -Atran(1,1); 0, -Atran(2,1)];
%-----------------------------------------------------------------------------
switch correction
case 0
   Ca=Ta*Cz*(Ta');
case 1
    % Yan's correction
   Ta_conj_trans = Ta';
   Ca(1,1) = (abs(Ta(1,1)))^2*Cz(1,1) + (abs(Ta(1,2)))^2*Cz(2,2)...
       + 2*real(Ta_conj_trans(1,1)*Ta(1,2)*Cz(2,1));
   Ca(1,2) = Ta(1,1)*Ta_conj_trans(1,2)*Cz(1,1)...
       +Ta(1,2)*Ta_conj_trans(1,2)*Cz(2,1)...
       +Ta(1,1)*Ta_conj_trans(2,2)*Cz(1,2)...
       +Ta(1,2)*Ta_conj_trans(2,2)*Cz(2,2);
   Ca(2,1) = Ca(1,2)';
   Ca(2,2) = (abs(Ta(2,1)))^2*Cz(1,1) + (abs(Ta(2,2)))^2*Cz(2,2)...
       + 2*real(Ta_conj_trans(2,2)*Ta(2,1)*Cz(1,2));
end
%-----------------------------------------------------------------------------
%15. calculate the open-short deembedded NFmin, Yopt and Rn
   temp=sqrt((Ca(1,1)*Ca(2,2)-(imag(Ca(1,2))^2)));
   NFmin_new(i)=log10(1+1/k/T*((real(Ca(1,2)))+temp))*10;
   im_NFmin_new(i)=imag(NFmin_new(i));
   Yopt_new=(temp+j*imag(Ca(1,2)))/Ca(1,1);
   re_Yopt_new(i)=real(Yopt_new);
   im_Yopt_new(i)=imag(Yopt_new);
   Zopt_new=1./Yopt_new;
   mag_Gama_new(i)=abs(-(50-Zopt_new)/(50+Zopt_new));
   ang_Gama_new(i)=angle(-(50-Zopt_new)/(50+Zopt_new))/pi*180;
   Rn_new(i)=real(Ca(1,1)/2/k/T);
%-----------------------------------------------------------------------------
%16. Yan:  Calculate Sig, Sid, and correlation
   temp=Ztran(1,1)*Ztran(2,2)-Ztran(1,2)*Ztran(2,1);
   Ytran=[Ztran(2,2),-Ztran(1,2);-Ztran(2,1),Ztran(1,1)];
   Ytran=Ytran/temp;
   Ytran_conj_trans = Ytran';
   Cy(1,1) = (abs(Ytran(1,1)))^2*Cz(1,1) ...
       + (abs(Ytran(1,2)))^2*Cz(2,2)...
       +2*real(Ytran_conj_trans(1,1)*Ytran(1,2)*Cz(2,1));
   Cy(1,2) = Ytran(1,1)*Ytran_conj_trans(1,2)*Cz(1,1)...
       +Ytran(1,2)*Ytran_conj_trans(1,2)*Cz(2,1)...
```

```
        +Ytran(1,1)*Ytran_conj_trans(2,2)*Cz(1,2)...
        +Ytran(1,2)*Ytran_conj_trans(2,2)*Cz(2,2);
    Cy(2,1) = Cy(1,2)';
    Cy(2,2) = (abs(Ytran(2,1)))^2*Cz(1,1) ...
        + (abs(Ytran(2,2)))^2*Cz(2,2)...
        + 2*real(Ytran_conj_trans(2,2)*Ytran(2,1)*Cz(1,2));
    Sig(i) = 2*Cy(1,1);
    Sid(i) = 2*Cy(2,2);
    Sigid(i) = 2*Cy(1,2);
    Cigid(i) = Sigid(i)./sqrt(Sig(i).*Sid(i));
%----------------------------------------------------------------------------
%17. Yan: Calculate Svh, Sih, and correlation
        Svh(i) = Sig(i)./(abs(Ytran(1,1))).^2;
        Sih(i)= Sid(i) + Sig(i).*(abs(Ytran(2,1)./Ytran(1,1))).^2-...
            2.*real(Ytran(2,1)./Ytran(1,1).*Sigid(i));
        Svhih(i) = conj(Ytran(2,1))./(abs(Ytran(1,1))).^2.*Sig(i) -...
            Sigid(i)./Ytran(1,1);
        Cvhih(i) = Svhih(i)./sqrt(Svh(i).*Sih(i));

end
```

APPENDIX B

DESSIS INPUT DECK AND MATLAB PROGRAMMING FOR SIGE HBT NOISE SIMULATION

B.1 5HP SiGe HBT

B.1.1 Mesh files

BND file

```
Oxide "DT" {rectangle[(2.3, 0.648) (2.8, 4.598)]}
Oxide "STI" {rectangle[(2.2, 0.248) (2.8, 0.648)]}
Oxide "STI2" {rectangle[(0.5, 0.248) (1.2, 0.648)]}
PolySi "PolySi" {polygon[(1.25, 0) (1.25, 0.068) (1.45, 0.068) (1.45, 0.148)
                         (1.95, 0.148) (1.95, 0.068) (2.15, 0.068) (2.15, 0)]}
Oxide "spacer1" {rectangle[(1.25, 0.068) (1.45,0.148)]}
Oxide "spacer2" {rectangle[(1.95, 0.068) (2.15, 0.148)]}
Silicon "Silicon1" {polygon[(0, 0.248) (0, 4.598) (2.3, 4.598) (2.3, 0.648)
                            (2.2, 0.648) (2.2, 0.248) (2.6, 0.248) (2.6, 0.24)
                            (0.8, 0.24) (0.8, 0.248) (1.2, 0.248) (1.2, 0.648)
                            (0.5, 0.648) (0.5, 0.248)]}
Silicon "Silicon2" {rectangle[(0.8, 0.148) (2.6, 0.1646)]}
SiliconGermanium "SiGe" {rectangle[(0.8, 0.1646) (2.6, 0.24)]}
Contact "Collector" {line[(0, 0.248) (0.47, 0.248)]}
Contact "Base1" {line[(0.8, 0.148) (1.2, 0.148)]}
Contact "Base2" {line[(2.2, 0.148) (2.6, 0.148)]}
Contact "Emitter" {line[(1.45, 0) (1.95, 0)]}
Contact "Psubstrate" {line[(0, 4.598) (2.3, 4.598)]}
```

CMD file

```
Title "BJT"

Definitions {
  # Refinement regions
    Refinement "all region"
    {
      MaxElementSize = (0.2 0.5)
      MinElementSize = (0.05 0.05)
      RefineFunction = MaxTransDiff(Variable="DopingConcentration" Value=1)
    }
    Refinement "sige"
```

```
{
  MaxElementSize = (0.05 0.005)
  MinElementSize = (0.02 0.002)
  RefineFunction = MaxTransDiff(Variable="xMoleFraction" Value=0.01)
}
Refinement "substrate region1"
{
  MaxElementSize = (0.15 0.15)
  MinElementSize = (0.08 0.08)
  RefineFunction = MaxTransDiff(Variable="DopingConcentration" Value=1)
}
Refinement "substrate region2"
{
  MaxElementSize = (0.08 0.1)
  MinElementSize = (0.03 0.005)
  RefineFunction = MaxTransDiff(Variable="DopingConcentration" Value=1)
}
Refinement "substrate region3"
{
  MaxElementSize = (0.1 0.05)
  MinElementSize = (0.05 0.005)
  RefineFunction = MaxTransDiff(Variable="DopingConcentration" Value=1)
}
Refinement "Oxide_shallow"
{
  MaxElementSize = (0.05 0.05)
  MinElementSize = (0.02 0.02)
}
Refinement "Oxide_DT"
{
  MaxElementSize = (0.1 0.1)
  MinElementSize = (0.05 0.05)
}
Refinement "Oxide_spacer"
{
  MaxElementSize = (0.04 0.04)
  MinElementSize = (0.02 0.01)
}
 Refinement "Emitter"
{
  MaxElementSize = (0.05 0.02)
  MinElementSize = (0.01 0.005)
```

```
    RefineFunction = MaxTransDiff(Variable="DopingConcentration" Value=1)
  }
  Refinement "eb_junction"
  {
    MaxElementSize = (0.05 0.02)
    MinElementSize = (0.025 0.002)
    RefineFunction = MaxTransDiff(Variable="DopingConcentration" Value=1)
  }
Refinement "cb_junctionup"
  {
    MaxElementSize = (0.05 0.05)
    MinElementSize = (0.01 0.01)
    RefineFunction = MaxTransDiff(Variable="DopingConcentration" Value=1)
  }

# Profiles
  Constant "psubstrate"
  {
    Species = "BoronActiveConcentration"
    Value = 2e+15
  }
  Constant "n_epi"
  {
    Species = "PhosphorusActiveConcentration"
    Value = 5e+16
  }
  AnalyticalProfile "emitter"
  {
    Function = subMesh1D(datafile = "as.dat"
      , Scale = 1,
      Range = line[(0 0), (0.598 0)]
      )
    LateralFunction = Erf(Factor = 0)
  }
  AnalyticalProfile "collector"
  {
    Function = subMesh1D(datafile = "phos.xy"
      , Scale = 1,
      Range = line[(0 0), (0.598 7.6364e+17)]
      )
    LateralFunction = Erf(Factor = 0)
  }
```

```
    AnalyticalProfile "n_buried layer"
    {
      Function = subMesh1D(datafile = "bu_asyan.xy"
    , Scale = 1, Range = line[(4.446e-1 1.5363805e+16), (2.720176 1.5363805e+16)]
    )
    LateralFunction = Erf(Factor=0)
    }
    AnalyticalProfile "intrinsic base"
    {
      Function = subMesh1D(datafile = "sims.dat"
        , Scale = 1,
        Range = line[(0 0), (0.598 0)]
        )
      LateralFunction = Erf(Factor = 0)
    }
    Constant "cc"
    { Species = "ArsenicActiveConcentration"
      Value = 1e+20
         }
    Constant "base"
    {
      Species = "BoronActiveConcentration"
      Value = 1e+16
    }
    Constant "extrinsic base"
    {
      Species = "BoronActiveConcentration"
      Value = 1.5e+19
    }
    AnalyticalProfile "xMoleBase"
    {
      Function = subMesh1D(datafile = "xMol10.xy"
        , Scale = 1,
       Range = line[(0.1646 0), (0.2774 0)]
       )
       LateralFunction = Erf(Factor = 0)
    }
}

Placements {
  # Refinement regions
    Refinement "all region"
```

```
{
  Reference = "all region"
  RefineWindow = rectangle [(0 0), (2.6 4.598)]
}
Refinement "substrate region1"
{
  Reference = "substrate region1"
  RefineWindow = rectangle [(0 0.248), (2.3 4.598)]
}
Refinement "emitter region"
{
  Reference =  "Emitter"
  RefineWindow = rectangle [(1.25 0) (2.15 0.08)]
}
Refinement "sige region"
{
  Reference =  "sige"
  RefineWindow = rectangle [(0.8 0.1646)(2.6 0.2774)]
}
Refinement "eb_junction"
{
  Reference = "eb_junction"
  RefineWindow = rectangle [(1.2 0.06), (2.6 0.16)]
}
Refinement "cb_junctionup"
{
  Reference = "cb_junctionup"
  RefineWindow = rectangle [(0 0.14), (2.35 1)]
}
Refinement "substrate region2"
{
  Reference = "substrate region2"
  RefineWindow = rectangle [(0 0.9), (2.6 1.2)]
}
 Refinement "ST1"
{
  Reference = "Oxide_shallow"
  RefineWindow = rectangle [(0.5 0.24) (1.2 0.69)]
}
Refinement "ST2"
{
  Reference = "Oxide_shallow"
```

```
    RefineWindow = rectangle [(2.25 0.24) (2.6 0.69)]
  }
  Refinement "DT"
  {
    Reference = "Oxide_DT"
    RefineWindow = rectangle[(2.3 0.248) (2.6 4.598)]
  }
  Refinement "spacer1"
  {
    Reference = "Oxide_spacer"
    RefineWindow = rectangle [(1.25 0.068) (1.45 0.148)]
  }
  Refinement "spacer2"
  {
    Reference = "Oxide_spacer"
    RefineWindow = rectangle [(1.95 0.068) (2.15 0.148)]
  }
  Refinement "substrate region3"
  {
    Reference = "substrate region3"
    RefineWindow = rectangle [(0 2.5), (2.6 2.65)]
  }
  Refinement "patch"
  {
    Reference = "sige"

    RefineWindow = rectangle [(0 0.248)(0.8 0.2774)]
  }

# Profiles
  Constant "psubstrate instance"
  {
    Reference = "psubstrate"
    EvaluateWindow
    {
      Element = rectangle [(0 2.58), (2.3 4.598)]
      DecayLength = 0
    }
  }
  AnalyticalProfile "intrinsic base instance"
  {
    Reference = "intrinsic base"
```

```
  ReferenceElement
  {
    Element = line [(0.8 0), (2.6 0)]
  }
  EvaluateWindow
  {
    Element = rectangle[(0.8 0), (2.6 0.598)]
  }
}
Constant "collectorwhole instance"
{
  Reference = "n_epi"
  EvaluateWindow
  {
   Element = rectangle [(0 0), (2.8 2.598)]
    DecayLength = 0
  }
}
AnalyticalProfile "emitter instance"
{
  Reference = "emitter"
  ReferenceElement
  {
    Element = line [(1.25 0), (2.15 0)]
  }
  EvaluateWindow
  {
    Element = polygon[(1.25 0) (1.25 0.068) (1.45 0.068)
                       (1.45 0.598) (1.95 0.598) (1.95 0.068)
                         (2.15 0.068) (2.15 0)]
  }
}
AnalyticalProfile "n_buried layer instance"
{
  Reference = "n_buried layer"
  ReferenceElement
    {
      Element = line[(0.5 0.4446) (2.3 0.4446)]
    }
  EvaluateWindow
  {
    Element = rectangle [(0.5 0.4446)(2.3 2.720176)]
```

```
    DecayLength = 0
  }
}
AnalyticalProfile "collector instance"
{
  Reference = "collector"
  ReferenceElement
  {
    Element = line [(1.35 0), (2.05 0)]
  }
  EvaluateWindow
  {
    Element = rectangle[(1.35 0)(2.05 0.598)]
  }
}
Constant "extrinsic base left instance"
{
  Reference = "extrinsic base"
  EvaluateWindow
  {
    Element = rectangle [(0.8 0.148), (1.35 0.258)]
    DecayLength = 0.010
  }
}
 Constant "extrinsic base right instance"
{
  Reference = "extrinsic base"
  EvaluateWindow
  {
    Element = rectangle [(2.05 0.148), (2.6 0.258)]
    DecayLength = 0.010
  }
}
Constant "Collector contact instance"
{
  Reference = "cc"
  EvaluateWindow
  {
    Element=rectangle[(0 0.248)(0.5 2.598)]
  }
}
AnalyticalProfile "xMolBase instance"
```

```
    {
      Reference = "xMoleBase"
      ReferenceElement
      {
        Element = line[(0.8 0.1646) (2.6 0.1646)]
        Direction = positive
      }
      EvaluateWindow
      {
        Element = polygon[(0.8 0.1646) (0.8 0.248) (1.2 0.248)
                          (1.2 0.598) (2.2 0.598) (2.2 0.248)
                          (2.6 0.248) (2.6 0.1646)]
      }
    }
}
```

B.1.2 Noise Simulation CMD file

```
Device BJT {

 Electrode {
   { Name="Emitter"   Voltage=0 }
   { Name="Base1"      Voltage=0 }
   { Name = "Base2"    Voltage = 0}
   { Name="Collector" Voltage=0 }
   { Name = "Psubstrate" Voltage = 0}
 }

 File {
   Grid      = "msh10_msh.grd"
   Doping    = "msh10_msh.dat"
   Current   = "ac10ddall_des.plt"
   Plot      = "ac10ddall_des.dat"
 }

 Physics{
    Areafactor= 1
    EffectiveIntrinsicDensity(BandgapNarrowing( Slotboom) )
    Mobility(
      PhuMob
      Highfieldsaturation
    )
```

```
   Fermi
   Noise ( DiffusionNoise )
}

Physics (material = "Silicon") {
   Recombination(
      SRH( DopingDependence )
      Auger
   )
}

Physics (material = "PolySi") {
   Recombination(
      SRH( DopingDependence )
      Auger
   )
}

}
*----------------------------------------------------------------------*
*--End of Device{}
*----------------------------------------------------------------------*

Plot {
   eDensity hDensity
   TotalCurrent/Vector eCurrent/Vector hCurrent/Vector

   ElectricField Potential SpaceCharge
   Doping DonorConcentration AcceptorConcentration

   SRH Auger
   eQuasiFermi hQuasiFermi
   eEparal hEparal

   eMobility hMobility
   eVelocity hVelocity

   xMoleFraction

   BandGap BandGapNarrowing
   Affinity
   ConductionBand ValenceBand
```

```
}
#NoisePlot {
#   AllLNS AllLNVSD AllLNVXVSD GreenFunctions
#}

Math {
   Extrapolate
   NotDamped=200
   Iterations=20
   NewDiscretization
   Derivatives
   RelerrControl
   Digits=6
}

File {
   Output  = "ac10ddall"
   ACExtract="ac10ddall"

}

System {
   BJT bjt (Base1=1  Base2 = 1 Collector=2 Emitter=0 Psubstrate=0)
   Vsource_pset vb (1 0){ dc = 0 }
   Vsource_pset vc (2 0){ dc = 0 }
}

Solve {
Coupled{Poisson Electron Hole  }
Quasistationary (
      InitialStep=0.1 Increment=1.4
      MinStep=1e-3 MaxStep=1
      Goal {Parameter=vc.dc Voltage=1.75}
      Goal {Parameter=vb.dc Voltage=0.75}
   ){
      Coupled{Poisson Electron Hole  }
    }
save(fileprefix = "17510dd")

newcurrent = "ac10ddbias"
load(fileprefix = "17510dd")
Quasistationary (
```

```
      InitialStep=1 Increment=1
      MinStep=1e-3 MaxStep=1
      Goal {Parameter=vc.dc Voltage=1.76}
      Goal {Parameter=vb.dc Voltage=0.76}
   ){
      Coupled{Poisson Electron Hole  }
    }
save(fileprefix = "17610dd")
Quasistationary (
      InitialStep=1 Increment=1
      MinStep=1e-3 MaxStep=1
      Goal {Parameter=vc.dc Voltage=1.77}
      Goal {Parameter=vb.dc Voltage=0.77}
   ){
      Coupled{Poisson Electron Hole  }
    }
save(fileprefix = "17710dd")
Quasistationary (
      InitialStep=1 Increment=1
      MinStep=1e-3 MaxStep=1
      Goal {Parameter=vc.dc Voltage=1.78}
      Goal {Parameter=vb.dc Voltage=0.78}
   ){
      Coupled{Poisson Electron Hole  }
    }
save(fileprefix = "17810dd")
Quasistationary (
      InitialStep=1 Increment=1
      MinStep=1e-3 MaxStep=1
      Goal {Parameter=vc.dc Voltage=1.79}
      Goal {Parameter=vb.dc Voltage=0.79}
   ){
      Coupled{Poisson Electron Hole  }
    }
save(fileprefix = "17910dd")
Quasistationary (
      InitialStep=1 Increment=1
      MinStep=1e-3 MaxStep=1
      Goal {Parameter=vc.dc Voltage=1.80}
      Goal {Parameter=vb.dc Voltage=0.80}
   ){
      Coupled{Poisson Electron Hole  }
```

```
    }
save(fileprefix = "18010dd")
Quasistationary (
      InitialStep=1 Increment=1
      MinStep=1e-3 MaxStep=1
      Goal {Parameter=vc.dc Voltage=1.81}
      Goal {Parameter=vb.dc Voltage=0.81}
   ){
      Coupled{Poisson Electron Hole  }
    }
save(fileprefix = "18110dd")
Quasistationary (
      InitialStep=1 Increment=1
      MinStep=1e-3 MaxStep=1
      Goal {Parameter=vc.dc Voltage=1.82}
      Goal {Parameter=vb.dc Voltage=0.82}
   ){
      Coupled{Poisson Electron Hole  }
    }
save(fileprefix = "18210dd")
Quasistationary (
      InitialStep=1 Increment=1
      MinStep=1e-3 MaxStep=1
      Goal {Parameter=vc.dc Voltage=1.83}
      Goal {Parameter=vb.dc Voltage=0.83}
   ){
      Coupled{Poisson Electron Hole  }
    }
save(fileprefix = "18310dd")
Quasistationary (
      InitialStep=1 Increment=1
      MinStep=1e-3 MaxStep=1
      Goal {Parameter=vc.dc Voltage=1.84}
      Goal {Parameter=vb.dc Voltage=0.84}
   ){
      Coupled{Poisson Electron Hole  }
    }
save(fileprefix = "18410dd")
Quasistationary (
      InitialStep=1 Increment=1
      MinStep=1e-3 MaxStep=1
      Goal {Parameter=vc.dc Voltage=1.85}
```

```
      Goal {Parameter=vb.dc Voltage=0.85}
   ){
      Coupled{Poisson Electron Hole  }
    }
save(fileprefix = "18510dd")
Quasistationary (
      InitialStep=1 Increment=1
      MinStep=1e-3 MaxStep=1
      Goal {Parameter=vc.dc Voltage=1.86}
      Goal {Parameter=vb.dc Voltage=0.86}
   ){
      Coupled{Poisson Electron Hole  }
    }
save(fileprefix = "18610dd")
Quasistationary (
      InitialStep=1 Increment=1
      MinStep=1e-3 MaxStep=1
      Goal {Parameter=vc.dc Voltage=1.87}
      Goal {Parameter=vb.dc Voltage=0.87}
   ){
      Coupled{Poisson Electron Hole  }
    }
save(fileprefix = "18710dd")
Quasistationary (
      InitialStep=1 Increment=1
      MinStep=1e-3 MaxStep=1
      Goal {Parameter=vc.dc Voltage=1.88}
      Goal {Parameter=vb.dc Voltage=0.88}
   ){
      Coupled{Poisson Electron Hole  }
    }
save(fileprefix = "18810dd")
Quasistationary (
      InitialStep=1 Increment=1
      MinStep=1e-3 MaxStep=1
      Goal {Parameter=vc.dc Voltage=1.89}
      Goal {Parameter=vb.dc Voltage=0.89}
   ){
      Coupled{Poisson Electron Hole  }
    }
save(fileprefix = "18910dd")
Quasistationary (
```

```
      InitialStep=1 Increment=1
      MinStep=1e-3 MaxStep=1
      Goal {Parameter=vc.dc Voltage=1.90}
      Goal {Parameter=vb.dc Voltage=0.90}
   ){
      Coupled{Poisson Electron Hole  }
    }
save(fileprefix = "19010dd")

newcurrent = "ac10ddall"
load(fileprefix = "17510dd")
    ACCoupled (
        StartFrequency = 1e9 EndFrequency = 20e9
        NumberofPoints =20   linear
        Node(1 2) Exclude(vb vc)
        ObservationNode(1 2)
        ACExtraction = "ac10ddall"
        NoiseExtraction = "ac10ddall"
        NoisePlot = "ac10ddall"
      )
      {Poisson Electron Hole  }
load(fileprefix = "17610dd")
    ACCoupled (
        StartFrequency = 1e9 EndFrequency = 20e9
        NumberofPoints = 20  linear
        Node(1 2) Exclude(vb vc)
        ObservationNode(1 2)
        ACExtraction = "ac10ddall"
        NoiseExtraction = "ac10ddall"
        NoisePlot = "ac10ddall"
      )
      {Poisson Electron Hole  }
load(fileprefix = "17710dd")
    ACCoupled (
        StartFrequency = 1e9 EndFrequency = 20e9
        NumberofPoints = 20  linear
        Node(1 2) Exclude(vb vc)
        ObservationNode(1 2)
        ACExtraction = "ac10ddall"
        NoiseExtraction = "ac10ddall"
        NoisePlot = "ac10ddall"
      )
```

```
      {Poisson Electron Hole  }
load(fileprefix = "17810dd")
    ACCoupled (
        StartFrequency = 1e9 EndFrequency = 20e9
        NumberofPoints = 20  linear
        Node(1 2) Exclude(vb vc)
        ObservationNode(1 2)
        ACExtraction = "ac10ddall"
        NoiseExtraction = "ac10ddall"
        NoisePlot = "ac10ddall"
      )
      {Poisson Electron Hole  }
load(fileprefix = "17910dd")
    ACCoupled (
        StartFrequency = 1e9 EndFrequency = 20e9
        NumberofPoints = 20  linear
        Node(1 2) Exclude(vb vc)
        ObservationNode(1 2)
        ACExtraction = "ac10ddall"
        NoiseExtraction = "ac10ddall"
        NoisePlot = "ac10ddall"
      )
      {Poisson Electron Hole  }
load(fileprefix = "18010dd")
    ACCoupled (
        StartFrequency = 1e9 EndFrequency = 20e9
        NumberofPoints = 20  linear
        Node(1 2) Exclude(vb vc)
        ObservationNode(1 2)
        ACExtraction = "ac10ddall"
        NoiseExtraction = "ac10ddall"
        NoisePlot = "ac10ddall"
      )
      {Poisson Electron Hole  }
load(fileprefix = "18110dd")
    ACCoupled (
        StartFrequency = 1e9 EndFrequency = 20e9
        NumberofPoints = 20  linear
        Node(1 2) Exclude(vb vc)
        ObservationNode(1 2)
        ACExtraction = "ac10ddall"
        NoiseExtraction = "ac10ddall"
```

```
        NoisePlot = "ac10ddall"
      )
      {Poisson Electron Hole  }
load(fileprefix = "18210dd")
    ACCoupled (
        StartFrequency = 1e9 EndFrequency = 20e9
        NumberofPoints = 20  linear
        Node(1 2) Exclude(vb vc)
        ObservationNode(1 2)
        ACExtraction = "ac10ddall"
        NoiseExtraction = "ac10ddall"
        NoisePlot = "ac10ddall"
      )
      {Poisson Electron Hole  }
load(fileprefix = "18310dd")
    ACCoupled (
        StartFrequency = 1e9 EndFrequency = 20e9
        NumberofPoints = 20  linear
        Node(1 2) Exclude(vb vc)
        ObservationNode(1 2)
        ACExtraction = "ac10ddall"
        NoiseExtraction = "ac10ddall"
        NoisePlot = "ac10ddall"
      )
      {Poisson Electron Hole  }
load(fileprefix = "18410dd")
    ACCoupled (
        StartFrequency = 1e9 EndFrequency = 20e9
        NumberofPoints = 20  linear
        Node(1 2) Exclude(vb vc)
        ObservationNode(1 2)
        ACExtraction = "ac10ddall"
        NoiseExtraction = "ac10ddall"
        NoisePlot = "ac10ddall"
      )
      {Poisson Electron Hole  }
load(fileprefix = "18510dd")
    ACCoupled (
        StartFrequency = 1e9 EndFrequency = 20e9
        NumberofPoints = 20  linear
        Node(1 2) Exclude(vb vc)
        ObservationNode(1 2)
```

```
        ACExtraction = "ac10ddall"
        NoiseExtraction = "ac10ddall"
        NoisePlot = "ac10ddall"
      )
      {Poisson Electron Hole  }
load(fileprefix = "18610dd")
    ACCoupled (
        StartFrequency = 1e9 EndFrequency = 20e9
        NumberofPoints = 20  linear
        Node(1 2) Exclude(vb vc)
        ObservationNode(1 2)
        ACExtraction = "ac10ddall"
        NoiseExtraction = "ac10ddall"
        NoisePlot = "ac10ddall"
      )
      {Poisson Electron Hole  }
load(fileprefix = "18710dd")
    ACCoupled (
        StartFrequency = 1e9 EndFrequency = 20e9
        NumberofPoints = 20  linear
        Node(1 2) Exclude(vb vc)
        ObservationNode(1 2)
        ACExtraction = "ac10ddall"
        NoiseExtraction = "ac10ddall"
        NoisePlot = "ac10ddall"
      )
      {Poisson Electron Hole  }
load(fileprefix = "18810dd")
    ACCoupled (
        StartFrequency = 1e9 EndFrequency = 20e9
        NumberofPoints = 20  linear
        Node(1 2) Exclude(vb vc)
        ObservationNode(1 2)
        ACExtraction = "ac10ddall"
        NoiseExtraction = "ac10ddall"
        NoisePlot = "ac10ddall"
      )
      {Poisson Electron Hole  }
load(fileprefix = "18910dd")
    ACCoupled (
        StartFrequency = 1e9 EndFrequency = 20e9
        NumberofPoints = 20  linear
```

```
        Node(1 2) Exclude(vb vc)
        ObservationNode(1 2)
        ACExtraction = "ac10ddall"
        NoiseExtraction = "ac10ddall"
        NoisePlot = "ac10ddall"
      )
      {Poisson Electron Hole  }
load(fileprefix = "19010dd")
    ACCoupled (
        StartFrequency = 1e9 EndFrequency = 20e9
        NumberofPoints = 20  linear
        Node(1 2) Exclude(vb vc)
        ObservationNode(1 2)
        ACExtraction = "ac10ddall"
        NoiseExtraction = "ac10ddall"
        NoisePlot = "ac10ddall"
      )
      {Poisson Electron Hole  }
}
```

B.1.3 Tecplot MCR file

Y parameters in this MCR file should be changed according to each bias and frequency.

```
#!MC 800
$!VarSet |MFBD| = '/home/tcad2/cuiyan1/cuiyan/Dessis/5hpdop/pmisimu'
$!VarSet |MFBD1| = '/home/tcad2/cuiyan1/cuiyan/Dessis/5hpdop/mesh'
$!Varset |fsel| = '10dd10g'
$!Varset |f| = 'jcp25'
#p = total(t), ee, hh
$!Varset |p| = 't'
$!Varset |num| = '00'
#other noise model calculation
$!Varset |freq| = 2.00000000000000E+09
$!Varset |omega| =(2*PI*|freq|)

$!Varset |ReY11| = 5.30793553232469E-05
$!Varset |ImY11| = (|omega|*2.40555589212422E-14 )

$!Varset |ReY12| =  -1.14676737756815E-06
$!Varset |ImY12| = (-2.13716228513946E-15*|omega|)

$!Varset |ReY21| = 4.08080901277576E-03
```

```
$!Varset |ImY21| = (-3.39993575257787E-14*|omega|)

$!Varset |ReY22| = 4.04802562859283E-06
$!Varset |ImY22| = ( 3.90143182411877E-15*|omega|)


#create 1.plt for Sv1
$!Newlayout
$!READDATASET  '"-ise:lay" "-ise:lc" "|MFBD1|/msh10_msh.grd"
  "|MFBD|/ac|fsel||f|_bjt_1_00|num|_acgf_des.dat.gz"'
  DATASETREADER = 'DF-ISE Loader'
$!ALTERDATA
  EQUATION = '{tLNVSD} = {LNVSD}'
$!ALTERDATA
  EQUATION = '{Sv1} = {|p|LNVSD}'
$!WRITEDATASET  "|MFBD|/1.dat"
  INCLUDEGEOM = NO
  INCLUDECUSTOMLABELS = NO
  VARPOSITIONLIST =  [1-2,29]
  BINARY = No
  USEPOINTFORMAT = Yes
  PRECISION = 9

#create 2.plt for Sv2
$!Newlayout
$!READDATASET  '"-ise:lay" "-ise:lc" "|MFBD1|/msh10_msh.grd"
  "|MFBD|/ac|fsel||f|_bjt_2_00|num|_acgf_des.dat.gz"'
  DATASETREADER = 'DF-ISE Loader'
$!ALTERDATA
  EQUATION = '{tLNVSD} = {LNVSD}'
$!ALTERDATA
  EQUATION = '{Sv2} = {|p|LNVSD}'
$!WRITEDATASET  "|MFBD|/2.dat"
  INCLUDEGEOM = NO
  INCLUDECUSTOMLABELS = NO
  VARPOSITIONLIST =  [1-2,29]
  BINARY = No
  USEPOINTFORMAT = Yes
  PRECISION = 9

#create 1_2.plt for ReSv12 and ImSv12
$!Newlayout
```

```
$!READDATASET  '"-ise:lay" "-ise:lc" "|MFBD1|/msh10_msh.grd"
  "|MFBD|/ac|fsel||f|_bjt_1_2_00|num|_acgf_des.dat.gz"'
  DATASETREADER = 'DF-ISE Loader'
$!ALTERDATA
  EQUATION = '{RetLNVXVSD} = {ReLNVXVSD}'
$!ALTERDATA
  EQUATION = '{ImtLNVXVSD} = {ImLNVXVSD}'
$!ALTERDATA
  EQUATION = '{ReSv12} = {Re|p|LNVXVSD}'
$!ALTERDATA
  EQUATION = '{ImSv12} = -{Im|p|LNVXVSD}'
$!WRITEDATASET  "|MFBD|/1_2.dat"
  INCLUDEGEOM = NO
  INCLUDECUSTOMLABELS = NO
  VARPOSITIONLIST =  [1-2,15-16]
  BINARY = No
  USEPOINTFORMAT = Yes
  PRECISION = 9

#combine Sv1, Sv2, Sv1v2 together

$!NEWLAYOUT
$!READDATASET  '"|MFBD|/1.dat" "|MFBD|/2.dat" "|MFBD|/1_2.dat" '
  READDATAOPTION = NEW
  RESETSTYLE = YES
  INCLUDEGEOM = NO
  INCLUDECUSTOMLABELS = NO
  VARLOADMODE = BYNAME
  INITIALFRAMEMODE = TWOD
  VARNAMELIST = '"X" "Y" "Sv1" "Sv2" "ReSv12" "ImSv12"'

$!Varset |Dataset| = |Numzones|
$!Varset |Dataset| /= 3

$!alterdata equation = "{h2} = 0"
$!alterdata equation = "{rh12} = 0"
$!alterdata equation = "{ih12} = 0"

$!Loop |dataset|
  $!Varset |Source1| = |Loop|
  $!Varset |Source1| += |dataset|
  $!Varset |Source2| = |Source1|
```

```
  $!Varset |Source2| += |dataset|
  $!Alterdata [|Loop|] equation = "{h2} = v4[|Source1|]"
  $!Alterdata [|Loop|] equation = "{rh12} = v5[|Source2|]"
  $!Alterdata [|Loop|] equation = "{ih12} = v6[|Source2|]"
$!endloop

$!varset |Deletezone| = |Dataset|
$!Varset |deletezone| += 1

$!Deletezones [|Deletezone| - |numzones|]
$!alterdata equation = "{Sv2} = {h2}"
$!Alterdata equation = "{ReSv12} = {rh12}"
$!Alterdata equation = "{ImSv12} = {ih12}"

$!WRITEDATASET  "|MFBD|/all.dat"
  INCLUDEGEOM = NO
  INCLUDECUSTOMLABELS = NO
  VARPOSITIONLIST =  [1-6]
  BINARY = no
  USEPOINTFORMAT = yes
  PRECISION = 9

$!NEWLAYOUT
$!READDATASET  '"|MFBD|/all.dat" '
  READDATAOPTION = NEW
  RESETSTYLE = YES
  INCLUDEGEOM = NO
  INCLUDECUSTOMLABELS = NO
  VARLOADMODE = BYNAME
  VARNAMELIST = '"X" "Y" "Sv1" "Sv2" "ReSv12" "ImSv12"'

$!Varset |abs2Y21| = (|ReY21|*|ReY21| + |ImY21|*|ImY21|)
$!Varset |abs2Y22| = (|ReY22|*|ReY22| + |ImY22|*|ImY22|)
$!Varset |Redelta0| = (|ReY11|*|ReY22|-|ImY11|*|ImY22|-|ReY12|*|ReY21|+|ImY12|*|ImY21|)
$!Varset |Imdelta0| = (|ReY11|*|ImY22|+|ReY22|*|ImY11|-|ReY12|*|ImY21|-|ReY21|*|ImY12|)
$!Varset |abs2delta0| = (|Redelta0|*|Redelta0| + |Imdelta0|*|Imdelta0|)
$!Varset |x| = (|Redelta0|*|ReY21|+|Imdelta0|*|ImY21|)
$!Varset |Redelta1| = (|x|/|abs2Y21|)
$!Varset |x| = (|Imdelta0|*|ReY21|-|Redelta0|*|ImY21|)
$!Varset |Imdelta1| = (|x|/|abs2Y21|)
$!Varset |abs2delta1| = (|Redelta1|*|Redelta1|+|Imdelta1|*|Imdelta1|)
```

```
$!Varset |x| = (|ReY22|*|ReY21|+|ImY22|*|ImY21|)
$!Varset |Redelta2| = (|x|/|abs2Y21|)
$!Varset |x| = (|ImY22|*|ReY21|-|ReY22|*|ImY21|)
$!Varset |Imdelta2| = (|x|/|abs2Y21|)
$!Varset |abs2delta2| = (|Redelta2|*|Redelta2|+|Imdelta2|*|Imdelta2|)
$!Varset |x| = (|Redelta0|*|ReY22|+|Imdelta0|*|ImY22|)
$!Varset |Redelta3| = (|x|/|abs2Y21|)
$!Varset |x| = (|Imdelta0|*|ReY22|-|Redelta0|*|ImY22|)
$!Varset |Imdelta3| = (|x|/|abs2Y21|)

#Sva, Sia
$!alterdata
  equation = "{Sva} = {Sv1}+|abs2delta2|*{Sv2}+2*({ReSv12}*|Redelta2|+{ImSv12}*|Imdelta
$!alterdata
  equation = "{Sia} = {Sv2}*|abs2delta1|"
$!alterdata
  equation = "{ReSiava} = |Redelta1|*{ReSv12}+|Imdelta1|*{ImSv12}+|Redelta3|*{Sv2}"
$!alterdata
  equation = "{ImSiava} = |Imdelta1|*{ReSv12}-|Redelta1|*{ImSv12}+|Imdelta3|*{Sv2}"

#Sin1, Sin2

$!Varset |abs2Y11| = (|ReY11|*|ReY11| + |ImY11|*|ImY11|)
$!Varset |abs2Y12| = (|ReY12|*|ReY12| + |ImY12|*|ImY12|)

$!Varset |Rex| =  (|ReY11|*|ReY12|+|ImY11|*|ImY12|)
$!Varset |Imx| =  (|ImY11|*|ReY12|-|ReY11|*|ImY12|)

$!Varset |Rey| =  (|ReY21|*|ReY22|+|ImY21|*|ImY22|)
$!Varset |Imy| =  (|ImY21|*|ReY22|-|ReY21|*|ImY22|)

$!Varset |Rez| =  (|ReY21|*|ReY11|+|ImY21|*|ImY11|)
$!Varset |Imz| =  (|ImY21|*|ReY11|-|ReY21|*|ImY11|)

$!Varset |Rew| =  (|ReY22|*|ReY12|+|ImY22|*|ImY12|)
$!Varset |Imw| =  (|ImY22|*|ReY12|-|ReY22|*|ImY12|)

$!Varset |Reu| =  (|ReY22|*|ReY11|+|ImY22|*|ImY11|)
$!Varset |Imu| =  (|ImY22|*|ReY11|-|ReY22|*|ImY11|)

$!Varset |Rev| =  (|ReY21|*|ReY12|+|ImY21|*|ImY12|)
$!Varset |Imv| =  (|ImY21|*|ReY12|-|ReY21|*|ImY12|)
```

```
$!alterdata
  equation = "{Sin1} = |abs2Y11|*{Sv1}+|abs2Y12|*{Sv2} + 2*(|Rex|*{ReSv12}-|Imx|*{ImSv1
$!alterdata
  equation = "{Sin2} = |abs2Y21|*{Sv1} + |abs2Y22|*{Sv2} + 2*(|Rey|*{ReSv12}-|Imy|*{ImS
$!alterdata
  equation = "{ReSi2i1} = |Rez|*{Sv1} + |Rew|*{Sv2} + |Reu|*{ReSv12}+|Imu|*{ImSv12} + |
$!alterdata
  equation = "{ImSi2i1} = |Imz|*{Sv1} + |Imw|*{Sv2} + |Imu|*{ReSv12} -|Reu|*{ImSv12}+|I

$!WRITEDATASET "|MFBD|/final|fsel||f||p||num|.dat"
  INCLUDEGEOM = NO
  INCLUDECUSTOMLABELS = NO
  VARPOSITIONLIST = [1-14]
  BINARY = no
  USEPOINTFORMAT = yes
  PRECISION = 9

$!FIELDLAYERS SHOWMESH = NO
$!Fieldlayers showcontour = Yes
$!TWODAXIS YDETAIL{ISREVERSED = YES}
$!GLOBALCONTOUR LEGEND{SHOW = YES}
$!FIELD [1-18]  CONTOUR{CONTOURTYPE = FLOOD}

$!ADDONCOMMAND
  ADDONID = 'ISE TCAD ADD-on'
  COMMAND = 'ORTHOSLICE X 1.75 Frame 001'

$!WRITEDATASET "|MFBD|/1dcut|fsel||f||p||num|.dat"
  INCLUDEGEOM = NO
  INCLUDECUSTOMLABELS = NO
  BINARY = no
  USEPOINTFORMAT = yes
  PRECISION = 9

$!RemoveVar |MFBD|
```

B.2 8HP SiGe HBT

B.2.1 Mesh files

BND file

```
#8hp 2D structure

Oxide "DT1" {polygon[(2.05, 0.19) (2.05, 0.53) (2.17, 0.53)
                     (2.17, 4.30) (2.39, 4.30) (2.39, 0.19)]}
Oxide "DT2" {polygon[(-2.05, 0.19) (-2.05, 0.53) (-2.17, 0.53)
                     (-2.17, 4.30) (-2.39, 4.30) (-2.39, 0.19)]}
Oxide "STI1" {rectangle[(0.35, 0.19) (1.35, 0.53)]}
Oxide "STI2"{rectangle[(-0.35, 0.19) (-1.35, 0.53)]}
Oxide "spacer1" {polygon[(0.06, 0.15) (0.06, 0) (0.36, 0) (0.36, 0.05)
                         (0.12, 0.05) (0.12, 0.15)]}
Oxide "spacer2" {polygon[(-0.06, 0.15) (-0.06, 0) (-0.36, 0) (-0.36, 0.05)
                         (-0.12, 0.05) (-0.12, 0.15)]}
PolySi "PolySi" {rectangle[(-0.06, 0.15) (0.06, 0.04)]
                }
PolySi "basesi1" {rectangle[(0.12, 0.15) (1.1, 0.05)]}
PolySi "basesi2" {rectangle[(-0.12, 0.15) (-1.1, 0.05)]}
Silicon "Silicon1" {polygon[(0.35, 0.19) (0.35, 0.53) (1.35, 0.53)
                            (1.35, 0.19) (2.05, 0.19) (2.05, 0.53)
                            (2.17, 0.53) (2.17, 4.30)
                            (-2.17, 4.30) (-2.17, 0.53)
                            (-2.05, 0.53) (-2.05, 0.19) (-1.35, 0.19)
                            (-1.35, 0.53) (-0.35, 0.53) (-0.35, 0.19)]
                    }
SiliconGermanium "SiGe" {rectangle[
                                 (1.1, 0.15) (-1.1 0.19) ]}
Contact "Collector1" {line[(1.35, 0.19) (2.05, 0.19)]}
Contact "Collector2" {line[(-1.35, 0.19) (-2.05, 0.19)]}
Contact "Base1" {line[(0.36, 0.05) (1.1, 0.05)]}
Contact "Base2" {line[(-0.36, 0.05) (-1.1, 0.05)]}
Contact "Emitter" {line[(-0.06, 0.04) (0.06, 0.04)]}
Contact "Psubstrate" {line[(2.39, 4.3) (-2.39, 4.3)]}
```

CMD file

```
Title "BJT"

Definitions {
```

```
# Refinement regions
  Refinement "all region"
  {
    MaxElementSize = (0.4 0.25)
    MinElementSize = (0.2 0.05)
    RefineFunction = MaxTransDiff(Variable="DopingConcentration" Value=1)
  }
  Refinement "ccontact"
  {
    MaxElementSize = (0.15 0.1)
    MinElementSize = (0.15 0.05)
    RefineFunction = MaxTransDiff(Variable="DopingConcentration" Value=1)
  }
  Refinement "cb1"
  {
    MaxElementSize = (0.05 0.02)
    MinElementSize = (0.025 0.005)
    RefineFunction = MaxTransDiff(Variable="DopingConcentration" Value=1)
  }
  Refinement "sige"
  {
    MaxElementSize = (0.004 0.002)
    MinElementSize = (0.002 0.001)
    RefineFunction = MaxTransDiff(Variable="DopingConcentration" Value=1)
  }
  Refinement "sige2"
  {
    MaxElementSize = (0.004 0.004)
    MinElementSize = (0.002 0.002)
    RefineFunction = MaxTransDiff(Variable="DopingConcentration" Value=1)
  }
  Refinement "sige3"
  {
    MaxElementSize = (0.008 0.008)
    MinElementSize = (0.004 0.004)
    RefineFunction = MaxTransDiff(Variable="DopingConcentration" Value=1)
  }
  Refinement "sige4"
  {
    MaxElementSize = (0.016 0.016)
    MinElementSize = (0.008 0.008)
    RefineFunction = MaxTransDiff(Variable="DopingConcentration" Value=1)
```

```
}
Refinement "sige5"
{
  MaxElementSize = (0.032 0.032)
  MinElementSize = (0.016 0.016)
  RefineFunction = MaxTransDiff(Variable="DopingConcentration" Value=1)
}
Refinement "sige6"
{
  MaxElementSize = (0.064 0.064)
  MinElementSize = (0.032 0.032)
  RefineFunction = MaxTransDiff(Variable="DopingConcentration" Value=1)
}
Refinement "substrate region1"
{
  MaxElementSize = (0.3 0.3)
  MinElementSize = (0.15 0.15)
  RefineFunction = MaxTransDiff(Variable="DopingConcentration" Value=1)
}
Refinement "substrate region2"
{
  MaxElementSize = (0.15 0.1)
  MinElementSize = (0.075 0.04)
  RefineFunction = MaxTransDiff(Variable="DopingConcentration" Value=1)
}
Refinement "Oxide_shallow"
{
  MaxElementSize = (0.1 0.1)
  MinElementSize = (0.05 0.01)
}
Refinement "Oxide_DT"
{
  MaxElementSize = (0.2 0.2)
  MinElementSize = (0.025 0.01)
}
Refinement "Oxide_spacer"
{
  MaxElementSize = (0.015 0.01)
  MinElementSize = (0.005 0.01)
}
 Refinement "Emitter0"
{
```

```
    MaxElementSize = (0.01 0.02)
    MinElementSize = (0.002 0.01)
    RefineFunction = MaxTransDiff(Variable="DopingConcentration" Value=0.1)
  }
   Refinement "Emitter1"
  {
    MaxElementSize = (0.02 0.02)
    MinElementSize = (0.01 0.01)
    RefineFunction = MaxTransDiff(Variable="DopingConcentration" Value=0.1)
  }
   Refinement "Emitter2"
  {
    MaxElementSize = (0.02 0.02)
    MinElementSize = (0.02 0.01)
    RefineFunction = MaxTransDiff(Variable="DopingConcentration" Value=0.1)
  }
   Refinement "Emitter3"
  {
    MaxElementSize = (0.08 0.04)
    MinElementSize = (0.04 0.01)
    RefineFunction = MaxTransDiff(Variable="DopingConcentration" Value=0.1)
  }

# Profiles
  Constant "psubstrate"
  {
    Species = "BoronActiveConcentration"
    Value = 1e+15
  }
  Constant "n_epi"
  {
    Species = "PhosphorusActiveConcentration"
    Value = 1e+16
  }
  AnalyticalProfile "collector"
  {
    Function = subMesh1D(datafile = "phos.dat"
      , Scale = 1,
      Range = line[(0 2.7940971e+15), (3.0  1.1610737e-195)]
      )
    LateralFunction = Erf(Factor = 0)
  }
```

```
    AnalyticalProfile "n_buri"
    {
      Function = subMesh1D(datafile = "asBuri.dat"
        , Scale = 1,
        Range = line[(0 2.2166889e+8), (3.0  2.4945547e+1)]
        )
      LateralFunction = Erf(Factor = 0)
    }
    AnalyticalProfile "emitter"
    {
      Function = subMesh1D(datafile = "as.dat"
        , Scale = 1,
        Range = line[(0 1e+21), (3.0 0)]
        )
      LateralFunction = Erf(Factor = 0)
    }
    AnalyticalProfile "intrinsic base"
    {
      Function = subMesh1D(datafile = "boron.dat"
        , Scale = 1,
        Range = line[(0 9.3631897e-224), (3.0 0)]
        )
      LateralFunction = Erf(Factor = 0)
    }
    Constant "cc"
        { Species = "ArsenicActiveConcentration"
          Value = 1e21
         }
    Constant "extrinsic base"
    {
      Species = "BoronActiveConcentration"
      Value = 5e20
    }
    AnalyticalProfile "xMoleBase"
    {
      Function = subMesh1D(datafile = "xmolg01.xy"
        , Scale = 1,
       Range = line[(0 0), (1.18 0)]
       )
       LateralFunction = Erf(Factor = 0)
    }
}
```

```
Placements {
  # Refinement regions
    Refinement "all region"
    {
      Reference = "all region"
      RefineWindow = rectangle [(-2.39 0), (2.39 4.30)]
    }
    Refinement "substrate region1"
    {
      Reference = "substrate region1"
      RefineWindow = rectangle [(-2.17 2.30), (2.17 4.30)]
    }
    Refinement "base region1"
    {
      Reference = "cb1"
      RefineWindow = polygon [(0.12 0.15), (0.12 0.05), (1.1 0.05),
                              (1.1 0.19), (-1.1 0.19), (-1.1 0.05),
                              (-0.12 0.05), (-0.12 0.15)]
    }
    Refinement "emitter region up"
    {
      Reference =  "Emitter2"
      RefineWindow = rectangle [(-0.06 0.04), (0.06 0.12)]
    }
    Refinement "emitter region middle"
    {
      Reference =  "Emitter1"
      RefineWindow = rectangle [(-0.06 0.12), (0.06 0.14)]
    }
    Refinement "emitter region down"
    {
      Reference =  "Emitter0"
      RefineWindow = rectangle [(-0.06 0.15), (0.06 0.14)]
    }
    Refinement "ccontact1"
    {
      Reference =  "ccontact"
      RefineWindow = rectangle [(-2.05 0.30)(-1.35 0.53)]
    }
    Refinement "ccontact2"
    {
      Reference =  "ccontact"
```

```
  RefineWindow = rectangle [(2.05 0.30)(1.35 0.53)]
}
Refinement "sige region6"
{
  Reference =  "sige6"
  RefineWindow = rectangle [(0.5 0.5)(-0.5 0.6)]
}
Refinement "sige region5"
{
  Reference =  "sige5"
  RefineWindow = rectangle [(0.4 0.15)(-0.4 0.50)]
}
Refinement "sige region4"
{
  Reference =  "sige4"
  RefineWindow = rectangle [(0.36 0.15)(-0.36 0.4)]
}
Refinement "sige region3"
{
  Reference =  "sige3"
  RefineWindow = rectangle [(0.14 0.15)(-0.14 0.3)]
}
Refinement "sige region2"
{
  Reference =  "sige2"
  RefineWindow = rectangle [(0.12 0.15)(-0.12 0.21)]
}
Refinement "sige region"
{
  Reference =  "sige"
  RefineWindow = rectangle [(0.08 0.15)(-0.08 0.19)]
}

Refinement "substrate region2"
{
  Reference = "substrate region2"
  RefineWindow = rectangle [(2.17 2.3), (-2.17 2.7)]
}
 Refinement "spacer1"
{
  Reference = "Oxide_spacer"
  RefineWindow = polygon [(0.36, 0) (0.06, 0) (0.06 0.15) (0.12 0.15)
```

```
                             (0.12 0.05) (0.36 0)]
  }
   Refinement "spacer2"
  {
    Reference = "Oxide_spacer"
    RefineWindow = polygon [(-0.36, 0) (-0.06, 0) (-0.06 0.15) (-0.12 0.15)
                            (-0.12 0.05) (-0.36 0)]
  }
   Refinement "ST1"
  {
    Reference = "Oxide_shallow"
    RefineWindow = rectangle [(0.35, 0.19) (1.35, 0.53)]
  }
  Refinement "ST2"
  {
    Reference = "Oxide_shallow"
    RefineWindow = rectangle [(-0.35, 0.19) (-1.35, 0.53)]
  }
  Refinement "DT1"
  {
    Reference = "Oxide_DT"
    RefineWindow = polygon[(2.05, 0.19) (2.05, 0.53) (2.17, 0.53)
                   (2.17, 4.30) (2.39, 4.30) (2.39, 0.19)]
  }
  Refinement "DT2"
  {
    Reference = "Oxide_DT"
    RefineWindow = polygon[(-2.05, 0.19) (-2.05, 0.53) (-2.17, 0.53)
                   (-2.17, 4.30) (-2.39, 4.30) (-2.39, 0.19)]
  }

# Profiles
  Constant "psubstrate instance"
  {
    Reference = "psubstrate"
    EvaluateWindow
    {
      Element = rectangle [(2.17 2.30), (-2.17 4.30)]
      DecayLength = 0
    }
  }
  Constant "n_epi instance"
```

```
{
  Reference = "n_epi"
  EvaluateWindow
  {
    Element = polygon[(0.35, 0.19) (0.35, 0.53) (1.35, 0.53)
                      (1.35, 0.19) (2.05, 0.19) (2.05, 0.53)
                      (2.17, 0.53) (2.17, 2.30)
                      (-2.17, 2.30) (-2.17, 0.53)
                      (-2.05, 0.53) (-2.05, 0.19) (-1.35, 0.19)
                      (-1.35, 0.53) (-0.35, 0.53) (-0.35, 0.19)]
    DecayLength = 0
  }
}
AnalyticalProfile "collector instance"
{
  Reference = "collector"
  ReferenceElement
  {
    Element = line [(-0.12 0.04), (0.12 0.04)]
  }
  EvaluateWindow
  {
    Element = rectangle[(-0.12 0.04)(0.12 2.30)]
  }
}
AnalyticalProfile "emitter instance"
{
  Reference = "emitter"
  ReferenceElement
  {
    Element = line [(-0.06 0.04), (0.06 0.04)]
  }
  EvaluateWindow
  {
    Element = rectangle[(-0.06, 0.53) (0.06, 0.04)]
    DecayLength = 0
  }
}
AnalyticalProfile "intrinsic base instance"
{
  Reference = "intrinsic base"
  ReferenceElement
```

```
  {
    Element = line [(-1.1 0.04), (1.1 0.04)]
  }
  EvaluateWindow
  {
    Element = rectangle[(-1.1 0.04), (1.1 0.53)]
  }
}
Constant "extrinsic base left instance"
{
  Reference = "extrinsic base"
  EvaluateWindow
  {
    Element = rectangle [(-0.12 0.05), (-1.1 0.15)]
    DecayLength = 0.005
  }
}
 Constant "extrinsic base right instance"
{
  Reference = "extrinsic base"
  EvaluateWindow
  {
    Element = rectangle [(0.12 0.05), (1.1 0.15)]
    DecayLength = 0.005
  }
}
AnalyticalProfile "n_buried layer instance"
{
  Reference = "n_buri"
  ReferenceElement
  {
    Element = line [(-2.17 0.04), (2.17 0.04)]
  }
  EvaluateWindow
  {
    Element = polygon[(0.35, 0.04) (0.35, 0.53) (1.35, 0.53)
                      (1.35, 0.19) (2.05, 0.19) (2.05, 0.53)
                      (2.17, 0.53) (2.17, 3)
                      (-2.17, 3) (-2.17, 0.53)
                      (-2.05, 0.53) (-2.05, 0.19) (-1.35, 0.19)
                      (-1.35, 0.53) (-0.35, 0.53) (-0.35, 0.04)]
    DecayLength = 0
```

```
      }
    }
    Constant "Collector contact instance left"
    {
      Reference = "cc"
      EvaluateWindow
      {
        Element=rectangle[(-1.35 0.19)(-2.17 1)]
      }
    }
    Constant "Collector contact instance right"
    {
      Reference = "cc"
      EvaluateWindow
      {
        Element=rectangle[(1.35 0.19)(2.17 1)]
      }
    }
    AnalyticalProfile "xMolBase instance"
    {
      Reference = "xMoleBase"
      ReferenceElement
      {
        Element = line[(-1.1 0.04) (1.1 0.04)]
        Direction = positive
      }
      EvaluateWindow
      {
        Element = rectangle[(-1.1 0.04) (1.1 0.19)]
      }
    }
}
```

B.2.2 Noise Simulation CMD file

```
Device BJT {

 Electrode {
   { Name="Emitter"   Voltage=0 }
   { Name="Base1"      Voltage=0 }
   { Name = "Base2"    Voltage = 0}
   { Name="Collector1" Voltage=0 }
```

```
  { Name="Collector2" Voltage=0 }
  { Name = "Psubstrate" Voltage = 0}
 }

 File {
  Grid      = "msh_msh.grd"
  Doping    = "msh_msh.dat"
  Current   = "achdet40g_des.plt"
  Plot      = "achdet40g_des.dat"
 }

 Physics{
    Areafactor= 1
    EffectiveIntrinsicDensity(BandgapNarrowing( Slotboom) )
    Mobility(
      PhuMob
      Highfieldsaturation(CarrierTempDrive)
    )
    Fermi
    Hydrodynamic(eTemp)
    Noise ( DiffusionNoise(eTemperature) )
 }

 Physics (material = "Silicon") {
    Recombination(
       SRH( DopingDependence )
       Auger
    )
 }

 Physics (material = "PolySi") {
    Recombination(
       SRH( DopingDependence )
       Auger
    )
 }

}
*-----------------------------------------------------------------------*
*--End of Device{}
*-----------------------------------------------------------------------*
```

```
Plot {
   eDensity hDensity
   TotalCurrent/Vector eCurrent/Vector hCurrent/Vector

   ElectricField Potential SpaceCharge
   Doping DonorConcentration AcceptorConcentration

   SRH Auger
   eQuasiFermi hQuasiFermi
   eEparal hEparal

   eMobility hMobility
   eVelocity hVelocity

   xMoleFraction

   BandGap BandGapNarrowing
   Affinity
   ConductionBand ValenceBand
}
#NoisePlot {
#   AllLNS AllLNVSD AllLNVXVSD GreenFunctions
#}


Math {
   Extrapolate
   NotDamped=200
   Iterations=20
   NewDiscretization
   Derivatives
   RelerrControl
   Digits=6
}

File {
   Output  = "achdet40g"
   ACExtract="achdet40g"

}

System {
```

```
   BJT bjt (Base1=1  Base2 = 1 Collector1=2 Collector2=2 Emitter=0 Psubstrate=0)
   Vsource_pset vb (1 0){ dc = 0 }
   Vsource_pset vc (2 0){ dc = 0 }
}

Solve {

   Coupled (Iterations=50) {Poisson }
   Coupled { Poisson Electron Hole }
   Coupled { Poisson Electron Hole ElectronTemperature}
Quasistationary (
      InitialStep=0.025 Increment= 1.4
      MinStep=1e-3 MaxStep=0.1
      Goal {Parameter=vc.dc Voltage=1.75}
      Goal {Parameter=vb.dc Voltage=0.75}
   ){
     Coupled {Poisson Electron Hole ElectronTemperature}
    }
save(fileprefix = "175hd")

newcurrent = "achdetbias"
load(fileprefix = "175hd")
Quasistationary (
      InitialStep=1 Increment=1
      MinStep=1e-3 MaxStep=1
      Goal {Parameter=vc.dc Voltage=1.76}
      Goal {Parameter=vb.dc Voltage=0.76}
   ){
      Coupled{Poisson Electron Hole ElectronTemperature}
    }
save(fileprefix = "176hd")
Quasistationary (
      InitialStep=1 Increment=1
      MinStep=1e-3 MaxStep=1
      Goal {Parameter=vc.dc Voltage=1.77}
      Goal {Parameter=vb.dc Voltage=0.77}
   ){
      Coupled{Poisson Electron Hole ElectronTemperature}
    }
save(fileprefix = "177hd")
Quasistationary (
      InitialStep=1 Increment=1
```

```
      MinStep=1e-3 MaxStep=1
      Goal {Parameter=vc.dc Voltage=1.78}
      Goal {Parameter=vb.dc Voltage=0.78}
   ){
      Coupled{Poisson Electron Hole ElectronTemperature}
    }
save(fileprefix = "178hd")
Quasistationary (
      InitialStep=1 Increment=1
      MinStep=1e-3 MaxStep=1
      Goal {Parameter=vc.dc Voltage=1.79}
      Goal {Parameter=vb.dc Voltage=0.79}
   ){
      Coupled{Poisson Electron Hole ElectronTemperature}
    }
save(fileprefix = "179hd")
Quasistationary (
      InitialStep=1 Increment=1
      MinStep=1e-3 MaxStep=1
      Goal {Parameter=vc.dc Voltage=1.80}
      Goal {Parameter=vb.dc Voltage=0.80}
   ){
      Coupled{Poisson Electron Hole ElectronTemperature}
    }
save(fileprefix = "180hd")
Quasistationary (
      InitialStep=1 Increment=1
      MinStep=1e-3 MaxStep=1
      Goal {Parameter=vc.dc Voltage=1.81}
      Goal {Parameter=vb.dc Voltage=0.81}
   ){
      Coupled{Poisson Electron Hole ElectronTemperature}
    }
save(fileprefix = "181hd")
Quasistationary (
      InitialStep=1 Increment=1
      MinStep=1e-3 MaxStep=1
      Goal {Parameter=vc.dc Voltage=1.82}
      Goal {Parameter=vb.dc Voltage=0.82}
   ){
      Coupled{Poisson Electron Hole ElectronTemperature}
    }
```

```
save(fileprefix = "182hd")
Quasistationary (
      InitialStep=1 Increment=1
      MinStep=1e-3 MaxStep=1
      Goal {Parameter=vc.dc Voltage=1.83}
      Goal {Parameter=vb.dc Voltage=0.83}
   ){
      Coupled{Poisson Electron Hole ElectronTemperature}
    }
save(fileprefix = "183hd")
Quasistationary (
      InitialStep=1 Increment=1
      MinStep=1e-3 MaxStep=1
      Goal {Parameter=vc.dc Voltage=1.84}
      Goal {Parameter=vb.dc Voltage=0.84}
   ){
      Coupled{Poisson Electron Hole ElectronTemperature}
    }
save(fileprefix = "184hd")
Quasistationary (
      InitialStep=1 Increment=1
      MinStep=1e-3 MaxStep=1
      Goal {Parameter=vc.dc Voltage=1.85}
      Goal {Parameter=vb.dc Voltage=0.85}
   ){
      Coupled{Poisson Electron Hole ElectronTemperature}
    }
save(fileprefix = "185hd")
Quasistationary (
      InitialStep=1 Increment=1
      MinStep=1e-3 MaxStep=1
      Goal {Parameter=vc.dc Voltage=1.86}
      Goal {Parameter=vb.dc Voltage=0.86}
   ){
      Coupled{Poisson Electron Hole ElectronTemperature}
    }
save(fileprefix = "186hd")
Quasistationary (
      InitialStep=1 Increment=1
      MinStep=1e-3 MaxStep=1
      Goal {Parameter=vc.dc Voltage=1.87}
      Goal {Parameter=vb.dc Voltage=0.87}
```

```
   ){
      Coupled{Poisson Electron Hole ElectronTemperature}
    }
save(fileprefix = "187hd")
Quasistationary (
      InitialStep=1 Increment=1
      MinStep=1e-3 MaxStep=1
      Goal {Parameter=vc.dc Voltage=1.88}
      Goal {Parameter=vb.dc Voltage=0.88}
   ){
      Coupled{Poisson Electron Hole ElectronTemperature}
    }
save(fileprefix = "188hd")
Quasistationary (
      InitialStep=1 Increment=1
      MinStep=1e-3 MaxStep=1
      Goal {Parameter=vc.dc Voltage=1.89}
      Goal {Parameter=vb.dc Voltage=0.89}
   ){
      Coupled{Poisson Electron Hole ElectronTemperature}
    }
save(fileprefix = "189hd")
Quasistationary (
      InitialStep=1 Increment=1
      MinStep=1e-3 MaxStep=1
      Goal {Parameter=vc.dc Voltage=1.90}
      Goal {Parameter=vb.dc Voltage=0.90}
   ){
      Coupled{Poisson Electron Hole ElectronTemperature}
    }
save(fileprefix = "190hd")

newcurrent = "achdet40g"
load(fileprefix = "175hd")
    ACCoupled (
        StartFrequency = 40e9 EndFrequency = 40e9
        NumberofPoints = 1  linear
        Node(1 2) Exclude(vb vc)
        ObservationNode(1 2)
        ACExtraction = "achdet40g"
        NoiseExtraction = "achdet40g"
        NoisePlot = "achdet40g175"
```

```
      )
      {Poisson Electron Hole ElectronTemperature}
load(fileprefix = "176hd")
    ACCoupled (
        StartFrequency = 40e9 EndFrequency = 40e9
        NumberofPoints = 1  linear
        Node(1 2) Exclude(vb vc)
        ObservationNode(1 2)
        ACExtraction = "achdet40g"
        NoiseExtraction = "achdet40g"
        NoisePlot = "achdet40g176"
      )
      {Poisson Electron Hole ElectronTemperature}
load(fileprefix = "177hd")
    ACCoupled (
        StartFrequency = 40e9 EndFrequency = 40e9
        NumberofPoints = 1  linear
        Node(1 2) Exclude(vb vc)
        ObservationNode(1 2)
        ACExtraction = "achdet40g"
        NoiseExtraction = "achdet40g"
        NoisePlot = "achdet40g177"
      )
      {Poisson Electron Hole ElectronTemperature}
load(fileprefix = "178hd")
    ACCoupled (
        StartFrequency = 40e9 EndFrequency = 40e9
        NumberofPoints = 1  linear
        Node(1 2) Exclude(vb vc)
        ObservationNode(1 2)
        ACExtraction = "achdet40g"
        NoiseExtraction = "achdet40g"
        NoisePlot = "achdet40g178"
      )
      {Poisson Electron Hole ElectronTemperature}
load(fileprefix = "179hd")
    ACCoupled (
        StartFrequency = 40e9 EndFrequency = 40e9
        NumberofPoints = 1  linear
        Node(1 2) Exclude(vb vc)
        ObservationNode(1 2)
        ACExtraction = "achdet40g"
```

```
        NoiseExtraction = "achdet40g"
        NoisePlot = "achdet40g179"
      )
      {Poisson Electron Hole ElectronTemperature}
load(fileprefix = "180hd")
    ACCoupled (
        StartFrequency = 40e9 EndFrequency = 40e9
        NumberofPoints = 1  linear
        Node(1 2) Exclude(vb vc)
        ObservationNode(1 2)
        ACExtraction = "achdet40g"
        NoiseExtraction = "achdet40g"
        NoisePlot = "achdet40g180"
      )
      {Poisson Electron Hole ElectronTemperature}
load(fileprefix = "181hd")
    ACCoupled (
        StartFrequency = 40e9 EndFrequency = 40e9
        NumberofPoints = 1  linear
        Node(1 2) Exclude(vb vc)
        ObservationNode(1 2)
        ACExtraction = "achdet40g"
        NoiseExtraction = "achdet40g"
        NoisePlot = "achdet40g181"
      )
      {Poisson Electron Hole ElectronTemperature}
load(fileprefix = "182hd")
    ACCoupled (
        StartFrequency = 40e9 EndFrequency = 40e9
        NumberofPoints = 1  linear
        Node(1 2) Exclude(vb vc)
        ObservationNode(1 2)
        ACExtraction = "achdet40g"
        NoiseExtraction = "achdet40g"
        NoisePlot = "achdet40g182"
      )
      {Poisson Electron Hole ElectronTemperature}
load(fileprefix = "183hd")
    ACCoupled (
        StartFrequency = 40e9 EndFrequency = 40e9
        NumberofPoints = 1  linear
        Node(1 2) Exclude(vb vc)
```

```
        ObservationNode(1 2)
        ACExtraction = "achdet40g"
        NoiseExtraction = "achdet40g"
        NoisePlot = "achdet40g183"
      )
      {Poisson Electron Hole ElectronTemperature}
load(fileprefix = "184hd")
    ACCoupled (
        StartFrequency = 40e9 EndFrequency = 40e9
        NumberofPoints = 1  linear
        Node(1 2) Exclude(vb vc)
        ObservationNode(1 2)
        ACExtraction = "achdet40g"
        NoiseExtraction = "achdet40g"
        NoisePlot = "achdet40g184"
      )
      {Poisson Electron Hole ElectronTemperature}
load(fileprefix = "185hd")
    ACCoupled (
        StartFrequency = 40e9 EndFrequency = 40e9
        NumberofPoints = 1  linear
        Node(1 2) Exclude(vb vc)
        ObservationNode(1 2)
        ACExtraction = "achdet40g"
        NoiseExtraction = "achdet40g"
        NoisePlot = "achdet40g185"
      )
      {Poisson Electron Hole ElectronTemperature}
load(fileprefix = "186hd")
    ACCoupled (
        StartFrequency = 40e9 EndFrequency = 40e9
        NumberofPoints = 1  linear
        Node(1 2) Exclude(vb vc)
        ObservationNode(1 2)
        ACExtraction = "achdet40g"
        NoiseExtraction = "achdet40g"
        NoisePlot = "achdet40g186"
      )
      {Poisson Electron Hole ElectronTemperature}
load(fileprefix = "187hd")
    ACCoupled (
        StartFrequency = 40e9 EndFrequency = 40e9
```

```
        NumberofPoints = 1  linear
        Node(1 2) Exclude(vb vc)
        ObservationNode(1 2)
        ACExtraction = "achdet40g"
        NoiseExtraction = "achdet40g"
        NoisePlot = "achdet40g187"
      )
      {Poisson Electron Hole ElectronTemperature}
load(fileprefix = "188hd")
    ACCoupled (
        StartFrequency = 40e9 EndFrequency = 40e9
        NumberofPoints = 1  linear
        Node(1 2) Exclude(vb vc)
        ObservationNode(1 2)
        ACExtraction = "achdet40g"
        NoiseExtraction = "achdet40g"
        NoisePlot = "achdet40g188"
      )
      {Poisson Electron Hole ElectronTemperature}
load(fileprefix = "189hd")
    ACCoupled (
        StartFrequency = 40e9 EndFrequency = 40e9
        NumberofPoints = 1  linear
        Node(1 2) Exclude(vb vc)
        ObservationNode(1 2)
        ACExtraction = "achdet40g"
        NoiseExtraction = "achdet40g"
        NoisePlot = "achdet40g189"
      )
      {Poisson Electron Hole ElectronTemperature}
load(fileprefix = "190hd")
    ACCoupled (
        StartFrequency = 40e9 EndFrequency = 40e9
        NumberofPoints = 1  linear
        Node(1 2) Exclude(vb vc)
        ObservationNode(1 2)
        ACExtraction = "achdet40g"
        NoiseExtraction = "achdet40g"
        NoisePlot = "achdet40g190"
      )
      {Poisson Electron Hole ElectronTemperature}
}
```

B.3 MATLAB Programming for Simulation Results

This is MATLAB Programming for 8HP DESSIS simulation results. The MATLAB programming is similar for 5HP SiGe HBT DESSIS simulation results.

B.3.1 Main file

```
close all; clear all; clc;
q = 1.6e-19;
kt = 0.0259*q;
datapath = 'D:\Yan\research\8hp\noisedata';
cd(datapath);
filename = {'hdetall','hd2etall','g05hdetall'};
legname = {'design I', 'design II', 'design III'};
x1 = 20;
fileNumber=length(filename);
datasel =1; %1: bias dependence, 2: frequency dependence

for filsel = [1:3],
    load(filename{filsel});
    rbrange = (num_of_freq-5):num_of_freq;
    Jc = Ic./0.12.*1e3; Jb = Ib./0.12.*1e3;
    nx = x1;
    for n = nx;
switch datasel
case 1 %bias dependence
    sv12x = conj(sv12); sv12eex = conj(sv12ee); sv12hhx = conj(sv12hh);
    SV = [sv1(:,n) sv12x(:,n) conj(sv12x(:,n)) sv2(:,n)];
    SVee = [sv1ee(:,n) sv12eex(:,n) conj(sv12eex(:,n)) sv2ee(:,n)];
    SVhh = [sv1hh(:,n) sv12hhx(:,n) conj(sv12hhx(:,n)) sv2hh(:,n)];
     Y = [Y11(:,n) Y12(:,n) Y21(:,n) Y22(:,n)]; Z = z_from_Y(Y);
    for x = 1: num_of_bias,
        Y11f = Y11(x,:); Y12f = Y12(x,:);Y21f = Y21(x,:);Y22f = Y22(x,:);
        h11f = 1./Y11f;
        Yf = [conj(Y11f') conj(Y12f') conj(Y21f') conj(Y22f')];
        Zf = Z_from_Y(Yf);
        Z11f = Zf(:,1); Z12f = Zf(:,2); Z21f = Zf(:,3); Z22f = Zf(:,4);
        rbh(x) = rb_from_h11(h11f(rbrange));
        rb(x) = rbh(x);         re(x) = 0;        rc(x) = 0;
    end
    numend = num_of_bias;
case 2 %frequency dependence
```

```
    sv12x = conj(sv12); sv12eex = conj(sv12ee); sv12hhx = conj(sv12hh);
    SV = [conj(sv1(n,:)') conj(sv12x(n,:)') sv12x(n,:)' conj(sv2(n,:)')];
    SVee = [conj(sv1ee(n,:)') conj(sv12eex(n,:)') ...
                sv12eex(n,:)' conj(sv2ee(n,:)')];
    SVhh = [conj(sv1hh(n,:)') conj(sv12hhx(n,:)') ...
                sv12hhx(n,:)' conj(sv2hh(n,:)')];
    Y = [conj(Y11(n,:)') conj(Y12(n,:)') conj(Y21(n,:)') conj(Y22(n,:)')];
    Z = z_from_Y(Y);
    h11 = 1./Y(:,1); rbh(n) = rb_from_h11(h11(rbrange));
    Z11f = Z(:,1); Z12f = Z(:,2); Z21f = Z(:,3); Z22f = Z(:,4);
    rb(n) = rbh(n);     re(n) = 0;    rc(n) = 0;
    numend = num_of_freq;
end
%-----------------------------------------------------------------------------
for x = 1:numend,
    y = Y(x,:); z = Z(x,:); a = a_from_y(y);
    cz = 0.5.*SV(x,:); ca = c_from_z_to_a(cz, a); cy = c_from_a_to_y(ca, y);
    nf = nf_from_ca(ca, 50);
    svb(x) = 2*cz(1); svc(x) = 2*cz(4);
    svbvcr(x) = 2*real(cz(2)); svbvci(x) = 2*imag(cz(2));
    cvbvcr(x) = svbvcr(x)/sqrt(svc(x)*svb(x));
    cvbvci(x) = svbvci(x)/sqrt(svc(x)*svb(x));
    sva(x) = 2*ca(1); sia(x) = 2*ca(4);
    siavar(x) = 2*real(ca(3)); siavai(x) = 2*imag(ca(3));
    ciavar(x) = siavar(x)/sqrt(sia(x)*sva(x));
    ciavai(x) = siavai(x)/sqrt(sia(x)*sva(x));
    sib(x) = 2*cy(1); sic(x) = 2*cy(4);
    sicibr(x) = 2*real(cy(3)); sicibi(x) = 2*imag(cy(3));
    cicibr(x) = sicibr(x)/sqrt(sib(x)*sic(x));
    cicibi(x) = sicibi(x)/sqrt(sib(x)*sic(x));
    nfmin(x) = nf(1);  rn(x) = nf(2); Yopt(x) = nf(3);

    czee = 0.5.*SVee(x,:); caee = c_from_z_to_a(czee, a);
    cyee = c_from_a_to_y(caee, y); nfee = nf_from_ca(caee, 50);
    svbee(x) = 2*czee(1); svcee(x) = 2*czee(4);
    svbvcree(x) = 2*real(czee(2)); svbvciee(x) = 2*imag(czee(2));
    cvbvcree(x) = svbvcree(x)/sqrt(svcee(x)*svbee(x));
    cvbvciee(x) = svbvciee(x)/sqrt(svcee(x)*svbee(x));
    svaee(x) = 2*caee(1); siaee(x) = 2*caee(4);
    siavaree(x) = 2*real(caee(3)); siavaiee(x) = 2*imag(caee(3));
    ciavaree(x) = siavaree(x)/sqrt(siaee(x)*svaee(x));
    ciavaiee(x) = siavaiee(x)/sqrt(siaee(x)*svaee(x));
```

```
    sibee(x) = 2*cyee(1); sicee(x) = 2*cyee(4);
    sicibree(x) = 2*real(cyee(3)); sicibiee(x) = 2*imag(cyee(3));
    cicibree(x) = sicibree(x)/sqrt(sibee(x)*sicee(x));
    cicibiee(x) = sicibiee(x)/sqrt(sibee(x)*sicee(x));
    nfminee(x) = nfee(1);  rnee(x) = nfee(2); Yoptee(x) = nfee(3);

    czhh = 0.5.*SVhh(x,:); cahh = c_from_z_to_a(czhh, a);
    cyhh = c_from_a_to_y(cahh, y); nfhh = nf_from_ca(cahh, 50);
    svbhh(x) = 2*czhh(1); svchh(x) = 2*czhh(4);
    svbvcrhh(x) = 2*real(czhh(2)); svbvcihh(x) = 2*imag(czhh(2));
    cvbvcrhh(x) = svbvcrhh(x)/sqrt(svchh(x)*svbhh(x));
    cvbvcihh(x) = svbvcihh(x)/sqrt(svchh(x)*svbhh(x));
    svahh(x) = 2*cahh(1); siahh(x) = 2*cahh(4);
    siavarhh(x) = 2*real(cahh(3)); siavaihh(x) = 2*imag(cahh(3));
    ciavarhh(x) = siavarhh(x)/sqrt(siahh(x)*svahh(x));
    ciavaihh(x) = siavaihh(x)/sqrt(siahh(x)*svahh(x));
    sibhh(x) = 2*cyhh(1); sichh(x) = 2*cyhh(4);
    sicibrhh(x) = 2*real(cyhh(3)); sicibihh(x) = 2*imag(cyhh(3));
    cicibrhh(x) = sicibrhh(x)/sqrt(sibhh(x)*sichh(x));
    cicibihh(x) = sicibihh(x)/sqrt(sibhh(x)*sichh(x));
    nfminhh(x) = nfhh(1);  rnhh(x) = nfhh(2); Yopthh(x) = nfhh(3);
end
for x = 1:numend,
    y = Y(x,:); z = Z(x,:);, a = a_from_y(y);
    switch datasel
    case 1
        rbx = rb(x); Ibx = Ib(x); Icx = Ic(x);
        rex = re(x); rcx = rc(x);
    case 2
        rbx = rb(n); Ibx = Ib(n); Icx = Ic(n);
        rex = re(n); rcx = rc(n);
    end
    zb = [rbx+rex rex rex rex+rcx]; czb = 2*kt.*zb;
    zi = z-zb; yi = y_from_z(zi); ai = a_from_y(yi);
    if x ==1, yix = yi(3); end
    cz = 0.5.*SV(x,:); ca = c_from_z_to_a(cz, a);
    cy = c_from_a_to_y(ca, y);
    czi = cz - czb; cai = c_from_z_to_a(czi, ai);
    cyi = c_from_a_to_y(cai, yi);
    sibi(x) = 2*cyi(1); sici(x) = 2*cyi(4);
    sicibri(x) = 2*real(cyi(3)); sicibii(x) = 2*imag(cyi(3));
    cicibri(x) = sicibri(x)./sqrt(sibi(x).*sici(x));
```

```
cicibii(x) = sicibii(x)./sqrt(sibi(x).*sici(x));

czhh = 0.5.*SVhh(x,:); cahh = c_from_z_to_a(czhh, a);
cyhh = c_from_a_to_y(cahh, y);
czihh = czhh - czb; caihh = c_from_z_to_a(czihh, ai);
cyihh = c_from_a_to_y(caihh, yi);
sibihh(x) = 2*cyihh(1); sicihh(x) = 2*cyihh(4);
sicibrihh(x) = 2*real(cyihh(3)); sicibiihh(x) = 2*imag(cyihh(3));
cicibrihh(x) = sicibrihh(x)./sqrt(sibihh(x).*sicihh(x));
cicibiihh(x) = sicibiihh(x)./sqrt(sibihh(x).*sicihh(x));

czee = 0.5.*SVee(x,:); caee = c_from_z_to_a(czee, a);
cyee = c_from_a_to_y(caee, y);
cziee = czee; caiee = c_from_z_to_a(cziee, ai);
cyiee = c_from_a_to_y(caiee, yi);
sibiee(x) = 2*cyiee(1); siciee(x) = 2*cyiee(4);
sicibriee(x) = 2*real(cyiee(3)); sicibiiee(x) = 2*imag(cyiee(3));
cicibriee(x) = sicibriee(x)./sqrt(sibiee(x).*siciee(x));
cicibiiee(x) = sicibiiee(x)./sqrt(sibiee(x).*siciee(x));

sibs(x) = 2*q*Ibx; sics(x) = 2*q*Icx; sicibrs(x) = 0; sicibis(x) = 0;
cysi = 0.5*[sibs(x), sicibrs(x) - j*sicibis(x),  ...
                 sicibrs(x) + j*sicibis(x), sics(x)];
casi = c_from_y_to_a(cysi, ai);
czsi = c_from_a_to_z(casi, zi); czs = czsi + czb;
cas = c_from_z_to_a(czs, a); nfs = nf_from_ca(cas, 50);
svas(x) = 2*cas(1); sias(x) = 2*cas(4);
siavars(x) = real(2*cas(3)); siavais(x) = imag(2*cas(3));
nfmins(x) = nfs(1); rns(x) = nfs(2); Yopts(x) = nfs(3);

sibv(x) = 4*kt*real(yi(1)) - 2*q*Ibx;
sicv(x) = 4*kt*real(yi(4)) + 2*q*Icx;
sicibrv(x) = 2*kt*real(yi(3)+y(2)'-yix);
sicibiv(x) = 2*kt*imag(yi(3)+y(2)');
cyvi = 0.5*[sibv(x), sicibrv(x) - j*sicibiv(x),  ...
                 sicibrv(x) + j*sicibiv(x), sicv(x)];
cavi = c_from_y_to_a(cyvi, ai); czvi = c_from_a_to_z(cavi, zi);
czv = czvi + czb;
cav = c_from_z_to_a(czv, a); nfv = nf_from_ca(cav, 50);
svav(x) = 2*cav(1); siav(x) = 2*cav(4);
siavarv(x) = real(2*cav(3)); siavaiv(x) = imag(2*cav(3));
nfminv(x) = nfv(1); rnv(x) = nfv(2); Yoptv(x) = nfv(3);
```

```
end
end
end
```

B.3.2 Z_from_Y.m

```
function Z = Z_from_Y(Y)
%Z = Z_from_Y(Y)
z0 = 50;
Y11 = Y(:,1);
Y12 = Y(:,2);
Y21 = Y(:,3);
Y22 = Y(:,4);
Y_delta = Y11.*Y22 - Y12.*Y21;
Z11 = Y22./Y_delta;
Z12 = -Y12./Y_delta;
Z21 = -Y21./Y_delta;
Z22 = Y11./Y_delta;
Z = [Z11, Z12, Z21, Z22];
```

B.3.3 rb_from_h11.m

```
function rb=rb_from_h11(h11)
%rb=rb_from_h11(h11)
rb=circle(h11);
```

B.3.4 circle.m

```
function rb=circle(h11)
%rb=circle(h11)
ydata=imag(h11); ydata=ydata(:);
xdata=real(h11); xdata=xdata(:);
[ymin, y_ind]=min(ydata);
nsize=size(ydata);
para0=[xdata(y_ind), abs(ymin)];
newPara=fminsearch('myCostFunc', para0,[],[xdata ydata])
rb=newPara(1)-newPara(2);
```

B.3.5 myCostFunc.m

```
function cost=myCostFunc(para, data)
%para(1) is x0, para(2) is r
cost=sum((sqrt(data(:,2).^2+(data(:,1)-para(1)).^2)-para(2)).^2);
```

B.3.6 c_from_z_to_a.m

```
function C_A = C_from_Z_to_A(C_Z, A)
%C_A = C_from_Z_to_A(C_Z, A)
k = size(A, 1);
for i = 1:k;
   CZ = [C_Z(i,1), C_Z(i,2); C_Z(i,3), C_Z(i,4)];
   A_temp = [A(i,1), A(i,2); A(i,3), A(i,4)];
   Trans = [1, -A_temp(1,1); 0, -A_temp(2,1)];
   Trans_conj_trans = [Trans(1,1)', Trans(2,1)'; Trans(1,2)', Trans(2,2)'];
   CA = Trans*CZ*Trans_conj_trans;
   C_A(i,1) = (abs(Trans(1,1)))^2*CZ(1,1) + (abs(Trans(1,2)))^2*CZ(2,2)...
       + 2*real(Trans_conj_trans(1,1)*Trans(1,2)*CZ(2,1));
   C_A(i,2) = Trans(1,1)*Trans_conj_trans(1,2)*CZ(1,1)...
       +Trans(1,2)*Trans_conj_trans(1,2)*CZ(2,1)...
       +Trans(1,1)*Trans_conj_trans(2,2)*CZ(1,2)...
       +Trans(1,2)*Trans_conj_trans(2,2)*CZ(2,2);
   C_A(i,3) = C_A(i,2)';
   C_A(i,4) = (abs(Trans(2,1)))^2*CZ(1,1) + (abs(Trans(2,2)))^2*CZ(2,2)...
       + 2*real(Trans_conj_trans(2,2)*Trans(2,1)*CZ(1,2));
end
```

B.3.7 c_from_a_to_y.m

```
function C_Y = C_from_A_to_Y(C_A, Y)
%C_Y = C_from_A_to_Y(C_A, Y)
k = size(Y, 1);
for i = 1:k;
   CA = [C_A(i,1), C_A(i,2); C_A(i,3), C_A(i,4)];
   Y_temp = [Y(i,1), Y(i,2); Y(i,3), Y(i,4)];
   Trans = [-Y_temp(1,1),1; -Y_temp(2,1),0];
   Trans_conj_trans = [Trans(1,1)', Trans(2,1)'; Trans(1,2)', Trans(2,2)'];
   CY = Trans*CA*Trans_conj_trans;
   C_Y(i,1) = (abs(Trans(1,1)))^2*CA(1,1) + (abs(Trans(1,2)))^2*CA(2,2)...
       + 2*real(Trans_conj_trans(1,1)*Trans(1,2)*CA(2,1));
   C_Y(i,2) = Trans(1,1)*Trans_conj_trans(1,2)*CA(1,1)...
       +Trans(1,2)*Trans_conj_trans(1,2)*CA(2,1)...
       +Trans(1,1)*Trans_conj_trans(2,2)*CA(1,2)...
       +Trans(1,2)*Trans_conj_trans(2,2)*CA(2,2);
   C_Y(i,3) = C_Y(i,2)';
   C_Y(i,4) = (abs(Trans(2,1)))^2*CA(1,1) + (abs(Trans(2,2)))^2*CA(2,2)...
       + 2*real(Trans_conj_trans(2,2)*Trans(2,1)*CA(1,2));
```

```
end
```

B.3.8 nf_from_ca.m

```
%function nf = nf_from_ca(ca,Z0);
function nf = nf_from_ca(ca,Z0);
k=1.38066e-023;
T=300;
kt = k*T;
sia = 2*ca(:,4);
siava = 2*ca(:,3);
sva = 2*ca(:,1);
gva1 = 4*kt/sva;
rn1 = 1/gva1/Z0;
gia1 = sia/(4*kt);
yc1 = siava/sva;
gc1 = real(yc1);
bc1 = imag(yc1);
gso1 = sqrt(gva1*gia1-bc1^2);
bso1 = -bc1;
yopt1 = gso1+j*bso1;
gammaopt1 = (1-yopt1*Z0)/(1+yopt1*50);
fmin1 = 1+2*(gso1+gc1)/gva1;
nfmin1 = 10*log10(fmin1);
nf = [nfmin1 rn1 yopt1];
```

B.3.9 y_from_z.m

```
function Y = Y_from_Z(Z)
%Y = Y_from_Z(Z)
Z11 = Z(:,1);
Z12 = Z(:,2);
Z21 = Z(:,3);
Z22 = Z(:,4);
delta = Z11.*Z22 - Z12.*Z21;
Y11 = Z22./delta;
Y12 = -Z12./delta;
Y21 = -Z21./delta;
Y22 = Z11./delta;
Y = [Y11, Y12, Y21, Y22];
```

B.3.10 a_from_y.m

```
function A = A_from_Y(Y);
%from Y parameter to ABCD = [A B C D], A = A_from_Y(Y)
z0 = 50;
   Y11 = Y(:,1);
   Y12 = Y(:,2);
   Y21 = Y(:,3);
   Y22 = Y(:,4);
   Y_delta = Y11.*Y22 - Y12.*Y21;
   A11 = -Y22./Y21;
   A12 = -1./Y21;
   A21 = -Y_delta./Y21;
   A22 = -Y11./Y21;
   A = [A11, A12, A21, A22];
```

APPENDIX C
DESSIS INPUT DECK AND MATLAB PROGRAMMING FOR 50 NM L_{eff} MOSFET NOISE SIMULATION

C.1 Mesh files

C.1.1 BND file

```
Oxide "leftox" {rectangle[(-0.081,-0.15 ) (-0.025, 0)]}
PolySi "gatepoly" {rectangle[(-0.025, -0.001) (0.025, -0.15)]}
Oxide "rightox" {rectangle[(0.025, -0.15) (0.081, 0)]}
Oxide "gateox" {rectangle[(-0.025, 0) (0.025, -0.001)]}
Silicon "chanelsi" {rectangle[(-0.525, 0) (0.525, 1)]}
Contact "drain" {line[(0.081, 0) (0.525, 0)]}
Contact "gate" {line[(-0.022, -0.15) (0.022, -0.15)]}
Contact "source" {line[(-0.525, 0) (-0.081, 0)]}
Contact "bulk" {line[(-0.525, 1) (0.525, 1)]}
```

C.1.2 CMD file

```
Title "nmos"

Definitions {
    Refinement "all region"
    {
      MaxElementSize = (0.05 0.1)
      MinElementSize = (0.0025 0.01)
      RefineFunction = MaxTransDiff(Variable="DopingConcentration" Value=0.1)
    }
    Refinement "oxide"
    {
      MaxElementSize = (0.04 0.04)
      MinElementSize = (0.005 0.01)
    }
    Refinement "source"
    {
      MaxElementSize = (0.05 0.005)
      MinElementSize = (0.025 0.0025)
      RefineFunction = MaxTransDiff(Variable="DopingConcentration" Value=0.01)
    }
    Refinement "source1"
    {
```

```
      MaxElementSize = (0.1 0.01)
      MinElementSize = (0.05 0.005)
      RefineFunction = MaxTransDiff(Variable="DopingConcentration" Value=0.1)
    }
    Refinement "gate"
    {
      MaxElementSize = (0.04 0.04)
      MinElementSize = (0.005 0.01)
      RefineFunction = MaxTransDiff(Variable="DopingConcentration" Value=0.1)

    }
    Refinement "gateoxide"
    {
      MaxElementSize = (0.001 0.00025)
      MinElementSize = (0.001 0.00025)

    }
    Refinement "drain"
    {
      MaxElementSize = (0.0025 0.005)
      MinElementSize = (0.001 0.001)
      RefineFunction = MaxTransDiff(Variable="DopingConcentration" Value=0.001)
    }
    Refinement "refine"
    {
      MaxElementSize = (0.001 0.001)
      MinElementSize = (0.0005 0.0005)
      RefineFunction = MaxTransDiff(Variable="DopingConcentration" Value=0.001)
    }
    Refinement "interface"
    {
      MaxElementSize = (0.01 0.005)
      MinElementSize = (0.0025 0.005)
    }
 # Profiles
    Constant "bulkboron"
    {
      Species = "BoronActiveConcentration"
      Value =1e+15
    }
    Constant "bulkarsen"
    {
```

```
  Species = "ArsenicActiveConcentration"
  Value =1e+5
}
Constant "npoly"
{
  Species = "ArsenicActiveConcentration"
  Value =1e+21
}
Constant "channeln"
{
  Species = "ArsenicActiveConcentration"
  Value =1e+12
}
Constant "channelp"
{
  Species = "BoronActiveConcentration"
  Value =1e17
}
Constant "channelp2"
{
  Species = "BoronActiveConcentration"
  Value =1e+18
}
AnalyticalProfile "bulkn"
{
  Species = "ArsenicActiveConcentration"
  Function = gauss(peakpos=0, PeakVal =1.5e21,
            ValatDepth = 1e20,
             depth = 0.015
             )
  lateralfunction = gauss(standarddeviation = 0.002)
}
AnalyticalProfile "bulkn1"
{
  Species = "ArsenicActiveConcentration"
  Function = gauss(peakpos=0, PeakVal =1.5e21,
            ValatDepth = 1e20,
             depth = 0.043
             )
  lateralfunction = gauss(standarddeviation = 0.0095) #0.00613758)
}
AnalyticalProfile "bulkpg"
```

```
{
  Species = "BoronActiveConcentration"
  Function = gauss(peakpos=0, PeakVal =1e19,
             ValatDepth = 1e18,
              depth = 0.015
              )
  lateralfunction = gauss(standarddeviation = 0.002)
}
AnalyticalProfile "bulkpg1"
{
  Species = "BoronActiveConcentration"
  Function = gauss(peakpos=0, PeakVal =1e19,
             ValatDepth = 1e18,
              depth = 0.043
              )
  lateralfunction = gauss(standarddeviation = 0.0095) #0.00613758)
}
AnalyticalProfile "bulkp"
{
  Species = "BoronActiveConcentration"
  Function = gauss(peakpos=0, PeakVal=6.5e+18,
              ValatDepth = 3e18
              depth = 0.005700
              )
  lateralfunction = gauss(standarddeviation = 0.006)
}
AnalyticalProfile "bulkp2"
{
  Species = "BoronActiveConcentration"
  Function = gauss(peakpos=0, PeakVal =1e18,
             ValatDepth = 1e15,
              depth = 0.4
              )
  lateralfunction = gauss(standarddeviation = 0.002)
}
AnalyticalProfile "bulkp1"
{
  Species = "BoronActiveConcentration"
  Function = gauss(peakpos=0, PeakVal=1.35e18,
              ValatDepth = 1.2e18
              depth = 0.030
              )
```

```
      lateralfunction = gauss(standarddeviation = 0.06)
    }

}

Placements {
  # Refinement regions
    Refinement "all region"
    {
      Reference = "all region"
      RefineWindow = rectangle [(-0.525 -0.15), (0.525 1)]
    }
    Refinement "leftoxide"
    {
      Reference = "oxide"
      RefineWindow = rectangle [(-0.081 0), (-0.025 -0.15)]
    }
    Refinement "rightoxide"
    {
      Reference = "oxide"
      RefineWindow = rectangle [(0.025 0), (0.081 -0.15)]
    }
    Refinement "source1 instant"
    {
      Reference = "source1"
      RefineWindow = rectangle [(-0.525 0), (0.525 0.045)]
    }
    Refinement "source instant"
    {
      Reference = "source"
      RefineWindow = rectangle [(-0.102 0), (0.102 0.045)]
    }
    Refinement "gate"
    {
      Reference =  "gate"
      RefineWindow = rectangle [(-0.025 -0.15) (0.025 -0.001)]
    }
    Refinement "gaterefine"
    {
      Reference =  "gateoxide"
      RefineWindow = rectangle [(-0.025 0) (0.025 -0.001)]
    }
```

```
  Refinement "undergate"
  {
    Reference = "drain"
    RefineWindow = rectangle [(-0.052 0) (0.052 0.045)]
  }
  Refinement "interface1"
  {
    Reference = "interface"
    RefineWindow = rectangle [(-0.525 0.044), (0.525 0.047)]
  }
  Refinement "interface2"
  {
    Reference = "interface"
    RefineWindow = rectangle [(-0.081 0.001), (0.081 -0.002)]
  }
  Refinement "underrefine"
  {
    Reference = "refine"
    RefineWindow = rectangle [(-0.025 0) (0.025 0.025)]
  }
# Profiles
  Constant "bulkarsen instance"
  {
    Reference = "bulkarsen"
    EvaluateWindow
    {
      Element = rectangle [(-0.525 0), (0.525 1)]
      DecayLength = 0
    }
  }
  Constant "bulkboron instance"
  {
    Reference = "bulkboron"
    EvaluateWindow
    {
      Element = rectangle [(-0.525 0), (0.525 1)]
      DecayLength = 0
    }
  }
  Constant "channelboron instance"
  {
    Reference = "channelp"
```

```
  EvaluateWindow
  {
    Element = rectangle [(-0.525 0.045), (0.525 0.05)]
  #  direction = positive
    DecayLength = 0.20
  }
}
Constant "npoly instance"
{
  Reference = "npoly"
  EvaluateWindow
  {
    Element = rectangle [(-0.025 -0.15), (0.025 -0.001)]
    DecayLength = 0
  }
}
AnalyticalProfile "sourcen"
{
  Reference = "bulkn"
  ReferenceElement
 {
    Element = line[(-0.525 0) (-0.025 0)]
    Direction =positive
  }
  EvaluateWindow
  {
      Element = rectangle[(-0.525 0) (0 0.045)
                        ]
  }
}
AnalyticalProfile "drain"
{
 Reference = "bulkn"
  ReferenceElement
  {
   Element = line[(0.025 0) (0.525 0)]
    Direction =positive
  }
 EvaluateWindow
  {
      Element = rectangle[(0 0) (0.525 0.045)
                        ]
```

```
  }
}
AnalyticalProfile "sourcep"
{
  Reference = "bulkpg"
  ReferenceElement
 {
    Element = line[(-0.525 0) (-0.025 0)]
    Direction =positive
  }
  EvaluateWindow
  {
      Element = rectangle[(-0.525 0) (0 0.045)
                        ]
  }
}
AnalyticalProfile "drainp"
{
 Reference = "bulkpg"
  ReferenceElement
  {
   Element = line[(0.025 0) (0.525 0)]
    Direction =positive
  }
 EvaluateWindow
  {
      Element = rectangle[(0 0) (0.525 0.045)
                        ]
  }
}
AnalyticalProfile "sourcenl"
{
  Reference = "bulkn1"
  ReferenceElement
 {
    Element = line[(-0.525 0) (-0.081 0)]
    Direction =positive
  }
  EvaluateWindow
 {
      Element = rectangle[(-0.525 0)
                        (-0.025 0.045) ]
```

```
  }
}
AnalyticalProfile "drainl"
{
  Reference = "bulkn1"
  ReferenceElement
  {
    Element = line[(0.081 0) (0.525 0)]
    Direction =positive
  }
 EvaluateWindow
  {
      Element = rectangle[(0.025 0) (0.525 0.045)
                        ]
  }
}
AnalyticalProfile "sourcepl"
{
  Reference = "bulkpg1"
  ReferenceElement
 {
    Element = line[(-0.525 0) (-0.081 0)]
    Direction =positive
  }
  EvaluateWindow
 {
      Element = rectangle[(-0.525 0)
                        (-0.025 0.045) ]
  }
}
AnalyticalProfile "draipl"
{
  Reference = "bulkpg1"
  ReferenceElement
  {
    Element = line[(0.081 0) (0.525 0)]
    Direction =positive
  }
 EvaluateWindow
  {
      Element = rectangle[(0.025 0) (0.525 0.045)
                        ]
```

```
   }
 }
AnalyticalProfile "undergateboron1"
 {
   Reference = "bulkp"
   ReferenceElement
   {
     Element = line[(-0.008 0) (-0.006 0)]
     Direction =positive
   }
  EvaluateWindow
   {
       Element = rectangle[(-0.525 0)(0.525 1)
                         ]
  }
 }
AnalyticalProfile "undergateboron2"
 {
   Reference = "bulkp"
   ReferenceElement
   {
     Element = line[(0.006 0) (0.008 0)]
     Direction =positive
   }
  EvaluateWindow
   {
       Element = rectangle[(-0.525 0)(0.525 1)
                         ]
  }
 }
AnalyticalProfile "undergateboron1_1"
 {
   Reference = "bulkp1"
   ReferenceElement
   {
     Element = line[(-0.025 0.045) (-0.024 0.045)]
   }
  EvaluateWindow
   {
       Element = rectangle[(-0.525 0)(0.525 1)
                         ]
  }
```

```
    }
   AnalyticalProfile "undergateboron2_1"
    {
      Reference = "bulkp1"
      ReferenceElement
      {
        Element = line[(0.024 0.045) (0.025 0.045)]
      }
     EvaluateWindow
      {
          Element = rectangle[(-0.525 0)(0.525 1)
                           ]
     }
    }
}
```

C.2 Noise Simulation CMD file

```
Device nmos {

 Electrode {
   { Name="drain"   Voltage=0 }
   { Name="source"      Voltage=0 }
   { Name = "gate"    Voltage = 0 }
   { Name="bulk" Voltage=0 }
 }

 File {
   Grid      = "msh_msh.grd"
   Doping    = "msh_msh.dat"
   Current   = "noiseqmhdetvdswp_des.plt"
   Plot      = "noiseqmhdetvdswp_des.dat"
 }

 Physics{
    Areafactor= 1
    EffectiveIntrinsicDensity( Slotboom )
    Hydrodynamic(eTemp)

    Mobility(
      dopingdependence(Masetti)
      enormal(Lombardi)
```

```
      Highfieldsaturation(CarrierTempDrive)
    )
    eQCvanDort
    Fermi
    Noise ( DiffusionNoise ( eTemperature ))
 }

}
*-----------------------------------------------------------------------*
*--End of Device{}
*-----------------------------------------------------------------------*

Plot {
   eDensity hDensity
   TotalCurrent/Vector eCurrent/Vector hCurrent/Vector

   ElectricField Potential SpaceCharge
   Doping DonorConcentration AcceptorConcentration

   SRH Auger
   eQuasiFermi hQuasiFermi
   eEparal hEparal

   eMobility hMobility
   eVelocity hVelocity

   xMoleFraction

   BandGap BandGapNarrowing
   Affinity
   ConductionBand ValenceBand
}

Math {
   Extrapolate
   NotDamped=200
   Iterations=20
   NewDiscretization
   Derivatives
   RelerrControl
   Digits=6
```

```
}

File {
   Output  = "noiseqmhdetvdswp"
   ACExtract="noiseqmhdetvdswp"

}

System {
   nmos NMOS (drain=2  gate=1 source=0 bulk=0)
   Vsource_pset vg (1 0){ dc = 0 }
   Vsource_pset vd (2 0){ dc = 0 }
}

Solve {
   Coupled (Iterations=50) {poisson}
   Coupled { poisson Electron }
   Coupled {poisson Electron ElectronTemperature}
Quasistationary (
      initialstep = 0.2 MinStep=1e-1 MaxStep=1
      Goal {Parameter=vd.dc Voltage=0}
      Goal {Parameter=vg.dc Voltage=0.1}
   ){
   Coupled {poisson Electron ElectronTemperature}
    }
save(fileprefix = "vd0vg0.1acqmhd")
load(fileprefix = "vd0vg0.1acqmhd")
Quasistationary (
      initialstep = 0.5 MinStep=1e-1 MaxStep=1
      Goal {Parameter=vg.dc Voltage=0.2}
   ){
   Coupled {poisson Electron ElectronTemperature}
    }
save(fileprefix = "vd0vg0.2acqmhd")
Quasistationary (
      initialstep = 0.5 MinStep=1e-1 MaxStep=1
      Goal {Parameter=vg.dc Voltage=0.3}
   ){
   Coupled {poisson Electron ElectronTemperature}
    }
save(fileprefix = "vd0vg0.3acqmhd")
Quasistationary (
```

```
      initialstep = 0.5 MinStep=1e-1 MaxStep=1
      Goal {Parameter=vg.dc Voltage=0.4}
   ){
   Coupled {poisson Electron ElectronTemperature}
    }
save(fileprefix = "vd0vg0.4acqmhd")
Quasistationary (
      initialstep = 0.5 MinStep=1e-1 MaxStep=1
      Goal {Parameter=vg.dc Voltage=0.5}
   ){
   Coupled {poisson Electron ElectronTemperature}
    }
save(fileprefix = "vd0vg0.5acqmhd")
Quasistationary (
      initialstep = 0.5 MinStep=1e-1 MaxStep=1
      Goal {Parameter=vg.dc Voltage=0.6}
   ){
   Coupled {poisson Electron ElectronTemperature}
    }
save(fileprefix = "vd0vg0.6acqmhd")
Quasistationary (
      initialstep = 0.5 MinStep=1e-1 MaxStep=1
      Goal {Parameter=vg.dc Voltage=0.7}
   ){
   Coupled {poisson Electron ElectronTemperature}
    }
save(fileprefix = "vd0vg0.7acqmhd")
Quasistationary (
      initialstep = 0.5 MinStep=1e-1 MaxStep=1
      Goal {Parameter=vg.dc Voltage=0.8}
   ){
   Coupled {poisson Electron ElectronTemperature}
    }
save(fileprefix = "vd0vg0.8acqmhd")
Quasistationary (
      initialstep = 0.5 MinStep=1e-1 MaxStep=1
      Goal {Parameter=vg.dc Voltage=0.9}
   ){
   Coupled {poisson Electron ElectronTemperature}
    }
save(fileprefix = "vd0vg0.9acqmhd")
Quasistationary (
```

```
      initialstep = 0.5 MinStep=1e-1 MaxStep=1
      Goal {Parameter=vg.dc Voltage=1}
   ){
   Coupled {poisson Electron ElectronTemperature}
    }
save(fileprefix = "vd0vg1acqmhd")

newcurrent = "vd0vg0p1acqmhd_"
Coupled {poisson Electron ElectronTemperature}
load(fileprefix = "vd0vg0.1acqmhd")
Quasistationary (
      initialstep = 0.05 Increment = 1 MinStep=1e-2 MaxStep=0.1
      Goal {Parameter=vd.dc Voltage=1}
   ){
ACCoupled (
    StartFrequency = 1e9 EndFrequency =4e10
    NumberOfPoints = 10  linear
    Node(1 2) Exclude(vd vg)
    ObservationNode(1 2)
    ACExtraction = "acqmhdetvdswp"
    NoiseExtraction = "acqmhdetvdswp"
    NoisePlot = "acqmhdetvdswp"
    ) {Poisson Electron ElectronTemperature}
    }
newcurrent = "vd0vg0p2acqmhd_"
load(fileprefix = "vd0vg0.2acqmhd")
Quasistationary (
      initialstep = 0.05 Increment = 1 MinStep=1e-2 MaxStep=0.1
      Goal {Parameter=vd.dc Voltage=1}
   ){
ACCoupled (
    StartFrequency = 1e9 EndFrequency =4e10
    NumberOfPoints = 10  linear
    Node(1 2) Exclude(vd vg)
    ObservationNode(1 2)
    ACExtraction = "acqmhdetvdswp"
    NoiseExtraction = "acqmhdetvdswp"
    NoisePlot = "acqmhdetvdswp"
    ) {Poisson Electron ElectronTemperature}
    }
newcurrent = "vd0vg0p3acqmhd_"
load(fileprefix = "vd0vg0.3acqmhd")
```

```
Quasistationary (
      initialstep = 0.05 Increment = 1 MinStep=1e-2 MaxStep=0.1
      Goal {Parameter=vd.dc Voltage=1}
   ){
ACCoupled (
    StartFrequency = 1e9 EndFrequency =4e10
    NumberOfPoints = 10  linear
    Node(1 2) Exclude(vd vg)
    ObservationNode(1 2)
    ACExtraction = "acqmhdetvdswp"
    NoiseExtraction = "acqmhdetvdswp"
    NoisePlot = "acqmhdetvdswp"
    ) {Poisson Electron ElectronTemperature}
    }
newcurrent = "vd0vg0p4acqmhd_"
load(fileprefix = "vd0vg0.4acqmhd")
Quasistationary (
      initialstep = 0.05 Increment = 1 MinStep=1e-2 MaxStep=0.1
      Goal {Parameter=vd.dc Voltage=1}
   ){
ACCoupled (
    StartFrequency = 1e9 EndFrequency =4e10
    NumberOfPoints = 10  linear
    Node(1 2) Exclude(vd vg)
    ObservationNode(1 2)
    ACExtraction = "acqmhdetvdswp"
    NoiseExtraction = "acqmhdetvdswp"
    NoisePlot = "acqmhdetvdswp"
    ) {Poisson Electron ElectronTemperature}
    }
newcurrent = "vd0vg0p5acqmhd_"
load(fileprefix = "vd0vg0.5acqmhd")
Quasistationary (
      initialstep = 0.05 Increment = 1 MinStep=1e-2 MaxStep=0.1
      Goal {Parameter=vd.dc Voltage=1}
   ){
ACCoupled (
    StartFrequency = 1e9 EndFrequency =4e10
    NumberOfPoints = 10  linear
    Node(1 2) Exclude(vd vg)
    ObservationNode(1 2)
    ACExtraction = "acqmhdetvdswp"
```

```
    NoiseExtraction = "acqmhdetvdswp"
    NoisePlot = "acqmhdetvdswp"
    ) {Poisson Electron ElectronTemperature}
    }
newcurrent = "vd0vg0p6acqmhd_"
load(fileprefix = "vd0vg0.6acqmhd")
Quasistationary (
      initialstep = 0.05 Increment = 1 MinStep=1e-2 MaxStep=0.1
      Goal {Parameter=vd.dc Voltage=1}
   ){
ACCoupled (
    StartFrequency = 1e9 EndFrequency =4e10
    NumberOfPoints = 10  linear
    Node(1 2) Exclude(vd vg)
    ObservationNode(1 2)
    ACExtraction = "acqmhdetvdswp"
    NoiseExtraction = "acqmhdetvdswp"
    NoisePlot = "acqmhdetvdswp"
    ) {Poisson Electron ElectronTemperature}
    }
newcurrent = "vd0vg0p7acqmhd_"
load(fileprefix = "vd0vg0.7acqmhd")
Quasistationary (
      initialstep = 0.05 Increment = 1 MinStep=1e-2 MaxStep=0.1
      Goal {Parameter=vd.dc Voltage=1}
   ){
ACCoupled (
    StartFrequency = 1e9 EndFrequency =4e10
    NumberOfPoints = 10  linear
    Node(1 2) Exclude(vd vg)
    ObservationNode(1 2)
    ACExtraction = "acqmhdetvdswp"
    NoiseExtraction = "acqmhdetvdswp"
    NoisePlot = "acqmhdetvdswp"
    ) {Poisson Electron ElectronTemperature}
    }
newcurrent = "vd0vg0p8acqmhd_"
load(fileprefix = "vd0vg0.8acqmhd")
Quasistationary (
      initialstep = 0.05 Increment = 1 MinStep=1e-2 MaxStep=0.1
      Goal {Parameter=vd.dc Voltage=1}
   ){
```

```
ACCoupled (
    StartFrequency = 1e9 EndFrequency =4e10
    NumberOfPoints = 10  linear
    Node(1 2) Exclude(vd vg)
    ObservationNode(1 2)
    ACExtraction = "acqmhdetvdswp"
    NoiseExtraction = "acqmhdetvdswp"
    NoisePlot = "acqmhdetvdswp"
    ) {Poisson Electron ElectronTemperature}
    }
newcurrent = "vd0vg0p9acqmhd_"
load(fileprefix = "vd0vg0.9acqmhd")
Quasistationary (
      initialstep = 0.05 Increment = 1 MinStep=1e-2 MaxStep=0.1
      Goal {Parameter=vd.dc Voltage=1}
   ){
ACCoupled (
    StartFrequency = 1e9 EndFrequency =4e10
    NumberOfPoints = 10  linear
    Node(1 2) Exclude(vd vg)
    ObservationNode(1 2)
    ACExtraction = "acqmhdetvdswp"
    NoiseExtraction = "acqmhdetvdswp"
    NoisePlot = "acqmhdetvdswp"
    ) {Poisson Electron ElectronTemperature}
    }
newcurrent = "vd0vg1acqmhd_"
load(fileprefix = "vd0vg1acqmhd")
Quasistationary (
      initialstep = 0.05 Increment = 1 MinStep=1e-2 MaxStep=0.1
      Goal {Parameter=vd.dc Voltage=1}
   ){
ACCoupled (
    StartFrequency = 1e9 EndFrequency =4e10
    NumberOfPoints = 10  linear
    Node(1 2) Exclude(vd vg)
    ObservationNode(1 2)
    ACExtraction = "acqmhdetvdswp"
    NoiseExtraction = "acqmhdetvdswp"
    NoisePlot = "acqmhdetvdswp"
    ) {Poisson Electron ElectronTemperature}
    }
```

```
}
```

C.3 MATLAB Programming for Simulation Results

C.3.1 Main file

```
close all; clear all; clc;
q = 1.6e-19;
kt = 0.0259*q;
datapath = 'D:\Yan\research\nmos\50nm\vdswpdata';
cd(datapath);
filename = {'vdswpvg0p1', 'vdswpvg0p2', 'vdswpvg0p3',...
                  'vdswpvg0p4', 'vdswpvg0p5', 'vdswpvg0p6',...
                  'vdswpvg0p7', 'vdswpvg0p8', 'vdswpvg0p9', 'vdswpvg1'};
x1 = 1;
Vdtmp = [0.025 0.05 0.075 0.1 0.125 0.15 0.175 0.2 0.225...
               0.25 0.275 0.3 0.325 0.35 0.375 0.4 0.425 0.45...
               0.475 0.5 0.525 0.55 0.575 0.6 0.625 0.65 0.675...
               0.7 0.725 0.75 0.775 0.8 0.825 0.85 0.875 0.9...
               0.925 0.95 0.975 1.0];
for vdsel = [1:length(Vdtmp)],
    Vdx = Vdtmp(vdsel);
fileNumber=length(filename);
datasel = 1; %1: bias dependence, 2: frequency dependence

for filsel = [1:10],
    load(filename{filsel});
Jd = Id./Area.*1e6; Jg = Ig./Area.*1e6;
nx = x1;
for n = [nx]; %frequency or bias point selection.
switch datasel
case 1 %bias dependence
    sv12x = conj(sv12); sv12eex = conj(sv12ee); sv12hhx = conj(sv12hh);
    SV = [sv1(:,n) sv12x(:,n) conj(sv12x(:,n)) sv2(:,n)];
    SVee = [sv1ee(:,n) sv12eex(:,n) conj(sv12eex(:,n)) sv2ee(:,n)];
    SVhh = [sv1hh(:,n) sv12hhx(:,n) conj(sv12hhx(:,n)) sv2hh(:,n)];
    Y = [Y11(:,n) Y12(:,n) Y21(:,n) Y22(:,n)]; Z = z_from_Y(Y);
    numend = num_of_bias;
case 2 %frequency dependence
    sv12x = conj(sv12); sv12eex = conj(sv12ee); sv12hhx = conj(sv12hh);
    SV = [conj(sv1(n,:)') conj(sv12x(n,:)') sv12x(n,:)' conj(sv2(n,:)')];
    SVee = [conj(sv1ee(n,:)') conj(sv12eex(n,:)') sv12eex(n,:)' conj(sv2ee(n,:)')];
```

```
    SVhh = [conj(sv1hh(n,:)') conj(sv12hhx(n,:)') sv12hhx(n,:)' conj(sv2hh(n,:)')];
    Y = [conj(Y11(n,:)') conj(Y12(n,:)') conj(Y21(n,:)') conj(Y22(n,:)')];
    Z = z_from_Y(Y); S = s_from_y(Y);
    numend = num_of_freq;
    Igx = Ig(x1);Idx = Id(x1);
    clear Ig; clear Id;
    Ig = Igx; Id = Idx;
end

for x = 1:numend,
    y = Y(x,:); z = Z(x,:); a = a_from_y(y);
    cz = 0.5.*SV(x,:); ca = c_from_z_to_a(cz, a);
    cy = c_from_a_to_y(ca, y);
    nf = nf_from_ca(ca, 50);
    ch = c_from_y_to_h(cy, y);
    svb(x) = 2*cz(1); svc(x) = 2*cz(4);
    svbvcr(x) = 2*real(cz(2)); svbvci(x) = 2*imag(cz(2));
    cvbvcr(x) = svbvcr(x)/sqrt(svc(x)*svb(x));
    cvbvci(x) = svbvci(x)/sqrt(svc(x)*svb(x));
    sva(x) = 2*ca(1); sia(x) = 2*ca(4);
    siavar(x) = 2*real(ca(3)); siavai(x) = 2*imag(ca(3));
    ciavar(x) = siavar(x)/sqrt(sia(x)*sva(x));
    ciavai(x) = siavai(x)/sqrt(sia(x)*sva(x));
    sib(x) = 2*cy(1); sic(x) = 2*cy(4);
    sicibr(x) = 2*real(cy(3)); sicibi(x) = 2*imag(cy(3));
    cicibr(x) = sicibr(x)/sqrt(sib(x)*sic(x));
    cicibi(x) = sicibi(x)/sqrt(sib(x)*sic(x));
    svh(x) = 2*ch(1); sih(x) = 2*ch(4);
    svhihr(x) = 2*real(ch(2)); svhihi(x) = 2*imag(ch(2));
    cvhihr(x) = svhihr(x)/sqrt(svh(x)*sih(x));
    cvhihi(x) = svhihi(x)/sqrt(svh(x)*sih(x));
    nfmin(x) = nf(1);  rn(x) = nf(2); Yopt(x) = nf(3);

    czee = 0.5.*SVee(x,:); caee = c_from_z_to_a(czee, a);
    cyee = c_from_a_to_y(caee, y); nfee = nf_from_ca(caee, 50);
    svbee(x) = 2*czee(1); svcee(x) = 2*czee(4);
    svbvcree(x) = 2*real(czee(2)); svbvciee(x) = 2*imag(czee(2));
    cvbvcree(x) = svbvcree(x)/sqrt(svcee(x)*svbee(x));
    cvbvciee(x) = svbvciee(x)/sqrt(svcee(x)*svbee(x));
    svaee(x) = 2*caee(1); siaee(x) = 2*caee(4);
    siavaree(x) = 2*real(caee(3)); siavaiee(x) = 2*imag(caee(3));
    ciavaree(x) = siavaree(x)/sqrt(siaee(x)*svaee(x));
```

```
    ciavaiee(x) = siavaiee(x)/sqrt(siaee(x)*svaee(x));
    sibee(x) = 2*cyee(1); sicee(x) = 2*cyee(4);
    sicibree(x) = 2*real(cyee(3)); sicibiee(x) = 2*imag(cyee(3));
    cicibree(x) = sicibree(x)/sqrt(sibee(x)*sicee(x));
    cicibiee(x) = sicibiee(x)/sqrt(sibee(x)*sicee(x));
    nfminee(x) = nfee(1);  rnee(x) = nfee(2); Yoptee(x) = nfee(3);

    czhh = 0.5.*SVhh(x,:); cahh = c_from_z_to_a(czhh, a);
    cyhh = c_from_a_to_y(cahh, y); nfhh = nf_from_ca(cahh, 50);
    svbhh(x) = 2*czhh(1); svchh(x) = 2*czhh(4);
    svbvcrhh(x) = 2*real(czhh(2)); svbvcihh(x) = 2*imag(czhh(2));
    cvbvcrhh(x) = svbvcrhh(x)/sqrt(svchh(x)*svbhh(x));
    cvbvcihh(x) = svbvcihh(x)/sqrt(svchh(x)*svbhh(x));
    svahh(x) = 2*cahh(1); siahh(x) = 2*cahh(4);
    siavarhh(x) = 2*real(cahh(3)); siavaihh(x) = 2*imag(cahh(3));
    ciavarhh(x) = siavarhh(x)/sqrt(siahh(x)*svahh(x));
    ciavaihh(x) = siavaihh(x)/sqrt(siahh(x)*svahh(x));
    sibhh(x) = 2*cyhh(1); sichh(x) = 2*cyhh(4);
    sicibrhh(x) = 2*real(cyhh(3)); sicibihh(x) = 2*imag(cyhh(3));
    cicibrhh(x) = sicibrhh(x)/sqrt(sibhh(x)*sichh(x));
    cicibihh(x) = sicibihh(x)/sqrt(sibhh(x)*sichh(x));
    nfminhh(x) = nfhh(1);  rnhh(x) = nfhh(2); Yopthh(x) = nfhh(3);
end
end
end
```

C.3.2 c_from_y_to_h.m

```
function x = c_from_y_to_h(cy, Y);
%function x = c_from_y_to_h(cy, Y);
Y11 = Y(1); Y21 = Y(3);
sin1 = cy(1); sin2 = cy(4); sin1in2 = cy(2); sin2in1 = cy(3);
        sv = sin1./(abs(Y11)).^2;
        si= sin2 + sin1.*(abs(Y21./Y11)).^2-...
            2.*real(Y21./Y11.*sin1in2);
        svi = conj(Y21)./(abs(Y11)).^2.*sin1 -...
            sin1in2./Y11;
x = [sv svi conj(svi) si];
```